COORDINATION AND REDOX CHEMISTRY OF ANTIMONY-BASED LIGANDS AND APPLICATIONS IN ORGANOMETALLIC CATALYSIS

A Dissertation

by

YING-HAO LO

Submitted to the Office of Graduate and Professional Studies of
Texas A&M University
in partial fulfillment of the requirements for the degree of

DOCTOR OF PHILOSOPHY

Chair of Committee,	François P. Gabbaï
Committee Members,	Michael B. Hall
	Michael Nippe
	Hung-Jen Wu
Head of Department,	Simon W. North

December 2019

Major Subject: Chemistry

ABSTRACT

The use of Z-ligands to modulate the electronic property of transition metal centers is a powerful strategy in catalyst design. Our group has shown that antimony-based ambiphilic ligand, accept electron density from adjacent metal centers by the σ* orbital of the antimony (V) center and thus increasing the electrophilic reactivity of the trancition metal center. In this thesis, we were eager to determine if the charge of the Z-type ligand can be used to further enhance this effect. To this end, we synthesized a dicationic gold complex [**46**]$^{2+}$ ([(*o*-(Ph_2P)C_6H_4)$_2$(*o*-Ph_2PO)C_6H_4)SbAuCl]$^{2+}$) featuring a dicationic antimony (V) ligand with a phosphine oxide arm coordinating to the antimony center. Both experimental and computational results show that the gold complex possess a strong Au→Sb interaction reinforced by the dicationic character of the antimony center. The gold-bound chloride anion of this complex is rather inert and necessitates the addition of excess $AgNTf_2$ to undergo activation. The activated complex, referred to as [**47**]$^{2+}$ ([((*o*-(Ph_2P)C_6H_4)$_2$(*o*-Ph_2PO)C_6H_4)SbAuNTf$_2$]$^{2+}$) readily catalyzes both the polymerization and the hydroamination of styrene. This atypical reactivity underscores the strong σ-accepting properties of the dicationic antimony ligand and its activating impact on the gold center.

Building on these original results, we have chosen to investigate antimony-substituted 2,2′-bipyridine (bipy) ligands in order to determine if the redox activity of the peripheral antimony center could be used to influence the reactivity of a transition metal coordinated to the bipy ligand. To this end, we synthesized 4-diphenylstibino-2,2′-

bipyridine (**54**), which could be obtained by reaction of 4-lithio-2,2′-bipyridine with Ph_2SbCl. The ligand **54** was treated with $Pt(CH_3CN)_2Cl_2$ to afford the platinum complex **55**. Interestingly, the latter reacts with $PhICl_2$ to afford **56**, a complex in which the peripheral stibine moiety has been converted into a dichlorostiborane. Complexes **55** and **56** have both been fully characterized. Computational, UV–vis, and cyclic voltammetry studies show that oxidation of the antimony atom leads to a lowering of the bipy-centered LUMO, indicating that **56** is more electron deficient than **55**. A congruent picture emerges from reactivity studies, which show that **56** is a more active catalyst for the hydroarylation of ethyl propiolate by mesitylene.

A similar concept was also applied to cyclometalated iridium(III) complexes. Reaction of 4-(diphenylstibino)-2,2′-bipyridine (**54**) with $[(ppy)_2Ir(\mu\text{-}Cl)]_2$ afforded the corresponding tris-chelate iridium complex $[(ppy)_2Ir(\mathbf{54})]^+$ ($[\mathbf{64}]^+$) which was isolated as a hexafluorophosphate salt ($[\mathbf{64}][PF_6]$). Reaction of $[\mathbf{64}][PF_6]$ with excess $PhICl_2$ in DMSO induced the conversion of the diphenylantimony moiety of $[\mathbf{65}]^+$ into an anionic diphenyltrichloroantimonate leading to a zwitterionic complex referred to as **65**-Cl. Complexes $[\mathbf{64}][PF_6]$ and **65**-Cl have been characterized by NMR and the structure of **65**-Cl confirmed using X-ray diffraction. DFT calculations and electrochemical measurments show that the electron-rich diphenyltrichloroantimonate moiety in **65**-Cl cathodically shifts the Ir(III/IV) redox couple. Luminescence measurements also show that **65**-Cl is less emissive than $[\mathbf{64}]^+$.

DEDICATION

For Mom, Dad and Wan-Shan

ACKNOWLEDGEMENTS

First, I would like to express my greatest appreciation to my research advisor, Prof. François Gabbaï, who gave me golden opportunity to join his research group and study these wonderful projects. His expertise, guidance and enduring patience support me to pursue my Ph.D. degree. I have learned significantly from him and growth as a better scientist during my career in graduate school. Thank you, François.

I am deeply thankful to the members of the Gabbaï group. Dr. Kewei Huang, Dr. Boris Vabre, Dr. Daniel Tofan, Dr. Guillaume Bélanger-Chabot, Dr. Sumit Sahu, Dr. Kantapat Chansaenpak, Dr. Haifeng Yang, Dr. Masato Hirai, Dr. James (Stuart) Jones, Dr. Anna Marie Christianson, Dr. Rajendra Kumar George, Dr. Rosmita Borthakur, Dr. Lewis Wilkins, Dr. Mohamed Saber, Dr. Mengxi Yang, Dr. Chang-Hong Chen, Dr. Srobona Sen, Ahmed Ali, Elham Tabei, Ying-Hao Lo, Di You, Kevin Jack, Mohammadjavad Karimi, Gyeong-Jin Park, Jesse Smith, Elisha Litle, Benyu Zhou. Very special thanks go to Masato, Stuart, Mengxi and Chang-Hong for their mentorship and guidance during the early years of my Ph.D. I would also like to thank my committee. Dr. Michael Hall, Dr. Michael Nippe and Dr. Hung-Jen Wu, who provide guidance through my Ph.D. career.

Finally, I sincerely thank my parents who always back me up in both mentally and materially. Without their assistance, I could not achieve this moment. I also want to thank my wife, Wan-Shan, who dedicates tremendous contribution to support my Ph.D. career and make our family precious.

CONTRIBUTORS AND FUNDING SOURCES

Contributors

This work was supervised by a dissertation committee consisting of Professor François P. Gabbaï (advisor), Professor Michael B. Hall and Prof. Michael Hall of the Department of Chemistry and Professor Hung-Jen Wu of the Department of Chemical Engineering.

The crystal structures of the complex [**51**][OTf]$_2$ mentioned in the **Chapter II** was solved by Dr. Nattamai Bhuvanesh. The ^{31}P MAS measurements on complex [**45a**][Cl] was performed by Dr. Vladimir Bakhmoutov of the Department of Chemistry.

The software and computational resources for computational studies were supported by the Laboratory for Molecular Simulation at Texas A&M University.

All other work conducted for the dissertation was completed by the student independently.

Funding Sources

This graduate work was supported by the National Science Foundation (CHE-1566474), the Welch Foundation (A-1423), and Texas A&M University (Arthur E. Martell Chair of Chemistry).

NOMENCLATURE

Bipy	bipyridine
COD	Cyclooctadiene
COE	Cyclooctene
DCM	Dichloromethane
DFT	Density functional theory
DMAP	4-Dimethylformamide
DMSO	Dimethyl sulfoxide
ESI	Electron spray ionization
GC	Gas chromatography
HOMO	Highest occupied molecular orbital
LUMO	Lowest unoccupied molecular orbital
MeCN	Acetonitrile
MLCT	Metal-to-ligand charge transfer
MS	Mass spectrometry
NBO	Naturel bond orbital
NFSI	N-fluorobenzenesulfonimide
NLMO	Natural localized molecular orbital
NMR	Nuclear magnetic resonance
NTO	Naturel transition orbital
Phen	phenanthroline

Phpy	2-phenylpyridine
TBAT	Tetra-n-butylammonium triphenyldifluorosilicate
TBAF	Tetra-n-butylammonium fluoride
TD-DFT	Time-dependent density functional theory
TFA	Trifluoroacetic acid
THF	Tetrahydrofuran
tht	Tetrahydrothiophene
TN	Transition metal
XRD	X-ray diffraction

TABLE OF CONTENTS

Page

LIST OF FIGURES

Page

LIST OF TABLES

Page

CHAPTER I

INTRODUCTION TO THE CHEMISTRY OF ANTIMONY SPECIES AND THEIR APPLICATIONS

1.1 Coordination chemistry of main group Lewis acids

1.1.1 Main group element as a Lewis acid

Lewis acidity is a term used to describe a molecule's ability to accept electron density from a Lewis base.[1] Upon accepting this electron densities, the adduct formed may be described as possessing a dative bond, and additional thermodynamic stabilization is observed.[2] A typical main group Lewis acid is $B(C_6F_5)_3$, which can serve as an electrophilic catalyst in organic synthesis[3-6] and as an activator for polymerization catalysts.[7-9] The acidity of these group 13 Lewis acids results from their empty p orbital and unsaturated coordinated center.[10] On the other hand, group 15 compounds have their inherent Lewis acidity resulting from their ability to form hypervalent compounds. For example, electrophilic phosphonium(V) cations are able to activate various organic reactions, such as hydroformylation[11] and the cyanosilylation of aldehydes.[12] Antimony (V) compounds are renowned for their strong Lewis acidity. For example, magic acid, a mixture of fluorosulfuric acid (HSO_3F) and pentafluoroantimony (SbF_5), shows a pKa of -20 which is 10^{10} stronger than HSO_3F alone. Additionally, experimental work by Gutmann has shown that $SbCl_5$ has a higher chloride affinity than BCl_3.[13] The Krossing group was able to draw similar conclusions computationally, finding that the gas phase fluoride ion affinity (FIA) of SbF_5 is higher than that of BF_3 by about 150 kJ/mol (489

kJ/mol versus 338kJ/mol).[14] Despite the incredible acidity displayed within these antimony-based inorganic molecules, their use has remained scared. Often the hygroscopic and corrosive nature of antimony species, such as SbF_5 deters prospective users from employing antimony halides in their synthetic endeavors, fearing they may produce HF. Since $B(C_6F_5)_3$ has enhanced stability in comparison to BF_3 while maintaining a comparable Lewis acidity,[15] our group formulated the idea of installing organic substituents to tame the high reactive antimony species. For example, triaryl-catecholate-stiboranes show a high tolerance toward water, while maintaining their ability to form adducts with Lewis bases, such as fluorides[16] and phosphine oxides.[17] Different from the group 13 compounds, the Lewis acidity of antimony-based compounds originates from their low-energy σ* orbital (Figure 1).[18-21] The large size of the atom and the high coordination numbers it can achieve are other positive factors contributing to the high Lewis acidity of antimony.

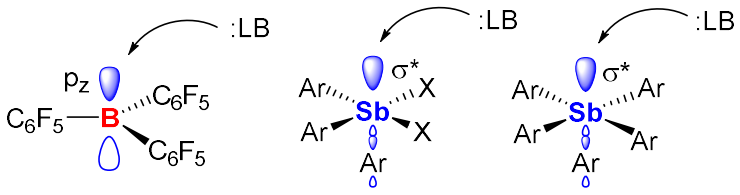

Figure 1. Illustration of empty p orbitals in boranes and σ* orbitals in stiboranes.

In addition to hypervalent Sb(V) species, Gutmann has shown that $SbCl_3$ is capable of forming an adduct with Et_3PO as the base and provided the trend in Lewis acidity for various inorganic chlorides:[13]

$$SbCl_5 > SnCl_4 > ZnCl_2 > SbCl_3 > PCl_5$$

Interestingly, $SbCl_3$ is even more acidic than PCl_5. It probably illustrated the importance of the stability in the conjugated bases, which the acidity of the P(V) might be attenuated due to high steric hindrance in the resulting species with high coordination number.

Organic antimony (III) chloride derivatives have also been explored as in compounds **1**, **2** and **3** (Figure 2).[22-25] The retention of Lewis acidic property was established by the presence of a strong dative bond formation via a nitrogen-containing donor. Moreover, the increasing number of halogen ligands on the antimony center enhances the Lewis acidity of the antimony (III) species. Perhaps most importantly, however, is the accessible two-electron oxidation of antimony to increase the Lewis acidity by generating associated hypervalent antimony (V) species, such as a neutral stiborane or cationic stibonium.

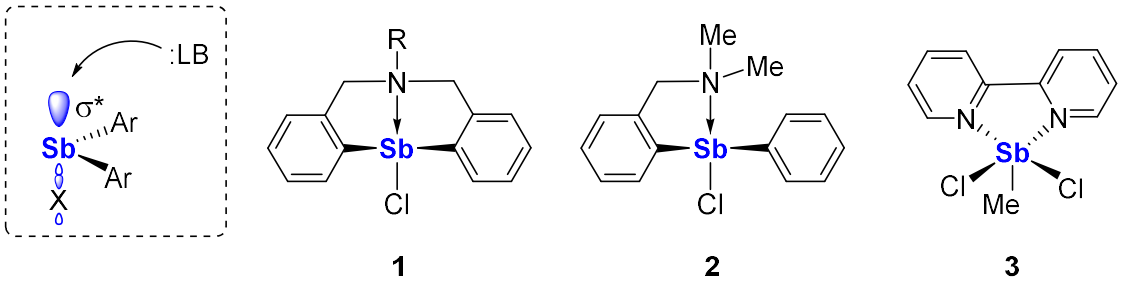

1 **2** **3**

Figure 2. Antimony(III) compounds containing Lewis acid-base adducts.

1.1.2 Group13 element-based Z-type ligands

The Lewis acidity of the main-group elements has triggered a new evolution of Z-type ligands.[26-28] Different form traditional anionic X-type or neutral L-type ligands,[29] which donate electrons toward transition metal centers, Z-type ligands accept an electron pair from a metal center into the main group moiety (Figure 3). These donor – acceptor

interactions, which have σ-character, originate from donation from the filled d-orbitals of a metal center to an empty orbital within the main group center and simultaneously stabilize the vacant p orbital of the metal.[30-33] The net effect of this stabilization results is an enhanced Lewis acidity of the transition metal.

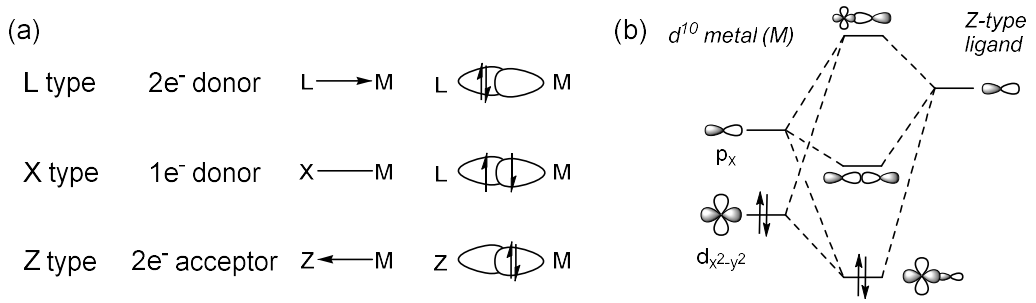

Figure 3. Orbital illustration of σ bond between metal and X-, L- or Z-type ligands.

The existence of a σ bond between a transition metal and a main group Lewis acid has been established for three main types of electron rich fragments: (a) $M(CO)_x$, M[34] = Cr, Mo, W, Co,[35] and Fe[36] ; (b) half-sandwich complexes of Fe,[36] , Ru[37], Ir[38] and Rh,[39] and (c) $Pt(PCy_3)_2$ complex which are shown in Figure 4.[40-42] The Lewis acid involved in these structures are all traditional moieties such as $AlCl_3$, $AlPh_3$, $GaCl_3$ and SO_2 serving to stabilize the metal complexes. A limit of this approach comes from the fact that the Lewis acid may abstract or interact with the ligands rather than the metal center.

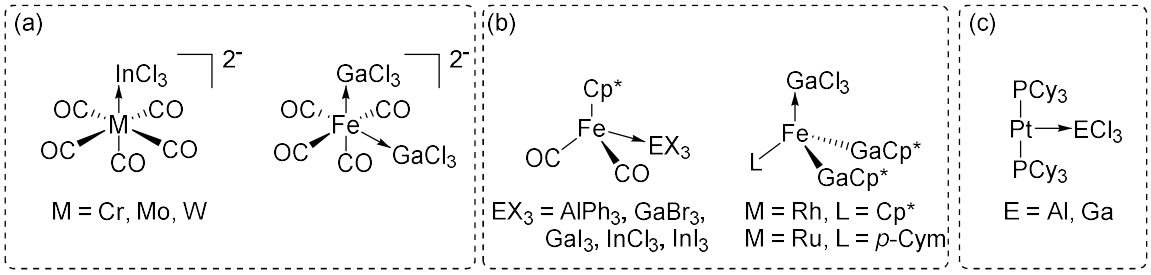

Figure 4. Selected examples of transition metal complexes featuring Z-type ligands.

Over the past 40 years, Z-type ligands have been developed into ambiphilic ligands, which combine L-type and Z-type ligand characteristics.[28] The former is employed to coordinate to the metal center and bring it close to the Z-type ligand. The rigidness in the structure of the ambiphilic ligand also prevents the interaction between the Lewis acidic center and other L type ligands. The first transition metal complexes of this type featured boron as Lewis acid as in the case of complex **4** which was prepared by Hill (Figure 5a).[43] The short distance (2.161(5) Å) between ruthenium and boron suggests the existence of a Ru→B interaction. This pioneering work initiated further efforts in the coordination chemistry of boron-based Z-type ligands. The Bourissou and Ozerov groups both investigated ambiphilic phosphine–borane ligands, and the corresponding complexes formed with group 9, 10, and 11 transition metals. (Figure 5b).[44-48] The supported phosphine ligands coordinate to the metal, bringing the Lewis acid close enough to interact with the metal center. The presence of a TM→B interaction is characterized by the short distance between the metal and the boron center. Another method to investigate the nature of the TM→B interaction is Natural Bond Orbital (NBO) analysis, which can provide insights about the donor-acceptor characteristic and

the strength of the dative bond. The TM→B bond reduces the electron density on the metal center, which would lead to increased electrophilicity and a change in the geometry at the metal center. Perhaps the most exciting aspect about these Z-ligands complexes is their applications within catalysis.

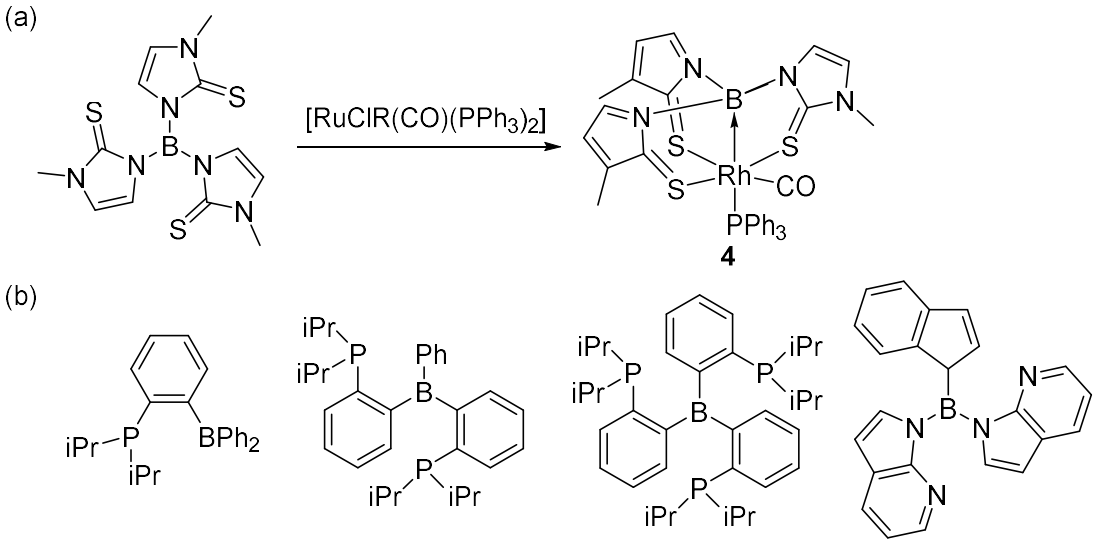

Figure 5. (a) First example of transition metal complex featuring the ambiphilic boron Z-ligand. (b) Examples of ambiphilic ligands featuring boron.

1.2 Antimony-based Z-type ligands for transition metals

Boron-based Z-type ligands have been categorized as σ-acceptors that increase the electrophilicity of a metal center. Inspired by this idea and the fact that antimony molecule displays strong Lewis acidity, we became eager to use an antimony atom as the Lewis acidic center of ambiphilic ligands.

1.2.1 Cationic antimony-based ambiphilic ligands for transition metals

Our exploration into the coordination chemistry of ambiphilic antimony ligands started with complexes featuring the 1,8-naphthalenediyl backbone **5** and [**6**][PF_6]

(Figure 6). These complexes feature an antimony (V) moiety and a mercury (**5**)[60] or gold metal center ([**6**]$^{+}$).[61] Both complexes show a donor-acceptor interaction between the metal and the antimony center. The Au–Sb distance (avg. 2.7616(8) Å) is shorter than the Hg–Sb distance (3.0601(7) Å) indicating that the gold(I) center is more the metallobasic than Hg(II) center. The combination of a highly Lewis acidic stibonium and an electron-rich late transition metal center lead to an electrophilic d-block metal center. The enhancement of Lewis acidity of the mercury center is reflected by its ability to bind halides (Cl^-, Br^-, I^-), N, N-dimethylaminopyridine (DMAP) and tetrahydrofuran (THF), while the diphenyl mercury ($HgPh_2$) does not show this Lewis acidic property (Figure 7a). These results show that Lewis acidic antimony center make the coordinated d-block metal center more electrophilic for anions.

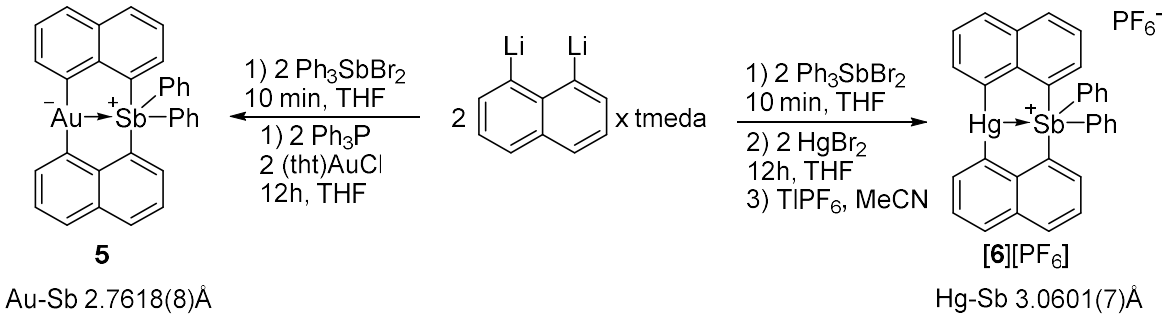

5

Au-Sb 2.7618(8)Å

[**6**][PF_6]

Hg-Sb 3.0601(7)Å

Figure 6. Synthesis of **5** and [**6**][PF_6]

The cationic antimony ligand, stabilized by donation for the metal, still presents Lewis acidity toward fluoride (Figure 7b). The antimony center in both complexes is able to bind fluoride, which suggest that the fluoride affinity of antimony is remains high.

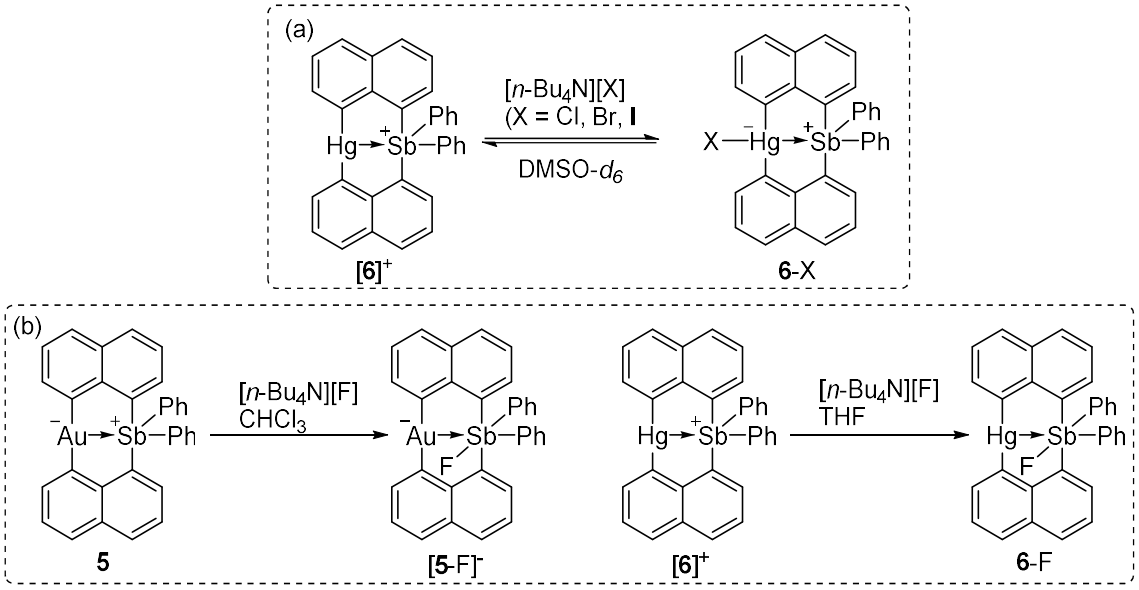

Figure 7. (a) Coordination chemistry at the mercury center in [**6**]$^{+}$. (b) The reaction of **5** and [**6**]$^{+}$ with F^{-}.

1.2.2 Antimony(III)-based ambiphilic ligands for Z-type ligands

Lewis acidic antimony (III) moieties have also been employed in Z-type ligands. Bis(phosphinyl)stibine ligands **7**-Ph and **7**-Cl were successfully coordinated to the gold to afford complexes **8** and **9** (Figure 8).[49] Although **8** and **9** are structurally similar, the nature of the interaction between Sb and Au are demonstrated to be different based on structural and computational analysis. The Sb–Au–Cl angle in **9** (141.73(4)°) shows greater linearity than that in **8** (115.09(2)°). These results suggest that the chlorostibine ligand serves as a Z-type ligand and make the coordination sphere on the gold center change. The second indicator is the computational results from NBO analysis. The donor-acceptor interaction in the Sb–Au in complex **9** has been assigned as a lp(Au)→σ*(Sb-Cl) interaction, while complex **8** shows both a lp(Sb)→p(Au) and a lp(Au)→σ*(Sb–C_{Ph}) interaction. This computational data suggests that the chlorostibine

moiety can be employed as a pure Z-type ligand, while the situation is more ambiguous in the case of the phenylstibine ligand.

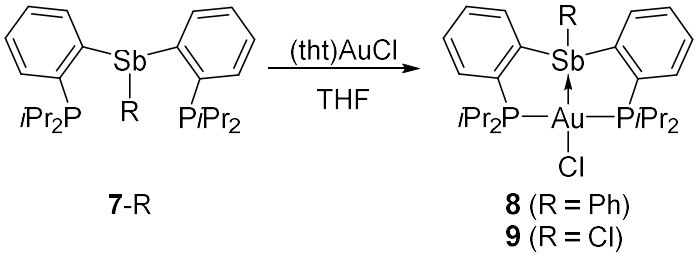

7-R

8 (R = Ph)
9 (R = Cl)

Figure 8. Synthesis of **8** and **9**.

1.2.3 Coordination sphere of the main group element acting as a Z-type ligand

Antimony Z-type ligands retain Lewis acidity and are capable of anion binding, despite the coordination of the metallobase.[50-59] The change in the coordination sphere of the antimony center results in an alternation of the M→Z characteristic, which has been termed as coordination non-innocence.[60] For example, the complex [**10**]$^+$ or [**11**]$^+$ (Figure 9), which is the isolobal to the anion-binding stibonium species **A**, has been transformed to the corresponding fluoride-coordinated complex.[50]

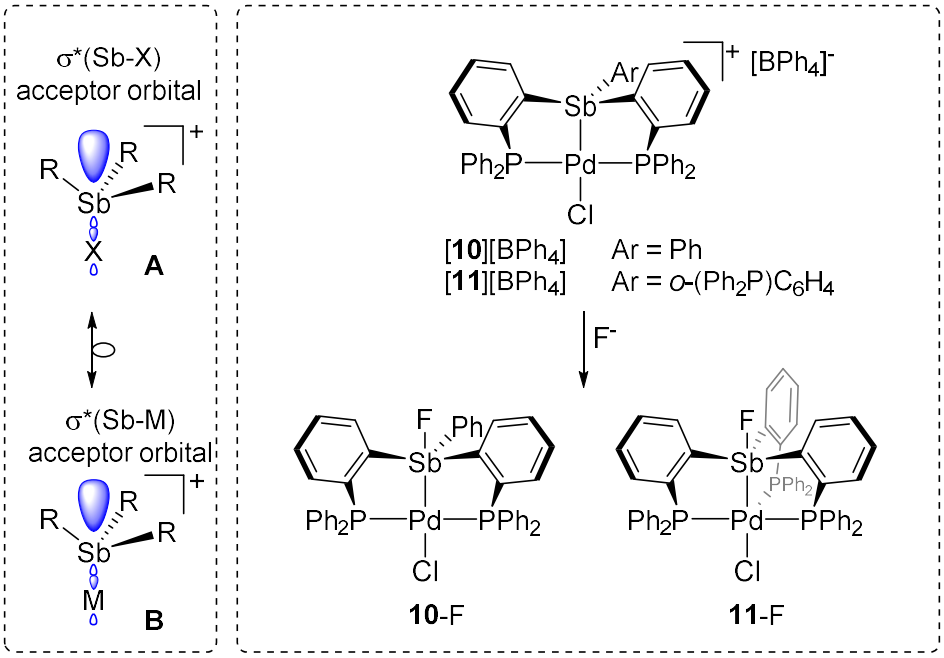

Figure 9. Isolobal relationship between $[R_3SbX]^+$ and $[(R_3Sb)Pd]^+$ (Left). Synthesis of [**10**][BPh_4], [**11**][BPh_4], and their fluoride adducts (Right).

The M→Z ligand interaction has been investigated experimentally and computationally for a series of platinum complexes $[\mathbf{12}]^{2+}$, $[\mathbf{13}]^+$ and **14** where the coordination sphere gets varied by the fluoride coordination (Figure 10).[55-57] The progressive coordination of fluoride to the antimony center leads to an increment of the Sb–Pt bond distance, indicating a weaker Sb–Pt interaction upon fluoride binding. This phenomenon is supported by NLMO calculations, which suggest the bonding pair is closer to the platinum after the coordination of fluoride anions, meaning a higher degree of polarization of the bonding pair toward platinum. Overall, the coordination noninnocence of the Sb–M complexes was demonstrated with fluoride anion binding and its ability to modulate the polarization of the M–Sb bond.

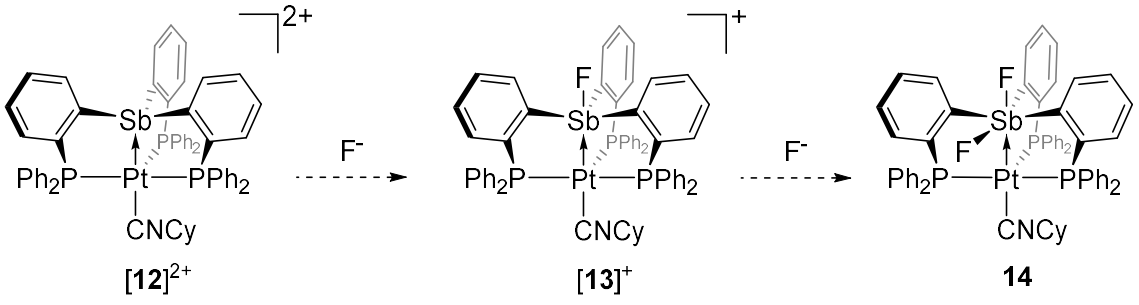

	[12]$^{2+}$	[13]$^{+}$	14
Sb-Pt (Å)	2.471(1)	2.624(1)	2.657(1)
NLMO Sb/Pt (%)	38.4/57.8	34.8/56.1	29.9/60.2

Figure 10. Structures of complexes [**12**]$^{2+}$**,** [**13**]$^{+}$ and **14** (top). Comparison of Sb–Pt bond distance and NLMO calculation among these complexes (bottom).

Through Z-type ligand coordination, the electronic nature of the transition metal center should be affected. Due to the high correlation between electrophilicity and reactivity, the M→Z interaction can be used to control the catalytic properties of the metal center.

1.2.4 Redox chemistry of antimony-transition metal complexes

The gold complex **15** can undergo a clean two electron oxidation at the antimony center with $PhICl_2$, yielding complex **16** (Figure 11). The gold geometry changes from distorted tetrahedral in **15** to square-planar in **16**, suggestive of a d^8 metal center. The bond distance between Au and Sb shortens from 2.8374(4) to 2.7089(9) Å, suggesting an increasing interaction between two heavy atoms upon oxidation. Moreover, the NBO analysis indicates that the interaction switches from Sb→Au in **15** to Au→Sb in **16**.

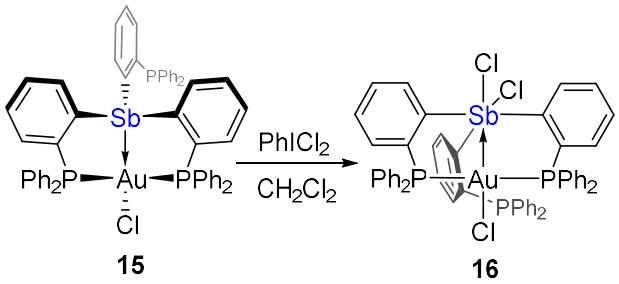

	15	16
Sb-Au (Å)	2.8374(4)	2.7089(9)

Figure 11. Structures of complexes **15** and **16** and their related bonding parameters.

Similar bond strengthening between Au and Sb was observed in the transformation from **17** to **18** upon oxidation of the antimony center by tetrachloro-1,2-benzoquinone (*o*-chloranil) (Figure 12). Synchronous with the geometry of the gold center changing from trigonal-pyramidal to distorted square-planar, the Sb–Au bond distances shrinks from 2.8669(4) in **17** to 2.6833(3) Å in **18**. The NLMO analysis shows an elevated orbital contributions from the gold center, which is aligned with a stonger Au→Sb interaction upon oxidation of the antimony center.

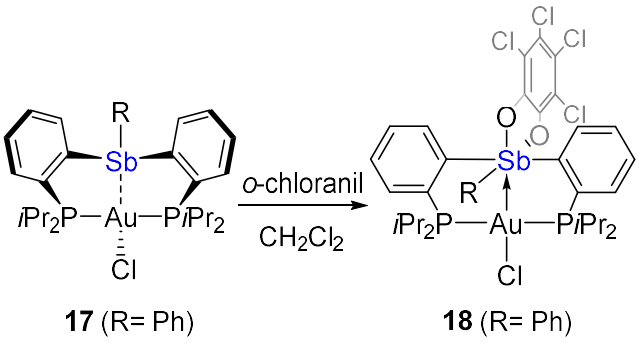

	17	18
Sb-Au (Å)	2.8669(4)	2.6833(3)

Figure 12. Structures of complexes **17** and **18** and their related bonding parameters.

1.3 Application of antimony-based Z-ligands in catalysis

1.3.1 Redox-controlled catalysis

As described previously, a hypervalent strong M→Z interaction was found in complexes featuring Sb(V) in lieu of Sb(III) moieties, and therefore the catalytic activity of the corresponding metal complexes should be varied accordingly. Gold complex [**19**]$^+$, which is synthesized from **5** shows poor catalytic activity in hydroamination of phenylacetylene with *p*-toluidine (Figure 13).[61] To increase the reactivity, the Sb(V)-based gold complex [**20**]$^+$, which was also derived from **5**, was synthesized. Based on the crystallographic and computational analysis, the Au→Sb interaction is stronger in [**19**]$^+$, leading to a more electrophilic gold center, which is able to bind Lewis bases such as water. Moreover, the catalytic activity of [**20**]$^+$ is expectedly increased, as evidenced by the higher yield of the hydroamination product under the same reaction conditions. These phenomena confirm that the oxidation state of the Z-ligand can be used to vary the catalytic activity of the coordinated metal center.

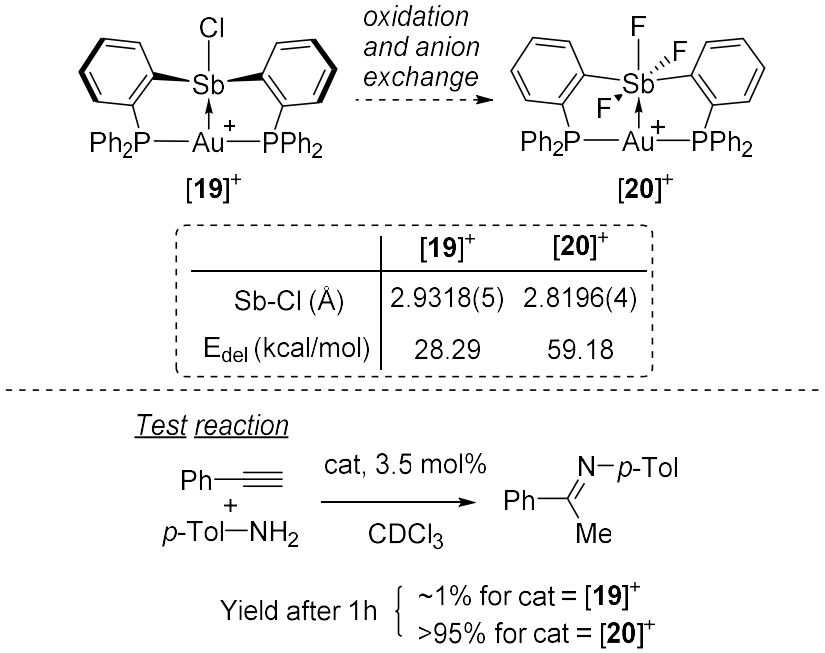

Figure 13. Structures of complexes [**19**]$^+$ and [**20**]$^+$ and their related bonding parameters (Top). Hydroamination of phenylacetylene catalyzed by [**19**]$^+$ and [**20**]$^+$.

1.3.2 Coordination-controlled catalysis

Due to the attractive properties of the trifluorostiborane ligand in complex [**20**]$^+$, the platinum complex **21** with the same ligand was synthesized and was used for catalysis (Figure 14).[62] NBO analysis shows that the Pt→Sb donor acceptor interaction of this complex originates from donation of filled platinum d-orbitals to a 5p orbital at the antimony center, which should increase the platinum centers electrophilicity, and hence its reactivity. However, complex **21** displays no catalytic activity towards enyne substitutes. Inspired by the variation of Pt→Sb interaction in the complex [**12**]$^{2+}$ as fluorides coordination, Gabbaï group decided to improve the catalytic activity by fluoride anion abstraction. Complex [**22**]$^+$ was isolated after reaction with $B(C_6F_5)_3$. The highly Lewis acidic difluorostibonium ligand is expected to be more accessible to accept

electron density from platinum, resulting in a more electrophilic platinum center. The stronger Pt–Sb interaction is supported by the Pt–Sb bond distance shortening, as well as computational results, which suggest a covalent bond between the two metals in [**22**]$^+$ instead of a donor-acceptor interaction in **21**. Importantly, the enyne cyclization can be promoted by [**22**]$^+$, which suggest that varying the coordination sphere around the main group element can change the catalytic activity of the adjacent metal center.

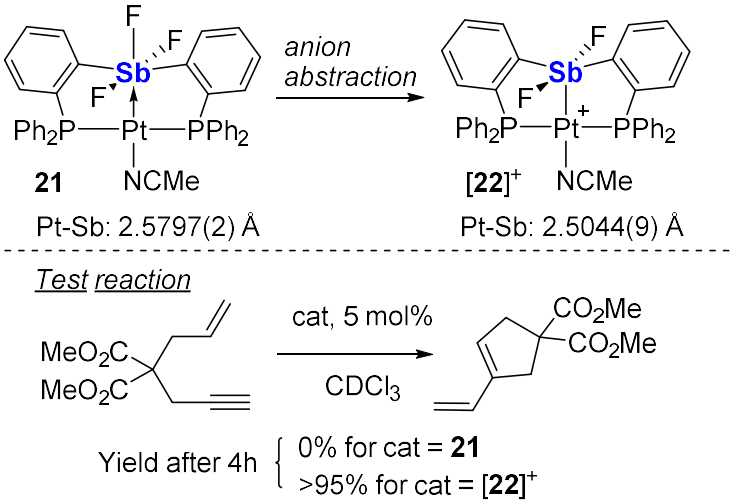

Figure 14. Structures of complexes **21** and [**22**]$^+$ (Top). Enyne cyclization of catalyzed by **21** and [**22**]$^+$.

1.3.3 Self-activating catalyst

Contrary to traditional spectator ligands, Lewis acidic Z-type ligands can actively participate in catalysis.[63-64] Our contribution to this field with the gold (**23**) and the platinum (**24**) complexes, which both feature an antimony-based Z-type ligands.[65-66] Both complexes show decent catalytic activity to alkyne activation without addition of activator (Figure 15). It has been proposed that the metal-bound chloride shifts to the

Lewis acidic antimony center, resulting in an empty site on the transition metal center, and hence rendering substrate coordination.

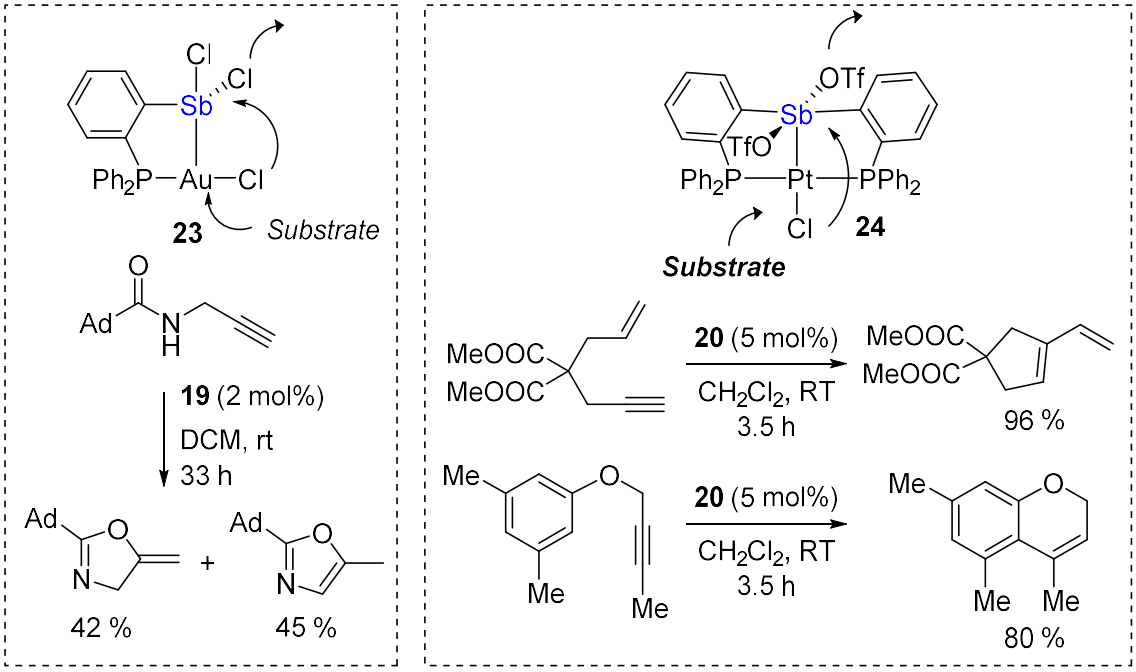

Figure 15. Activation of M-Cl bond by a dichlorostibine and a stiboranyl ligand.

1.4 Cationic Z-type ligand for transition metals

1.4.1 Cationic Tl(I) as a Z-type ligand for Ni complexes

The coordination of Lewis acid to the metal has been developed as a strategy for protecting the metal. With the intent to synthesize Ni(0) tris-isocyanide complexes, Figueroa group used the Tl(I) cation as a Z-type ligand to prevent coordination of a fourth isocyanide to the nickel center (Figure 16a).[67-68] For example, treatment of complex **25** was treated with TlOTf led to [**26**]$^+$, a complex featuring a Ni→Tl interaction. This interaction was further confirmed by the blue shift of the υ(CN) IR bands (2070 and 2000 cm^{-1} in [**26**]$^+$; 2045 and 1977 cm^{-1} in **25**) (Figure **16**b). It is worth

noting the preserve of a short Tl–O interaction (2.696(2) Å) between the triflate anion and the thallium cation. To understand the influence of this interaction, complex [**26**]$^{+}$ was subjected to an anion exchange reaction with $NaBAr^{F}_{4}$ (BAr^{F}_{4} = [B(3,5-$(CF_3)_2C_6H_3)_4]^-$), leading to complex [**27**]$^{+}$, which contains separated cation/anion pairs confirmed by X-ray structural analysis. The shorter Ni–Tl bond distance (2.853(2)Å) and a more noticeable shift of the υ(CN) IR bands (2013 and 2056 cm^{-1}) in complex [**27**]$^{+}$ indicate a stronger Ni→Tl interaction in complex [**27**]$^{+}$ than in [**26**]$^{+}$. This phenomenon was explained by the removal of the coordinated OTf^- anion by a weakly coordinationg $[BAr^{F}_{4}]^-$ leading to an increased Lewis acidity of the thallium cation and a stronger Ni→Tl interaction. The resulting stronger Ni→Tl interaction reduce the electron density of the nickel center and thus the backbonding from nickel to the isocyanide ligands.

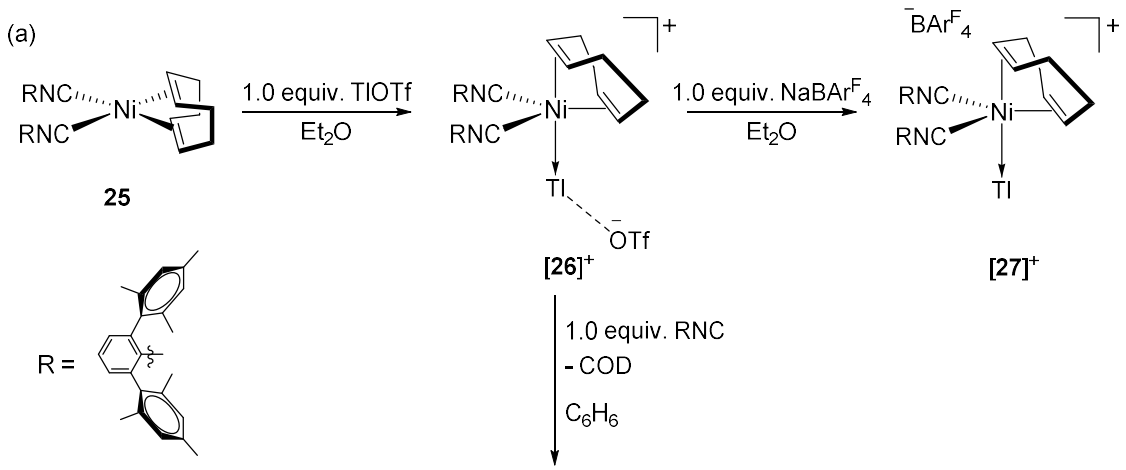

(b)

	υ(CN) (cm^{-1})	Ni-Tl (Å)
25	2045, 1977	
[**26**]$^+$	2070, 2000	3.0235(4)
[**27**]$^+$	2103, 2056	2.853(2)

Figure 16. (a) Synthesis of **25** – **29**. (b) Related structural parameter of **25** – [**27**]$^+$.

Addition of 1 equivalent of CNAr^{Mes2} to complex [**26**]$^+$ led to the substitution of the COD ligand and conversion to complex **28** without dissociation of the thallium cation, which indicated the robustness of the Ni–Tl bond in complex [**26**]$^+$ and [**27**]$^+$. In fact, complex **28** is stable even upon the addition of 20 equivalents of CNAr^{Mes2}. Removal of the thallium cation was achieved by the addition of potassium iodide, resulting in the tris-isocyanide nickel complex **29** .

Taken together, these interesting results show that: (1) the Lewis acidic Tl(I) cation behaves as a Z-type ligand, which modulate the electron density of the nickel (0) center, reducing the back-donation to the isocyanide ligand, (2) the coordination of the Lewis acid to the electron-rich metal can be a synthetic strategy, which protect

coordination sites on the metal, (3) the coordinating strength of the counter anions affect the electron-accepting ability of the Z-type ligands.

1.4.2 Tl(I) and Ag(I) as cationic Z-type ligand for Pd(0) and Pt(0) bis isocyanide complexes

In addition to the nickel complex **25** showing metallobasicity towards Tl(I), Figueroa also demonstrated that palladium(0) and platinum(0) complexes can act as Lewis bases toward Lewis acidic cations (Figure 17a).[69] Reaction of $M(CNAr^{Dipp2})_2$ (**30**^{M}) with TlOTf yielded complex [**31**^{M}]$^+$, in which the palladium and platinum atom adopt a T-shaped geometry with an unsupported M→Tl Lewis pair (M = Pd or Pt). This σ-type interaction induced blue shifts of the isocyanide υ(CN) IR bands by approximately 50 cm^{-1} for both complexes (Figure 17b), which is consistent with the enhanced electrophilicity on platinum or palladium due to the electron donation to the thallium cation. The triflate anion got exchanged to a weakly coordinating anion $BAr^F{}_4^-$ by addition of $NaBAr^F{}_4$ to complex [**32**^{M}]$^+$, leading to a shortening of the M–Tl distances and a longer blue shift of the isocyanide u(CN) IR bands, which showed stronger M→Tl interaction due to the higher Lewis acidity because of removal of the coordinated OTf^- anion. Last, the ^{195}Pt NMR resonance of [**32**^{M}]$^+$ is a 1:1 doublet signal, because of coupling with the ^{203}Tl/^{205}Tl (I = 1/2) nuclei. The absence of the coupling in complex [**31**^{M}]$^+$ suggested a rapid equilibrium in coordination of the thallium due to weaker M→Tl interaction.

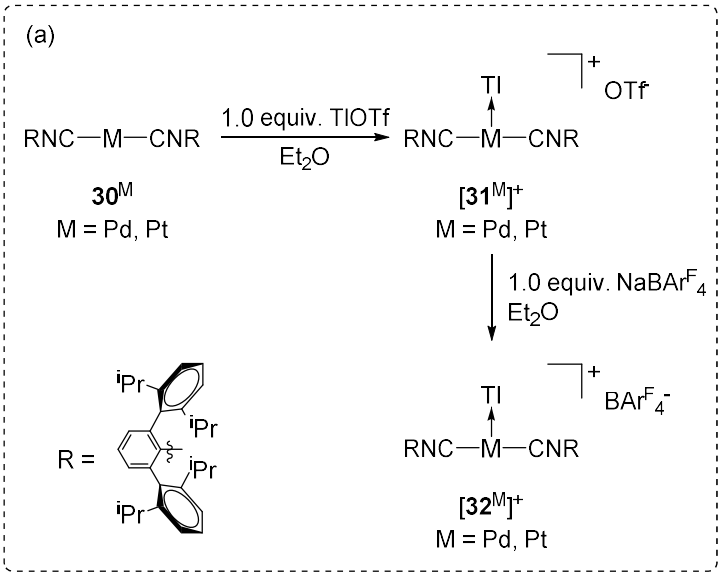

(b)

	ν(CN) (cm^{-1})	M-Tl (Å)
30^{Pt}	2065, 2020	
[**31**^{Pt}]$^+$	2112	2.8617(3)
[**32**^{Pt}]$^+$	2121	2.7659(5)
30^{Pd}	2070, 2005	
[**31**^{Pd}]$^+$	2097	2.855(1)
[**32**^{Pd}]$^+$	2116	2.7770(2)

Figure 17. (a) Synthesis of **30**^{M} – [**32**^{M}]$^+$. (b) Related structural parameter of **30**^{M} – [**32**^{M}]$^+$.

When **30**^{M} was treated with AgOTf, formation of complexes of type [**31**^{M}]$^+$ was observed (Figure 18). The most notable difference between the thallium-coordinated complexes is the square-planar geometry around the group 10 metal in complexes [**33**^{M}]$^+$ with an extra solvent coordination, such as THF, benzene or toluene. These are the first two examples of ligand additions to **30**^{M}. The atypical solvent binding to the metal center was due to stabilization of the group 10 metal p orbital upon silver cation coordination. The lowering of this orbital facilitates the binding of the ligand to the metal center. The formation of Lewis acid-base pair induced by a cationic Z-type ligand has also been observed in the Hg complexes [**6**]$^+$ in which the stibonium ligand also increases the Lewis acidity of the mercury center.

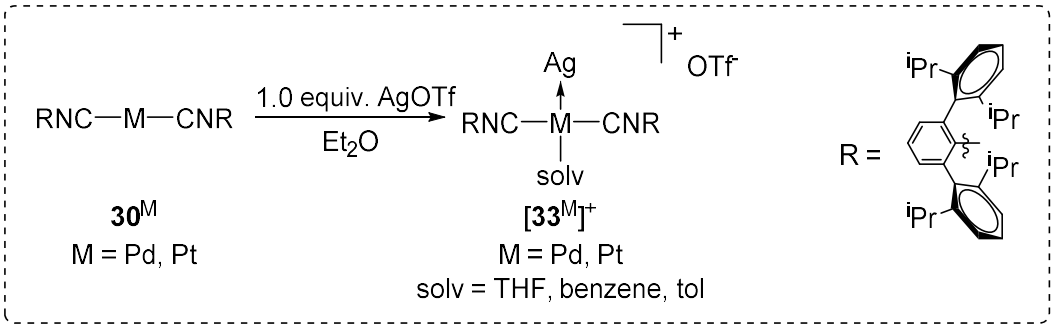

Figure 18. Synthesis of [**33**^{M}]$^{+}$.

1.4.3 Cationic PEP ambiphilic ligands for transition metal complexes

Cationic Z-type ligands can increase the electrophilicity of a metal center. To further elaborate on this strategy, double decker ligands that position a cation in proximity to a metal center have been developed, for example by Iwasawa and co-workers.[70] The double decker palladium complexes **34**^{E}, in which three different group 13 elements can be at the lower deck, show that the Pd→E strength is increased when the group 13 element gets heavier based on the analysis of covalent ratios (Figure 19). Moreover, the Pd–Cl bond distances becomes shorter in the presence of heavier group 13 elements, which suggests that the choice of the main group element can not only modulate the M→Z interaction, but also affect the trans influence of the ligand on the M–Z axis.

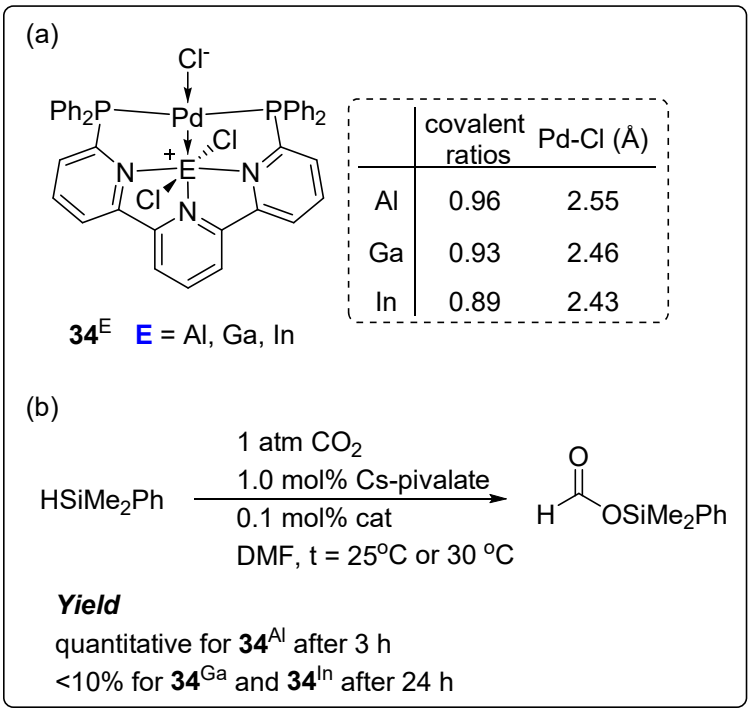

Figure 19. (a) Structure of complexes $\mathbf{34}^{E}$ and related bonding parameters between E and M. (b) CO_2 hydrosilylation catalyzed by $\mathbf{34}^{E}$.

The catalytic activity of complexes $\mathbf{34}^{E}$ for the hydrosilylation of CO_2 is shows an unexpected dependence on the Pd→E interaction (Figure 19b). Despite the weaker Pd→E interaction in $\mathbf{34}^{Al}$ than $\mathbf{34}^{Ga}$ and $\mathbf{34}^{In}$, the aluminum complex possesses the highest turnover frequency (TOF) of 19300h^{-1} among three complexes.

The cationic Z-type ligand changes the properties of the group 10 metal complexes. Taucher and co-workers showed that a stronger M→E interaction can be achieved by increasing the positive charge of the Z-type ligand (Figure 20).[71] The strength of the Rh→E interaction can be determined as $Cu^{I} < Li^{I} < Zn^{II}$, according to NMR experiments. Formation of $[\mathbf{35}^{Zn}]^{2+}$ was observed when $[\mathbf{35}^{Cu}]^{+}$ and $[\mathbf{35}^{Li}]^{+}$ were treated with $Zn(NTf_2)_2$. Treatment of complex $[\mathbf{35}^{Cu}]^{+}$ with $LiNTf_2$ resulted in complex

$[\mathbf{35}^{Li}]^+$, and no reaction was observed when $[\mathbf{35}^{Zn}]^{2+}$ was mixed with $LiNTf_2$ or $[Cu(MeCN)_4][OTf]$. The stretching frequency of υ(CO) of complexes $[\mathbf{35}^{E}]^{n+}$,1973 cm^{-1} for $[\mathbf{35}^{Cu}]^+$, 1984 cm^{-1} for $[\mathbf{35}^{Li}]^+$ and 2025 cm^{-1} for $[\mathbf{35}^{Zn}]^{2+}$, followed the same order as that of the Rh→M strength. . The increase of the energy of the CO stretching band reflects the decrease of the electron density on the rhodium center induced by a Z-type ligand with higher positive charges.

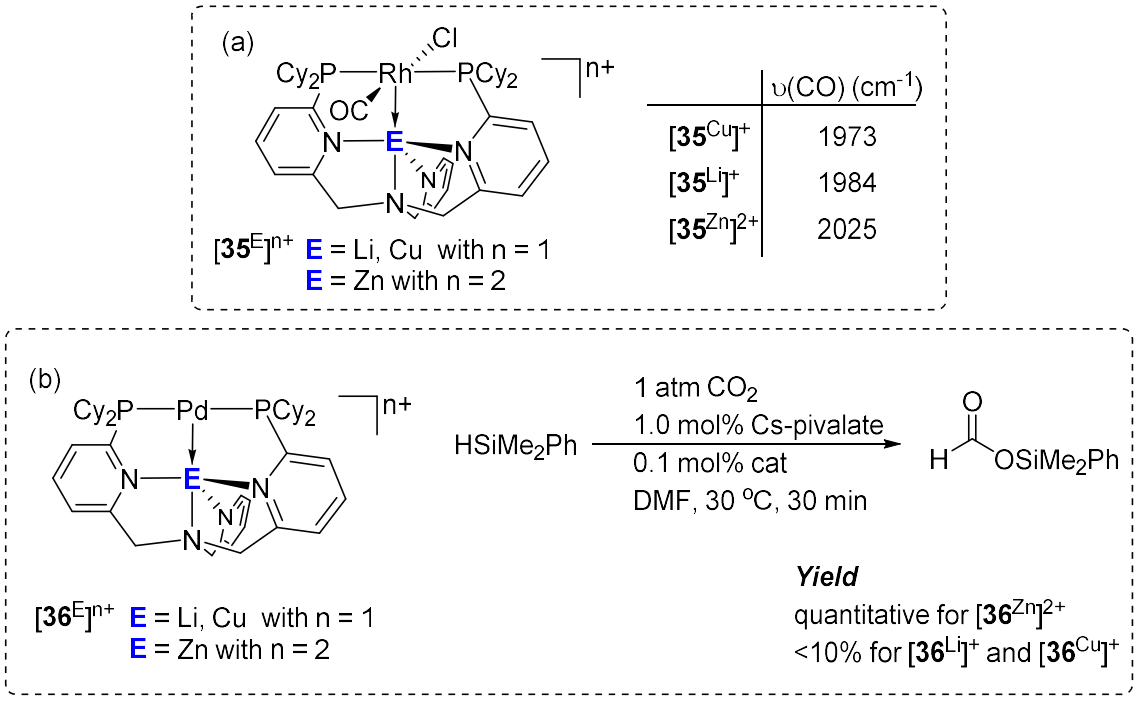

Figure 20. (a) Structure of complexes $[\mathbf{35}^{E}]^{n+}$ and related CO stretching frequency. (b) CO_2 hydrosilylation catalyzed by $[\mathbf{36}^{E}]^{n+}$.

A similar influence of the charge of cationic Z-type ligands was also observed in palladium complexes $[\mathbf{36}^{E}]^{n+}$ (Figure 20b). The magnitude of the Pd→E interaction for these three complexes was compared by structural and computational analysis, showing that $[\mathbf{36}^{Zn}]^{2+}$ featured the strongest Pd→E interaction among the three complexes.

Furthermore, the catalytic activity is also the highest among the three, which reflects the positive correlation existing with the strength of the Pd→E interaction.[71]. These results show how the magnitude of the M→Z interaction plays an important role in the modulation of the catalytic activities of the complexes.

1.5. Remote control of the properties of metal complexes by peripheral substituents appended to the ligands

1.5.1. Substituent effect on the electronic property of metal complexes

Despite the large distance existing a metal center and substituents appended to the ligands, the electronic property of a metal center can still be modulated by varying the nature of these substituents.[72-83] For example, the introduction of a nitro group to the phenylpyridine ligand of the $[(bpy)_2Ru(ppy)]^+$ results in a blue shift in the MLCT bands from 543 to 495 nm and an anodic shift of the oxidation potential of ruthenium center (Figure 21).[84] These changes are caused by the negative interactive influence of the nitro group, which render the metal more electron poor, raising the energy of the MLCT transition from the metal to the bipy π* orbital.

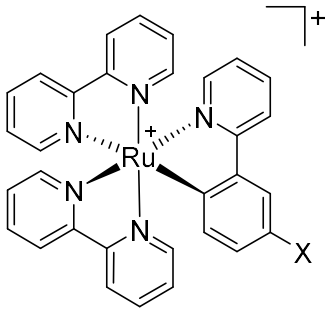

$[\mathbf{37}^X]^+$

X	λ_{max}(MLCT)	$E^{1/2}$ (Ru^{II}/Ru^{III})
H	543 nm	0.66 V
NO_2	495 nm	0.78 V

Figure 21. Structure of complexes $[\mathbf{37}^X]^+$ and related photophysical and eletrohemical properties. The oxidation potential is referenced to SCE.

Incorporation of a polypyridine ligand such as bipyridine facilitate the manipulation of the photophysical and redox properties of these complexes. Owing to the weaker donation of the neutral bipyridine ligand, the LUMO of the resulting complex is largely distributed on the bipyridine ligand, providing another handle to tune the energy state of the LUMO for different demanding HOMO–LUMO gap. Namely, electron-withdrawing substituents draw away electron density from bipyridine, stabilizing the LUMO and inducing a red shift of MLCT band, while electro-donating group raise the HOMO and induce red shift of the absorption. For example, the emission wavelength of complex $[\mathbf{38}^{X}]^{+}$ shows a progressive red shift as the substituent becomes more electron-withdrawing (Figure 22a).[85] Computational results show that the electron-withdrawing groups on the ligand decreases the HOMO–LUMO gap, leading to a red shift of the emission. These substituents do not affect as much the metal-centered HOMO.[75, 86] However, the substituents influence the electrochemical properties of theses iridium complexes.[87-89] These complexes have a reduction potential that is highly correlated with the substituent on the bipyridine ligand. For instance, the redox wave corresponding to the one-electron reduction of the bipy displays a progressive anodic shift upon introduction of electron-withdrawing groups.

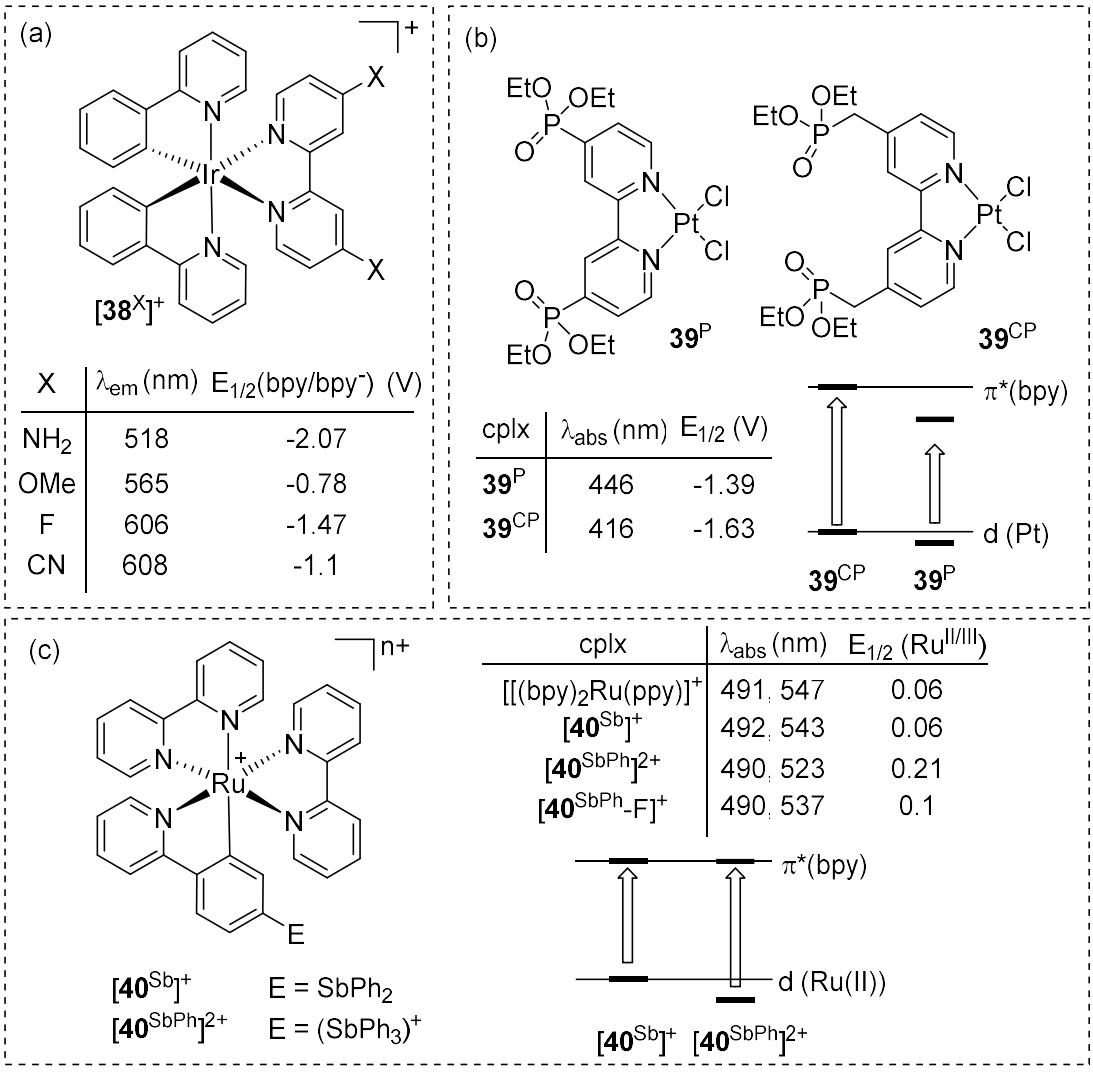

Figure 22. (a) Structures of iridium complexes showing substituent effect and their relative experimental data. (b) Structures of platinum complexes showing substituent effect and their relative experimental data. (c) Structures of ruthenium complexes showing antimony substituent effect and their relative experimental data. Potentials are referenced to ferrocene.

A related trend was also observed for the the bipyridine platinum complexes **39**^{CP} and **39**^{P} (Figure 22b).[82] The metal-to ligand charge-transfer (MLCT) band of complex **39**^{P} with peripheral phosphonate ester group is 500 nm, but that of complex **39**^{CP} is at about 450 nm. The noticeable shift originates from a difference in the substituents,

which is the linkage. In complex **39**^{CP}, the methylene decreases the electron-withdrawing effect of the hypervalent phosphorous moiety, leading to less stabilization of the LUMO and hence a larger HOMO-LUMO band gap (Figure 22b). The anodic shift of the redox potential for the one electron reduction of the bipyridine ligand also establishes the fact that complex **39**^{P} is more electrophilic due to the electron withdrawing group directly attached to the ligand. Overall, these results suggest that the peripheral substituent on the ligand can be used to control the electronic property of the complex.

A previous co-worker incorporated a Lewis acid antimony moiety in a cyclometalated ruthenium complex and investigated the substituent effect induced by the redox chemistry of the antimony center (Figure 22c).[90] Complex [**40**^{Sb}]$^{+}$ exhibits MLCT absorption bands with maxima at 492 and 543 nm which is very close to the parent cationic $[(bpy)_2Ru(ppy)]^{+}$ complex, indicating that the stibine moiety has limited influence to the electronic property of the complex. On the other hand, the Sb(V) moiety attached to the outer rim of the cyclometalated ligand initiates a 10 to 20 nm blue shift of the MLCT band. This shift can be explained by the electron withdrawing effect of the Sb(V) substituent, which stabilizes the metal orbitals (Figure 22c), a conclusion corroborated by cyclic voltammetry. The redox couple corresponding to the Ru(II/III) oxidation is at 0.21 V in complex [**40**^{SbPh}]$^{2+}$, and 0.06 V in complex [**40**^{Sb}]$^{+}$. This net anodic shift indicates that the ruthenium metal center is more electron deficient within the Sb(V) present in the ligand. Both photophysical and electrochemical analysis suggest that the Sb(V) substituent can be used as an electron withdrawing group to remotely tune the electrophilicity of the cyclometallated metal complex.

1.5.2 Applications

As mentioned above, the peripheral substituents are able to impact the electronic properties of the complexes, leading to different photophysical and electrochemical behavior. This level of control can be exploited in various applications in chelating anion sensing and catalysis.

1.5.2.1 Applications in anion sensing

The cyclometalated ruthenium complex [**41**]$^{+}$, within a boron-based phenylpyridine ligand (Figure 23a) binds both fluoride and cyanide anions.[91] UV-vis spectrum displays a significant red shift of the MLCT band upon anion binding, leading to a color change from deep purple to nearly black. This MLCT shift comes from the destabilization of the HOMO because a stronger donor upon anion binding (Figure 23b). Besides, the redox potential corresponding to the $Ru^{II/III}$ oxidation shows a cathodic shift upon anion binding. The same trend was also observed when [**40**^{SbPh}]$^{2+}$ was treated with fluoride anion (Figure 22c). Binding of a fluoride to the antimony center increases the electron donating properties of the substituent leading to a red shift of the MLCT band and a cathodic shift of the $Ru^{II/III}$ oxidation. Altogether, the immediate change of the photophysical property in these two ruthenium complexes leads to obvious color change from purple to black, suggesting their possible use as naked eye fluoride sensors.

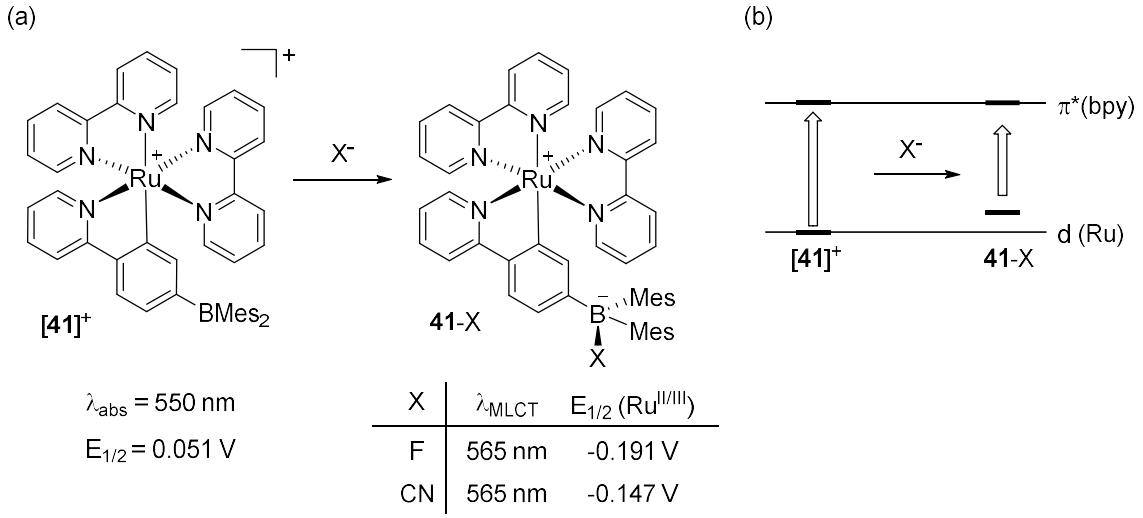

X	λ_{MLCT}	$E_{1/2}$ ($Ru^{II/III}$)
F	565 nm	-0.191 V
CN	565 nm	-0.147 V

Figure 23. (a) Structures of ruthenium complexes [**41**]$^{+}$ and relevant experimental data illustrating the peripheral substituent effect. (b) Orbital energy diagram upon anion binding to a cyclometalated complex.

1.5.2.2 Application of substituent effect in the catalysis

As mentioned above, modification of the peripheral substituents of the coordinated ligands can effectively alter the nature of the transition metal center, and hence the reactivity of the metal center should also be modulated. A series of palladium complexes **42**^{X}, coordinated by 4,4'-disubstituted-2,2'-bipyridine ligand were investigated for substituent effect and catalytic activity (Figure 24a).[81] The palladium-catalyzed oxidation of 2-hexanol was used as a model reaction to correlate electron donating ability of the substituents with the catalytic activity. These results indicate that the peripheral substituent, despite the large separation from the reaction center, can be used to alter the reactivity of the transition metal center. Another example is the hydroarylation of ethylene catalyzed by a series of platinum complexes **43**^{X} (Figure 24b).[92] The ratio of the two possible products, ethylbenzene or styrene, is affected by the

electron-donating ability on the bipyridine group. The generation of styrene is largely promoted by more electron-withdrawing bipyridine ligand. From the mechanistic study, the more electron rich platinum complex should be more accessible to oxidative addition of benzene, followed by the formation of styrene. Instead, the relatively electron-poor platinum complex is more likely to undergo an β-hydride elimination leading to styrene production. This research demonstrated that the variation of the substituents on the bipyridine ligand can be used to control the reactivity of the transition metal center.

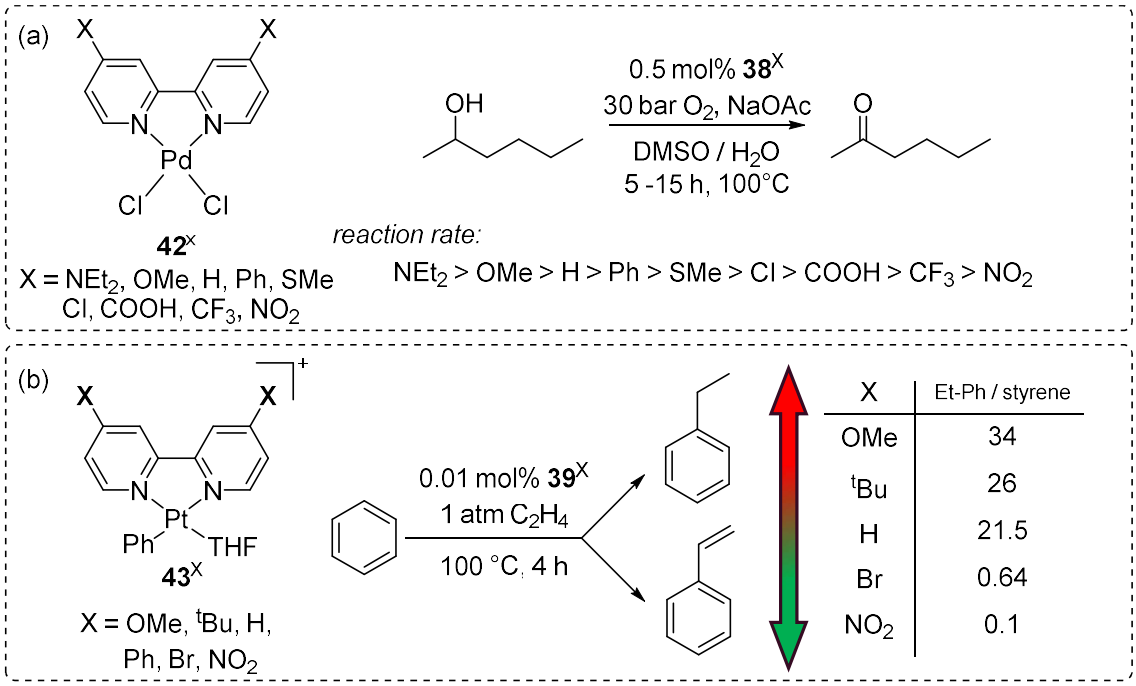

Figure 24. Examples showing how substituents on bipyridine influence the catalytic activity of the transition metal center.

1.6 Objectives

1.6.1 Modulating the M→Sb interaction by varying coordinated sphere at Sb

In this thesis, I propose to investigate the chemistry of gold complexes featuring ambiphilic L_2/Z ligands comprised of two phosphine donors and of a Z-type antimony moiety. The central objective of this research will be to determine if the charge of the antimony Z-type ligand can be used to modulate the electrophilic character and catalytic properties of the gold center. This idea will be tested by synthesizing a series of dinuclear complexes with a gold atom held in close proximity to a pentavalent cationic antimony center. My primary intent to target complexes in which the antimony center is dicationic. Given the predicted reactivity of such dications, the coordination of phosphine oxide ligands to the antimony atom will be considered as a means to tame these reactive species. The presence of a dicationic Z-type antimony moiety should promote the formation of a strong Au→Sb interaction, augment the electrophilic character of the gold center, and positively impact the range of reactions that these gold-antimony complexes can catalyze. The extent of activation experienced by the gold center will be derived from an experimental determination of its ability to catalyze reactions involving alkenes and alkynes. This project will also showcase how these ligand effects can be used to drastically alter the reactivity of a transition metal.

1.6.2 Control reactivity of complexes by peripheral Sb-based substituent

Varying the peripheral substituent at the ligand is a powerful approach to manipulate the electronic properties of a complex. However, most transformations require harsh reaction conditions, which are difficult to perform on an already assembled

metal complex. The mild reaction conditions used to convert antimony(III) to antimony(V) served as an inspiration for the synthesis of bipy ligands, derivatized at their periphery by a $SbPh_2$ moiety. The primary objective of these investigations was to demonstrate that such a ligand could be complexes to a metal and subsequently subjected to oxidation conditions in order to convert the Sb(III) moiety in a Sb(V) moiety, without affecting the transition metal. The secondary objective of these investigations will be to test the impact of this oxidation in the realm of organometallic catalysis and photophysics.

CHAPTER II

AN ANTIMONY(V) DICATION AS A Z-TYPE LIGAND: TURNING ON STYRENE ACTIVATION AT GOLD*

2.1 Introduction

Although traditionally regarded as laboratory curiosities, Z-type, Lewis acidic ligands and the complexes they form with transition metals are now gaining increasing validation in the area of catalysis[60, 69, 93-104] where the electron accepting properties of the Lewis acidic center can be used to modulate the electron density and catalytic reactivity of the adjacent metal center.[105-110] The accepting properties of Z-type ligands can be influenced by a variety of factors including the nature of the atom acting as the Lewis acid,[111-112] its redox state or its coordination environment[60, 101]. Examples that illustrate the tunability of these ligand systems include double-decker complexes of type **I** where variation of the group 13 element allows for a precise control of the Ni-E interaction[113] or complexes of type **II** where the redox state of the antimony center can be used to adjust the strength of the Au-Sb interaction (Figure 25).[61, 114] Based on the principle that cationic main group compounds are more Lewis acidic than their neutral counterparts,[115-116] we have been interested in an approach whereby anion abstraction serves to enhance the σ-accepting properties of the Z-type ligand.[50] We demonstrated

---

* Reprinted in part with permission from: "An antimony(V) dication as a Z-type ligand: Turning on styrene activation at gold"; Lo, Y.-H.; Gabbaï F. P. *Angew. Chem. Int. Ed.* **2019**, *58*, 10194-10197. Copyright 2019 by John Wiley & Sons, Inc.

this idea in the case of complex **III** which, upon conversion into **IV** by fluoride anion abstraction, became catalytically active as a result of a stronger Pt→Sb interaction.[62] With the view of further augmenting the accumulation of positive charges on the Lewis acidic main group element, we are now investigating ligand platforms that would support the formation of antimony dications, within the coordination sphere of a late transition metal. It occurred to us that isolating such a complex may necessitate the use of auxiliary donor functionalities introduced to tame the high reactivity of the dicationic antimony moieties.[117] The work of Burford on species such as **V** shows that phosphine oxides are privileged ligands for antimony cations.[118-119] The donor properties of the phosphine oxide ligand can be rationalized by considering the ylidic resonance structural (**b**), in which the dicationic complex is described as a bis-phosphonium stiborane derivative rather than an antimony dication (Figure 25).

As part of this thesis, we have decided to target complexes of type **VI** in which one of the phosphine oxide donors is replaced by a metalloligand. In this chapter, we describe our first implementation of this idea and its application to gold mediated catalysis.

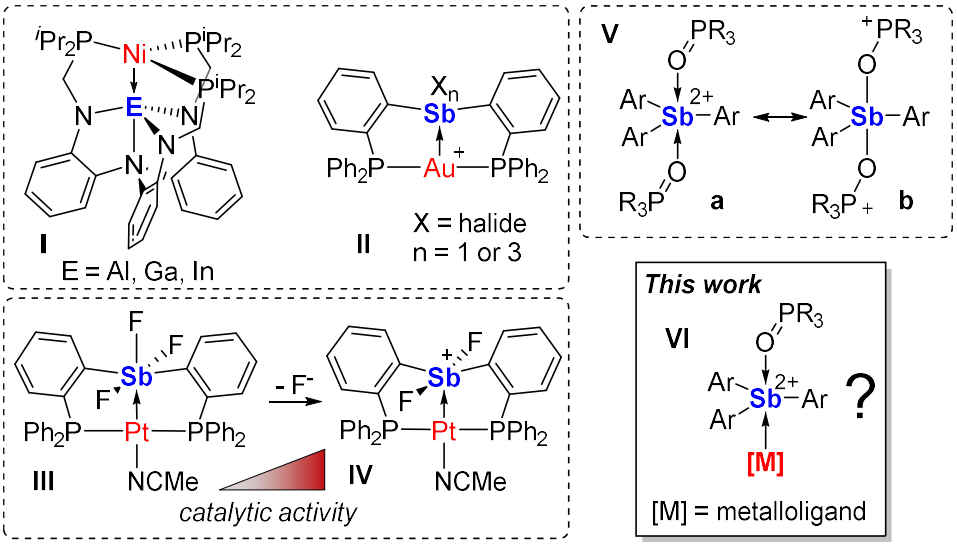

Figure 25. Examples of transition metal complexes that contain Z-type ligands (I to IV) and outline of work mentioned within (V and VI).

2.2 Synthesis and characterization of the dicationic gold complex

As an entry point for the synthesis of a complex of type VI, we considered complex **44**, a known gold complex which features a phosphino arm free of metal coordination.[120] To test if this unit could be converted into the corresponding phosphine oxide, complex **44** was combined with one equivalent of hydrogen peroxide (Figure 26). This reaction afforded complex [**45a**][Cl] as an air stable solid, the crystal structure of which (*vide infra*) confirmed the successful conversion of one of the three phosphino arms of the ligand into a phosphine oxide. This complex has also been characterized by EA and ^{31}P MAS NMR spectroscopy. The latter shows two signals at 60.2 ppm and 41.6 ppm. The respective 2:1 intensity ratio measured for these two resonances indicates that they correspond to the gold-coordinated phosphine and the phosphine oxide units, respectively. When in solution, [**45a**][Cl] gives rise to a second isomer (**45b**-Cl) for

which the ^{31}P nucleus of the phosphine and phosphine oxide units resonates at 96.1 ppm and 44.3 ppm. respectively. The structure of **45b**-Cl is proposed to be that depicted in Figure 26, based on the similarity of the phosphine chemical shift with that of ((*o*-$(Ph_2P)C_6H_4)_2SbCl_3$)AuCl (79.2 ppm).[61] To confirm that these two isomers differ in the way they interact with the chloride counterions, we treated [**45a**][Cl]/**45b**-Cl with 2 equivalents of $AgNTf_2$. In situ ^{31}P NMR spectroscopy indicated the emergence of a new species, [**46**][NTf_2]$_2$, characterized by a single set of resonances at 68.7 ppm and 42.3 ppm (2:1 integration ratio).

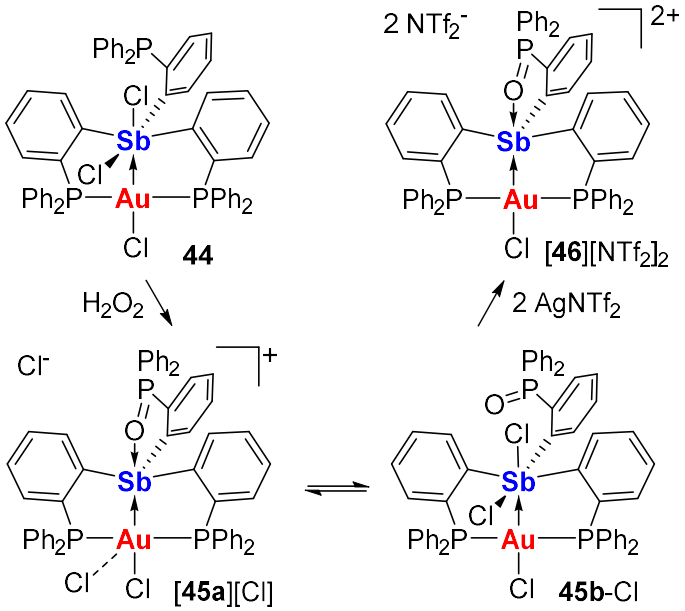

Figure 26. Synthesis of [**45a**][Cl] and [**46**][NTf_2]$_2$.

The structures of [**45a**][Cl] and [**46**][NTf_2]$_2$ have been established in the solid-state (Figure 27).[121] The Au–Sb bond distances of 2.613(7) Å in [**45a**][Cl] and 2.6269(7) Å in [**46**][NTf_2]$_2$ are significantly shorter than in **44** (2.709(9) Å) thus indicating a strengthening of the Au−Sb interaction triggered by the increased Lewis

acidity of the antimony center. In accordance with the bonding situation depicted for model complex **VI**, the coordination geometry of the antimony center in both complexes is distorted trigonal bipyramidal with the gold atom and the oxygen atom of the phosphine oxide occupying the apical sites. A further indicator of this coordination geometry comes from the sum of C−Sb−C angles which approaches the ideal value of 360° in both structures ($\Sigma_{(C-Sb-C)}$ = 356.1(4) for [**45a**][Cl] and 356.7(4)° for [**46**][NTf_2]$_2$). The values of the P−Au−P (167.30(9) for [**45a**][Cl] and 166.25(9)° for [**46**][NTf_2]$_2$) and Cl−Au−Sb (172.79(6) for [**45a**][Cl] and 176.39(6)° for [**46**][NTf2]2) angles indicates that the four primary ligands bound to gold are arranged in a square planar geometry, with the chloride ligand (Cl1) positioned trans from the antimony atom. This square planar geometry is consistent with the strong donation of a gold d-orbital lone pair to antimony, leading to an electronic configuration that approaches that of a classical d^8 metal center. In the case of [**45a**][Cl], the square planar gold atom is capped by a chloride ligand that forms a long Au–Cl interaction of 2.910(2) Å.

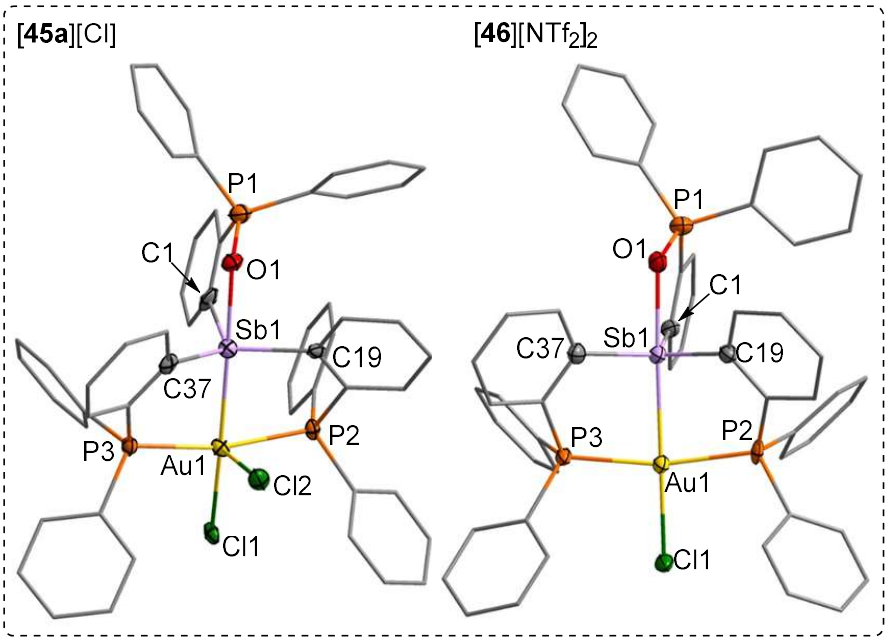

Figure 27. Solid-state structure of [**45a**][Cl] and [**46**][NTf_2]$_2$. Thermal ellipsoids are drawn at the 50% probability level. The phenyl groups are drawn in wireframe, the. hydrogen atoms, interstitial solvent molecules and counteranions are omitted for clarity.

2.3 Computational study on the dicationic gold complex

To provide additional insights into the structure of such species, we optimized the structure of [**46**]$^{2+}$. The computed Sb–Au bond in [**46**]$^{2+}$ (2.665 Å) is close to that observed experimentally indicating the appropriateness of the computational method adopted. A Natural Bond Orbital (NBO) analysis of [**46**]$^{2+}$ (Figure 28) affords a bonding description in which a dicationic triarylantimony unit is stabilized intramolecularly by donation from the phosphine oxide functionality and from the metallobasic gold atom. Indeed, the NBO method describes the Sb–O interaction as a lp(O)→p(Sb) donor acceptor interaction which contributes to the stability of the complex by $E^{(2)}$ = 69.7 kcal/mol. The Sb-Au linkage is also donor acceptor in character and involves a d_x^2-

$_y^2$(Au)→p(Sb) and a d_z^2(Au)→p(Sb) interactions which stabilize the complex by $E^{(2)}$ = 39.3 kcal/mol and 10.5 kcal/mol, respectively. Taken together, the second order perturbation energies suggest that the dative bonds formed by the two donors have a similar strength. This bonding description supports the formulation of complex [**46**]$^{2+}$ as a stibonium dication stabilized intramolecularly by two Lewis bases.

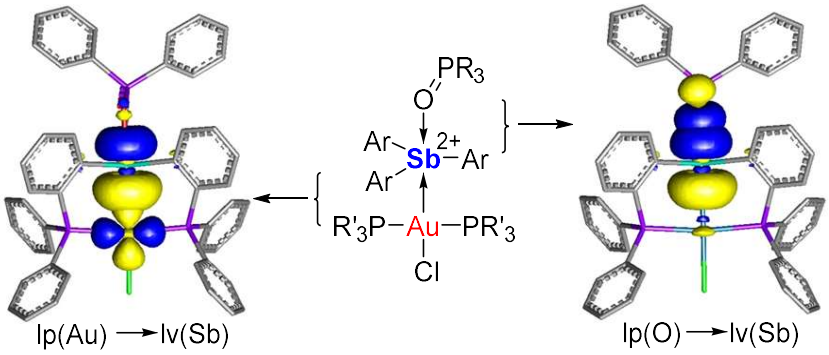

Figure 28. NBO plots of the (a) Sb–Au and (b) O–Sb major bonding interactions in [**46**]$^{2+}$ (isodensity value 0.05). Hydrogen atoms are omitted.

2.4 Styrene activation catalyzed by the dicationic gold complex

2.4.1 Gold center activation by silver bis(trifluoromethanesulfonyl)imide

Complex [**46**]$^{2+}$ can be regarded as a dicationic analog of complex (*o*-$(Ph_2P)C_6H_4)_2SbF_3$)AuCl,[61] a complex which we successfully converted into the catalytically active cation [**20**]$^+$ ([((*o*-$(Ph_2P)C_6H_4)_2SbF_3$)Au]$^+$) by abstraction of the chloride anion.[61] With the view of carrying out the same transformation, we treated [**46**]$^{2+}$ with an additional equivalent of $AgNTf_2$ in dichloromethane (Figure 29). ^{31}P NMR spectroscopy showed the emergence two new resonances at 67.9 ppm and 49.1 ppm (2:1 intensity) which we assign to the formation of [**47**][NTf_2]$_2$, a complex in which the gold-bound chloride anion is replaced by a triflimide anion. Formation of

[**47**][NTf_2]$_2$ is however partial and only reaches 55% conversion after addition of 7 equivalents of $AgNTf_2$. The stability of the Au-Cl bond of [**46**]$^{2+}$ is assigned to the dicationic nature of the complex and its reluctance to acquire a greater positive character by replacement of the chloride by a much weaker coordinating triflimide counteranion. We note that the phosphine oxide resonance of [**47**]$^{2+}$ undergoes a small but noticeable upfield shift which we assign to a change in the polarity of the medium as excess of $AgNTf_2$ is added to the solution

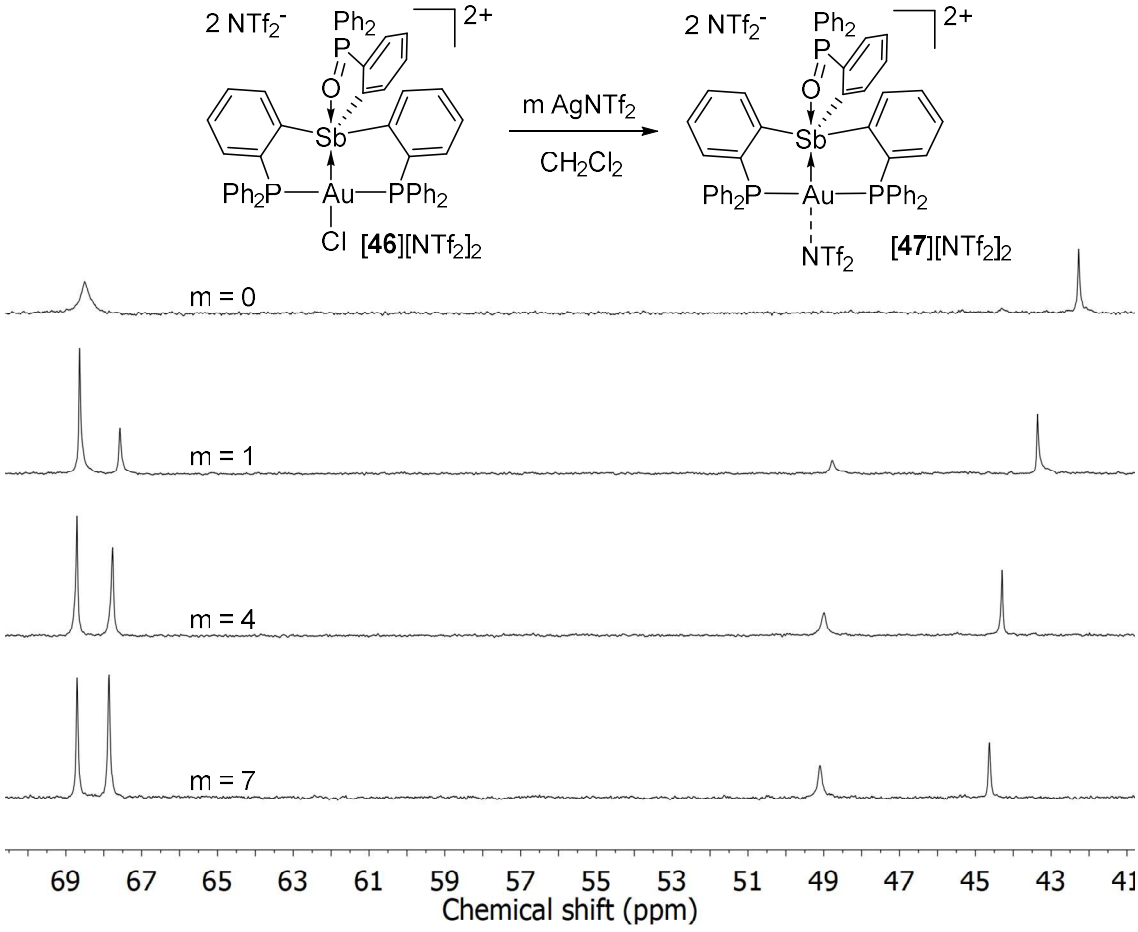

Figure 29. Chloride abstraction from [**46**][NTf_2]$_2$ by addition of equivalents of $AgNTf_2$.

2.4.2 Styrene activation catalyzed by [47][NTf_2]$_2$

Given the weakly coordinating nature of the triflimide anion and its extensive use as a counteranion in gold mediated catalysis,[122-123] we became eager to test the catalytic properties of [**47**][NTf_2]$_2$. When [**47**][NTf_2]$_2$ was generated *in situ* by addition of 3 equivalents of $AgNTf_2$ to [**45**][Cl], we observed that styrene is readily polymerized (Figure 30). ^{1}H NMR monitoring indicated that the reaction had reached >95% completion after 1 h. Prior examples involved cyclometallated gold(III) complexes, carbene gold(III) complexes or systems generated by combining AuCl and a halide abstracting activator.[124-127] The emergence of such a reactivity for a bis(phosphine)gold moiety such as that in [**47**][NTf_2]$_2$ is surprising and reflective of the reactivity enhancement achieved in the polycationic gold complex.[128-129]

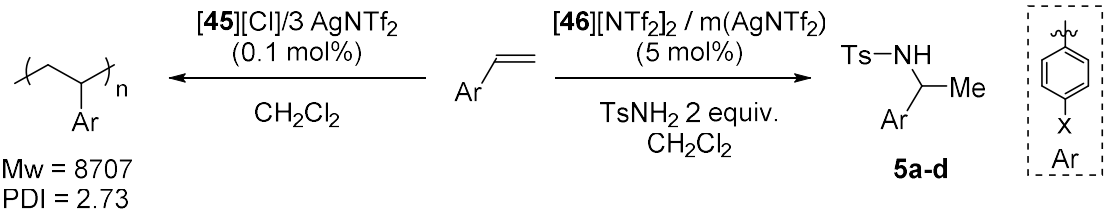

Figure 30. Hydroamination of styrene catalyzed by [**46**]$^{2+}$/ $AgNTf_2$ and polymerization of styrene catalyzed by or [**45**]$^+$/ 3 $AgNTf_2$.

Encouraged by these findings, we decided to test whether this catalyst could also promote hydroamination of the substrate. We first tested the reaction of styrene and *p*-toluenesulfonamide ($TsNH_2$) and observed the clean formation of the Markovnikov hydroamination product which was obtained in high yield after 6 h (Table 1, entry 1). Given the stoichiometry of the chloride abstraction reaction established by NMR

spectroscopy, we decided to vary the [**46**]$^{2+}$/$AgNTf_2$ ratio from 1/1 to 1/7 (entries 2-4). NMR monitoring indicates that additional equivalents of $AgNTf_2$ results in a higher yield of the product after the first hour. This result support the notion that the putative triflimide complex is indeed the catalyst. We propose that the activity of this catalyst results from dissociation of the triflimide anion from the gold center, followed by activation of styrene and addition of the sulfonamide and protodeauration (Figure 31).

Table 1. Hydroamination of styrene and substituted styrenes by $TsNH_2$.

Entry	Precatalyst	X	m[a]	T (°C)	Time	Yield [b]	Product
1	[**46**][NTf_2]$_2$	H	1	35	6 h	94%	5a
2	[**46**][NTf_2]$_2$	H	1	35	1 h	20%	5a
3	[**46**][NTf_2]$_2$	H	4	35	1 h	29%	5a
4	[**46**][NTf_2]$_2$	H	7	35	1 h	44%	5a
5	[**45a**][Cl]	H	3	35	6 h	93%	5a
6	[**45a**][Cl]	H	3	35	1 h	19%	5a
7	[**45a**][Cl]	H	6	35	1 h	29%	5a
8	[**45a**][Cl]	H	9	35	1 h	46%	5a
9	[**46**][NTf_2]$_2$	F	1	35	6 h	96%	5b
10	[**46**][NTf_2]$_2$	Cl	1	35	6 h	42%	5c
11	[**46**][NTf_2]$_2$	Me	1	25	20 min	32%	5d

[a] m refers to the number of equivalents of $AgNTf_2$. [b] The yield was measured by ^{1}H NMR spectroscopy using 1,2-dichloroethane as an internal standard.

We were also eager to test whether [**47**][NTf_2]$_2$ could be generated in situ, starting from [**45a**][Cl]. We found that when generated in this way, [**47**][NTf_2]$_2$ showed

a catalytic activity in the hydroamination of styrene that is almost identical to that observed when [**46**][NTf_2]$_2$ is used as a pre-catalyst (entries 5-8). We have verified that this reaction is not activated by complex [**46**]$^{2+}$ or $AgNTf_2$ alone. When 5 mol% $HNTf_2$ was employed as a catalyst, only 16% of hydroamination product was formed, and formation of polystyrene was observed. This poor selectivity adds credence to the involvement of the gold-antimony complex as the active species. Complex [**47**][NTf_2]$_2$ appears significantly more active than other gold-based catalysts such as Ph_3PAuCl/AgOTf or $(PhO)_3PAuCl$/AgOTf.[130-131] These two catalysts also promote the reaction of styrene with *p*-toluenesulfonamide but necessitate high temperatures (85°C) and extended reaction times (14 h) to afford the hydroamination product in only moderate yields (50-60%). Finally, we have also tested the reactivity of substituted styrenes. 4-Fluorostyrene is also efficiently hydroaminated, a results expected based on the similar Hammet parameters[132-133] of hydrogen ($\sigma_p = 0$) and fluorine ($\sigma_p = 0.06$) (entry 9). Reaction of the more electron-poor 4-chlorostyrene ($\sigma_p = 0.23$) is distinctly slower in agreement with the proposed electrophilic mechanism (entry 10). Further support for this electrophilic mechanism is provided by the behavior of 4-methylstyrene which is fully consumed after 20 mins at room temperature. In this case, however, only about 32% of the hydroamination product is formed along with unidentified products and oligomers (entry 11).

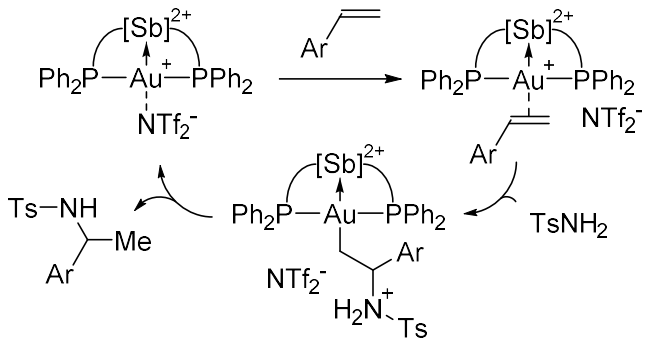

Figure 31. Proposed mechanism for hydroamination catalyzed by [**47**]$^{2+}$.

Overall, we describe the synthesis and characterization of a gold chloride complex, [**46**][NTf_2]$_2$, featuring a Z-type dicationic antimony ligand. Formation of this complex is made possible by the coordination of a neutral phosphine oxide donor that attenuates the reactivity of the dicationic antimony center. Despite its electron-deficient nature, the gold center of [**46**]$^{2+}$ can be activated by conversion into the proposed triflimide complex [**47**]$^{2+}$. Generation of this complex is accompanied by the emergence of atypical reactivity toward styrene[134-135] which is readily polymerized or converted into the hydroamination Markovnikov product when in the presence of *p*-toluenesulfonamide. These unusual reactions highlight the unique activation resulting from the coordination of the dicationic antimony Z-type ligand to the gold center.

2.5 Anion effect on the catalytic activity of the gold complex

2.5.1 Synthesis of mono-cationic gold complex with SbF_6^- as counter anions

The potential of complex **44** forming di-cationic or tri-cationic complex prompted us to treat it with a silver salt for chloride anion abstraction. Complex **44** reacts with 1 equivalent of $AgSbF_6$ cleanly, resulting in complex [**48**][SbF_6] (Figure 32).

This cationic complex was characterized by ^{31}P NMR spectroscopy showing a sharp singlet at 42.7 ppm, indicating that the third phosphine ligand is coordinated to the gold center.

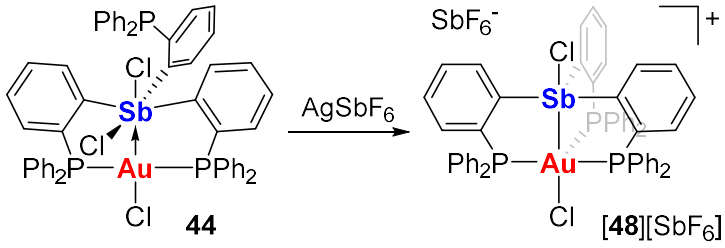

Figure 32. Synthesis of [**48**][SbF_6].

The coordination of the three phosphine was further confirmed by the solid-state structure (Figure 33a). The gold center adopts a distorted trigonal bipyramidal geometry with antinomy and chloride at the apexes. It sits below the trigonal plane defined by the three P atoms by a distance of 0.36 Å towards the chloride ligand. The antimony center is also in a distorted trigonal bipyramidal geometry ($\Sigma_{(C–Sb–C)}$ = 360.1(2)°) and is separated from the gold center by 2.7778(5) Å, which is longer than the Sb–Au distance of 2.7086(9) Å in complex **44**. The lengthening of the Sb–Au distance suggests a weaker bond interaction between these two metals, which is likely caused by the coordination of the third phosphine. The NBO analysis shows a [**48**]$^+$ possess a Au→Sb donor–acceptor interaction (Figure 33b). This interaction is originated from the filled gold d_z^2 orbital donating to the vacant σ* orbital of Sb–Cl bond with the $E^{(2)}$ = 28.44

kcal/mol.

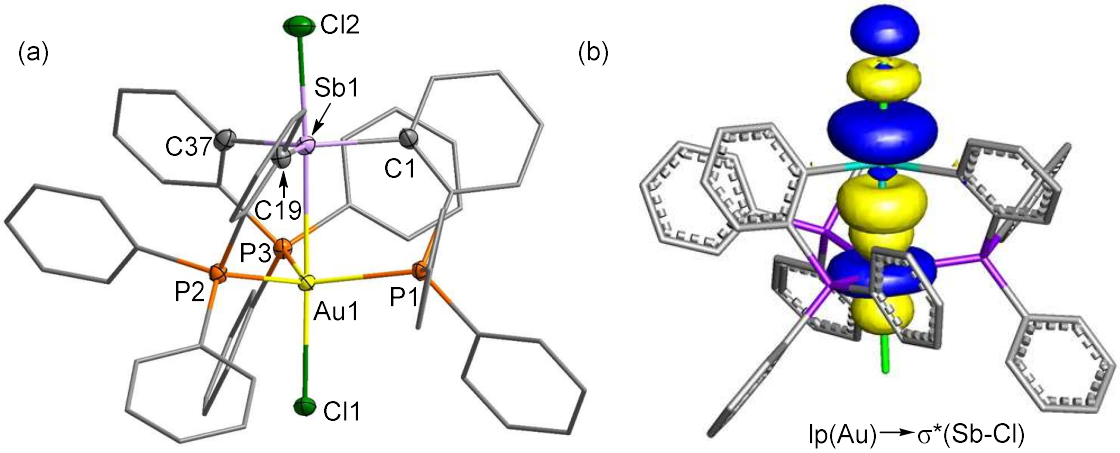

Figure 33. (a) Solid-state structure of [**48**][SbF_6]. Thermal ellipsoids are drawn at the 50% probability level. The phenyl groups are drawn in wireframe, the. hydrogen atoms, interstitial solvent molecules and counter anions are omitted for clarity. (b) NBO plots of the Sb–Au bonding interactions in [**48**]$^+$ (isodensity value 0.05). Hydrogen atoms are omitted.

Additions of 1 equivalents $AgSbF_6$ to complex [**48**][SbF_6] leads to emergence of several signals in the ^{31}P NMR spectrum (Figure 34), and the characterization of the resulting products was not successful. The reluctance of complex [**48**][SbF_6] to react cleanly with silver salts suggests that the resulting di-cationic complex is not stable.

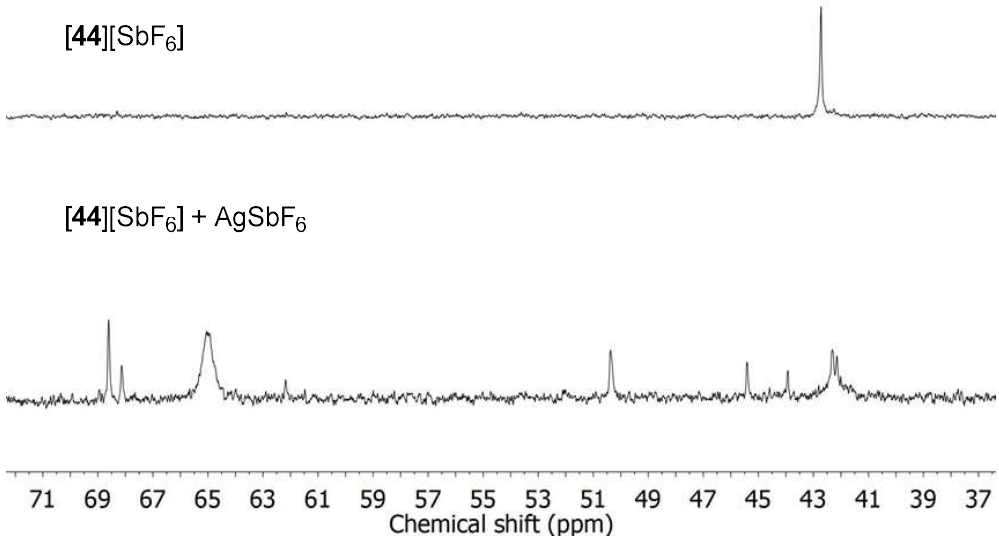

Figure 34. $^{31}P\{^{1}H\}$ NMR spectra of a reaction mixture containing [**48**][SbF_6] and $AgSbF_6$.

2.5.2 Synthesis of di-cationic gold complexes with SbF_6^- as counter anions

The successful formation of the di-cationic complex [**46**][NTf_2]$_2$ and the failure when attempting to form di-cationic complex based on [**48**][SbF_6] indicates that the additional donation to the di-cationic antimony center to stabilize the complex is important. Hence, we decided to apply [**46**]$^{2+}$ as a platform to study anion influence on the catalytic activity. Treating complex [**45a**][Cl] with 2 equivalents of $AgSbF_6$ affords the colorless air-stable complex [**49**][SbF_6]$_2$ (Figure 35a). which displays ^{31}P NMR resonances at 69.3 ppm and 42.5 ppm, the chemical shifts similar to those of [**46**]$^{2+}$. The structure of [**49**][SbF_6]$_2$ was confirmed by a single-crystal diffraction, which reveals a dicationic complex with the same connectivity as in the NTf_2^- salt (Figure 35b). The sum of the C–Sb–C angles is 357.0(3)°, which is close to 360°. Based on the P–Au–P angle (167.56(6)) and the Sb–Au–Cl angle (175.18(7)), the gold center adopts a distorted

square-planar geometry, which is typically found at d^8 metal centers. The short Sb–Au bond distance (2.619(2) Å) again implies a bonding situation similar to that in the NTf_2^- salt. We note that in the solid structure of [**46**][NTf_2]$_2$, there is a NTf_2^- anion interacting weakly with the gold center. However, no such interaction was found in [**49**][SbF_6]$_2$, suggesting that these two anions have a different influence on the nature of the dicationic complex.

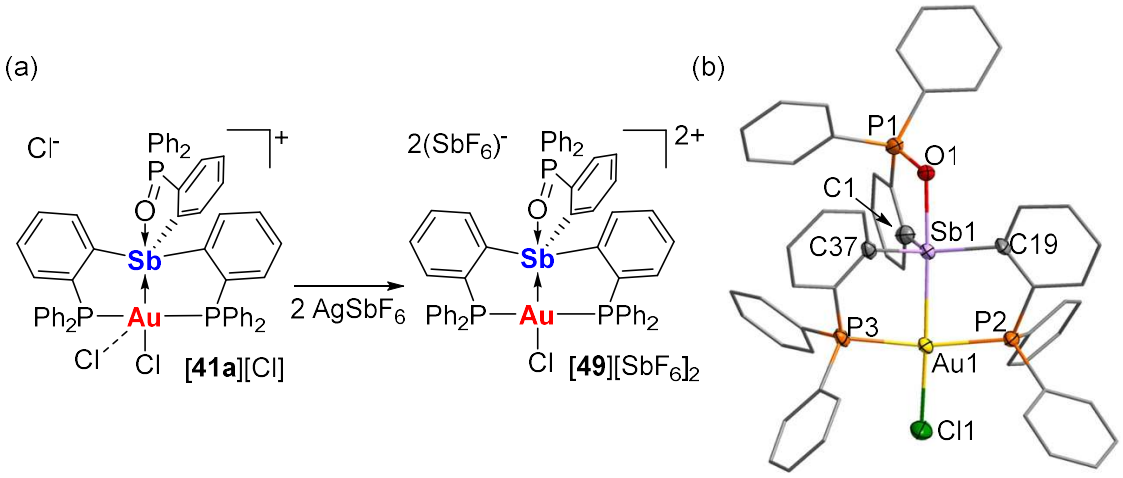

Figure 35. (a) Synthesis of [**49**][SbF_6]$_2$. (b) Solid-state structure of [**49**][SbF_6]$_2$. Thermal ellipsoids are drawn at the 50% probability level. The phenyl groups are drawn in wireframe, the. hydrogen atoms, interstitial solvent molecules and counter anions are omitted for clarity.

2.5.3 Activation of [49][SbF$_6$]$_2$ by silver salt

To better understand the catalytic species in the reaction, we titrated [**49**][SbF_6]$_2$ with AgOTf. A species was formed when progressively adding AgOTf as indicated by ^{31}P NMR spectroscopy (Figure 36). The need for eight equivalents to complete the conversion indicates the robustness of the Au–Cl bond in [**49**][SbF_6]$_2$. The resulting complex, assigned to be [**50**][SbF_6]$_2$, could not be isolated in a crystalline form.

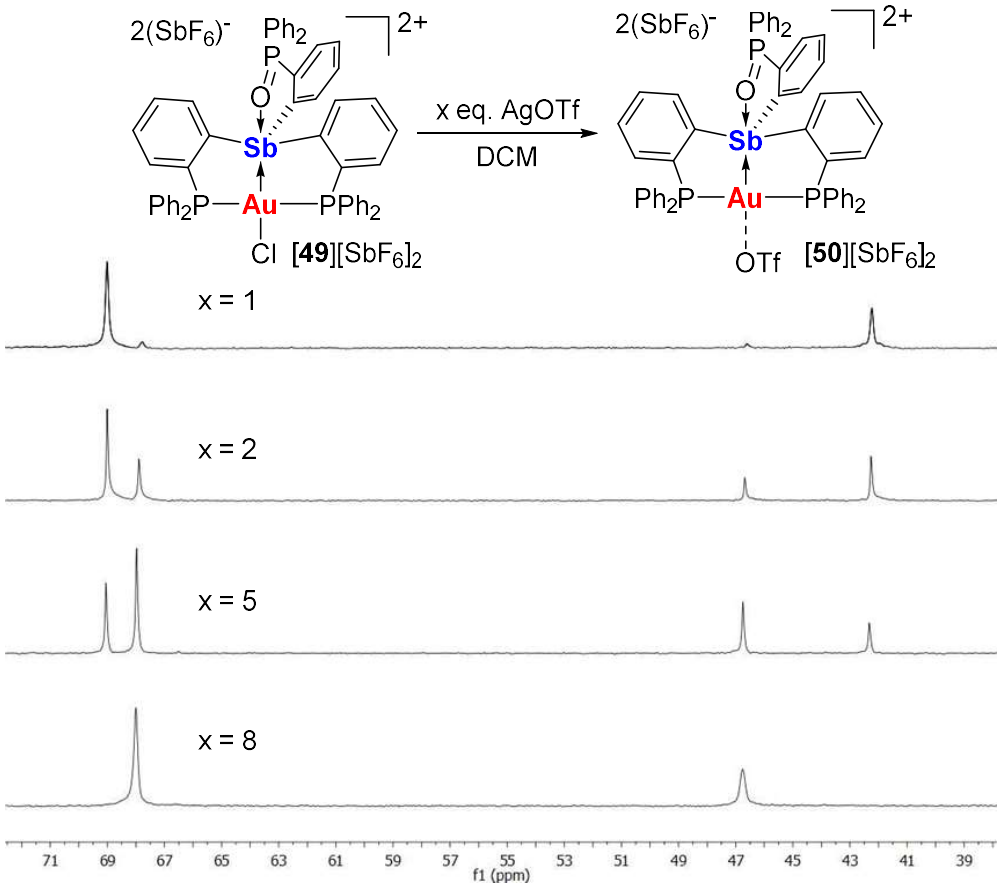

Figure 36. Chloride abstraction from [**49**][SbF_6]$_2$ by addition of equivalents of AgOTf.

*2.5.3 Styrene activation by [**49**][SbF_6]$_2$*

Having noticed that the reactivity of [**47**]$^{2+}$ in the polymerization and hydroamination of styrene, we decided to use these two reactions to bench mark the anion effect. The polymerization of styrene catalyzed by [**49**][SbF_6]$_2$/$AgSbF_6$ was highly exothermic and completed almost instantaneously (Figure 37). The polystyrene was characterized by GPC, which afforded Mw = 25,059 and PDI = 3.18. Slower polymerization of styrene (3 hours) was observed when the co-catalyst was AgOTf. The resulting polymer was also confirmed by GPC (Mw = 21568, PDI = 2.16). The

difference in reaction rate is assumed to be due to the higher affinity of the triflate anion for the gold center ($OTf^- > SbF_6^-$).[122, 136-138] The more weakly coordinating SbF_6^- anion facilitates the coordination of the substrate as well as its activation. As a result, the reaction is shortened.

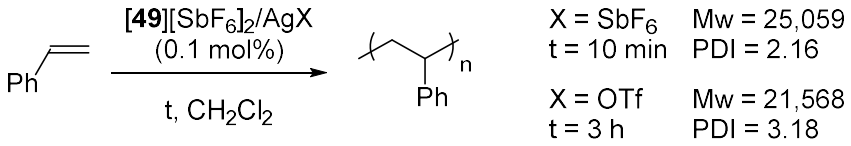

Figure 37. Polymerization of styrene catalyzed by [**49**][SbF_6]$_2$/AgX.

In the presence of *p*-toluenesulfonamide ($TsNH_2$), the Markovnikov hydroamination product was obtained in high yield after 1 hour when [**49**][SbF_6]$_2$/AgOTf (5 mol%) is used at 35°C (Entry 1, Table 2). These reaction conditions are less aggressive than those used with PPh_3AuCl/AgOTf or HOTf as catalyst, which both require higher temperature (85°C) and longer reaction time (14 h). Hence the proton-catalyzed mechanism is excluded. Interestingly, the amounts of AgOTf affects the reactivity of the gold center. NMR monitoring indicates that additional equivalents of AgOTf reduce the reaction time from 1 hour to under 20 minutes (Entry 1–4), suggesting that the progressive formation of the catalytic active complex upon addition of excess AgOTf. However, 16 equivalents of AgOTf slows the reaction (Entry 5). This result indicates that it is important to control the concentration of the triflate anion, which might block gold center and interfere with the coordination of substrates at higher concentration.

Table 2. Hydroamination of styrene catalyzed by [**49**][SbF_6]$_2$/m (AgOTf)

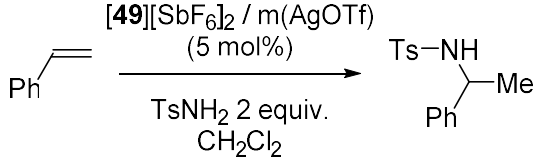

Entry	m	Time	Yield[a]
1	1	1 h	> 95%
2	1	20 min	52%
3	4	20 min	82%
4	8	20 min	95%
5	16	20 min	50%

[a] The yield was measured by ^{1}H NMR spectroscopy using 1,2-dichloroethane as an internal standard.

Silver salt accompanied with different anion was applied to activate gold center for hydroamination of styrene (Table 3). We found out [**49**][SbF_6]$_2$/$AgNTf_2$ promoted 90% yield of the Markovnikov hydroamination product, which was achieved after 30 minutes when a 5 mol% catalyst loading was employed. The reaction is faster than using AgOTf as the co-catalyst, which is consistent with the fact that the OTf^- anion is more coordinating anion to gold than NTf_2^-.[122, 136-138] Then we were eager to apply $AgSbF_6$, containing a weaker donating anion, as the co-catalysis to examine if the catalytic activity of the catalyst is higher. While the styrene was fully consumed in 10 minutes when [**49**][SbF_6]$_2$/$AgSbF_6$ was used as catalyst, polystyrene was the dominant product, instead of the hydroamination product. The least coordinating anion SbF_6^- makes the catalyst more carbophilic and leads to polymerization prior to the hydroamination. These results again verify our hypothesis that the coordinating strength of the counter anion affect the catalytic activity.[122, 136-138]

Table 3. Hydroamination of styrene catalyzed by [**49**][SbF_6]$_2$/ AgX

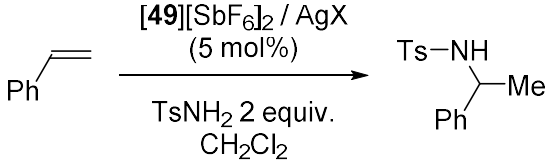

Entry	X	Time	Yield[a]
1	OTf	1 h	95%
2	NTf_2	30 min	90%
3	SbF_6	10 min	0%[b]

[a]The yield was measured by ^{1}H NMR spectroscopy using 1,2-dichloroethane as an internal standard. [b]Quantitative conversion of styrene was observed, and polystyrene was isolated with 81% of yield.

2.5.4 Synthesis of the dicationic gold complex with OTf⁻ as counter anions

To verify that the gold-bound chloride can indeed be displaced by weakly coordination anions, the complex [**45a**][Cl] was treated with 10 equivalents of AgOTf, leading to the clean formation of the resulting cationic complex [**51**][OTf]$_2$ (Figure 38a). The ^{31}P NMR spectrum of the corresponding complex features resonance at 67.5 ppm and 42.2 ppm. This complex crystallizes in the $P2_1/n$ space group with three closely identical molecules in the asymmetric unit (Figure 38b). The most important aspect is the verification that the gold-bound chloride is replaced by a triflate anion. The average Au–O distance is 2.256(7) Å and it is longer than the Au–O distance in tris(o-tolyl)phosphine-gold(I) triflate complex (2.110(3) Å), due to the sterically crowded environment around the gold center. The square planar geometry of the gold center suggests the donation from gold to antimony and forms an electronic configuration close to d^8 metal center. The average Au–Sb distance is 2.638(1) Å is slightly longer than the

that of [**49**][SbF_6]$_2$ (2.619(2) Å) and this trend is also reflected computationally (2.668 Å in [**51**]$^{2+}$ and 2.665 Å in [**46**]$^{2+}$). The bond elongation presents a change in dative nature of the interaction, which is more polarized in [**46**]$^{2+}$, paralleled with the gold affinity of different anions (Cl^- > OTf^-).[122, 136-138] The gold atom in the square planar is capped by a triflate anion, forming an Au–O interaction of avg. 2.680(7) Å. This Au–O bond distance is shorter than the one in [**46**][NTf_2]$_2$ of 2.958(8) Å, which is consistent with the gold affinity of these anions (OTf^- > NTf_2^-).

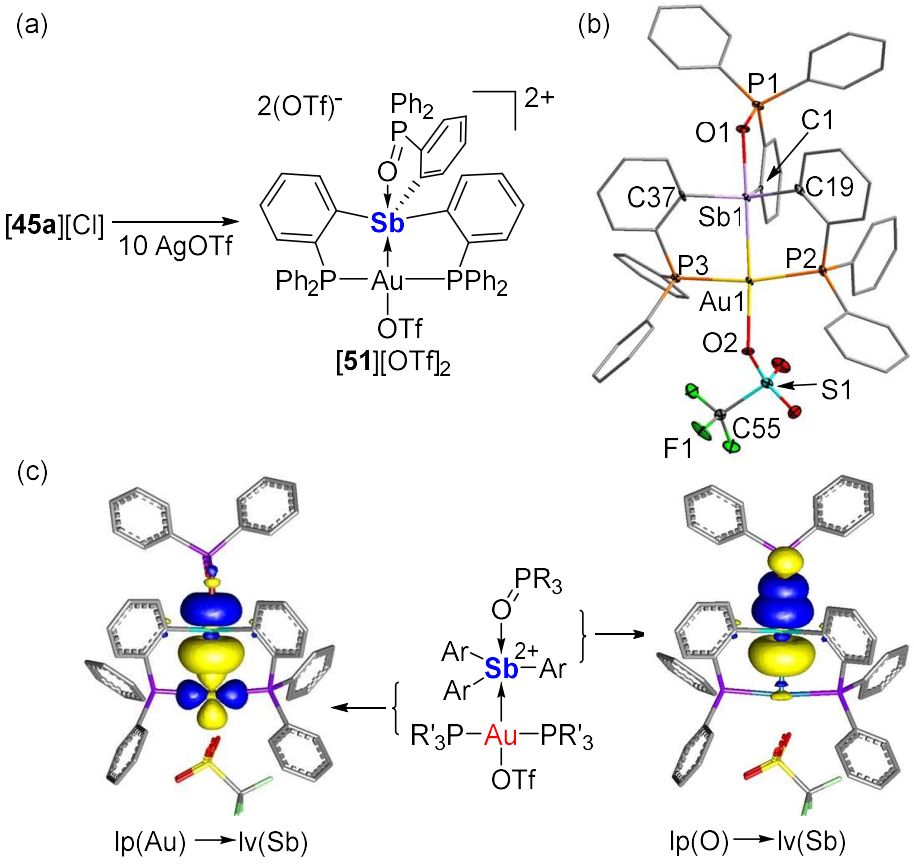

Figure 38. (a) Synthesis of [**51**][OTf]$_2$. (b) Solid-state structure of [**51**][OTf]$_2$. Thermal ellipsoids are drawn at the 50% probability level. The phenyl groups are drawn in wireframe, the. hydrogen atoms, interstitial solvent molecules and counter anions are omitted for clarity. (c) NBO plots of the (left) Sb–Au and (right) O–Sb major bonding interactions in [**51**]$^{2+}$ (isodensity value 0.05). Hydrogen atoms are omitted.

The NBO analysis also shows two donations to the dicationic antimony center for stabilization (Figure 38c). In fact, the orbitals involved in these two interactions are the same as those in [**46**]$^{2+}$ but the strength of the donation varies along with the donating strength of gold-bound X-ligand. The lp(O)→p(Sb) donation in [**51**]$^{2+}$ provides stability to the complex by $E^{(2)}$ = 79.9 kcal/mol, which is slightly larger than that in [**46**]$^{2+}$. In contrast, the d_{x2-y2}(Au)→p(Sb) and a d_{z2}(Au)→p(Sb) interactions in [**51**]$^{2+}$, contribute $E^{(2)}$ = 36.84 kcal/mol and 8.93 kcal/mol, which are smaller than that in [**46**]$^{2+}$. These results again align with trend of the ligand strength (OTf^- > Cl^-). In other words, the weaker donating strength of triflate anion makes Au→Sb donation weaker due to the decreased electron density on the gold center. At the same time, the increased O→Sb interaction becomes necessary for compensation to stabilize the dicationic complex.

Despite the higher lability of triflate than chloride, [**51**][OTf]$_2$ showed no catalytic activity to hydroamination of styrene with $TsNH_2$. The addition of AgOTf to [**51**][OTf]$_2$ didn't show any reactivity, suggesting the silver cation is not necessary for the catalytic species (Entry 1, Table 4). Interestingly, the presence of $AgSbF_6$ in the mixture slightly revived the catalytic activity (Entry 2, Table 4). The results align the stronger binding of anion to the gold center prevents the activation of the substrate, leading to the poorly reactive system. the reported binding affinity toward gold complex

Table 4. Hydroamination of α- and β-substituted styrene catalyzed by [**51**][OTf]$_2$/ AgX.

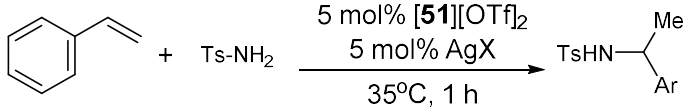

Entry	X	Yield (%)[a]
1	OTf	0
2	SbF_6	12

[a]The yield was measured by ^{1}H NMR spectroscopy using 1,2-dichloroethane as an internal standard.

2.6 Exploration of new reaction related to olefin activation

2.6.1 Hydroarylation of styrene

Inspired by the fact that [**50**]$^{2+}$ is catalytically active for styrene hydroamination, we turned our focus to building a C–C bond with styrene activation through electrophilic catalysis. To our delight, when phenol was added as the nucleophile, we found the formation of hydroarylation products in 74% yield, as a mixture of 47% ortho and 27% para products (Entry 1, Table 5). The temperature required in our system is lower than that as using Bronsted acid catalyst or main group catalysts. For example, refluxing in 1,2-dichloroethane is necessary for a catalyst like $KHSO_4$,[139] 80°C for $FeCl_3$,[140] and refluxing in toluene for $GaCl_3$.[141] The [**50**]$^{2+}$ provides another synthetic route for complex molecule due to a lower possibility for the decomposition of the substrate and occurrence of side reactions under milder reaction condition. The higher rate of the reaction was observed when nucleophile is *p*-cresol, in which the methyl group act as a stronger electron-donating substituent (Entry 2, Table 5). Hence, the electron richness of the aromatic ring affects the reactivity of the substrate in our system, which supports the electrophilic mechanism that we proposed.

Table 5. Hydroarylation of styrene catalyzed by [**49**][SbF_6]$_2$/ AgOTf.

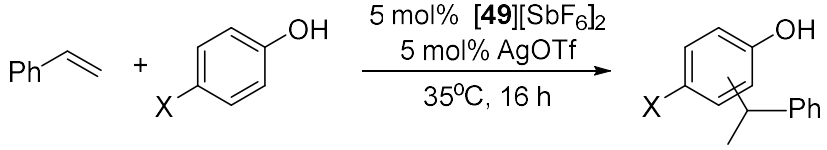

Entry	X	Yield (%)[a]
1	H	*p*: 47% *o*: 27%
2	Me	>95%

[a]The yield was measured by ^{1}H NMR spectroscopy using 1,2-dichloroethane as an internal standard.

2.6.2 Other olefins activation

In addition to styrene, we are interested in the reactivity of complex [**50**]$^{2+}$ toward other olefins. At first, vinyl ether, which is assumed to be a highly reactive olefin due to the electron richness was selected for catalyzed polymerization.[142] Polymerization of the substrate catalyzed by [**49**]$^{2+}$/$AgSbF_6$ (0.1 mol%) was observed and confirmed by the comparison of the ^{1}H NMR spectra with literature (Figure 39).[143] It takes less than 5 minutes for complex [**50**]$^{2+}$ to reach full conversion of the olefin. Compared to the full conversion after 30 minutes for using $Ph_2CH_2Br/AgClO_4$ (0.5 mol%) as catalyst,[143] or 50% conversion after 30 minutes for $AgSbF_6$, [**50**]$^{2+}$ is highly reactive to vinyl ether. The stronger donating anion is believed to tame the catalytic activity of [**50**]$^{2+}$ in the case of hydroamination of styrene, so we switched from $AgSbF_6$ to AgOTf to study the hydroamination of ethyl vinyl ether.[144-145] However, no hydroamination was observed. Instead, only broaden ^{1}H NMR signals, matched with the corresponding polymer was found. These results suggest that the ethyl vinyl ether is so reactive that the presence of

triflate anion and the $TsNH_2$ substrate are not able to stop the "activated olefin" from polymerization.

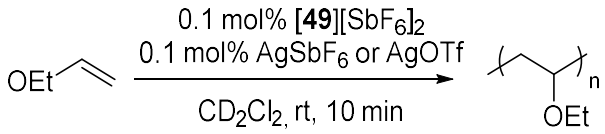

Figure 39. Polymerization of ethyl vinyl ether catalyzed by [**49**][SbF_6]$_2$/AgX.

While we were testing the substrate scope for hydroamination, vinyl acetate was chosen for the catalysis. Surprisingly, a clean hydroacetoxylation was observed in high yield when a 5 mol% loading of [**49**][SbF_6]$_2$ and AgOTf (Figure 40a). To the best of our knowledge, this reaction has only been reported once, catalyzed by ruthenium complex.[146] The proposed mechanism from the study suggest the formation of benzene from the trimerization of the released acetylene at 140°C. However, neither benzene or acetylene was not observed in the NMR spectrum.

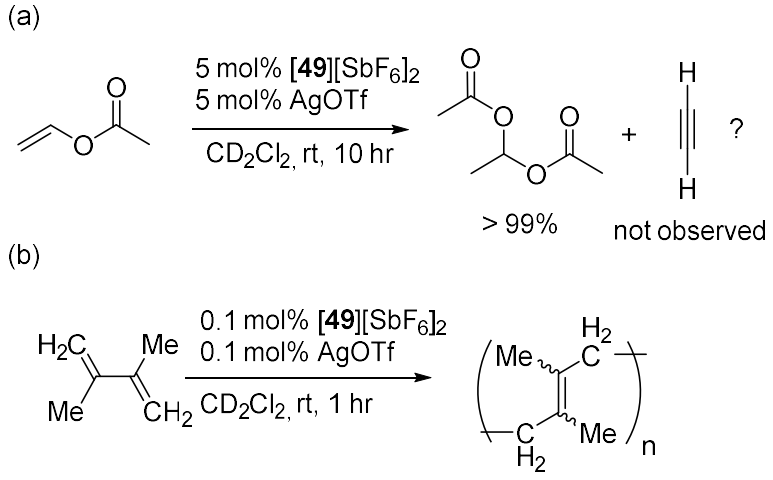

Figure 40. (a) hydroacetoxylation of vinyl acetate catalyzed by [**49**][SbF_6]$_2$/AgOTf. (b) polymerization of DMBD catalyzed by [**49**][SbF_6]$_2$/AgOTf.

Additionally, conjugated diene, a more challenging substrate, was chosen for examination of the reaction catalyzed by [**49**][SbF_6]$_2$/AgOTf (Figure 40(b)). Delightfully, the 1,4-polymerization of 2,3-dimethyl-1,3-butadiene (DMBD) was observed by ^{1}H NMR, providing the spectra matched with the assignment from literatures.[147] However, the presence of $TsNH_2$ eliminate the reactivity of the gold complex toward DMBD, so no hydroamination product was found.

2.7 Conclusion

In conclusion, we describe the synthesis and characterization of a gold chloride complex, [**46**][NTf_2]$_2$, featuring a Z-type dicationic antimony ligand. Formation of this complex is made possible by the coordination of a neutral phosphine oxide donor that attenuates the reactivity of the dicationic antimony center. Despite its electron-deficient nature, the gold center of [**46**]$^{2+}$ can be activated by conversion into the proposed triflimide complex [**47**]$^{2+}$. Generation of this complex is accompanied by the emergence of atypical reactivity toward styrene which is readily polymerized or converted into the hydroamination Markovnikov product when in the presence of *p*-toluenesulfonamide. This unusual reaction highlights the unique activation resulting from the coordination of the dicationic antimony Z-type ligand to the gold center.

The donation strength of counter anion in the dicationic complex plays important role to control the catalytic activity. The complex with OTf^- coordinated to the gold center shows ability to tame the reactivity for hydroamination or hydroarylation of styrene, instead of polymerization. Interestingly, the high concentration of OTf^- reduce the catalytic activity in [**51**][OTf]$_2$, indicating the substrate activation is precluded as a

concentrated coordinated anion. To better control the reactivity of the dicationic complex, it is necessary to search for a sweet spot of an equilibrium between the counter anion and the substrate coordination to the gold center.

2.8 Experimental Section

General Consideration. Complex **44** was prepared according to the reported procedures.[120] Dichloromethane and chloroform were dried over CaH_2. Diethyl ether was dried over Na/K. All other solvents were used as received. Complex [**45**][Cl] was synthesized on the benchtop. Complexes [**46**][NTf_2]$_2$ – [**51**][OTf]$_2$ were synthesized under a dry N_2 atmosphere employing either a glovebox or standard Schlenk techniques. Commercially available chemicals were purchased and used as provided (commercial source: Alfa Aesar for $AgNTf_2$, J. T. Baker for hydrogen peroxide, Acros Organics for HNTf). Ambient-temperature NMR spectra were recorded on a Varian Unity Inova 500 FT NMR spectrometer (499.42 MHz for ^{1}H, 125.58 MHz for ^{13}C, 469.89 MHz for ^{19}F, 202.16 MHz for ^{31}P), a Varian Unity Inova 400 FT NMR (161.74 MHz for ^{31}P). ^{1}H and $^{13}C\{^1H\}$ NMR chemical shifts (δ) are given in ppm and are referenced against the solvent signals. $^{31}P\{^1H\}$ NMR chemical shifts are given in ppm and are referenced against H_3PO_4 as an external standard. $^{31}P\{^1H\}$ MAS NMR spectrum was recorded on a Bruker Avance–400 Solids NMR spectrometer (162 MHz for ^{31}P) equipped with a standard 7mm MAS NMR probe head, Standard 7mm Zirconium oxide rotor has been applied. The ^{31}P chemical shifts are given in ppm and referenced to external H_3PO_4. Elemental analyses (EA) were performed at Atlantic Microlab (Norcross, GA).

Crystallographic Measurements. All crystallographic measurements were performed at 110(2) K using a Bruker SMART APEX II diffractometer or a Brucker D8 QUEST diffractometer (graphite monochromated Mo-Kα radiation, λ = 0.71073 Å). In each case, a specimen of suitable size and quality was selected and mounted onto a nylon loop. The structures were solved by direct methods, which successfully located most of the non-hydrogen atoms. The semiempirical method SADABS was applied for absorption correction.[148] Subsequent refinement on F^2 using the SHELXTL/PC package (version 6.1)[149] allowed location of the remaining non-hydrogen atoms. Structural refinements were performed using Olex2.[150] The data has been deposited to the Cambridge data base under the following numbers: CCDC 1905863-1905864.

Table 6. Crystal data and structure refinement for [**45a**][Cl].

Identification code	y_a_sq	
Empirical formula	C54 H42 Au Cl3 O P3 Sb	
Formula weight	1224.85	
Temperature	273.15 K	
Wavelength	0.71073 Å	
Crystal system	Triclinic	
Space group	P-1	
Unit cell dimensions	a = 10.8165(9) Å	α= 88.150(3)°.
	b = 16.2607(13) Å	β= 71.610(3)°.
	c = 16.9196(13) Å	γ = 85.953(3)°.
Volume	2816.7(4) $Å^3$	
Z	2	
Density (calculated)	1.444 Mg/m^3	
Absorption coefficient	3.342 mm^{-1}	
F(000)	1200	
Crystal size	0.35 x 0.04 x 0.03 mm^3	
Theta range for data collection	2.281 to 26.482°.	
Index ranges	-13<=h<=13, -20<=k<=20, -21<=l<=21	
Reflections collected	44395	
Independent reflections	11581 [R(int) = 0.0832]	
Completeness to theta = 25.242°	99.7 %	
Absorption correction	Semi-empirical from equivalents	
Max. and min. transmission	0.7454 and 0.5439	
Refinement method	Full-matrix least-squares on F^2	
Data / restraints / parameters	11581 / 0 / 568	
Goodness-of-fit on F^2	1.042	
Final R indices [I>2sigma(I)]	R1 = 0.0705, wR2 = 0.1489	
R indices (all data)	R1 = 0.0976, wR2 = 0.1656	
Extinction coefficient	n/a	
Largest diff. peak and hole	2.521 and -3.422 $e.Å^{-3}$	

Table 7. Crystal data and structure refinement for [**46**][NTf_2]$_2$.

Identification code	y_a	
Empirical formula	C58 H42 Au Cl F12 N2 O9 P3 S4 Sb	
Formula weight	1714.25	
Temperature	110.06 K	
Wavelength	0.71073 Å	
Crystal system	Monoclinic	
Space group	P 1 21/c 1	
Unit cell dimensions	a = 19.315(3) Å	α= 90°.
	b = 17.669(3) Å	β= 92.432(5)°.
	c = 20.852(3) Å	γ = 90°.
Volume	7110.0(18) Å^3	
Z	4	
Density (calculated)	1.601 Mg/m^3	
Absorption coefficient	2.745 mm^{-1}	
F(000)	3360	
Crystal size	0.4 x 0.3 x 0.23 mm^3	
Theta range for data collection	2.111 to 26.514°.	
Index ranges	-24<=h<=24, -22<=k<=22, -26<=l<=26	
Reflections collected	127988	
Independent reflections	14590 [R(int) = 0.0817]	
Completeness to theta = 25.242°	99.9 %	
Absorption correction	Semi-empirical from equivalents	
Max. and min. transmission	0.7454 and 0.3598	
Refinement method	Full-matrix least-squares on F^2	
Data / restraints / parameters	14590 / 123 / 820	
Goodness-of-fit on F^2	1.074	
Final R indices [I>2sigma(I)]	R1 = 0.0707, wR2 = 0.1777	
R indices (all data)	R1 = 0.1007, wR2 = 0.2109	
Extinction coefficient	n/a	
Largest diff. peak and hole	5.975 and -2.504 e.Å^{-3}	

Table 8. Crystal data and structure refinement for [**48**][SbF_6].

Identification code	y_a	
Empirical formula	C54 H42 Au Cl2 F6 P3 Sb2	
Formula weight	1409.15	
Temperature	110.0 K	
Wavelength	0.71073 Å	
Crystal system	Triclinic	
Space group	P-1	
Unit cell dimensions	a = 12.6943(12) Å	α= 72.524(2)°.
	b = 15.3315(14) Å	β= 71.908(2)°.
	c = 16.2127(15) Å	γ = 79.442(2)°.
Volume	2846.8(5) $Å^3$	
Z	2	
Density (calculated)	1.644 Mg/m^3	
Absorption coefficient	3.743 mm^{-1}	
F(000)	1360	
Crystal size	0.35 x 0.25 x 0.04 mm^3	
Theta range for data collection	2.630 to 26.430°.	
Index ranges	-15<=h<=15, -19<=k<=19, -20<=l<=20	
Reflections collected	49709	
Independent reflections	11687 [R(int) = 0.0352]	
Completeness to theta = 25.242°	99.8 %	
Absorption correction	Semi-empirical from equivalents	
Max. and min. transmission	0.4908 and 0.3201	
Refinement method	Full-matrix least-squares on F^2	
Data / restraints / parameters	11687 / 0 / 676	
Goodness-of-fit on F^2	1.084	
Final R indices [I>2sigma(I)]	R1 = 0.0400, wR2 = 0.1043	
R indices (all data)	R1 = 0.0446, wR2 = 0.1082	
Extinction coefficient	n/a	
Largest diff. peak and hole	4.950 and -2.281 $e.Å^{-3}$	

Table 9. Crystal data and structure refinement for [**49**][SbF_6]$_2$.

Identification code	y_a	
Empirical formula	C58 H48 Au Cl F12 N2 O P3 Sb3	
Formula weight	1707.56	
Temperature	110.0 K	
Wavelength	0.71073 Å	
Crystal system	Monoclinic	
Space group	P 1 21/c 1	
Unit cell dimensions	a = 24.568(4) Å	α= 90°.
	b = 13.335(2) Å	β= 105.184(3)°.
	c = 20.769(3) Å	γ = 90°.
Volume	6566.9(17) Å^3	
Z	4	
Density (calculated)	1.727 Mg/m^3	
Absorption coefficient	3.634 mm^{-1}	
F(000)	3280	
Crystal size	0.29 x 0.24 x 0.12 mm^3	
Theta range for data collection	2.135 to 26.455°.	
Index ranges	-30<=h<=30, -16<=k<=16, -25<=l<=25	
Reflections collected	172118	
Independent reflections	13488 [R(int) = 0.0938]	
Completeness to theta = 25.242°	99.9 %	
Absorption correction	Semi-empirical from equivalents	
Max. and min. transmission	0.7454 and 0.4821	
Refinement method	Full-matrix least-squares on F^2	
Data / restraints / parameters	13488 / 0 / 760	
Goodness-of-fit on F^2	1.029	
Final R indices [I>2sigma(I)]	R1 = 0.0559, wR2 = 0.1226	
R indices (all data)	R1 = 0.0766, wR2 = 0.1308	
Extinction coefficient	n/a	
Largest diff. peak and hole	3.848 and -1.706 e.Å^{-3}	

Table 10. Crystal data and structure refinement for [**51**][OTf]$_2$.

Identification code	3otf	
Empirical formula	C59 H46 Au Cl4 F9 O10 P3 S3 Sb	
Formula weight	1735.56	
Temperature	110.0 K	
Wavelength	0.71073 Å	
Crystal system	Monoclinic	
Space group	P 1 21/c 1	
Unit cell dimensions	a = 23.6441(18) Å	α= 90°.
	b = 17.5106(13) Å	β= 100.135(2)°.
	c = 47.455(4) Å	γ = 90°.
Volume	19341(3) Å^3	
Z	12	
Density (calculated)	1.788 Mg/m^3	
Absorption coefficient	3.112 mm^{-1}	
F(000)	10224	
Crystal size	0.327 x 0.314 x 0.204 mm^3	
Theta range for data collection	2.096 to 27.610°.	
Index ranges	-30<=h<=30, -22<=k<=22, -61<=l<=61	
Reflections collected	461056	
Independent reflections	44469 [R(int) = 0.0593]	
Completeness to theta = 25.242°	99.8 %	
Absorption correction	Semi-empirical from equivalents	
Max. and min. transmission	0.4305 and 0.1739	
Refinement method	Full-matrix least-squares on F^2	
Data / restraints / parameters	44469 / 3627 / 2341	
Goodness-of-fit on F^2	1.378	
Final R indices [I>2sigma(I)]	R1 = 0.0941, wR2 = 0.1684	
R indices (all data)	R1 = 0.1111, wR2 = 0.1768	
Extinction coefficient	n/a	
Largest diff. peak and hole	2.958 and -2.720 e.Å^{-3}	

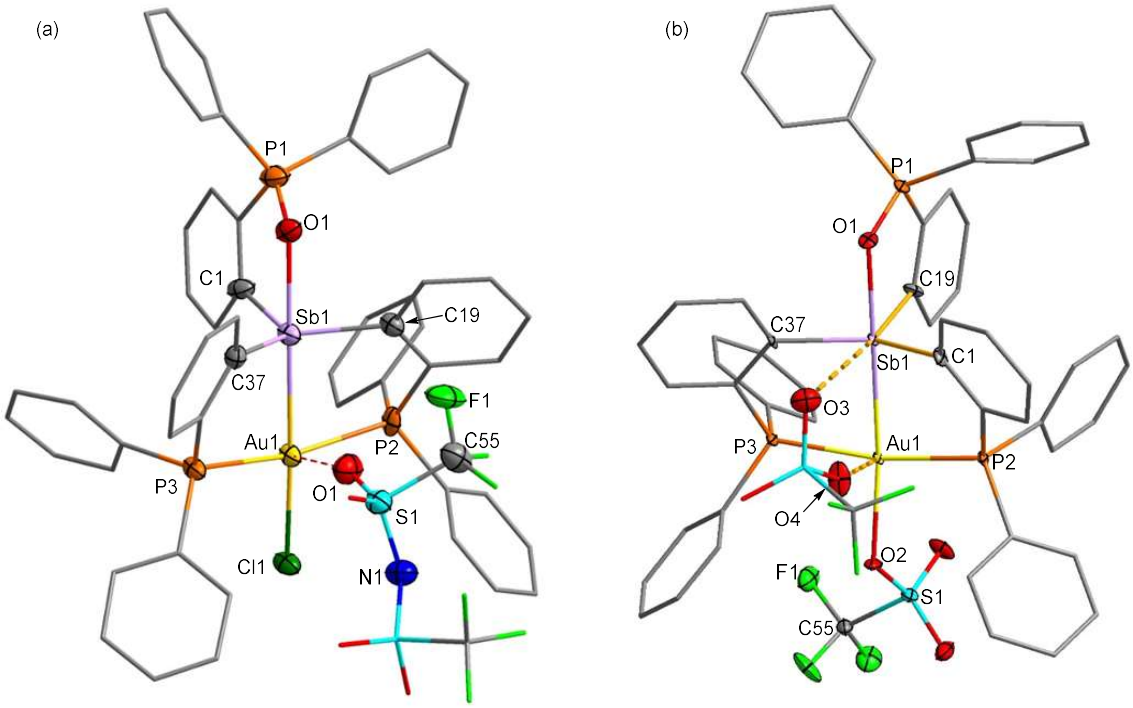

Figure 41. (a) Structure of [**46**][NTf_2]$_2$ with one of the triflimide counter anion shown. This triflimide anion forms a weak contact with the gold center (Au1–O1: 2.958(8)Å). (b) Structure of [**51**][OTf]$_2$ with two of the triflate counter anions shown. Triflate anions form an interaction with the gold center respectively (Au1–O2: 2.256(7)Å, Au1–O3: 2.680(7)Å and Sb1–O4: 3.621(9)Å).

Computational Details. The structure of the complex was optimized using Density Functional Theory (DFT) as implemented in Gaussian 09 (functional B3LYP;[151-152] mixed basis set Sb/Au cc-pVTZ-PP[153]; P/Cl/O 6-31g(d'), C/O/H 6-31g. with effective core potentials for the heavy elements).[154-155] The optimized structures were subjected to a NBO analysis, performed with the B3LYP functional using the NBO 6.0 program.[156] The resulting NBOs were visualized and plotted using the Jimp 2 program.[157-159] The energy of the Sb-Au interaction was derived from the second order perturbation energy associated with the donor-acceptor interaction shown in Figure 28.

Table 11. XYZ coordinates of the optimized geometry of [**46**]$^{2+}$.

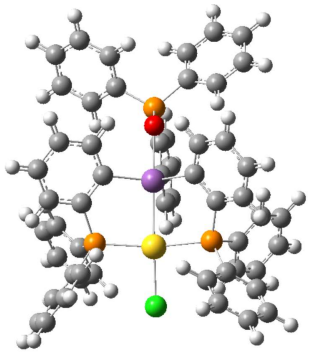

Sb	-0.683599	-0.083850	-0.603204	Cl	4.052111	0.171910	1.175114
P	-3.972480	-0.141763	-0.149328	P	1.886087	-2.330453	-0.077068
P	1.625174	2.430614	-0.045186	O	-2.822264	-0.263187	-1.213926
C	-1.643727	-0.136552	1.338200	C	-3.053642	-0.139824	1.416214
C	-3.682766	-0.176610	2.671726	H	-4.765720	-0.194059	2.741196
C	-2.914343	-0.200700	3.840778	H	-3.404285	-0.231015	4.807406
C	-1.517389	-0.191288	3.761193	H	-0.921348	-0.212970	4.666692
C	-0.880372	-0.159891	2.513078	H	0.203678	-0.157927	2.471381
C	-5.081473	-1.555765	-0.241181	C	-6.397123	-1.474016	0.262775
H	-6.784456	-0.537794	0.649930	C	-7.220575	-2.603319	0.246722
H	-8.232225	-2.536409	0.630878	C	-6.744317	-3.813319	-0.273123
H	-7.388830	-4.685308	-0.289417	C	-5.440294	-3.897938	-0.777956
H	-5.077032	-4.833902	-1.187780	C	-4.606443	-2.777188	-0.760439
H	-3.600576	-2.844631	-1.158652	C	-4.932106	1.372496	-0.308080
C	-4.691115	2.485825	0.523388	H	-3.955563	2.429744	1.318159
C	-5.414554	3.667150	0.335508	H	-5.236646	4.516865	0.985251
C	-6.373932	3.750652	-0.681041	H	-6.937354	4.666945	-0.819500
C	-6.613935	2.650769	-1.515781	H	-7.359834	2.715145	-2.300047
C	-5.900207	1.464353	-1.333154	H	-6.102351	0.614209	-1.976325
C	0.674045	-2.749678	-1.396989	C	-0.424112	-1.916750	-1.712076
C	-1.305899	-2.263731	-2.747460	H	-2.147264	-1.625166	-2.980606
C	-1.092460	-3.438345	-3.481886	H	-1.762051	-3.689391	-4.297275
C	-0.015958	-4.275008	-3.172426	H	0.150278	-5.184044	-3.739538
C	0.860526	-3.935137	-2.136677	H	1.701661	-4.582337	-1.914817
C	1.416010	-3.203594	1.448933	C	2.138321	-2.916902	2.628871
H	2.946675	-2.191464	2.614226	C	1.821260	-3.582439	3.816155
H	2.386491	-3.370049	4.717062	C	0.786052	-4.527292	3.840769
H	0.547861	-5.045671	4.763189	C	0.064578	-4.808248	2.674805
H	-0.732126	-5.543905	2.692025	C	0.374487	-4.150532	1.478911
H	-0.183841	-4.384178	0.579271	C	3.492639	-2.967799	-0.635919
C	4.071309	-4.107107	-0.044537	H	3.578938	-4.612306	0.777960
C	5.297156	-4.589338	-0.516766	H	5.740548	-5.465597	-0.057161
C	5.949955	-3.942070	-1.571280	H	6.902521	-4.316184	-1.929816
C	5.378323	-2.805825	-2.160635	H	5.888158	-2.299503	-2.972595
C	4.157489	-2.315918	-1.695169	H	3.731998	-1.425710	-2.148185
C	0.317211	2.761942	-1.292941	C	0.322975	4.002476	-1.963004
H	1.098523	4.728769	-1.746180	C	-0.650340	4.299429	-2.922890
H	-0.624206	5.254324	-3.435874	C	-1.644437	3.364204	-3.224331
H	-2.393009	3.586928	-3.976640	C	-1.673281	2.128915	-2.563877

Table 11 Continued

H	-2.449584	1.411528	-2.792318	C	-0.693951	1.823480	-1.606823
C	3.139788	3.196455	-0.695378	C	3.616667	2.790335	-1.960347
H	3.073264	2.053290	-2.544500	C	4.790136	3.342964	-2.474449
H	5.151629	3.031600	-3.448269	C	5.501215	4.297133	-1.732714
H	6.415297	4.721776	-2.132733	C	5.033620	4.700539	-0.477832
H	5.582124	5.438509	0.096668	C	3.856937	4.153197	0.045935
H	3.508501	4.470594	1.021328	C	1.168708	3.246548	1.517751
C	0.141314	4.208157	1.582047	H	-0.420915	4.475389	0.694471
C	-0.151488	4.835594	2.797848	H	-0.936650	5.582664	2.840648
C	0.572794	4.512131	3.951282	H	0.347608	5.007609	4.889419
C	1.593302	3.553939	3.892812	H	2.161025	3.307550	4.783438
C	1.892888	2.916729	2.684943	H	2.691602	2.181813	2.645389
Au	1.861579	0.056176	0.175606				

Table 12. . XYZ coordinates of the optimized geometry of [**51**]$^{2+}$.

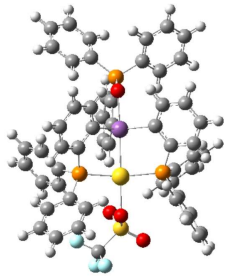

Au	-1.379917	0.140421	-0.241045	C	0.391187	3.920977	-2.398704
Sb	1.238881	-0.075678	-0.701904	H	-0.400418	4.657617	-2.318519
S	-4.009493	0.544665	1.593954	C	-0.537650	3.377381	1.117193
P	-1.436137	-2.256058	-0.541697	C	0.344371	4.477788	1.072709
P	-1.029218	2.521741	-0.416524	H	0.780067	4.799944	0.134068
P	4.391279	-0.255731	0.213810	C	0.657387	5.170646	2.245525
F	-6.376463	-0.408544	0.775232	H	1.327783	6.022180	2.202213
F	-4.931378	-1.954736	1.518128	C	0.098193	4.777024	3.468006
F	-5.978748	-0.608310	2.973040	H	0.334877	5.324658	4.373763
O	3.389655	-0.315662	-1.005655	C	-0.771560	3.681817	3.518737
O	-3.564660	0.304986	0.130997	H	-1.214238	3.377789	4.460704
O	-2.963146	0.041796	2.534812	C	-1.087931	2.976736	2.352438
O	-4.569115	1.883346	1.835104	H	-1.765774	2.133935	2.417486
C	-0.176465	-2.593961	-1.836050	C	-2.499554	3.323080	-1.111165
C	0.998658	-1.815941	-1.945067	C	-3.297565	4.172013	-0.321417
C	1.971486	-2.122665	-2.908383	H	-3.026300	4.391572	0.703643
H	2.875650	-1.532484	-2.980554	C	-4.464058	4.725667	-0.858749
C	1.764776	-3.195121	-3.787766	H	-5.077395	5.375878	-0.245740
H	2.507279	-3.415820	-4.546735	C	-4.842121	4.434809	-2.173577
C	0.601727	-3.965176	-3.696423	H	-5.749347	4.864508	-2.583683
H	0.438446	-4.790427	-4.380409	C	-4.053182	3.584434	-2.962129
C	-0.360699	-3.671695	-2.723225	H	-4.346488	3.360530	-3.981855
H	-1.260108	-4.273932	-2.658912	C	-2.889486	3.023051	-2.435675
C	-0.975914	-3.242040	0.919536	H	-2.284902	2.367778	-3.056010
C	0.001581	-4.255144	0.843192	C	1.875950	-0.182861	1.361553
H	0.516331	-4.456406	-0.089282	C	3.260868	-0.237866	1.633634

Table 12 Continued

C	0.301770	-5.021920	1.973889	C	3.703069	-0.314186	2.964629
H	1.046804	-5.807295	1.907509	H	4.763623	-0.370484	3.187599
C	-0.365234	-4.786308	3.181959	C	2.774326	-0.328708	4.011498
H	-0.135546	-5.388815	4.054092	H	3.120352	-0.389909	5.037075
C	-1.333969	-3.777618	3.262806	C	1.403844	-0.270012	3.735625
H	-1.856369	-3.595836	4.195579	H	0.683374	-0.285421	4.545574
C	-1.641240	-3.001445	2.141292	C	0.949163	-0.196785	2.411284
H	-2.390559	-2.222324	2.223047	H	-0.119054	-0.155604	2.225224
C	-3.035188	-2.840681	-1.164054	C	5.439620	-1.715673	0.230614
C	-3.601012	-4.040176	-0.688116	C	5.016935	-2.884675	-0.434002
H	-3.101379	-4.618023	0.080469	H	4.095793	-2.883172	-1.005210
C	-4.824343	-4.482360	-1.201424	C	5.798402	-4.041180	-0.372112
H	-5.258704	-5.404388	-0.831699	H	5.478188	-4.936668	-0.893037
C	-5.489449	-3.734355	-2.179685	C	6.995830	-4.043606	0.354814
H	-6.441883	-4.077352	-2.568472	H	7.599942	-4.943055	0.399755
C	-4.933552	-2.536775	-2.650266	C	7.419569	-2.885122	1.018393
H	-5.455825	-1.951402	-3.398513	H	8.350291	-2.885905	1.574412
C	-3.713662	-2.085839	-2.143906	C	6.649711	-1.720459	0.957391
H	-3.303670	-1.145351	-2.498052	H	6.999183	-0.823769	1.458064
C	0.333339	2.744265	-1.626094	C	5.415074	1.220454	0.211131
C	1.367923	1.790502	-1.762660	C	6.553733	1.267061	-0.624331
C	2.443240	2.024163	-2.632642	H	6.839949	0.401918	-1.212915
H	3.242157	1.299809	-2.718897	C	7.325906	2.428935	-0.686393
C	2.480193	3.199950	-3.394338	H	8.202170	2.459526	-1.324121
H	3.303964	3.368695	-4.078993	C	6.974855	3.547829	0.081001
C	1.454682	4.142758	-3.281209	H	7.583120	4.444643	0.037410
H	1.477625	5.048823	-3.876311	C	5.845447	3.509337	0.908378
H	5.580346	4.374122	1.506274	H	4.193411	2.332398	1.622457
C	5.062742	2.353521	0.974471	C	-5.418683	-0.670758	1.721928

Table 13. Selected bond lengths (Å) and angles (°) for complexes [**46**][NTf_2]$_2$ as determined crystallographically and optimized computationally.

Parameter	[**46**][NTf_2]$_2$	[**46**]$^{2+}$
	X-ray	DFT
Sb(1)-Au(1)	2.6269(7)	2.6654
Au(1)-Cl(1)	2.398(2)	2.4105
Au(1)-O(2)	2.958(8)	
Sb(1)-O(1)	2.206(7)	2.2314
Sb(1)-Au(1)-Cl(1)	176.39(6)	172.49
Sb(1)-Au(1)-O(2)	75.62(17)	
C(37)-Sb(1)-C(19)	119.8(4)	119.55

Table 13 Continued

Parameter	[**46**][NTf_2]$_2$	[**46**]$^{2+}$
	X-ray	DFT
C(1)-Sb(1)-C(19)	116.8(4)	115.89
C(37)-Sb(1)-C(1)	120.1(4)	120.86
O(1)-Sb(1)-Au(1)	177.27(17)	178.08
P(2)-Au-P(3)	166.25(9)	167.58

Table 14. Selected bond lengths (Å) and angles (°) for complexes [**49**][SbF_6]$_2$ and [**51**][OTf]$_2$ as determined crystallographically and optimized computationally.

Parameter	[**49**][SbF_6]$_2$	[**49**]$^{2+}$	[**51**][OTf]$_2$	[**51**]$^{2+}$
	X-ray	DFT	X-ray	DFT
Sb(1)-Au(1)	2.6191(6)	2.66535	2.6330(7)	2.66781
Au(1)-Cl(1)	2.389(2)	2.41057	-	-
Au(1)-Cl(2)	-		-	-
Au(1)-O(2)	-	-	2.241(6)	2.22230
Sb(1)-O(1)	2.181(5)	2.23137	2.162(6)	2.18533
Sb(1)-Au(1)-Cl(1)	175.18(7)	172.49232	-	-
Sb(1)-Au(1)-Cl(2)	-	-	-	-
Sb(1)-Au(1)-O(2)	-	-	170.20(19)	179.49095
C(37)-Sb(1)-C(19)	124.4(3)	120.86178	124.6(4)	115.05517
O(1)-Sb(1)-Au(1)	176.73(15)	178.07427	177.90(17)	177.45288
P(2)-Au-P(3)	167.56(6)	167.57992	169.45(8)	166.68127

Synthesis of [45][Cl]. A CH_2Cl_2 solution (5 mL) of complex **44** (200 mg, 0.165 mmol) was treated with one equivalent of H_2O_2 (13 μl, 0.165 mmol). After the resulting mixture was stirred for 30 min, the solvent was evaporated under vacuum. Recrystallization of the residue from CH_2Cl_2/pentane yielded a pale-yellow solid (146

mg, 72%). Single crystals of [**45a**][Cl] suitable for X-ray diffraction were obtained by diffusion of diethyl ether into a concentrated CH_2Cl_2 solution of [**45a**][Cl]/ **45b**-Cl at room temperature. $^{31}P\{^1H\}$ NMR (202.16 MHz; CD_2Cl_2): δ 96.08 (s, 2 P), 61.67 (s, 0.9 P), 44.31 (s, 1 P), 41.69 (s, 0.45 P). Elemental analysis calcd (%) for $C_{54}H_{42}AuCl_3OP_3Sb$: C, 52.95; H, 3.46. Found: C, 52.66; H, 3.74.

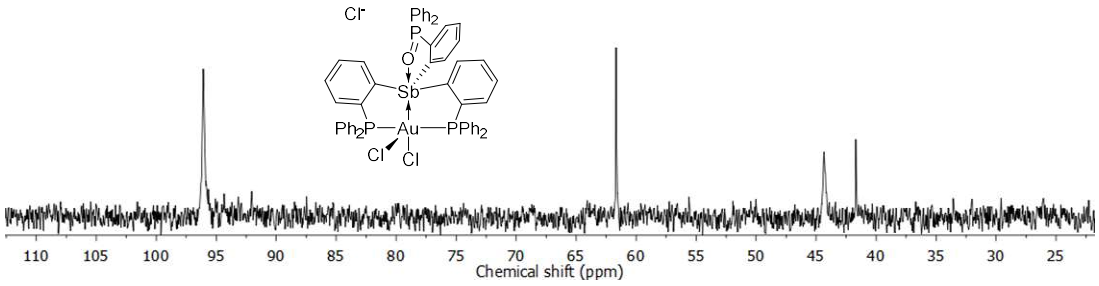

Figure 42. $^{31}P\{^1H\}$ NMR spectrum of [**45**][Cl] in CD_2Cl_2 showing the co-existence of [**45a**][Cl] and **45b-**Cl.

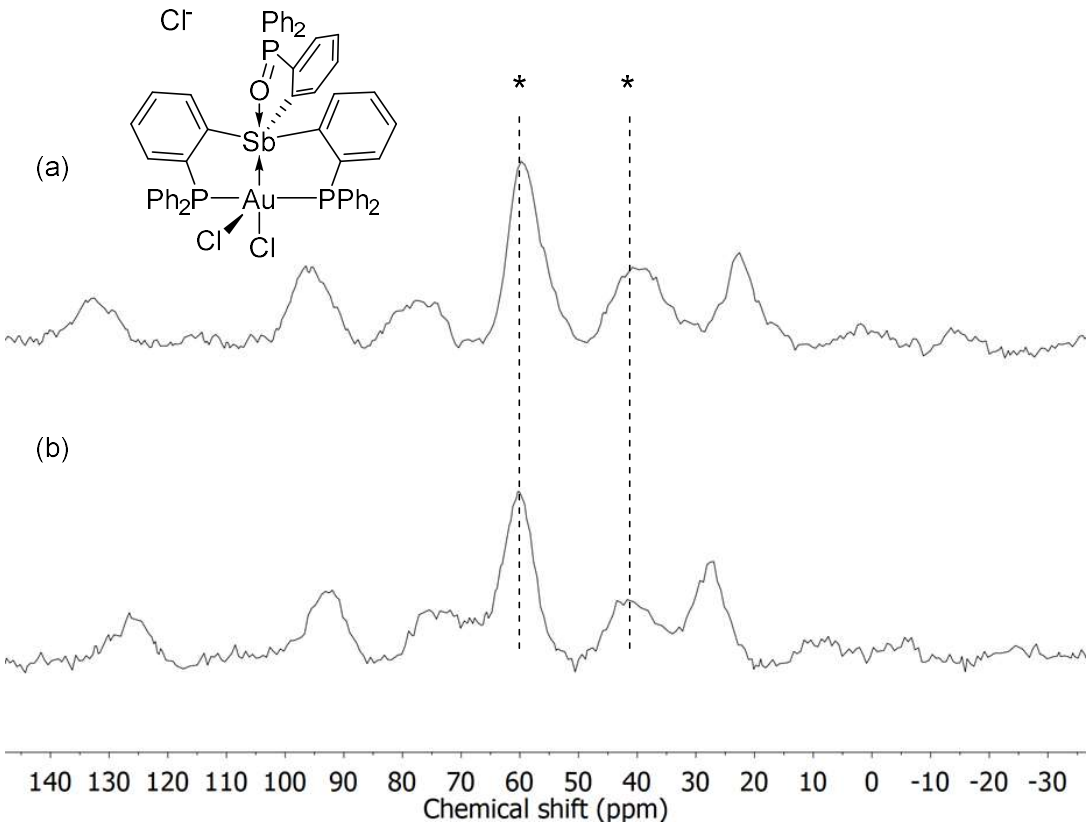

Figure 43. ^{31}P MAS NMR spectrum of [**45a**][Cl] at (a) 6.0 kHz and (b) 5.2 kHz. The relevant peaks have been marked by an asterisk (*).

Synthesis of [46][NTf$_2$]$_2$ To a stirred solution of [**45**][Cl] (195 mg, 0.159 mmol) in CH_2Cl_2 (5 mL) was added solid $AgNTf_2$ (124 mg, 0.320 mmol). After the resulting mixture was stirred for 1 h, the solution was filtered through Celite. The filtrate was brought to dryness. Recrystallization of the residue from CH_2Cl_2/pentane yielded a colorless solid (218 mg, 80%). Single crystals of [**46**][NTf_2]$_2$ suitable for X-ray diffraction were obtained by diffusion of diethyl ether into a concentrated CH_2Cl_2 solution of [**46**][NTf_2]$_2$ at room temperature. ^{1}H NMR (499.42 MHz; CD_2Cl_2): δ 6.53 (d, $^3J_{H\text{-}H}$ = 7.7 Hz, 1H), 6.71 (t, $^3J_{H\text{-}H}$= 7.7 Hz, 1H), 7.31–7.47 (m, 15H), 7.49–7.56 (m, 3H),

7.57–7.65 (m, 12H), 7.69–7.77 (m, 4H), 7.77–7.83 (m, 4H), 8.78 (d, , 2H, *o*-P(Sb)C_6H_4, $^3J_{H\text{-}H}$= 7.9 Hz). $^{13}C\{^1H\}$ NMR (125.58 MHz; CD_2Cl_2): δ 120.14 (q, NTf_2, J = 321.42 Hz), 123.28 (s), 123.73 (m), 124.73 (s), 127.80 (s), 128.61 (s), 128.64 (t, J = 32.02 Hz), 130.37 (m), 132.73 (d, $J_{C\text{-}P}$ = 12.02 Hz), 133.16 (t, $J_{C\text{-}P}$= 6.29 Hz), 133.69 (d, $J_{C\text{-}P}$ = 12.40 Hz), 134.32 (s), 134.50 (m), 134.83 (t, $J_{C\text{-}P}$ = 4.42 Hz), 135.07 (t, $J_{C\text{-}P}$ = 6.94), 135.63 (s), 135.74 (s), 136.11(d, $J_{C\text{-}P}$ = 2.77 Hz), 136.63 (d, $J_{C\text{-}P}$ = 8.05 Hz), 137.31 (t, $J_{C\text{-}P}$ = 4.23), 138.25 (t, $J_{C\text{-}P}$ = 8.11), 145.23 (t, $J_{C\text{-}P}$ = 16.83). $^{31}P\{^1H\}$ NMR (202.16 MHz; CD_2Cl_2): □ 68.65 (s, 2P), 42.29 (s, 1P). Elemental analysis calcd (%) for $C_{54}H_{42}AuClF_{12}OP_3Sb_3$: C, 40.64; H, 2.4und: C,40.28; H, 2.46.

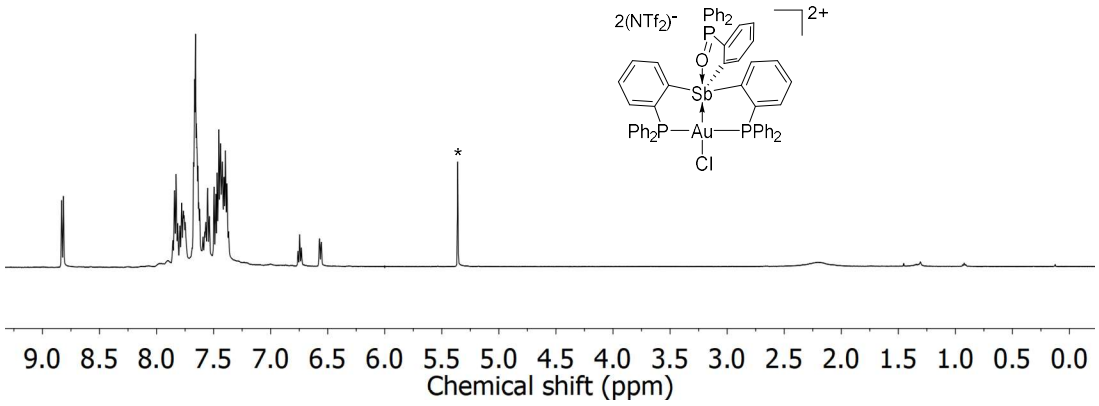

Figure 44. ^1H NMR spectrum of [**46**][NTf_2]$_2$ in CD_2Cl_2. The CD_2Cl_2 solvent peak has been marked by an asterisk (*).

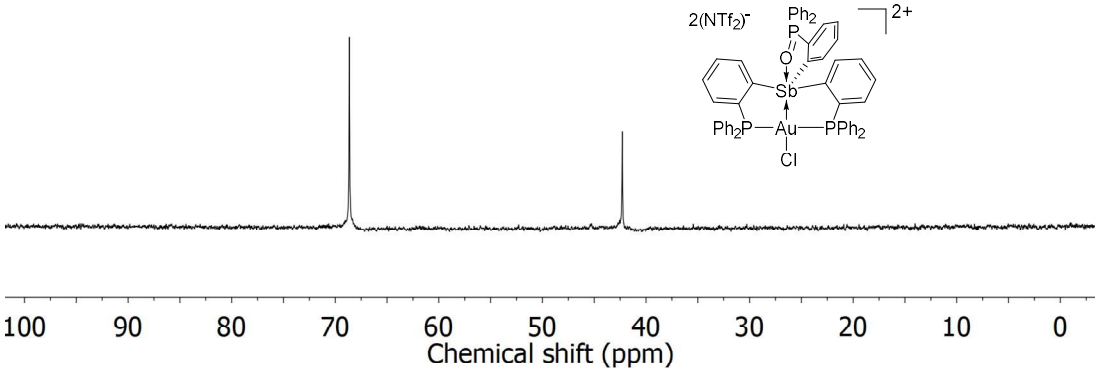

Figure 45. $^{31}P\{^1H\}$ NMR spectrum of [**46**][NTf_2]$_2$ in CD_2Cl_2.

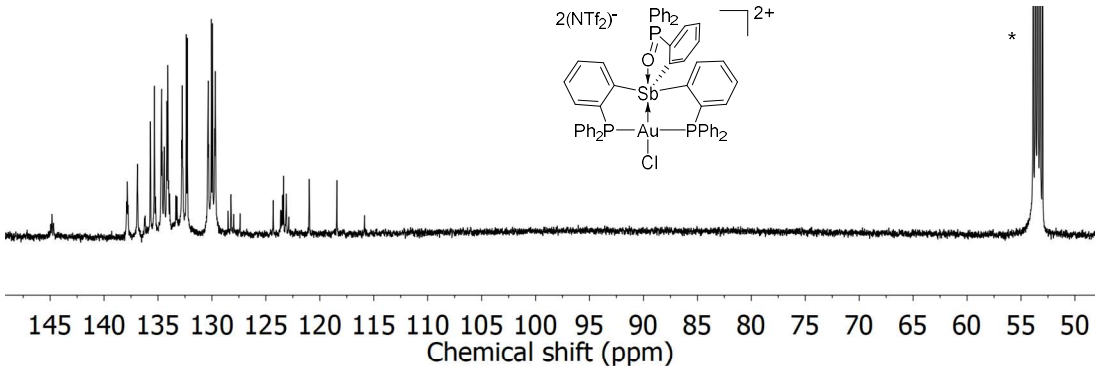

Figure 46. $^{13}C\{^{1}H\}$ NMR spectrum of [**46**][NTf_2]$_2$ in CD_2Cl_2. The CD_2Cl_2 solvent peak has been truncated and marked by an asterisk (*).

Generation of [47][NTf_2]$_2$. To a solution of [**45**][Cl] (10 mg, 0.012 mmol) in CH_2Cl_2 (0.5 mL) was added solid $AgNTf_2$ (9.5 mg, 0.036 mmol). The generation of [**47**][NTf_2]$_2$ was observed in situ by $^{31}P\{^{1}H\}$ NMR. $^{31}P\{^{1}H\}$ NMR (202.16 MHz; CD_2Cl_2): δ 67.91(s, 2P), 49.13 (s, 1P).

Synthesis of [48][SbF_6] To a stirred solution of **44** (50 mg, 0.04 mmol) in CH_2Cl_2 (5 mL) was added solid $AgNTf_2$ (16 mg, 0.04 mmol). After the resulting mixture was stirred for 10 minutes, the solution was filtered through Celite. The filtrate was brought to dryness. Recrystallization of the residue from CH_2Cl_2/pentane yielded a colorless solid. (47 mg, 83%). Single crystals of [**48**][SbF_6] suitable for X-ray diffraction were obtained by diffusion of diethyl ether into a concentrated acetonitrile solution of [**48**][SbF_6] at room temperature. $^{31}P\{^{1}H\}$ NMR (202.16 MHz; CD_2Cl_2): δ 42.72. Elemental analysis calcd (%) for $C_{54}H_{42}AuCl_2F_6P_3Sb2$: C, 46.02; H, 3.00. Found: C, 45.82; H, 3.05.

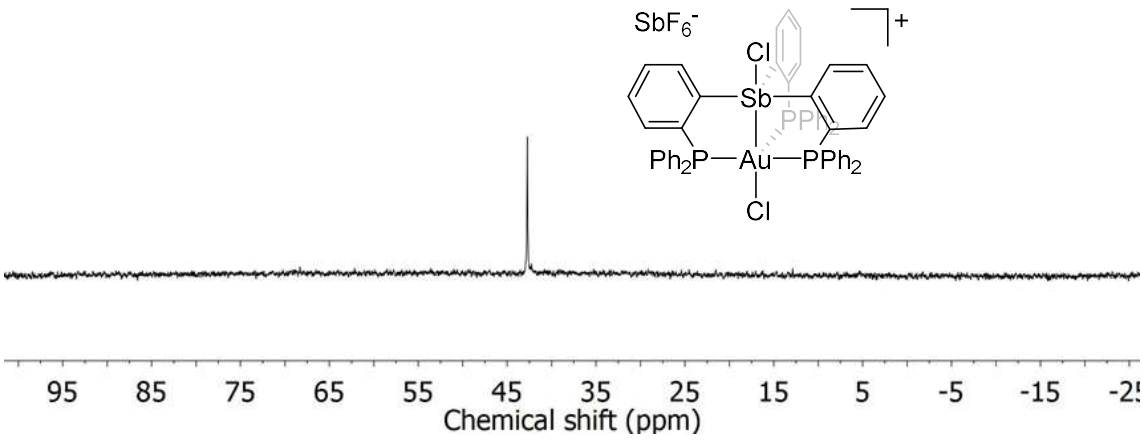

Figure 47. $^{31}P\{^{1}H\}$ NMR spectrum of [**48**][SbF_6] in CD_2Cl_2.

Synthesis of [49][SbF_6]$_2$ To a stirred solution of [**45**][Cl] (195 mg, 0.159 mmol) in $CHCl_3$ (5 mL) was added solid $AgSbF_6$ (110 mg, 0.320 mmol). After the resulting mixture was stirred for 16 h, the solution was filtered. The precipitate was extracted by CH_2Cl_2 and the filtered through Celite. The filtrate was brought to dryness. The recrystallization of the residue from CH_2Cl_2/pentane yielded a colorless solid (218 mg, 86%). Single crystals of [**49**][SbF_6]$_2$ suitable for X-ray diffraction were obtained by slowly vaporization of $CHCl_3$ solution at room temperature. ^{1}H NMR (499.42 MHz; CD_2Cl_2): δ 6.59 (dd, J= 7.7, 2.4 Hz, 1H), 6.77 (tt, J= 7.7, 1.3 Hz, 1H), 7.37–7.48 (m, 15H), 7.53–7.57 (m, 3H), 7.59–7.66 (m, 12H), 7.73–7.87 (m, 8H), 8.81 (d, J= 7.9 Hz, 2H). $^{13}C\{^{1}H\}$ NMR (125.58 MHz; CD_2Cl_2): δ 122.83–123.61 (m), 124.28 (s), 127.40 (s), 128.41 (t, J = 28.5 Hz), 130.11 (dd, J = 52.8, 39.3 Hz), 132.43 (d, J = 11.7 Hz), 132.81 (s), 133.55 (d, J = 11.7 Hz), 134.20 (s), 134.63 (s), 135.21 (s), 135.42 (s), 135.79 (s), 136.70 (s), 137.19 (s), 138.47 (s), 144.91 (t, J = 14.3 Hz). $^{31}P\{^{1}H\}$ NMR (202.16

MHz; CD_2Cl_2): δ 69.33, 42.49. Elemental analysis calcd (%) for $C_{54}H_{42}AuClF_{12}OP_3Sb_3$: C, 39.90; H, 2.60. Found: C, 39.73; H, 2.40.

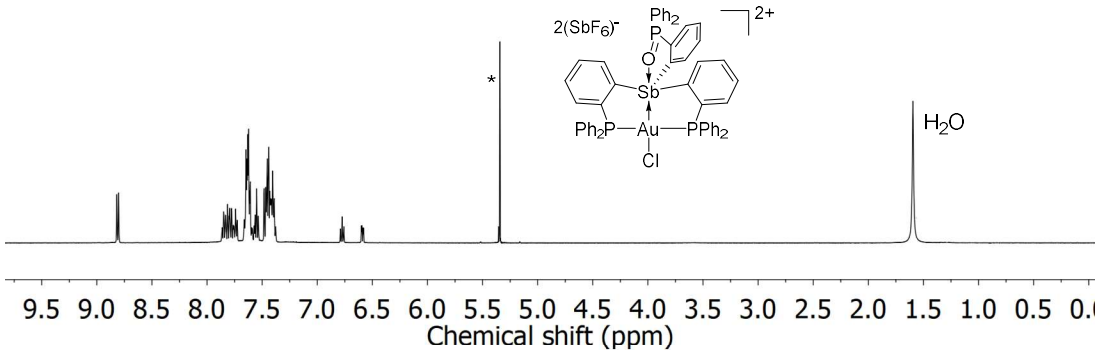

Figure 48. ^{1}H NMR spectrum of [**49**][SbF_6]$_2$ in CD_2Cl_2. The CD_2Cl_2 solvent peak has been marked by an asterisk (*).

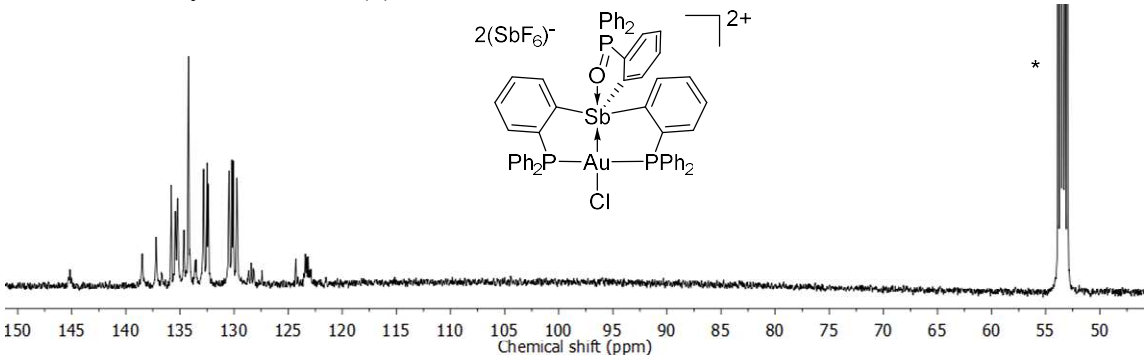

Figure 49. $^{13}C\{^{1}H\}$ NMR spectrum of [**45**][SbF_6]$_2$ in CD_2Cl_2. The CD_2Cl_2 solvent peak has been truncated and marked by an asterisk (*).

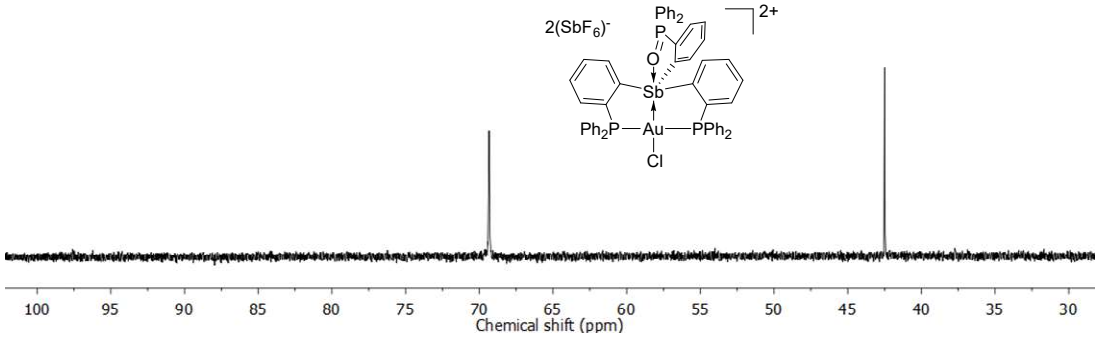

Figure 50. $^{31}P\{^{1}H\}$ NMR spectrum of [**49**][SbF_6]$_2$ in CD_2Cl_2.

Generation of [50][SbF_6]$_2$. To a solution of [**49**][SbF_6]$_2$ (10 mg, 0.012 mmol) in CH_2Cl_2 (0.5 mL) was added solid AgOTf (3.1 mg, 0.012 mmol). The generation of [**50**][SbF_6]$_2$ was observed in situ by $^{31}P\{^1H\}$ NMR (202.16 MHz; CD_2Cl_2): δ 68.01(s, 2P), 46.76 (s, 1P).

Synthesis of [51][OTf]$_2$ To a stirred solution of [**45**][Cl] (100 mg, 0.082 mmol) in CH_2Cl_2 (5 mL) was added solid AgOTf (210 mg, 0.817 mmol). After the resulting mixture was stirred for 1 h, the solution was filtered and the solvent was evaporated under vacuum. Recrystallization of the residue from CH_2Cl_2/diethyl ether yielded a colorless solid of [**51**][OTf]$_2$•2(CH_2Cl_2) (73mg, 74%). Single crystals of [**51**][OTf]$_2$ suitable for X-ray diffraction were obtained by pentane slowly diffusion into a CH_2Cl_2 solution at room temperature. ^1H NMR (499.42 MHz; CD_2Cl_2): δ 6.90–6.99 (m, 2H), 7.29 (ddd, J = 8.8, 6.1, 1.1 Hz, 2H), 7.34–7.40 (m, 8H), 7.42–7.47 (m, 2H), 7.47–7.55 (m, 5H), 7.60–7.69 (m, 9H), 7.72–7.82 (m, 8H), 7.82–7.90 (m, 4H), 8.76 (d, J = 8.0 Hz, 2H). $^{13}C\{^1H\}$ NMR (125.58 MHz; CD_2Cl_2): δ 118.99 (br), 122.36 (m), 127.09, 127.90, 128.90, 129.16, 129.42, 129.68 (t, J = 6.4 Hz), 130.15, 130.27 (m), 132.43 (d, J = 12.3 Hz), 133.20 (t, J = 6.1 Hz), 134.08, 134.39, 134.76, 135.06(m), 135.18, 135.74 (d, J = 11.4 Hz), 136.06 (d, J = 2.5 Hz), 136.59 (br), 136.96 (t, J = 8.1 Hz), 143.40 (t, *J* = 15.4 Hz). $^{31}P\{^1H\}$ NMR (202.16 MHz; CD_2Cl_2): δ 67.09, 46.41. Elemental analysis calcd (%) for $C_{59}H_{46}AuF_9O_{10}P_3S_3SbCl_2$: C, 40.83; H, 2.67. Found: C, 40.74; H, 2.70.

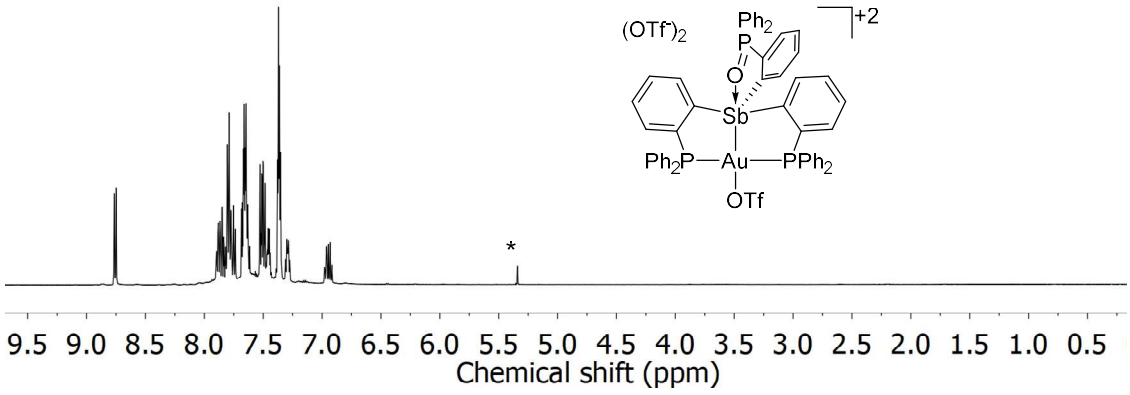

Figure 51. ^{1}H NMR spectrum of [**51**][OTf]$_2$ in CD_2Cl_2. The CD_2Cl_2 solvent peak has been marked by an asterisk (*).

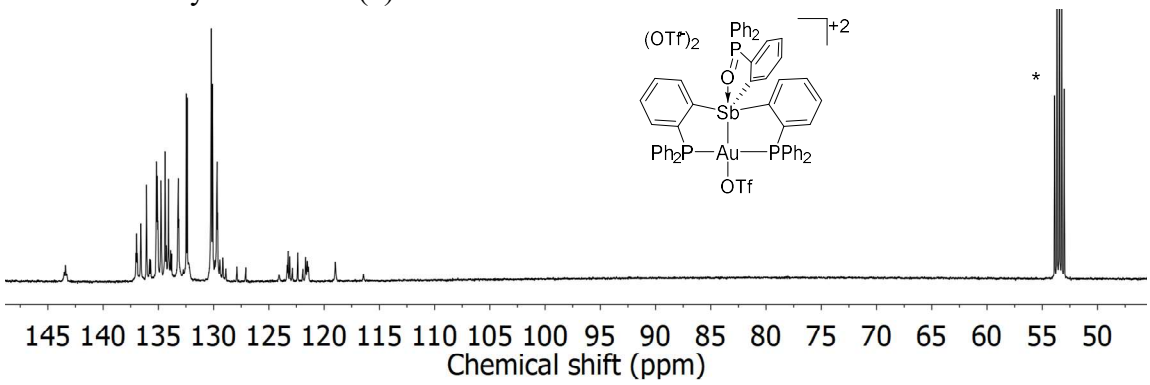

Figure 52. $^{13}C\{^{1}H\}$ NMR spectrum of [**51**][OTf]$_2$ in CD_2Cl_2. The CD_2Cl_2 solvent peak has been truncated and marked by an asterisk (*).

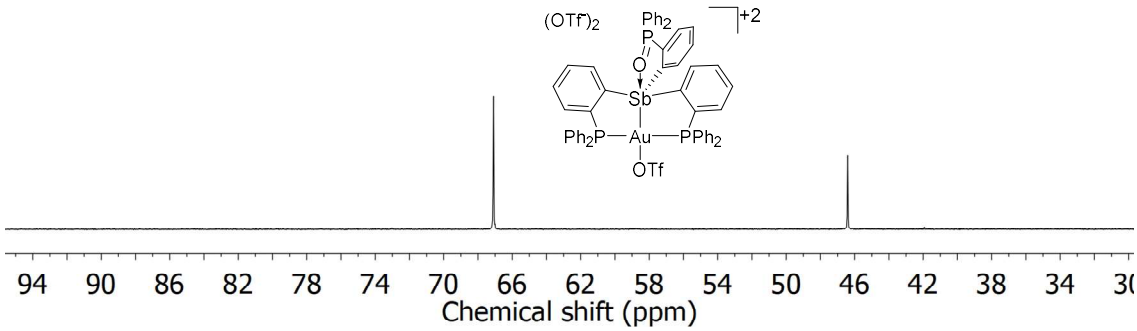

Figure 53. $^{31}P\{^{1}H\}$ NMR spectrum of [**51**][OTf]$_2$ in CD_2Cl_2.

Polymerization of styrene. Styrene (610 mg, 5.83 mmol) was mixed with the [**45**][Cl] (0.1 mol%, 10 mg, 0.008 mmol) and $AgNTf_2$ (0.3 mol%, 9.5 mg, 0.024 mmol)

in CD_2Cl_2 (0.5 mL). The solvent was evaporated under vacuum and the residue was taken up in CH_2Cl_2 (5 mL) and filtered through Celite. The filtrate was concentrated. Precipitation of the polymer was induced by addition of 10 mL of methanol. The polymer was collected by filtration and washed with methanol (3 × 2 mL), diethyl ether (3 × 2 mL), and dried under vacuum (445 mg, 73% yield).

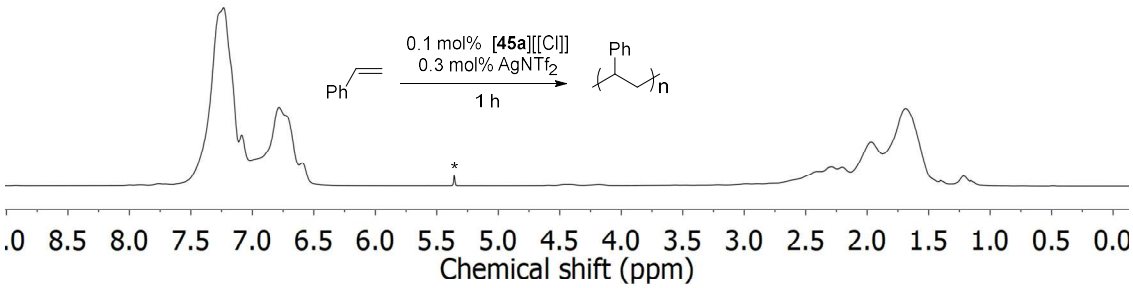

Figure 54. ^{1}H NMR spectrum for styrene polymerization catalyzed by [**45a**][Cl]/3 $AgNTf_2$ in CD_2Cl_2. The CD_2Cl_2 solvent peak has been marked by an asterisk (*).

General Procedure for the hydroamination of styrene and substituted styrenes with $TsNH_2$. Catalytic reactions were carried out under N_2. In a typical experiment, styrene (12.0 mg, 0.12 mmol) was mixed with the [**46**][NTf_2]$_2$ (5 mol%, 10 mg, 0.006 mmol), $AgNTf_2$ (5 mol%, 2.3 mg, 0.006 mmol) and $TsNH_2$ (39.9 mg, 0.23 mmol) in CD_2Cl_2 (0.5 mL). The yield was established by ^{1}H NMR spectroscopy using 1,2-dichloroethane (4.3 mg, 0.043 mmol) as an internal standard.

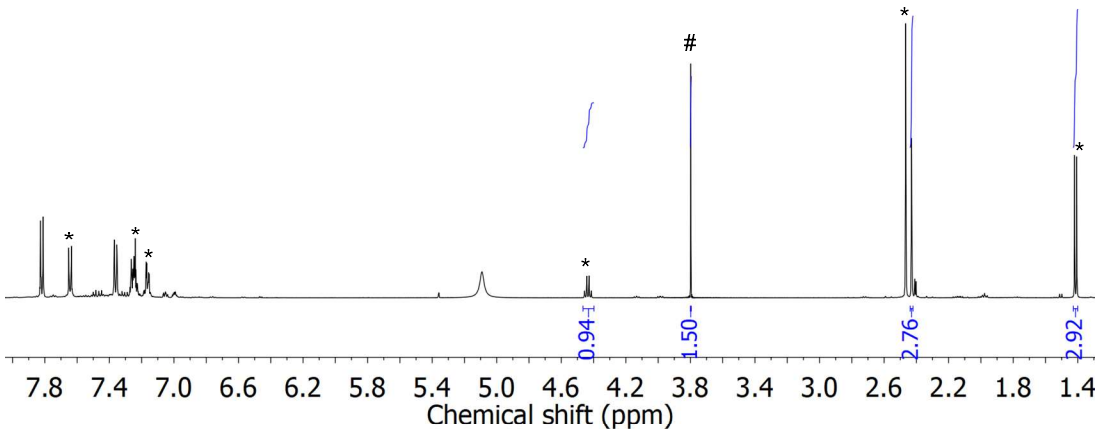

Figure 55. ^{1}H NMR spectrum measured during the hydroamination of styrene catalyzed by [**46**][NTf_2]$_2$/ $AgNTf_2$ in CD_2Cl_2. The hydroamination product peak is marked by an asterisk (*). The internal standard is marked by a pound sign (#).

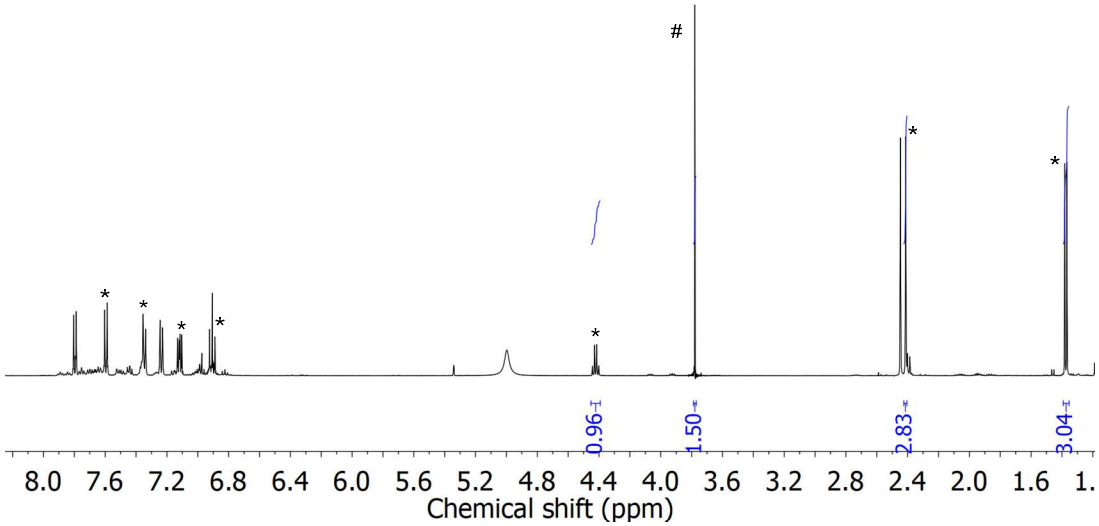

Figure 56. ^{1}H NMR spectrum measured during the hydroamination of 4-fluoro styrene catalyzed by [**46**][NTf_2]$_2$/ $AgNTf_2$ in CD_2Cl_2. The hydroamination product peak is marked by an asterisk (*). The internal standard is marked by a pound sign (#).

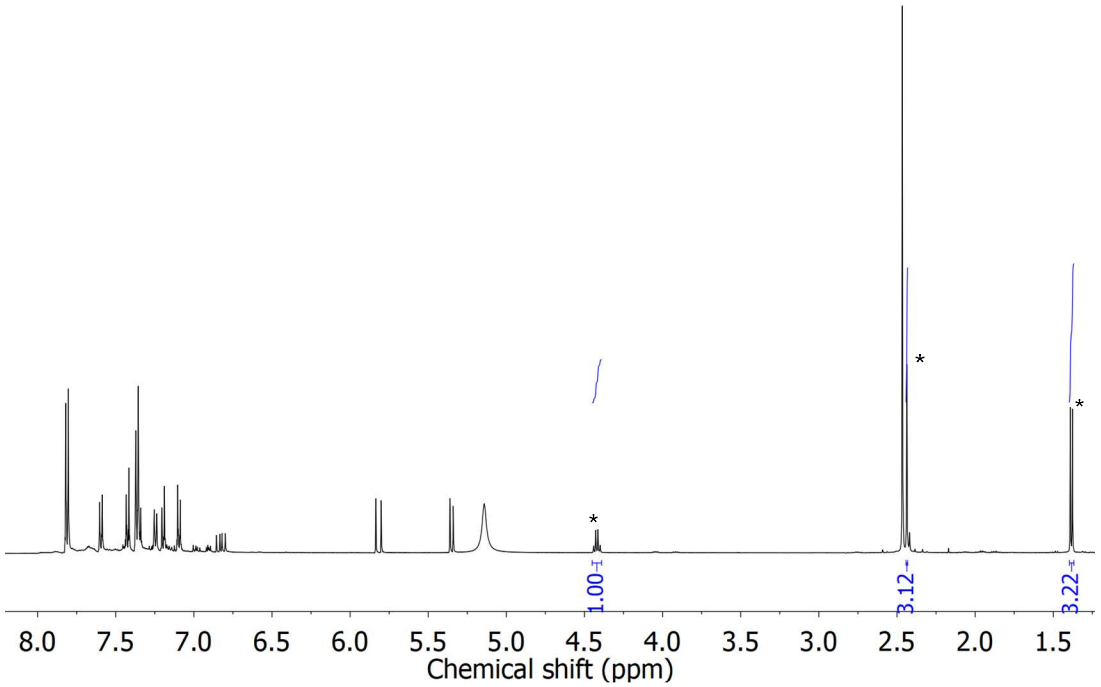

Figure 57. ^{1}H NMR spectrum measured during the hydroamination of 4-chloro styrene catalyzed by [**46**][NTf_2]$_2$/ $AgNTf_2$ in CD_2Cl_2. The hydroamination product peak is marked by an asterisk (*).

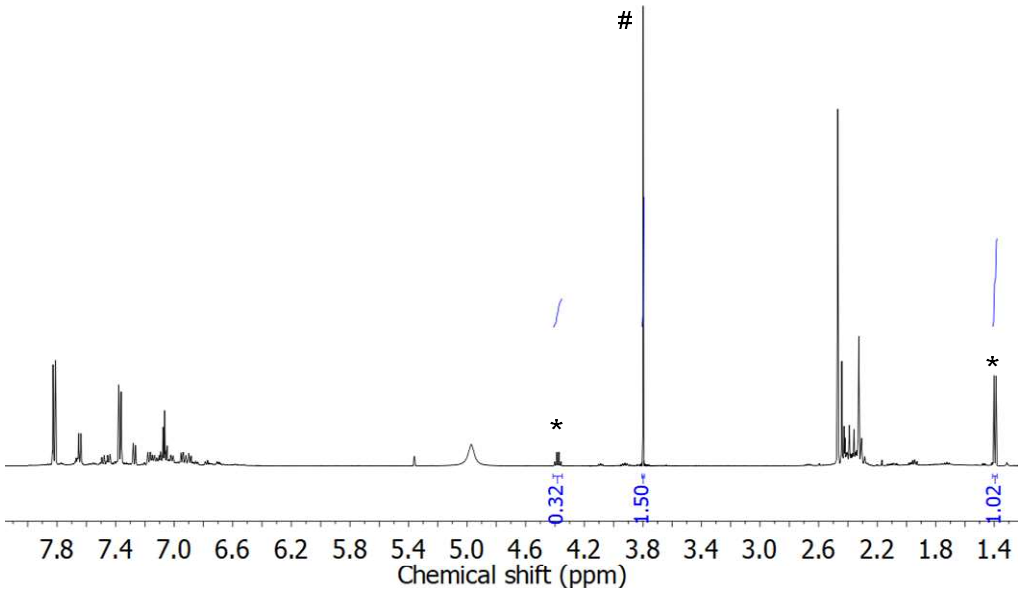

Figure 58. ^{1}H NMR spectrum measured during the hydroamination of 4-methyl styrene catalyzed by [**46**][NTf_2]$_2$/ $AgNTf_2$ in CD_2Cl_2. The hydroamination product peak is marked by an asterisk (*). The internal standard is marked by a pound sign (#).

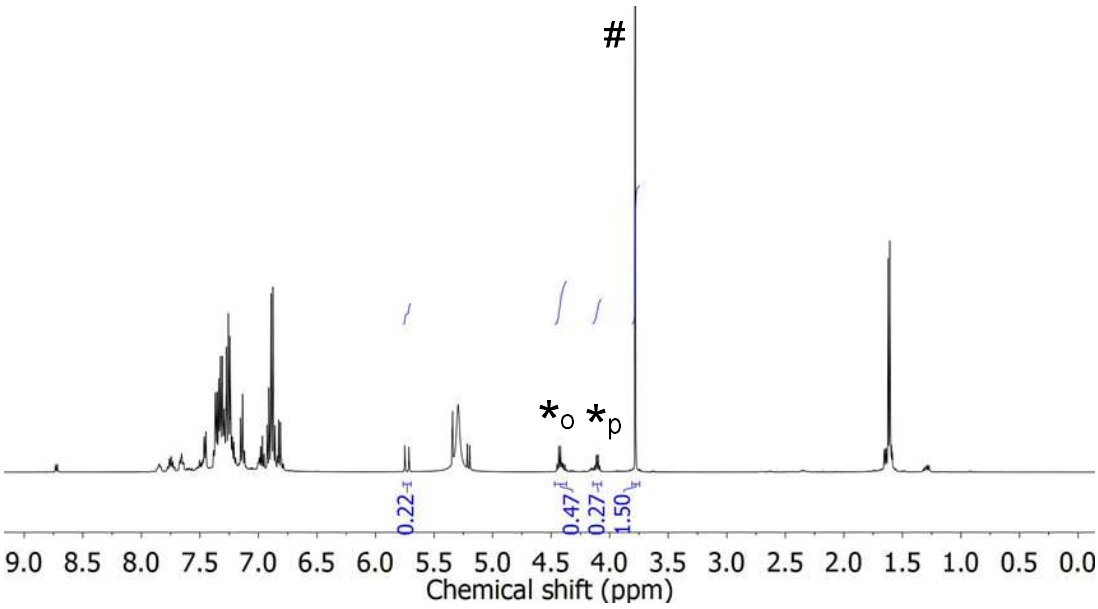

Figure 59. ^{1}H NMR spectrum measured during the hydroarylation of styrene with phenol catalyzed by [**49**][SbF_6]$_2$/ AgOTf in CD_2Cl_2. The hydroarylation product peak is marked by an asterisk (*$_o$ for *ortho-substituted and* *$_p$ for para-substituted). The internal standard is marked by a pound sign (#).

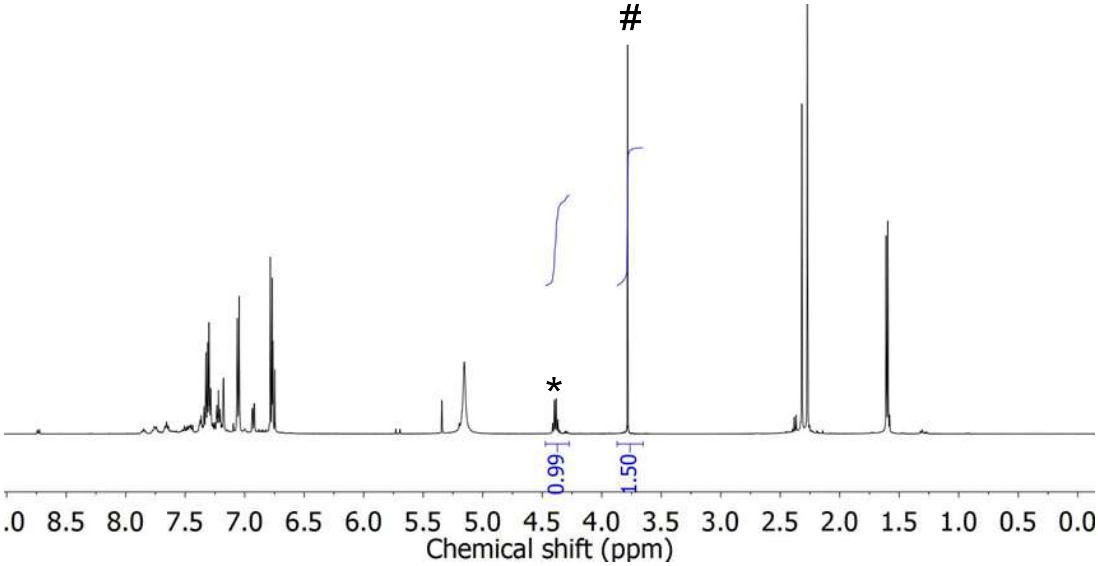

Figure 60. ^{1}H NMR spectrum measured during the hydroarylation of styrene with *p*-cresol catalyzed by [**49**][SbF_6]$_2$/ AgOTf in CD_2Cl_2. The hydroarylation product peak is marked by an asterisk (*). The internal standard is marked by a pound sign (#).

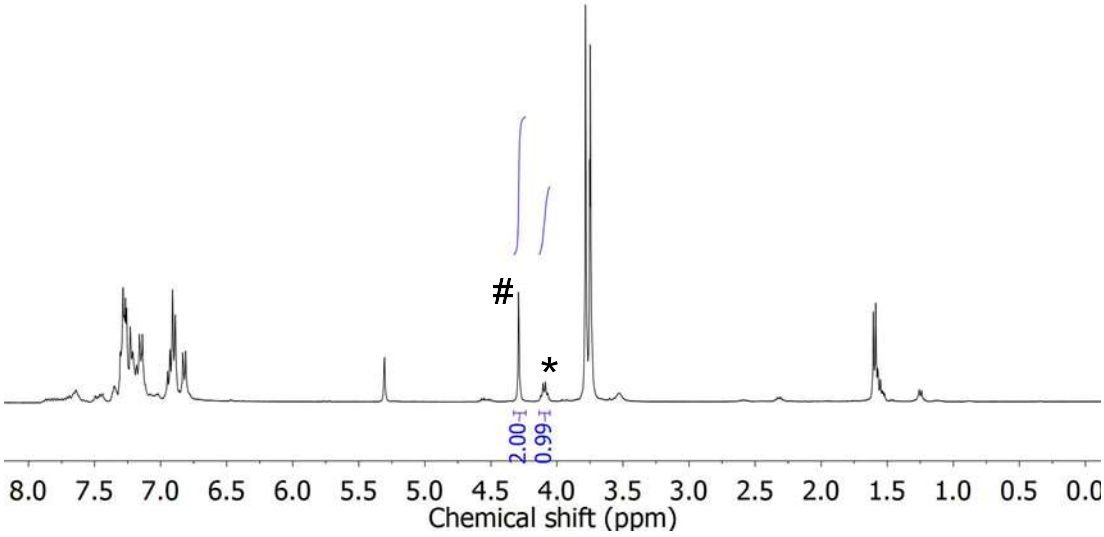

Figure 61. ^{1}H NMR spectrum measured during the of styrene with anisole catalyzed by [**49**][SbF_6]$_2$/ AgOTf in CD_2Cl_2. The hydroarylation product peak is marked by an asterisk (*). The internal standard is marked by a pound sign (#).

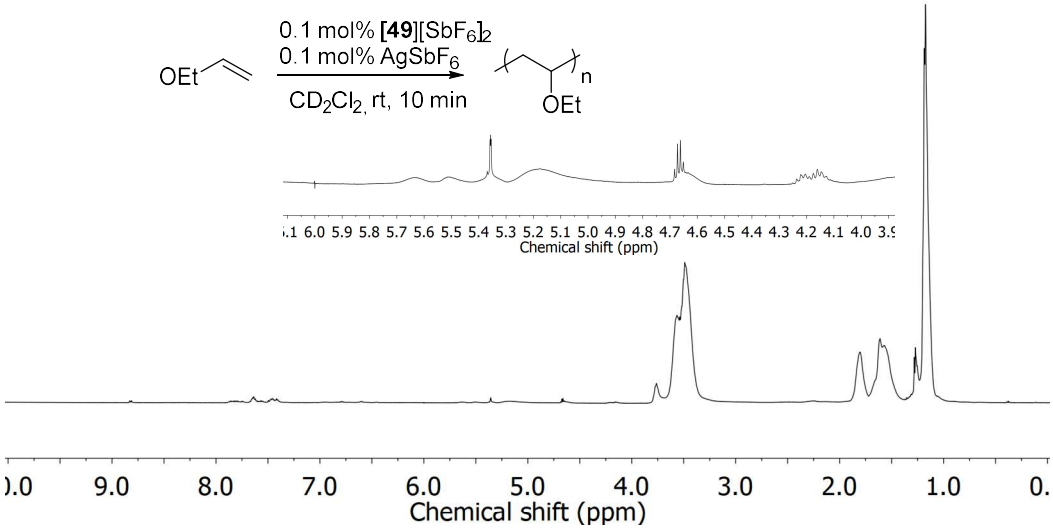

Figure 62. ^{1}H NMR spectrum measured during the polymerization of ethyl vinyl ether catalyzed by [**49**][SbF_6]$_2$/ $AgSbF_6$ in CD_2Cl_2.

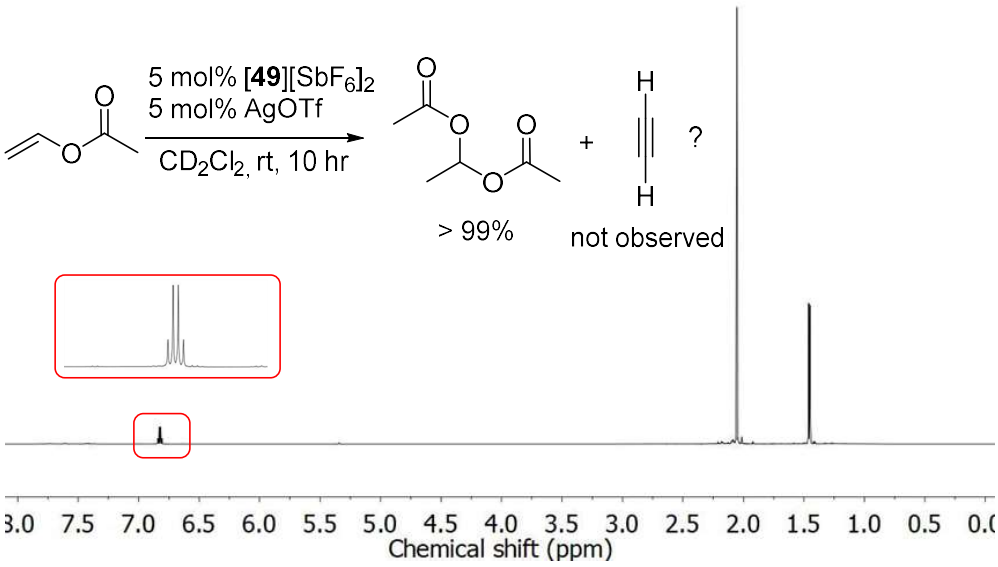

Figure 63. ^{1}H NMR spectrum measured during the polymerization of vinyl acetate catalyzed by [**49**][SbF_6]$_2$/ AgOTf in CD_2Cl_2.

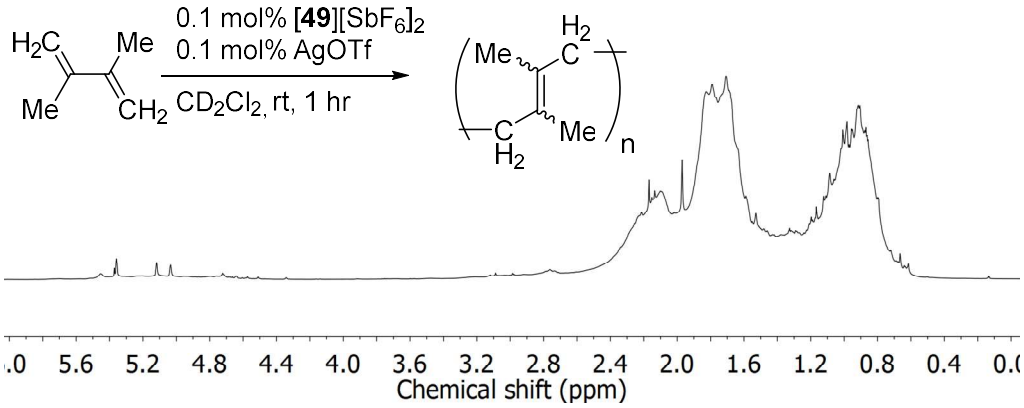

Figure 64. ^{1}H NMR spectrum measured during the polymerization of 2,3-dimethyl-1,3-butadiene catalyzed by [**49**][SbF_6]$_2$/ $AgSbF_6$ in CD_2Cl_2.

Gel Permeation Chromatography (GPC). GPC was conducted on a system equipped with a Waters Chromatography, Inc. model 1515 isocratic pump, a model 2414 differential refractometer, and a three-column set of Polymer Laboratories, Inc. Styragel columns (PLgel 5 μmMixed C, 500 Å, and 104 Å, 300 × 7.5 mm columns). The system

was equilibrated at 35°C in THF, which served as the polymer solvent with 1.00 mL/min flow rate. Polymer solutions were prepared at a known concentration (ca. 5 mg/mL) and an injection volume of 50 μL was used.

CHAPTER III

CONTROLLING THE PROPERTIES OF A 2,2'-BIPY-PLATINUM DICHLORIDE COMPLEX VIA OXIDATION OF A PERIPHERAL STIBINE MOIETY*

3.1 Introduction

Antimony (V) compounds are emerging as powerful Lewis acid catalysts for a number of organic transformations. Earlier studies showed that stibonium cations such as $[Ph_4Sb]^+$ catalyze the addition of isocyanates to epoxides.[160-161] More recently, stibonium cations[118, 162-163] have found use as catalysts for the allylstannation and the hydrosilylation of various aldehydes[164-165] among other reactions.[117, 166-168] Antimony-based Lewis acids can also activate transition metal catalysts by abstraction of an anionic ligand.[55, 60, 169] Such a possibility is illustrated by the properties of complex **52**[66] or **53**[53] which catalyze reactions involving alkynyl substrates (Figure 65). In both cases, it has been proposed that the Lewis acidic antimony center of these complexes engages the metal-bound chloride anion, leading to the generation of an exposed, electrophilic metal center available for substrate activation.

---

* Reprinted with permission from: "Controlling the properties of a 2,2'-bipy-platinum dichloride complex via oxidation of a peripheral stibine moiety"; Lo, Y.-H.; Gabbaï F. P. *Organometallic* **2018**, *37(15)*, 2500-2506. Copyright 2018 by American Chemical Society.

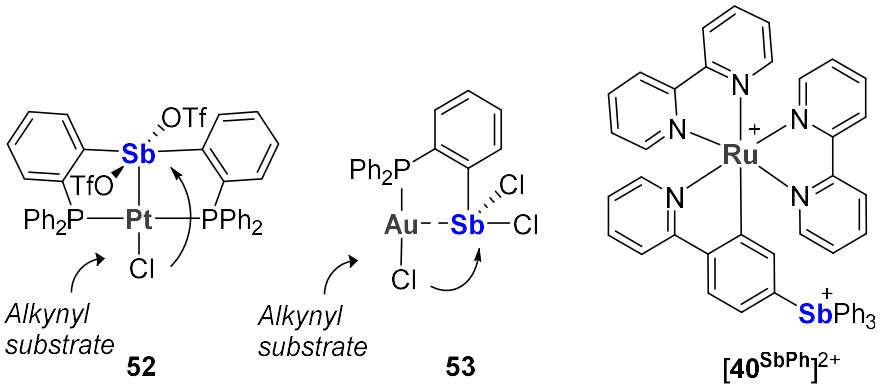

Figure 65. Complex **52** and **53**: Stibonium-promoted activation of a transition metal halide bond by an incoming substrate. Complex [**40**^{SbPh}]$^{2+}$: Sb(V)-substituted cyclometalated Ru(II) polypyridyl complex.

A situation that has received less attention is that involving transition metal complexes where the antimony moiety is positioned at the outer rim of a coordination complex as in the case of [**40**^{SbPh}]$^{2+}$.[90] A detailed study of this complex showed that the antimony moiety, despite its large separation from the metal center, alters the redox properties of the latter. Indeed, we observed a net anodic shift in the Ru(II/III) redox couple upon oxidation of the antimony center leading us to conclude that the high valent antimony moiety is electron-withdrawing. Building on these original results, antimony-substituted 2,2'-bipyridine ligands were selected as a model system in order to determine if the redox activity of the peripheral antimony center can be used to influence the reactivity of a transition metal coordinated to the 2,2'-bipyridine ligand (Figure 66). In this article, we describe the synthesis of an antimony-substituted ligand and its coordination to platinum. We also describe how oxidation of the antimony center affects the photophysical properties of the complex as well as its reactivity.

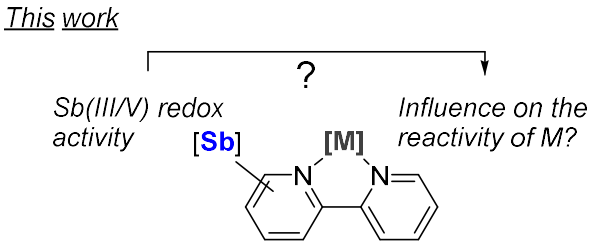

Figure 66. Outline of work mentioned within.

3.2 Synthesis and characterizaion of Pt complexes with Sb-substituted bipyridine ligands

The synthesis of the 4-(diphenylstibino)-2-2'-bipyridine ligand **54** was achieved by lithiation of 4-bromobipyridine followed by reaction with Ph_2SbCl (Figure 67a).[170] This ligand is an air-stable solid which could be easily crystallized. The ^1H NMR spectrum is consistent with that expected for a 4-substituted 2,2'-bipyridine derivative with each hydrogen on the ligand backbone being chemically distinct. This ligand crystallizes in the $P2_1/n$ space group with two nearly identical molecules in the asymmetric unit. The geometry of the antimony atom is close to that expected for a triarylstibine, with C—Sb—C bond angles close to 90° (Figure 67b).

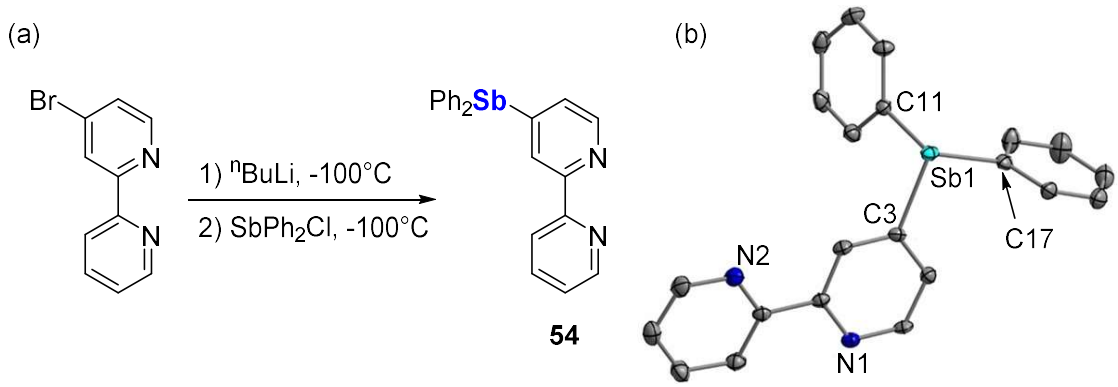

Figure 67. (a) Synthesis of **54**. (b) Solid-state structure of **54**. Thermal ellipsoids are drawn at the 50% probability level. The phenyl groups are drawn in wireframe, the hydrogen atoms, interstitial solvent molecules and counter anions are omitted for clarity.

This ligand reacts cleanly with $[(CH_3CN)_2PtCl_2]$ in acetonitrile to afford the corresponding platinum (II) complex **55** as an air-stable yellow solid (Figure 68).[171] Inspection of the ^{1}H NMR spectrum of **55** shows that complexation of the platinum ion induces a notable downfield shift of the proton attached to the 3-position of the bipyridine backbone from $\delta = 8.5$ ppm to $\delta = 8.7$ ppm. Given that both the antimony and platinum centers of **55** could be oxidized by two electrons[118, 167, 172], we became eager to interrogate the compound by addition of iodobenzene dichloride ($PhICl_2$). When attempted in acetonitrile, this reaction gave an intractable mixture of compounds which we assign to the poor solubility of **55** in this solvent. Gratifyingly, the reaction proceeded cleanly in DMSO to afford complex **56** as the oxidized product. The ^{1}H NMR spectrum of complex **56** shows a further downfield shift of the ^{1}H NMR resonances. The first hint that oxidation had occurred at the antimony atom was provided by the resonance of the antimony-bound Ph groups which appear in 7.2—7.4 ppm range for **55** and the 7.5—7.8 ppm range for **56**. Oxidation of the antimony center was

confirmed by the structural characterization of **56** (*vide infra*). It is interesting to note that addition of up to four equivalents of $PhICl_2$ did not alter the fate of this reaction, indicating that the platinum center resists oxidation to the tetravalent state.

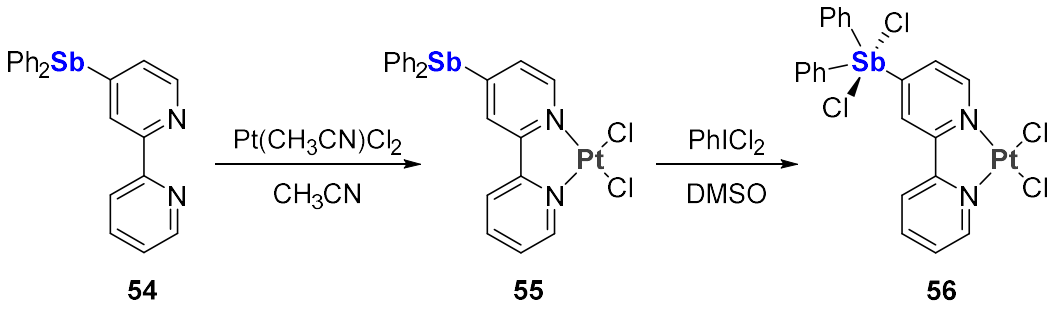

54 **55** **56**

Figure 68. Synthesis of complex **55** and **56**.

The structure of complexes **55** and **56** have been determined using X-ray diffraction analysis (Figure 69). The asymmetric unit of both complexes contains two independent molecules which display very similar geometries. In the case of **55**, the two independent molecules are engaged in the formation of an extended stack. Within this stack, the bipyridyl-platinum dichloride units of the successive molecules are essentially parallel to each other and are separated by an average distance of 3.40 Å (See SI). In the case of **56**, the two independent molecules form a stacked dimer with a separation of 3.32 Å between the bipyridyl-platinum dichloride units of the two molecules (See SI). In both complexes, the platinum(II) atoms are tetracoordinate in a square planar geometry, as expected for a heavy metal center with a d^8 electronic configuration. The N-Pt-N bond angles for complexes **55** and **56** are compressed to av. 80.5(4)° and av. 80.3(4)° respectively, relative to the ideal value of 90°, which is characteristic of Pt(II) bipyridine and diamine complexes.[173] Complex **56** contains a pentacoordinated antimony

center that adopts a distorted trigonal bipyramidal geometry with the two chloride ligands occupying the axial positions (av. Cl-Sb-Cl =176.12(13)°). This geometry follows the apicophilicity of the electronegative halogen ligands as typically observed for dihalotriarylstiboranes.[174] Interestingly, the Pt—Cl bonds involving the chlorine trans to the antimony-substituted pyridine ring are marginally shorter in complex **56** than that in complex **55** (av. 2.293(3) Å vs. av. 2.318(3) Å), suggesting a reduction of the trans influence of the N1 atom upon oxidation.[175] This result suggests that the oxidation state of the antimony center can be used to adjust the donor strength of the bipyridine ligand.

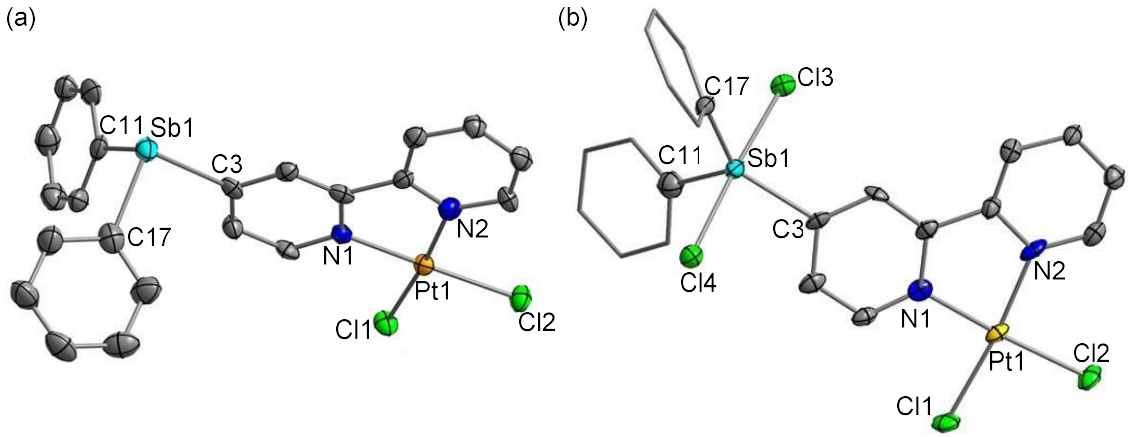

Figure 69. Solid-state structure of (a) **55** and (b) **56**. Thermal ellipsoids are drawn at the 50% probability level. The phenyl groups are drawn in wireframe, the hydrogen atoms, interstitial solvent molecules and counter anions are omitted for clarity.

3.3 Photophysical properties and computational study of complex 55 and 56

The photophysical properties of platinum(II) complexes featuring bipyridyl ligands can be used to map the electronic structure of the complexes.[176] Such complexes are characterized by two main absorption features. The low energy feature is a metal-to-ligand charge transfer (MLCT) band which is followed at higher energy by a ligand

centered π-π* transition (Figure 70).[177] While the π-π* transitions are often obscured by other high energy bands, the MLCT appear at lower energy, in an area that does not suffer from such interferences. For this reason, we decided to focus on the MLCT band. The λ_{max} of the MLCT band of **55** (λ_{max} = 387 nm) shows a small but noticeable red shift when compared to the parent complex (bipy)$PtCl_2$ (λ_{max} = 383 nm). This small shift indicates that incorporation of the diphenylantimony moiety alters the electronic properties of the bipy ligand only to a very small extent. A more noticeable shift of 10 nm is observed upon oxidation of the antimony center as in (λ_{max} (**56**) = 397 nm). This effect is consistent with a lowering of the bipyridine π* orbitals upon oxidation of the antimony center.

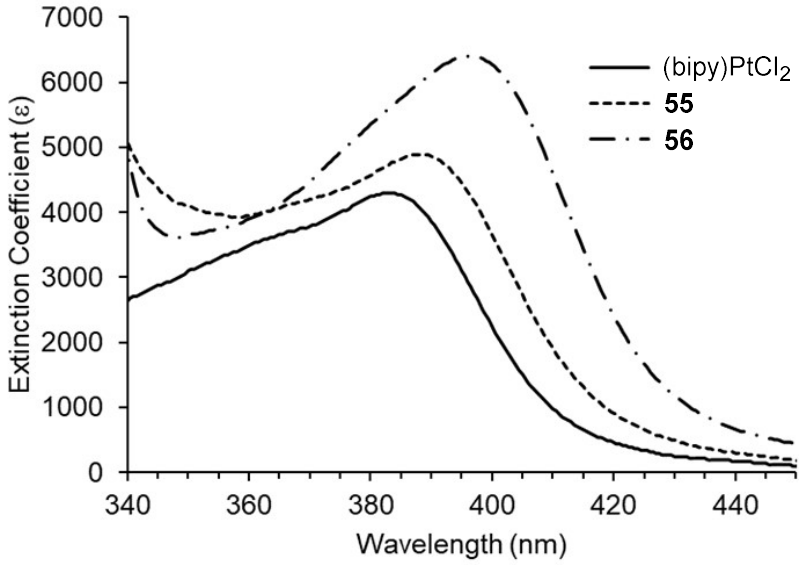

Figure 70. Experimental UV-vis. spectra of **55**, **56** and (bipy)$PtCl_2$ in MeCN at room temperature.

The gas-phase optimized structures of **55** and **56** using DFT methods are in reasonable agreement with the structures determined experimentally (see Supporting Information). The contours and energies of the Kohn-Sham LUMO and HOMO are presented in Table 15. In both complexes, the HOMO can be described as an antibonding Pt(d_{yz})-Cl(p_z) π*-orbital, the energy of which is lowered by 0.14 eV upon oxidation. The LUMO of both complexes is based on the antimony-substituted bipy ligand. This orbital, which has π* character, shows a lowering of 0.21 eV upon conversion of **55** into **56**. The net effect of these changes is a decrease of the HOMO-LUMO gap from 2.87 eV (432 nm) in **55** to 2.79 eV (444 nm) in **56**, which is in good agreement with the red shift observed by UV-vis. spectroscopy

Table 15. Frontier Molecular Orbitals (Isovalue 0.05) and Energies (eV) of **55** and **56**.

	55	**56**
LUMO	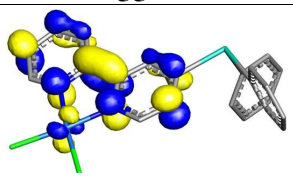 -2.77452 eV	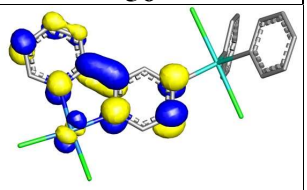 -2.98647 eV
HOMO	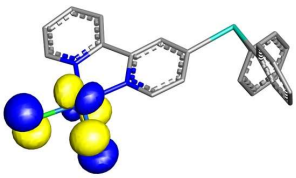 -5.64705 eV	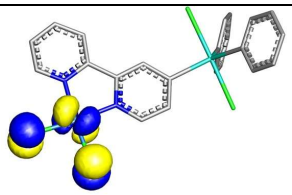 -5.78313 eV

The electronic absorption bands of **55** and **56** were examined with time-dependent (TD) calculations using the solute electron density-based implicit solvation model (SMD) with MeCN as a solvent. These calculations indicate that the MLCT band in both complexes is dominated by a distinctly intense single electronic excitation at 378

nm for **55** ($f = 0.14$) and 382 nm of **56** ($f = 0.15$) (Figure 71). Weaker excitations are observed at 383 nm and 434 nm for **56** and 379 nm and 415 nm for **55**. Analysis of the TD-DFT output using the natural transition orbital (NTO) methods shows that these low energy excitations have the expected MLCT character as indicated by inspection of the dominant NTOs given in Table 16 for the first three excited singlet states. It is also important to note that the electronic excitations identified for **56** are at lower energy than those of **55**, again in agreement with the red shift observed experimentally

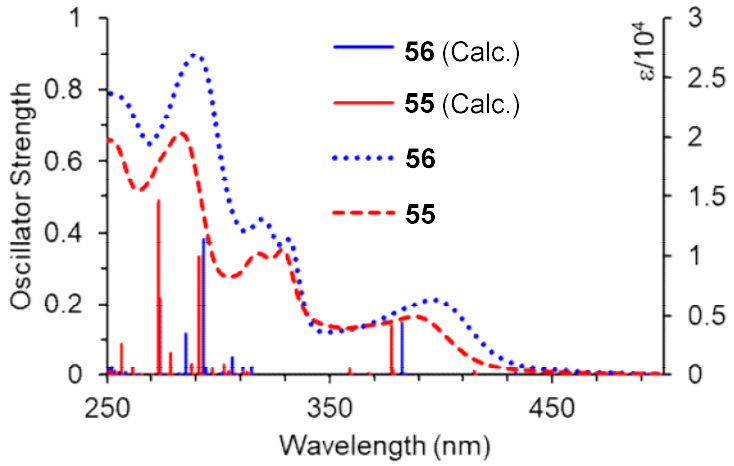

Figure 71. Experimental UV-vis spectrum and calculated vertical electronic transitions (represented by bars) of **55** and **56** in MeCN. The wavelengths of the calculated transitions are plotted against the oscillator strength.

On the basis of the NTOs shown in Table 16, it appears that transitions with low oscillator strengths are those for which the platinum-centered donor orbital has poor overlap with the ligand π* acceptor orbital. The most intense transitions in both complexes are those involving the third donor orbital. The oscillator strengths of these transitions are at least 10 times larger than those of the first and second transition, a

result that can be explained on the basis of the apparent better overlap existing between the donor and acceptor NTOs.[178]

Table 16. Dominant NTOs, calculated wavelengths (λ) and oscillator strength (*f*) for the first three excited singlet states of **55** and **56**.[a]

	55	**56**
Acceptor NTO[a]	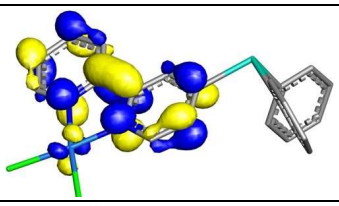	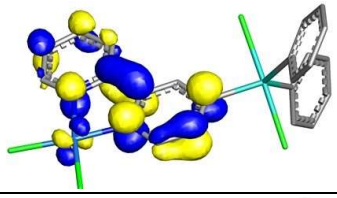
Donor NTO for the 1st transition	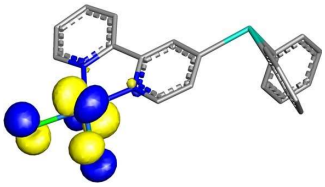 λ = 415 nm, *f* = 0.011	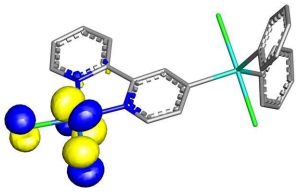 λ = 434 nm, *f* = 0.007
Donor NTO for the 2nd transition	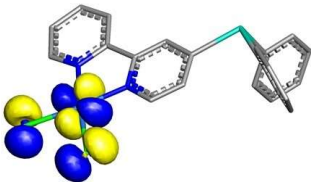 λ = 379 nm, *f* = 0.013	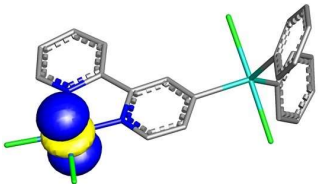 λ = 383 nm, *f* = 0.004
Donor NTO for the 3rd transition	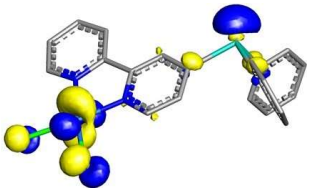 λ = 378 nm, *f* = 0.139	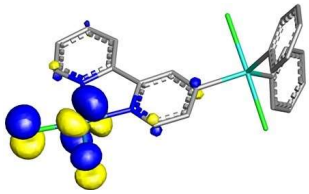 λ = 382 nm, *f* = 0.147

[a]The acceptor orbitals are the same for all three transitions.

3.4 Electrochemical property of complex 55 and 56

The electrochemistry of **55**, **56** and (bipy)$PtCl_2$ was also investigated using cyclic voltammetry (CV) (Figure 73). Compound **55** and (bipy)$PtCl_2$ both display a quasi-reversible reduction wave at $E_{1/2}$ = -1.57V and -1.590V, respectively, corresponding to

the reduction of the bipyridine ligand.[176] The similarity of these potentials indicates that the diphenylantimony moiety is innocent and only induces a very minor perturbation of the electronic properties of the ligand. The voltammogram of complex **56** features two irreversible reduction events and thus differs markedly from that of **55** and (bipy)$PtCl_2$. While it is difficult to assign the nature of these reductions, we will note that the first event occurs at E_p -1.2V. This potential is distinctly more anodic than the first reduction of **55** and (bipy)$PtCl_2$ indicating the **56** is a more electron deficient compound.

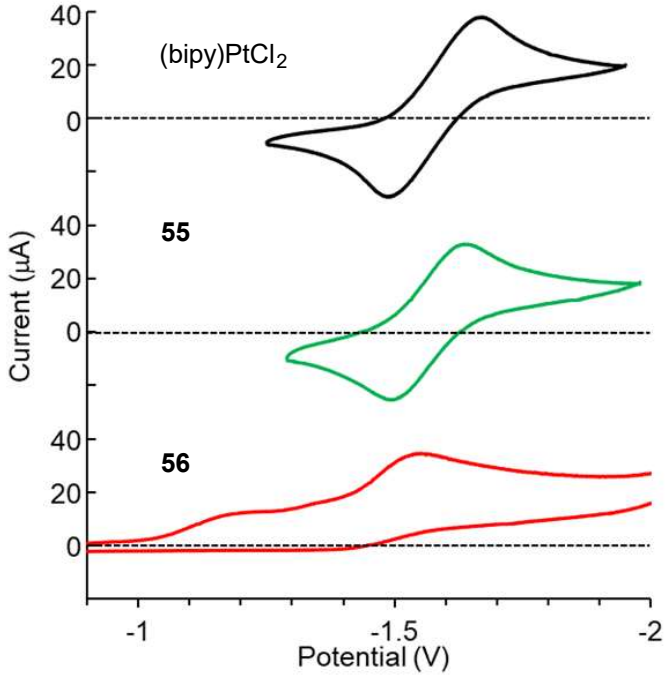

Figure 72. Cyclic voltammograms of **55**, **56** and (bipy)$PtCl_2$ in DMF with 0.1 M [^{n}Bu$_4$N][PF_6] as electrolyte. Scan rate 0.1 V/s, potentials referenced to Fc/Fc^+ in the same solvent.

3.5 Catalytic hydroarylation of ethylpropiolate with mesitylene

Having measured the effect of oxidation on the optoelectronic properties of these complexes, we next became interested in probing whether the reactivity of the platinum center could also be affected by oxidation of the peripheral antimony atom. We have observed such cooperative effects in the case of the antimony gold complex [**19**]$^+$ which becomes catalytically active upon conversion into [**20**]$^+$ by oxidation of the antimony atom (Figure 73).[61]

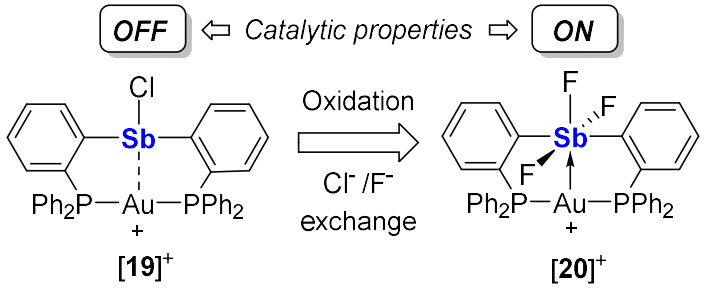

Figure 73. Cooperative effects in the case of antimony gold complex.

In the present case however, we questioned whether the greater separation would cancel any cooperative effects between antimony and platinum. To address this question, we selected a simple reaction that would allow us to interrogate the electrophilic character of the platinum center, especially after oxidation. We selected the hydroarylation of ethyl propiolate by mesitylene, a reaction known to be accelerated by platinum catalysts.[179-181] This reaction was carried out in trifluoroacetic acid and the results are compiled in Table 17. As shown by entries 1 and 2, catalyst **56** is markedly more active than **55**, leading to a ~two-fold increase of the yield in the monohydroarylation product **57** after four hours. The reaction also proceeded at room

temperature over the course of 24 hours (entries 3and 4). Under these conditions, a greater differential was observed between the two catalysts, with again catalyst **56** affording a markedly higher yield of **57**. Carrying out the reaction at room temperature also improved selectivity for the monohydroarylation product. These results suggest that oxidation of the antimony atom positively impacts the catalytic properties of the metal center. The lack of reaction observed when Ph_3SbCl_2 is used alone underscores the catalytic function of the platinum atom in these reactions (entry 5). We also tested the catalytic activity of (bipy)$PtCl_2$ and found it to be as active as **55**, suggesting that the diphenylantimony moiety present in **55** has no influence on the catalytic activity of these complexes (entry 6). Finally, we also tested the (bipy)$PtCl_2$/Ph_3SbCl_2 system and found it to be as active as **55** and (bipy)$PtCl_2$ (entry 7). This last experiment points to the importance of the intramolecular connection between the diphenyldichloroantimony moiety and the bipy ligand in **56**.

Table 17. Pt(II)-catalyzed hydroarylation of ethylpropiolate with mesitylene[a]

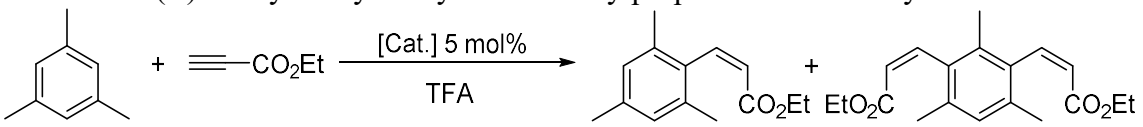

52 **53**

Entry	[Cat.] (5 mol%)	Temp.	Yield (%)[b]	
			57	**58**
1	**55**	60 °C	32	33
2	**56**	60 °C	62	21
3	**55**	25 °C	13	Trace
4	**56**	25 °C	50	6
5	$SbPh_3Cl_2$	60 °C	< 1	<1
6	$(bipy)PtCl_2$	60 °C	30	25
7	$(bipy)PtCl_2 + Ph_3SbCl_2$	60 °C	31	22

[a] Reaction conditions: Mesitylene (0.28 mmol), ethyl propiate (0.28 mmol), TFA (1 mL) at 60°C for 4 h.
[b] ^1H NMR yields relative to 1,2-dichloroethane added at the end of the reaction.

3.6 Synthesis of bipyridine platinum(IV) complexes with peripheral antimony(V) substituents

Complex **55** features two metal centers, which can both undergo two electron oxidation. We have shown that selective oxidation at the antimony center in complex **55** can be achieved in DMSO with $PhICl_2$. To obtain a platinum (IV) complexes, complex **56** was treated with additional equivalents of $PhICl_2$, but no reaction was observed. However, treating complex **55** with $PhICl_2$ (4 equiv) in acetonitrile leads to complex **59** as a yellow and air-stable powder in 68% yield (Figure 74). Complex **59** displays poor solubility in organic solvents, including DMSO, which complicates its characterization by NMR spectroscopy.

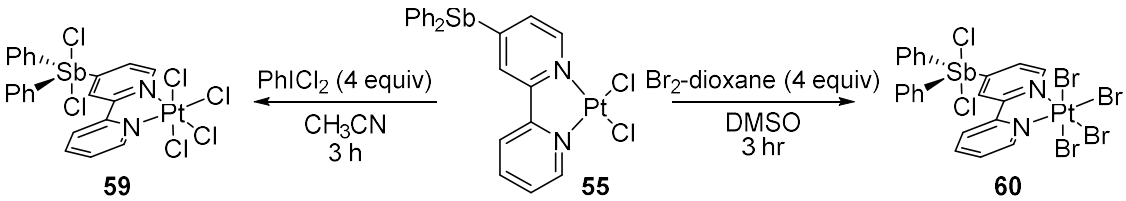

Figure 74. Synthesis of complex **59** and **60**.

Complex **55** was treated with 4 equivalents of bromine-1, 4-dioxane in DMSO to afford complex **60** as a red and air-stable powder (Figure 74). The structure of complexes **59** and **60** were determined by X-ray diffraction (Figure 75). The antimony center adopts a trigonal bipyramidal geometry in both complexes with $\Sigma_{(C-Sb-C)}$ = 359.8(5)° in **59** and 360.0(6)° in **60**. Interestingly, in complex **60**, the chloride ligands originally bound to platinum center migrate to the antimony (V) center. In both complexes, the platinum center adopts a distorted octahedral geometry with a N1-Pt-N2 angle of 79.0(1) ° in **59** and 80.8(6) ° in **60**.

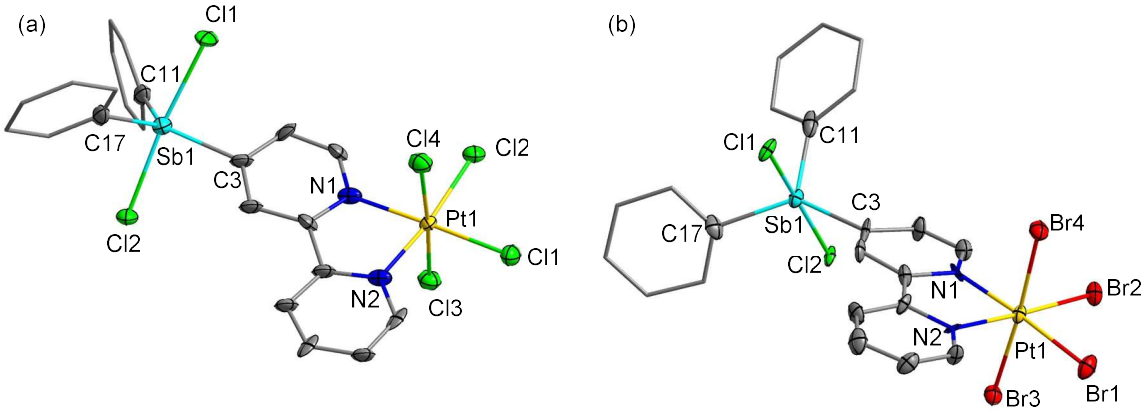

Figure 75. Solid-state structure of **59** and **60**. Thermal ellipsoids are drawn at the 50% probability level. The hydrogen atoms are omitted for clarity.

3.7 Synthesis of bipyridine palladium(II) complexes with peripheral antimony(V) substituents

We have demonstrated that the 4-(diphenylstibino)-2-2'-bipyridine ligand (**54**) can coordinate to platinum(II) centers. We are eager to examine the reactivity of the ligand toward another d^8 metal, such as palladium(II). Similar to the synthetic procedure of used to access **55**, treating ligand **54** with 1 equivalent of $Pd(CH_3CN)Cl_2$ in acetonitrile at 50°C leads to an orange and air-stable precipitate, referred as complex **61** (Figure 76). The subsequent oxidation on **61** was not successful, so we attempted to oxidize the antimony center in ligand **54** first, and then carry out complexation. Ligand **54** was cleanly oxidized by o-chloranil in dichloromethane to afford the pre-oxidized ligand **62**.

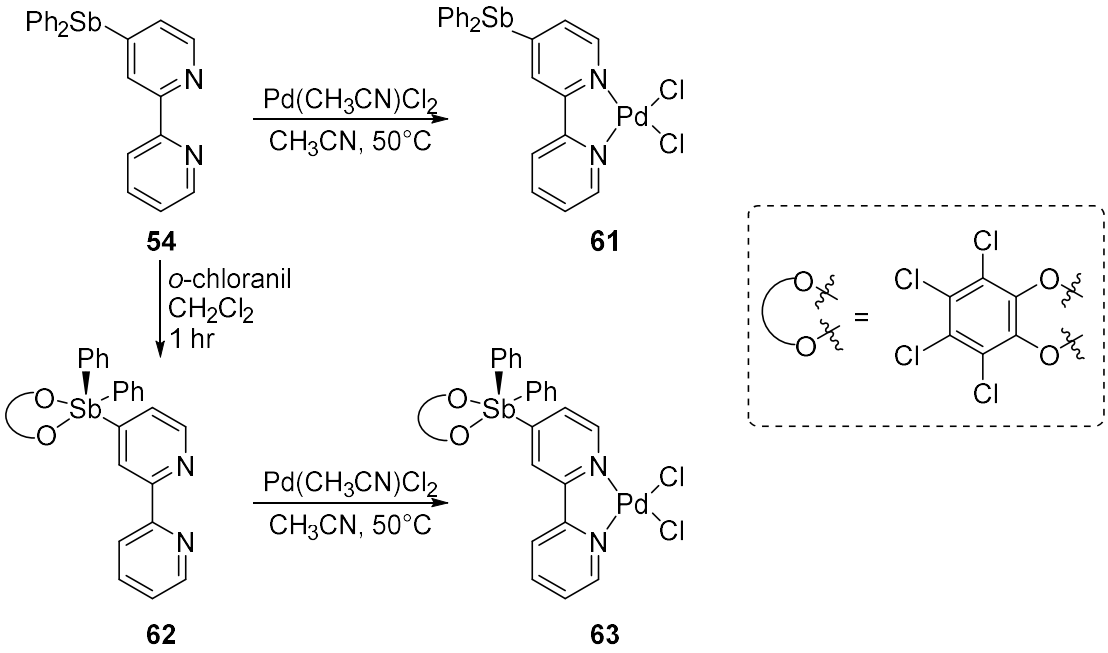

Figure 76. Synthesis of ligand **62**, complex **61** and **63**.

The ^{1}H NMR resonances of **62** show prominent down-fielded shifts compared to those of **54** (Figure 77). The diagnostic signal corresponding to the 3 position of the bipyridine ligands shifts from 8.56 ppm to 8.82 ppm and that to the phenyl group on the antimony center shifts from 7.30 ppm to 7.62 ppm and 7.45 ppm to 7.82 ppm upon oxidation. The pre-oxidized ligand **62** was reacted with $Pd(CH_3CN)_2Cl_2$ to afford complex **63**. Similar to the case of the platinum complexes **55** and **56**, the ^{1}H NMR signals corresponding to the phenyl group on the antimony center display a down-fielded shift from 7.30-7.45 ppm to 7.55-7.70 ppm, consistent with the oxidation at the antimony center (Figure 78). Another evidence of the antimony oxidation is the structure of **63** (Figure 79). The antimony adopts a distorted square pyramidal geometry ($\Sigma_{(E–Sb–E)}$ = 352.9(6), E = C or O), which is reminiscent of the observation for other catecholato-triaryl-stiboranes. The distorted planar geometry of palladium center is evidenced by $\Sigma_{(E–Pt–E)}$ = 360.0(4) (E = N or Cl).

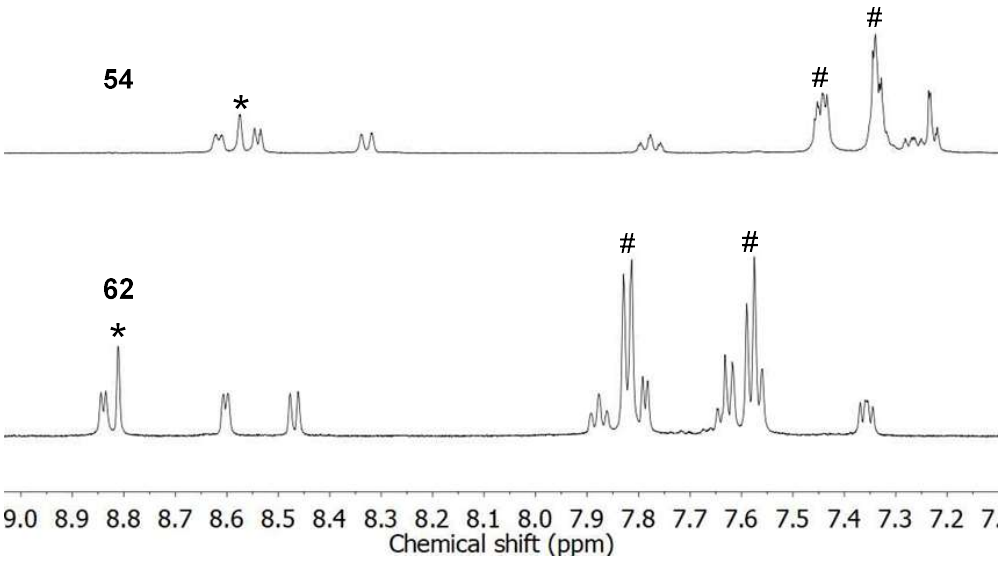

Figure 77. ^{1}H NMR spectra of ligand **54** and **62** in CD_2Cl_2. The proton corresponding to the 3 position at the pyridine ring of the ligand is indicated by an asterisk (*) for each spectrum. The protons corresponding to the phenyl group on the antimony are indicated by a pound sing (#).

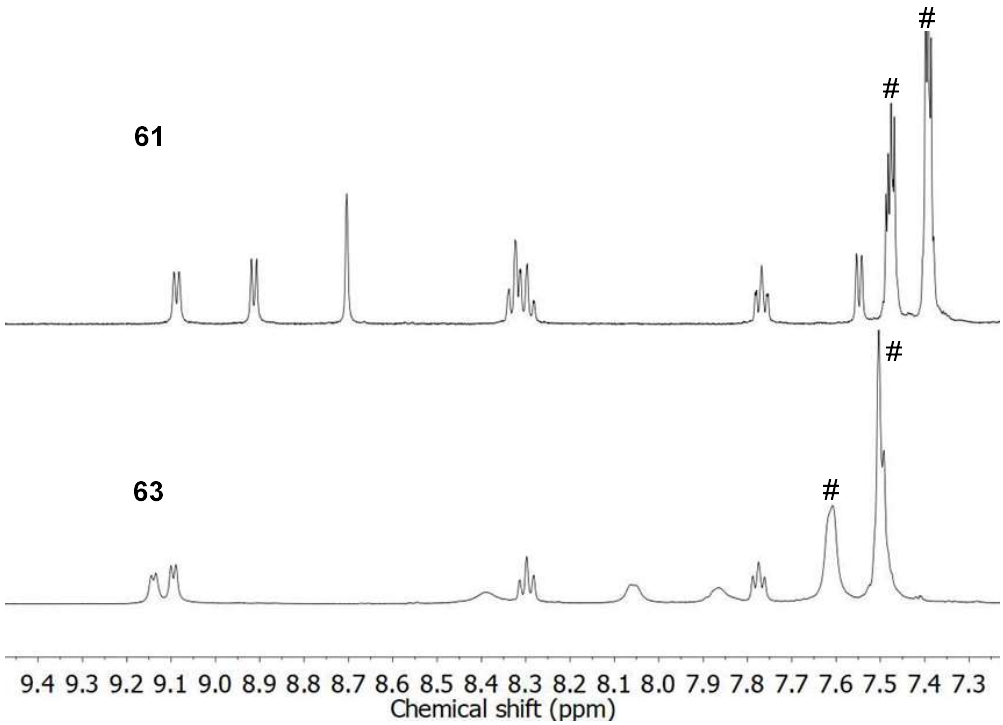

Figure 78. ^{1}H NMR spectra of complexes **61** and **63** in d_6-DMSO. The protons corresponding to the phenyl group on the antimony are indicated by a pound sing (#).

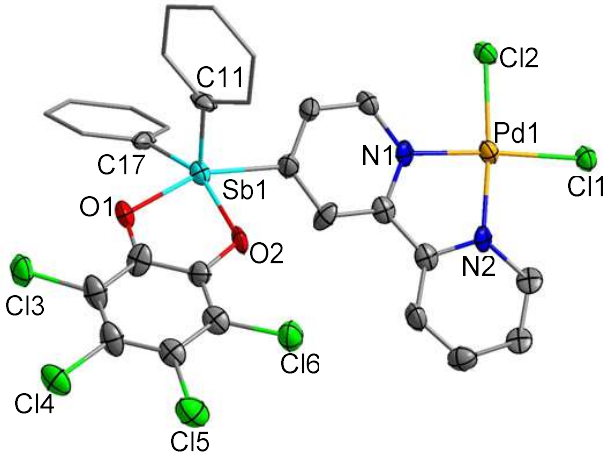

Figure 79. Solid-state structure of **63**. Thermal ellipsoids are drawn at the 50% probability level. The hydrogen atoms are omitted for clarity.

3.7 Conclusion

The results presented in this article demonstrate that the redox activity of a stibine ligand installed at the periphery of a bipyridine ligand can be used to influence the electronic properties of the latter. This conclusion is supported by an investigation of the corresponding platinum dichloride complexes and the observation that oxidation of the stibine induces a red shift of the MLCT UV-vis absorption band and an anodic shift of the reduction potential. These experimental observations are corroborated by DFT calculations which show that this antimony-centered oxidation lowers the energy of the LUMO. Last, we have also measured the impact of these changes on the reactivity of the platinum center using the hydroarylation of ethyl propiolate by mesitylene as a benchmark reaction. These results indicate that the oxidized complex **56** is more electrophilic, leading to greater product yields.

3.8 Experimental Section

General Consideration. All preparations were carried out under an N_2 atmosphere using standard Schlenk techniques unless otherwise stated. 4-Bromobipyridine, Ph_2SbCl,[182] [183] $PhICl_2$,[184] (bipy)$PtCl_2$[185] were prepared according to previously reported procedures. Et_2O and THF were dried by refluxing under N_2 over Na/K. CH_3CN was dried over CaH_2. All other solvents were ACS reagent grade and used as received. All chemicals were purchased from Sigma-Aldrich, Merck, or Spectrochem and used as received. Thin-layer chromatography (TLC) was performed on a Merck 60 F254 silica gel plate (0.25 mm thickness). Column chromatography was performed on a Merck 60 silica gel (100−200 mesh). Ambient temperature NMR spectra

were recorded on a Varian Unity Inova 500 FT NMR (499.42 MHz for ^{1}H, 125.58 MHz for ^{13}C) spectrometer. Chemical shifts (δ) are given in ppm and are referenced against the solvent signals (^{1}H, ^{13}C). Elemental analyses were performed at Atlantic Microlab (Norcross, GA). Absorbance measurements were taken on a Shimadzu UV-2502PC UV-Vis spectrophotometer against a solvent reference.

Computational details. Density functional theory (DFT) structural optimizations were conducted using the Gaussian 09 program.[186] In all cases, the structures were optimized using the B3LYP[151-152] functional which has been widely applied for the study of bipy-platinum complexes.[178, 187-188] In order to optimize the efficiency of our computations while still treating the heavy atoms at a sufficient level of theory, we used the following mixed basis set: Sb/Pt, cc-pVTZ-PP[153]; C/H/N, 6-31g; Cl, 6-31g(d') with effective core potentials for the heavy elements.[154-155] Optimizations with the MPW1PW91 functional and the same basis sets were considered but abandoned because they afforded geometries exhibiting large deviations from the experimental ones. For all optimized structures, frequency calculations were carried out to confirm the absence of imaginary frequencies. TD-DFT calculations were carried out using the B3LYP functional and the SMD solvation model. The molecular orbitals were visualized and plotted using the Jimp2 program.[157-159]

Table 18. Selected X-ray and DFT (gas-phase) metrical parameters (distance in Å and angles in °) for **55** and **56**.

	X-ray		DFT	
Complex	**55**	**56**	**55**	**56**
Pt1—N1	2.008(7)	2.003(7)	2.037	2.032
Pt1—N2	2.041(7)	2.024(8)	2.038	2.041
Pt1—Cl1	2.297(2)	2.298(3)	2.314	2.313
Pt1—Cl2	2.319(2)	2.291(2)	2.315	2.311
Sb1—C3	2.203(9)	2.127(9)	2.187	2.169
Sb1—Cl3		2.474(3)		2.514
Sb1—Cl4		2.457(3)		2.487
N1—Pt1—N2	80.4(3)	80.4(3)	80.0	80.0
Cl3—Sb1—Cl4		176.56(9)		178.96

Crystallography. All crystallographic measurements were performed at 110(2) K using a Bruker SMART APEX II diffractometer with a CCD area detector (graphite monochromated Mo Kα radiation, λ = 0.71073 Å, ω-scans with a 0.5° step in ω). In each case, a specimen of suitable size and quality was selected and mounted onto a nylon loop. The semiempirical method SADABS[148] was applied for absorption correction. The structures were solved by direct methods and refined by the full-matrix least-squares technique against F^2 with anisotropic temperature parameters for all non-hydrogen atoms. All H atoms were geometrically placed and refined using the riding model approximation. Data reduction and further calculations were performed using the Bruker Apex2 (2013) and SHELXTL[149] program packages. Structural refinements were performed using Olex2.[150]

Table 19. Crystallographic table for **54**.

Identification code	y
Empirical formula	C22 H17 N2 Sb
Formula weight	431.12
Temperature	110.0 K
Wavelength	0.71073 Å
Crystal system	Monoclinic
Space group	P 1 21/n 1
Unit cell dimensions	a = 11.0321(6) Å α= 90°.
	b = 16.2239(9) Å β= 100.603(2)°.
	c = 20.9042(12) Å γ = 90°.
Volume	3677.6(4) $Å^3$
Z	8
Density (calculated)	1.557 Mg/m^3
Absorption coefficient	1.506 mm^{-1}
F(000)	1712
Crystal size	0.5 x 0.3 x 0.2 mm^3
Theta range for data collection	2.324 to 30.603°.
Index ranges	-15<=h<=15, -23<=k<=23, -29<=l<=29
Reflections collected	106532
Independent reflections	11287 [R(int) = 0.0469]
Completeness to theta = 25.242°	99.8 %
Absorption correction	Semi-empirical from equivalents
Max. and min. transmission	0.7461 and 0.5005
Refinement method	Full-matrix least-squares on F^2
Data / restraints / parameters	11287 / 0 / 451
Goodness-of-fit on F^2	1.152
Final R indices [I>2sigma(I)]	R1 = 0.0282, wR2 = 0.0594
R indices (all data)	R1 = 0.0361, wR2 = 0.0629
Extinction coefficient	n/a
Largest diff. peak and hole	0.600 and -1.171 $e.Å^{-3}$

Table 20. Crystallographic table for **55**.

Identification code	z
Empirical formula	C23 H19 Cl4 N2 Pt Sb
Formula weight	782.04
Temperature	110 K
Wavelength	0.71073 Å
Crystal system	Triclinic
Space group	P-1
Unit cell dimensions	a = 11.839(7) Å α= 79.530(8)°.
	b = 13.177(8) Å β= 70.672(7)°.
	c = 16.649(10) Å γ = 83.918(8)°.
Volume	2407(3) $Å^3$
Z	4
Density (calculated)	2.158 Mg/m^3
Absorption coefficient	7.386 mm^{-1}
F(000)	1472
Crystal size	0.6 x 0.4 x 0.07 mm^3
Theta range for data collection	1.573 to 27.447°.
Index ranges	-15<=h<=15, -16<=k<=17, -21<=l<=21
Reflections collected	86931
Independent reflections	10901 [R(int) = 0.1127]
Completeness to theta = 25.242°	99.9 %
Absorption correction	Semi-empirical from equivalents
Max. and min. transmission	0.7456 and 0.5547
Refinement method	Full-matrix least-squares on F^2
Data / restraints / parameters	10901 / 0 / 559
Goodness-of-fit on F^2	1.027
Final R indices [I>2sigma(I)]	R1 = 0.0459, wR2 = 0.1013
R indices (all data)	R1 = 0.0823, wR2 = 0.1179
Extinction coefficient	n/a
Largest diff. peak and hole	1.650 and -1.854 $e.Å^{-3}$

Table 21. Crystallographic table for **56**.

Identification code	y
Empirical formula	C22 H17 Cl4 N2 Pt Sb
Formula weight	768.01
Temperature	110 K
Wavelength	0.71073 Å
Crystal system	Monoclinic
Space group	P 1 21/c 1
Unit cell dimensions	a = 18.507(8) Å α= 90°.
	b = 14.400(6) Å β= 104.249(6)°.
	c = 17.294(8) Å γ = 90°.
Volume	4467(3) $Å^3$
Z	8
Density (calculated)	2.284 Mg/m^3
Absorption coefficient	7.958 mm^{-1}
F(000)	2880
Crystal size	0.15 x 0.1 x 0.07 mm^3
Theta range for data collection	1.135 to 26.444°.
Index ranges	-23<=h<=23, -17<=k<=17, -21<=l<=21
Reflections collected	88057
Independent reflections	9119 [R(int) = 0.1308]
Completeness to theta = 25.242°	100.0 %
Absorption correction	Semi-empirical from equivalents
Max. and min. transmission	0.7454 and 0.5057
Refinement method	Full-matrix least-squares on F^2
Data / restraints / parameters	9119 / 0 / 541
Goodness-of-fit on F^2	1.029
Final R indices [I>2sigma(I)]	R1 = 0.0438, wR2 = 0.0855
R indices (all data)	R1 = 0.0873, wR2 = 0.1054
Extinction coefficient	n/a
Largest diff. peak and hole	1.885 and -1.743 $e.Å^{-3}$

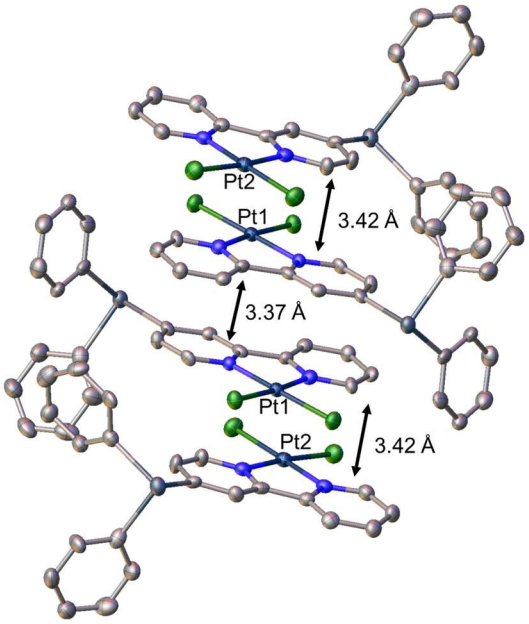

Figure 80. Portion of a stack observed in the solid-state structure of **55**. Thermal ellipsoids are drawn at the 50% probability level. The hydrogen atoms are omitted for clarity.

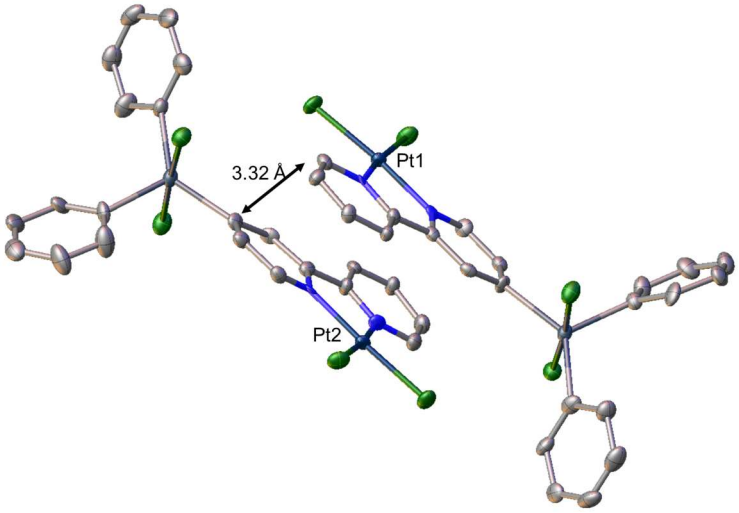

Figure 81. Stacking observed between the two independent molecules of **56** in the solid-state. Thermal ellipsoids are drawn at the 50% probability level. The hydrogen atoms are omitted for clarity.

Electrochemistry. Electrochemical experiments were performed with an electrochemical analyzer from CH Instruments (model 610A) with a glassy-carbon working electrode and a platinum auxiliary electrode. The reference electrode was built from a silver wire inserted into a small glass tube fitted with a porous Vycor frit at the tip and filled with a THF solution containing tetrabutylammonium hexafluorophosphate ($TBAPF_6$, 0.1 M) and $AgNO_3$ (0.005 M). All three electrodes were immersed in a deoxygenated DMF solution (5 mL) containing $TBAPF_6$ (0.1 M) as a support electrolyte and platinum complexes (**55**, **56** and (bipy)$PtCl_2$) (0.001 M). Ferrocene was used as an internal standard, and all potentials are reported with respect to $E_{1/2}$ of the Fc / Fc^+ redox couple.

Synthesis of 54. *n*-butyllithium (1.0 mL, 2.6 M in hexane, 2.6 mmol) was added dropwise to an Et_2O (5 mL) solution of 4-bromo-2-2'-bipyridine (510 mg, 2.17 mmol) cooled to -100 °C. Once addition was complete, the resulting orange suspension was kept at this temperature and stirred for an additional 30 minutes. This solution was kept at -100 °C and combined with a THF (5 mL) solution of Ph_2SbCl (0.82 g, 2.63 mmol) which was added slowly using a cannula. The resulting mixture was stirred at -100 °C for an additional hour, before being allowed to warm to room temperature. After 12 hours, the solvents were evaporated under vacuum. The residue was taken in CH_2Cl_2 (20 mL) and filtered through Celite. The filtrate was brought to dryness and the resulting thick oily product mixture purified by flash chromatography on silica gel (mobile phase: 1% ethyl acetate in hexanes). The third major fraction was evaporated to an oily residue, which was washed with pentane to yield **54** as a white solid. Yield: 620

mg (45%). Single crystals of **54** suitable for X-ray diffraction were obtained by evaporation of a pentane/CH_2Cl_2 solution at room temperature. ^{1}H NMR (499.42 MHz, $CDCl_3$) δ 8.56 (d, J = 4.0 Hz, 1H), 8.52 (s, 1H), 8.49 (d, J = 4.7 Hz, 1H), 8.28 (d, J = 8.0 Hz, 1H), 7.72 (td, J = 7.8, 1.8 Hz, 1H), 7.42 – 7.36 (m, 4H), 7.28 (m, 6H), 7.21 (ddd, J = 7.4, 4.8, 1.0 Hz, 1H), 7.19 – 7.16 (m, 1H). ^{13}C NMR (125.58 MHz, $CDCl_3$) δ 156.15, 155.18, 150.43, 149.17, 148.74, 137.28, 136.87, 136.30, 130.58, 129.11, 128.99, 128.85, 123.65, 121.32. Elemental analysis (%) calculated for $C_{22}H_{17}N_2Sb$: C, 61.29; H, 3.97. Found: C, 61.59; H, 4.33.

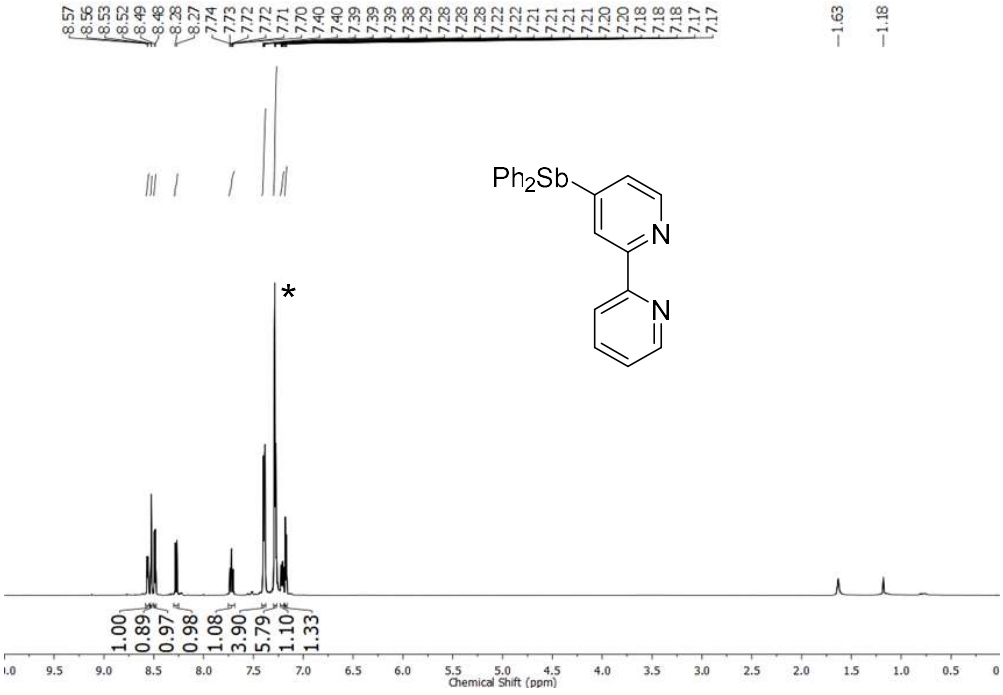

Figure 82. ^{1}H NMR spectrum of **54** in $CDCl_3$. The resonance marked with an asterisk belong to $CDCl_3$.

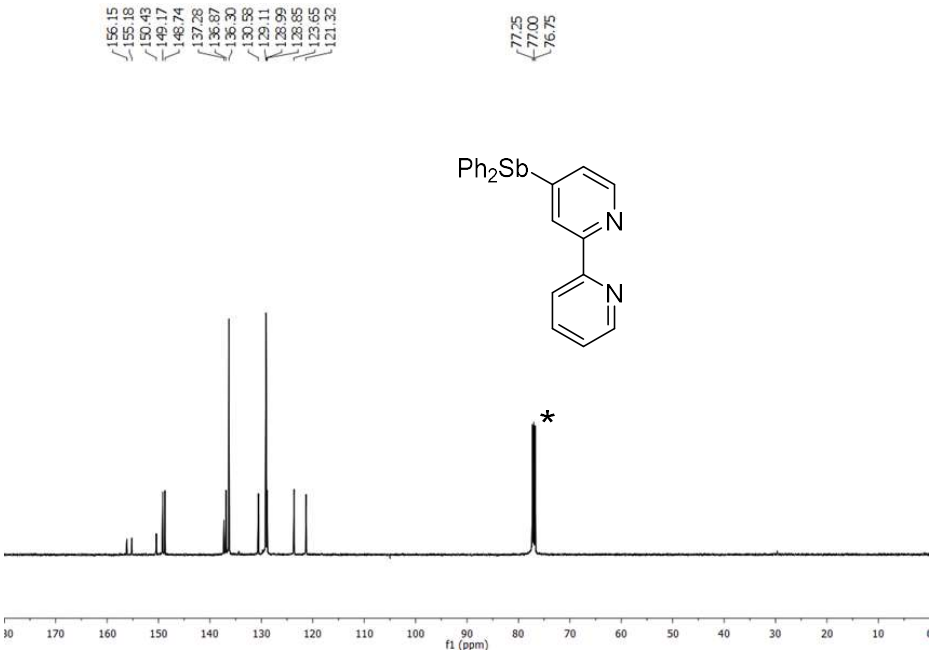

Figure 83. ^{13}C NMR spectrum of **54** in $CDCl_3$. The resonance marked with an asterisk belong to $CDCl_3$.

Synthesis of 55. The ligand **54** (150 mg, 0.35 mmol) and $Pt(CH_3CN)_2Cl_2$ (115 mg, 0.33 mmol) were combined in acetonitrile (5 ml). The resulting mixture was warmed to 50°C and stirred for 5 hours. The precipitate obtained was filtered, washed with CH_2Cl_2 (3 × 2 mL), Et_2O (3 × 2 mL) and dried under vacuum to give a **55** as a pale yellow solid. Yield: 240 mg (82%). Single crystals of **55** suitable for X-ray diffraction were obtained by diffusion of pentane into a solution of the compound in CH_2Cl_2 inside an NMR tube. ^1H NMR (499.42 MHz, $(CD_3)_2SO$) δ 9.47 (d, J = 5.9 Hz, 1H), 9.29 (d, J = 5.8 Hz, 1H), 8.71 (s, 1H), 8.36 (m, 2H), 7.81 (t, J = 6.1 Hz, 1H), 7.58 (d, J = 5.9 Hz, 1H), 7.55 – 7.47 (m, 4H), 7.46 – 7.36 (m, 6H). ^{13}C NMR (125.58 MHz, $(CD_3)_2SO$) δ 156.66, 154.96, 148.45, 146.67, 140.49, 137.82, 136.21, 134.02, 131.19, 129.21, 129.15,

128.89, 127.62, 123.97. Elemental analysis (%) calculated for $C_{22}H_{17}N_2SbPtCl_2$: C, 37.90; H, 2.46. Found: C, 38.15; H, 2.55.

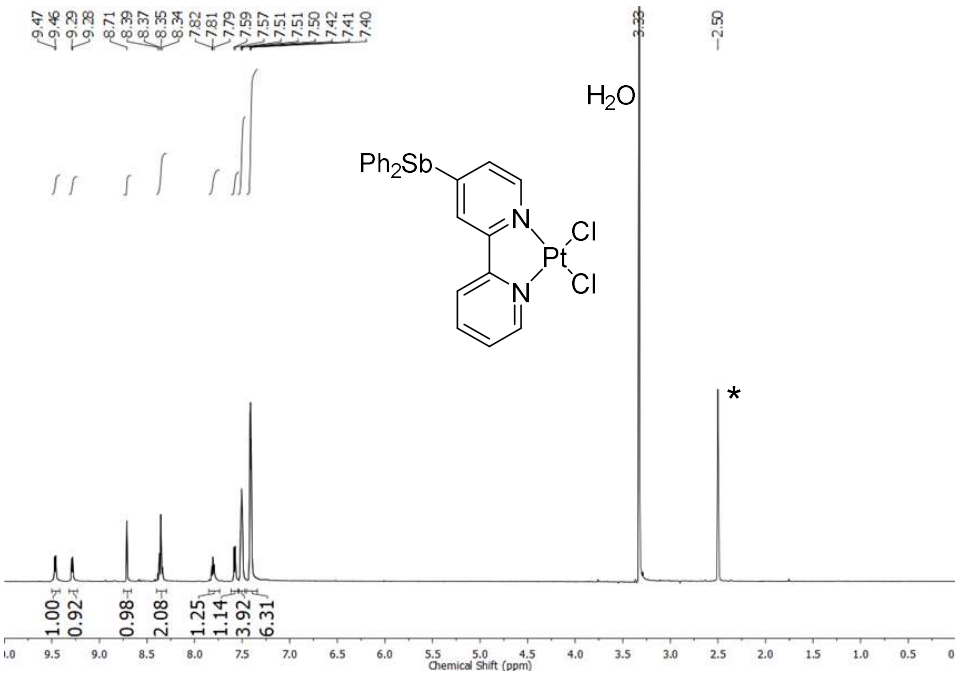

Figure 84. ^{1}H NMR spectrum of **55** in $(CD_3)_2SO$. The resonance marked with an asterisk belong to $(CD_3)_2SO$.

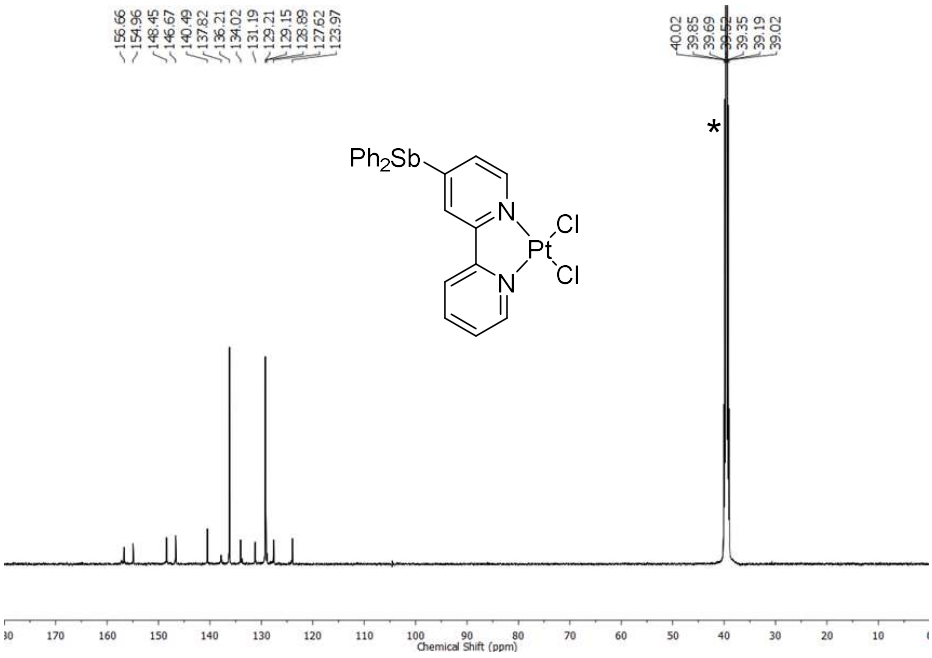

Figure 85. ^{13}C NMR spectrum of **55** in $(CD_3)_2SO$. The resonance marked with an asterisk belong to $(CD_3)_2SO$.

Synthesis of 56. Complex **55** (100 mg. 0.14 mmol) was dissolved in DMSO (5 mL) and treated with a DMSO (1 mL) solution of $PhICl_2$ (160 mg, 0.6 mmol). The resulting yellow suspension was stirred for 1 hour. The residue was extracted with pentane (3 × 3 mL), Et_2O (3 × 2 mL) and recrystallized from CH_2Cl_2/Et_2O to yield a yellow solid. Yield: 70 mg (64%). Single crystals of **56** suitable for X-ray diffraction were obtained by diffusion of pentane into a solution of the compound in CH_2Cl_2 inside an NMR tube. ^1H NMR (499.42 MHz, $(CD_3)_2SO$) δ 9.50 (m, 2H), 8.68 (s, 1H), 8.35 (td, J = 7.9, 1.3 Hz, 1H), 8.26 – 8.16 (m, 2H), 7.91 - 7.80 (m, 5H), 7.48 – 7.38 (m, 7H). ^{13}C NMR (125.58 MHz, $(CD_3)_2SO$) δ 166.56, 156.34, 155.65, 153.06, 148.65, 147.57, 140.91, 132.71, 132.14, 129.76, 128.43, 127.83, 127.58, 123.82. Elemental analysis (%) calculated for $C_{22}H_{17}N_2SbPtCl_4$: C, 34.40; H, 2.23. Found: C, 34.33; H, 2.31.

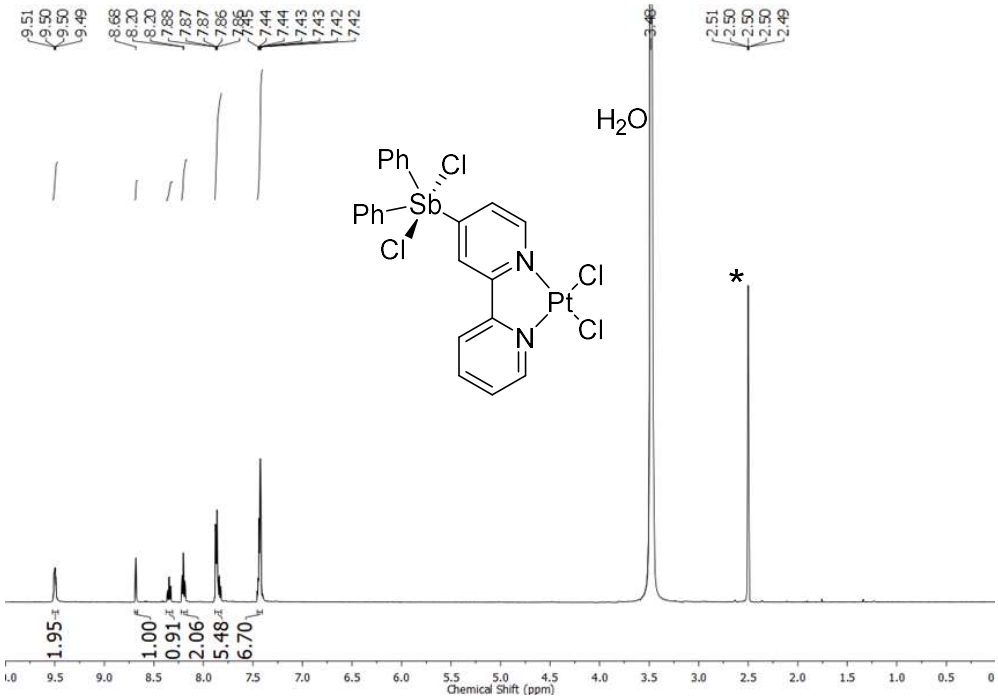

Figure 86. ^{1}H NMR spectrum of **56** in $(CD_3)_2SO$. The resonance marked with an asterisk belong to $(CD_3)_2SO$.

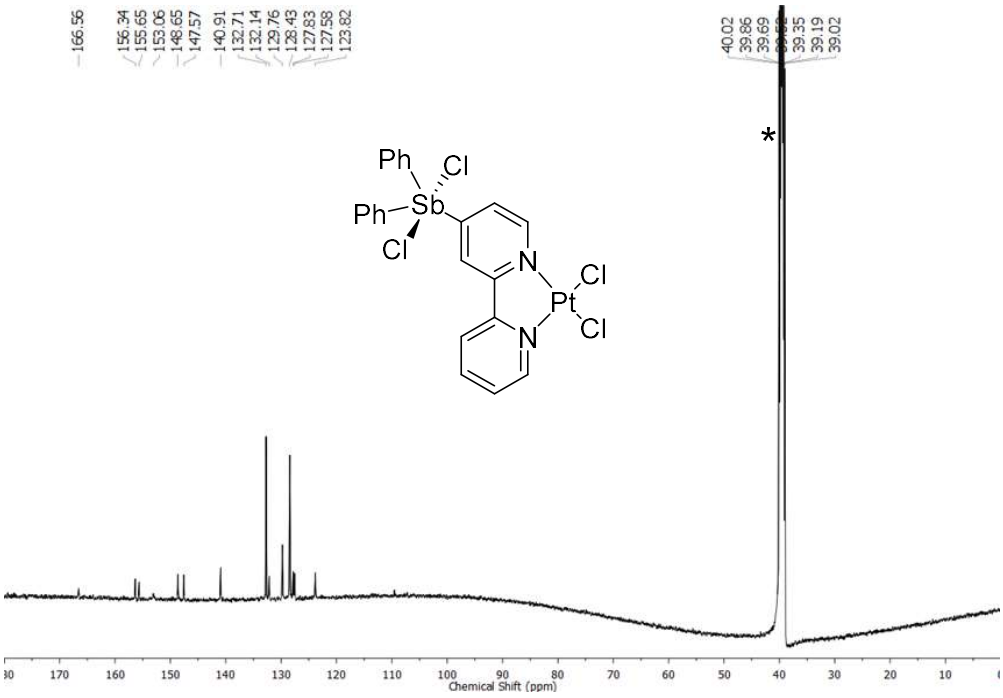

Figure 87. ^{13}C NMR spectrum of **56** in $(CD_3)_2SO$. The resonance marked with an asterisk belong to $(CD_3)_2SO$.

Synthesis of 59. Complex **55** (50 mg. 0.07 mmol) was suspended in CH_3CN (5 mL) and treated with a CH_3CN (1 mL) solution of $PhICl_2$ (80 mg, 0.28 mmol). The resulting yellow suspension was stirred for 1 hour. The residue was concentrated and the precipitated was filtered. The solid obtained was washed with dichloromethane (3 × 1 mL), Et_2O (3 × 2 mL), pentane (3 × 3 mL), and dried under vacuum. Yield: 24 mg (41%). Single crystals of **59** suitable for X-ray diffraction were obtained by diffusion of pentane into a solution of the compound in THF inside an NMR tube. The solubility is too low in organic solvent for NMR measurement.

Synthesis of 60. Complex **55** (50 mg. 0.07 mmol) was dissolved in DMSO (5 mL) and treated with a DMSO (1 mL) solution of Br_2-dioxane (69 mg, 0.28 mmol). The resulting yellow suspension was stirred for 1 hour. The residue was extracted with pentane (3 × 3 mL), Et_2O (3 × 2 mL) and recrystallized from CH_2Cl_2/Et_2O to yield a yellow solid. Yield: 23 mg (33%). Single crystals of **60** suitable for X-ray diffraction were obtained by diffusion of pentane into a solution of the compound in CH_2Cl_2 inside an NMR tube.

Synthesis of 61. The ligand **54** (100 mg, 0.23 mmol) and $Pd(CH_3CN)_2Cl_2$ (50 mg, 0.23 mmol) were combined in acetonitrile (5 ml). The resulting mixture was warmed to 50°C and stirred for 5 hours. The precipitate obtained was filtered, washed with CH_2Cl_2 (3 × 2 mL), Et_2O (3 × 2 mL) and dried under vacuum to give a **61** as a pale yellow solid. Yield: 67 mg (48%). ^{1}H NMR (499.42 MHz, DMSO-d_6) δ 9.09 (d, J = 5.7 Hz, 1H), 8.91 (d, J = 5.7 Hz, 1H), 8.70 (s, 1H), 8.36 – 8.24 (m, 2H), 7.77 (ddd, J = 7.4,

5.7, 1.7 Hz, 1H), 7.58 – 7.52 (m, 1H), 7.50 – 7.45 (m, 4H), 7.39 (dd, J = 4.2, 2.2 Hz, 6H).

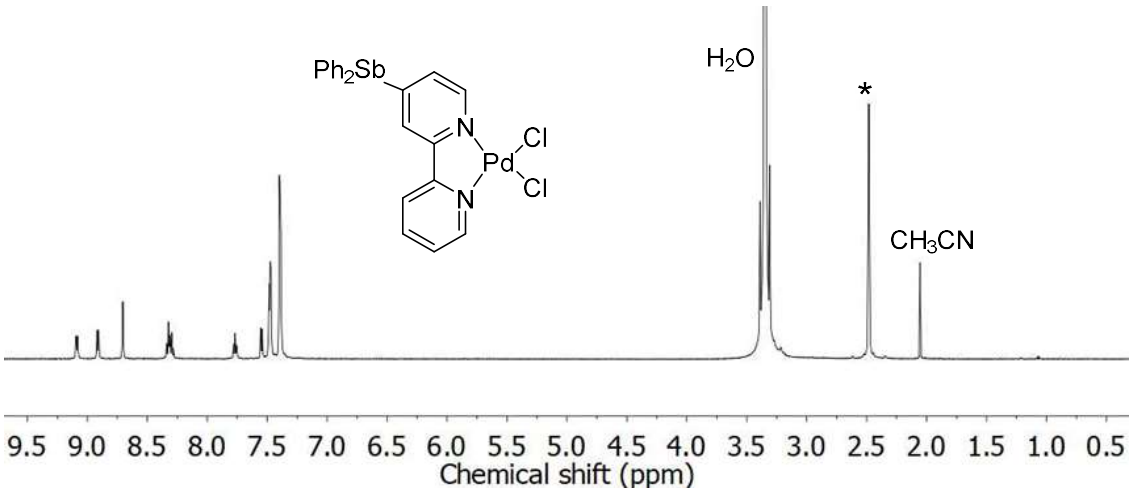

Figure 88. ^{1}H NMR spectrum of **61** in d_6-DMSO. The resonance marked with an asterisk belong to DMSO.

Synthesis of 62. To the ligand **54** (150 mg, 0.35 mmol) in dichloromethane (3 mL), 3,4,5,6-tetrachloro-1,2-benzoquinone (*o*-chloranil) (86 mg, 0.35 mmol) in dichloromethane (5 mL) were dropwise added. The resulting solution was stirred for 10 minutes, and then concentrated. The residue was recrystallized by adding pentane (5 mL) and the precipitate obtained was filtered, washed with pentane (3 × 2 mL) and dried under vacuum to give **62** as a white solid. Yield: 182 mg (77%). ^{1}H NMR (499.42 MHz, CD_2Cl_2) δ 8.84 (d, J = 4.8 Hz, 1H), 8.82 – 8.80 (m, 1H), 8.62 – 8.58 (m, 1H), 8.47 (d, J

= 7.9 Hz, 1H), 7.88 (t, *J* = 7.6 Hz, 1H), 7.85 – 7.80 (m, 4H), 7.79 (dd, *J* = 5.0, 1.4 Hz, 1H), 7.63 (t, *J* = 7.4 Hz, 2H), 7.60 – 7.54 (m, 4H), 7.36 (dd, *J* = 7.5, 5.0 Hz, 1H).

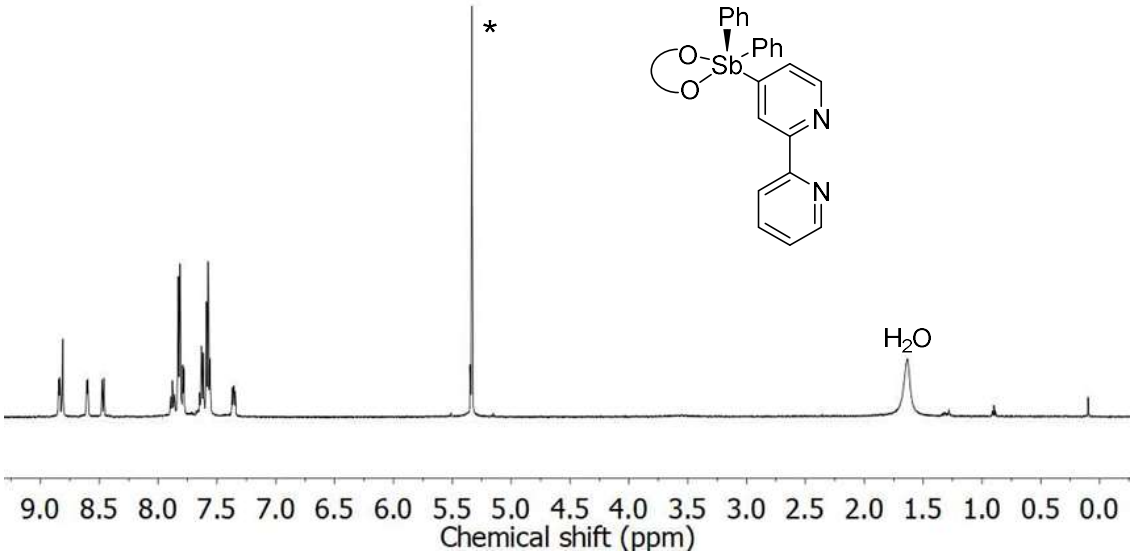

Figure 89. ^{1}H NMR spectrum of **62** in CD_2Cl_2. The resonance marked with an asterisk belong to CD_2Cl_2.

Synthesis of 63. The ligand **62** (50 mg, 0.07 mmol) and $Pt(CH_3CN)_2Cl_2$ (16 mg, 0.33 mmol) were combined in acetonitrile (3 ml). The resulting mixture was warmed to 50°C and stirred for 5 hours. The precipitate obtained was filtered, washed with CH_2Cl_2 (3 × 2 mL), Et_2O (3 × 2 mL) and dried under vacuum to give a **63** as a pale yellow solid. Yield: 31 mg (51%). Single crystals of **63** suitable for X-ray diffraction were obtained by diffusion of pentane into a solution of the compound in $CHCl_3$ inside an NMR tube. ^{1}H NMR (499.42 MHz, DMSO-d_6) δ 9.17 – 9.12 (m, 1H), 9.09 (d, *J* = 5.8 Hz, 1H), 8.39 (s,

1H), 8.30 (dd, *J* = 8.8, 7.3 Hz, 1H), 8.06 (s, 1H), 7.86 (s, 1H), 7.77 (t, *J* = 6.8 Hz, 1H), 7.65 – 7.56 (m, 4H), 7.56 – 7.44 (m, 6H).

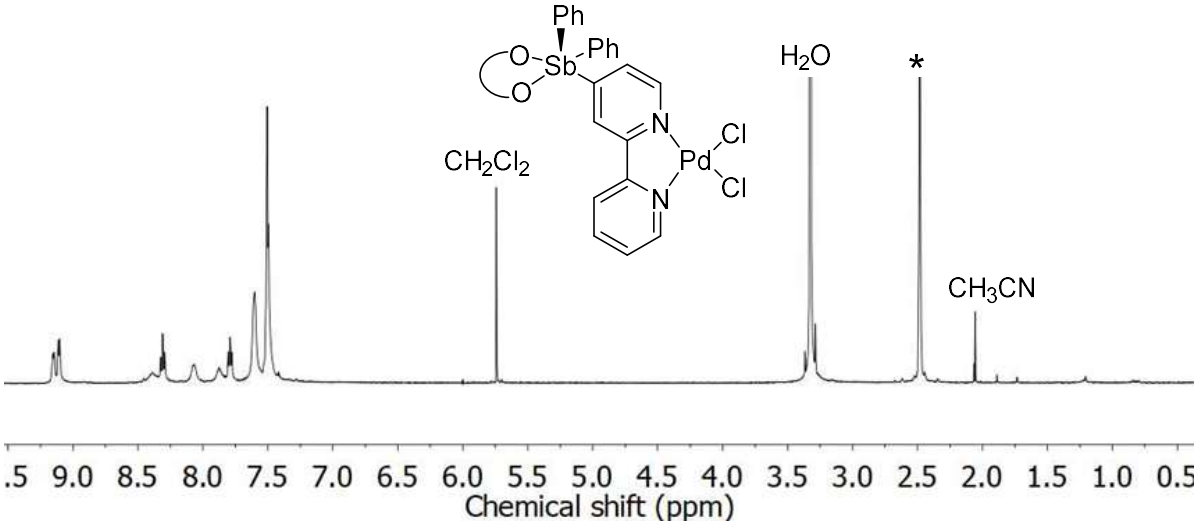

Figure 90. ^{1}H NMR spectrum of **63** in d_6-DMSO. The resonance marked with an asterisk belong to DMSO.

General procedure for the hydroarylation of ethyl propiolates. The catalyst (5 mol%) was combined with mesitylene (40 μL, 0.28 mmol) in TFA (1 mL). After stirring for 5 min at room temperature, this solution was treated with ethyl propiolate (29 μL, 0.28 mmol), which was added with a microsyringe. After 4 hours at 60 °C, 1,2-dichloroethane (0.07 mmol) was added as an internal standard to the solution. A portion of the solution (50 μL) was dissolved in $CDCl_3$ (0.4 mL) for NMR analysis. The product yields shown in Table 1 were based on integration of the NMR spectra. The nature of the hydroarylation products (2Z)-ethyl-3-mesitylpropenaote and (2Z)-ethyl-3-{2,4,6-trimethyl-3[(1Z)-2-ethoxycarbonylethylenyl]}-phenyl}propenoate was confirmed by their isolation and their purification by column chromatography on silica gel (mobile

phase: 10% ethyl acetate in hexanes). The NMR data collected match those reported in the literature.[181]

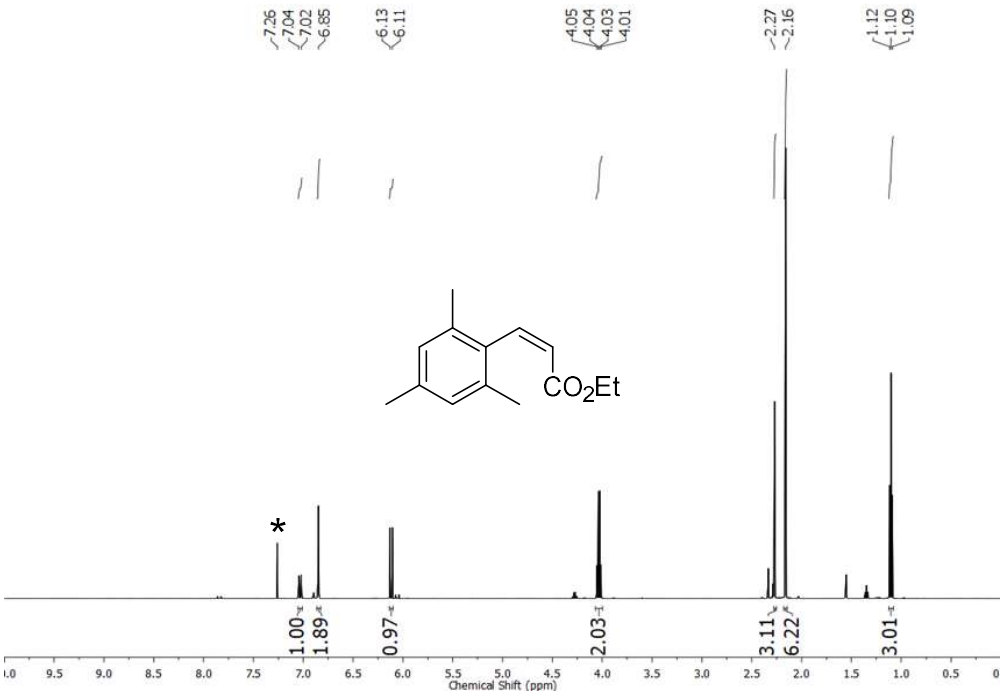

Figure 91. ^{1}H NMR spectrum of (2Z)-ethyl-3-mesitylpropenaote in $CDCl_3$. The resonance marked with an asterisk belong to $CDCl_3$.

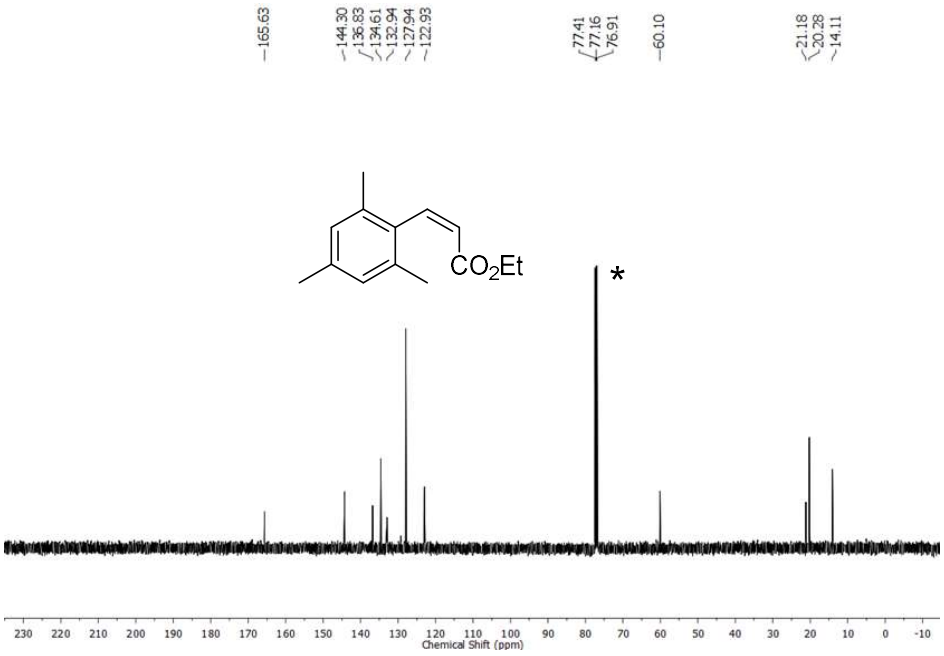

Figure 92. ^{13}C NMR spectrum of (2Z)-ethyl-3-mesitylpropenaote in $CDCl_3$. The resonance marked with an asterisk belong to $CDCl_3$.

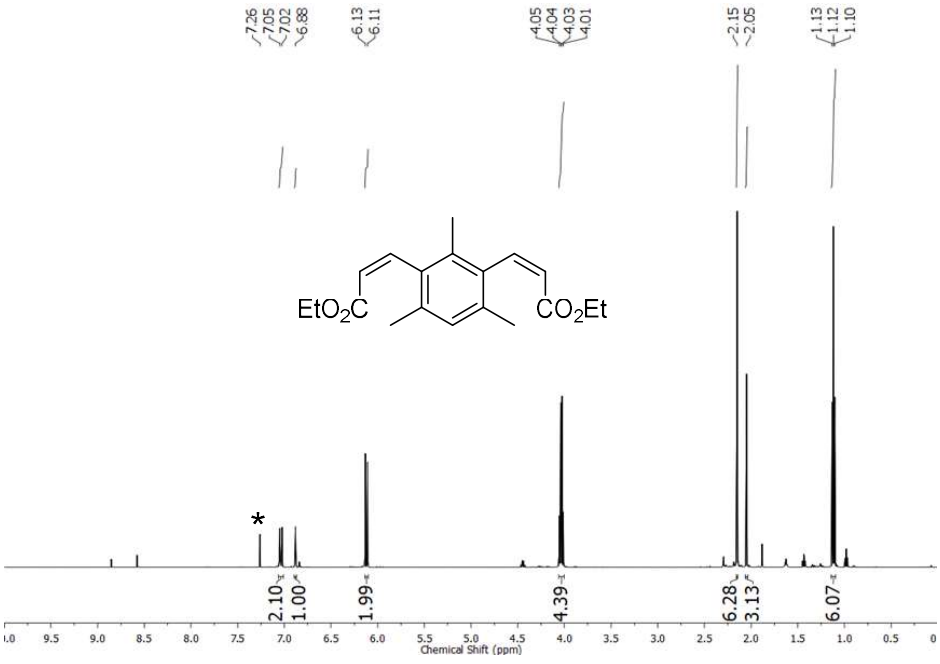

Figure 93. ^{1}H NMR spectrum of (2Z)-ethyl-3-{2,4,6-trimethyl-3[(1Z)-2-ethoxycarbonylethylenyl]}-phenyl}propenoate in $CDCl_3$. The resonance marked with an asterisk belong to $CDCl_3$.

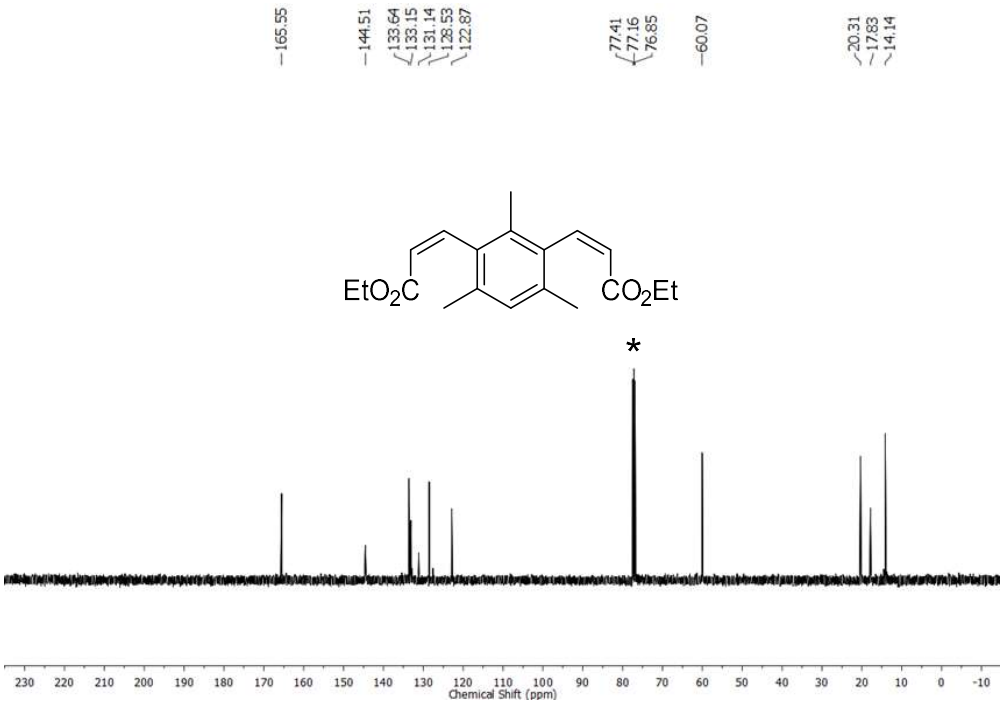

Figure 94. ^{13}C NMR spectrum of (2Z)-ethyl-3-{2,4,6-trimethyl-3[(1Z)-2-ethoxycarbonylethylenyl]}-phenyl}propenoate in $CDCl_3$. The resonance marked with an asterisk belong to $CDCl_3$.

CHAPTER IV

CYCLOMETALATED IRIDIUM BIPYRIDINE COMPLEXES WITH PERIPHERAL ANTIMONY SUBSTITUENTS*

4.1 Introduction

The chemistry of organoantimony(V) compounds is experiencing a resurgence that has led to the development of new applications in the area of catalysis,[117, 160-161, 164-165, 167-168, 189-193] small molecule activation,[17, 194-196] anion sensing,[16, 18, 197-203] and anion transport.[204-205] The most important characteristic of these compounds is the Lewis acidity of the antimony center which can be adjusted by varying the electronic properties of the substituents. These substituents can also be used to impart specific optoelectronic properties which could in principle become useful in the domain of anion sensing. Based on the anion binding reactions shown in Figure 95, we have shown that appending simple chromophores as in **A**-**C** can afford fluorescent turn-on sensors that we have used for the detection of fluoride or cyanide anions at low concentrations (Figure 96).[16, 197, 199] We have also considered the use of metal containing chromophores as in the case **D**, a complex in which the tetraaryl stibonium cation is installed at the periphery of a cyclometalated ruthenium polypyridyl core (Figure 96).[90] Our investigation of the properties of this complex showed that anion coordination at the antimony centers triggers electrochemical and photophysical changes that can be used to report the

---

* Reprinted with permission from: "Cyclometalated iridium bipyridine complexes with peripheral antimony substituents"; Lo, Y.-H.; Gabbaï F. P. *Z. Anorg. Allg. Chem.* **2019**, *accepted author manuscript.* DOI: 10.1002/zaac.201900186.

chemistry taking place at the Lewis acidic main group center. Building on these recent results, we have now become interested in installing antimony(V) moieties at the periphery of other metal complexes.

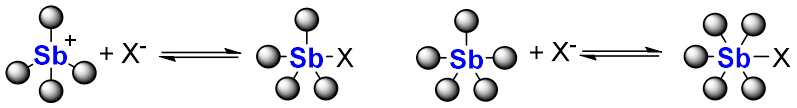

Figure 95. Anion binding reaction involving antimony(V) species (X = halogen).

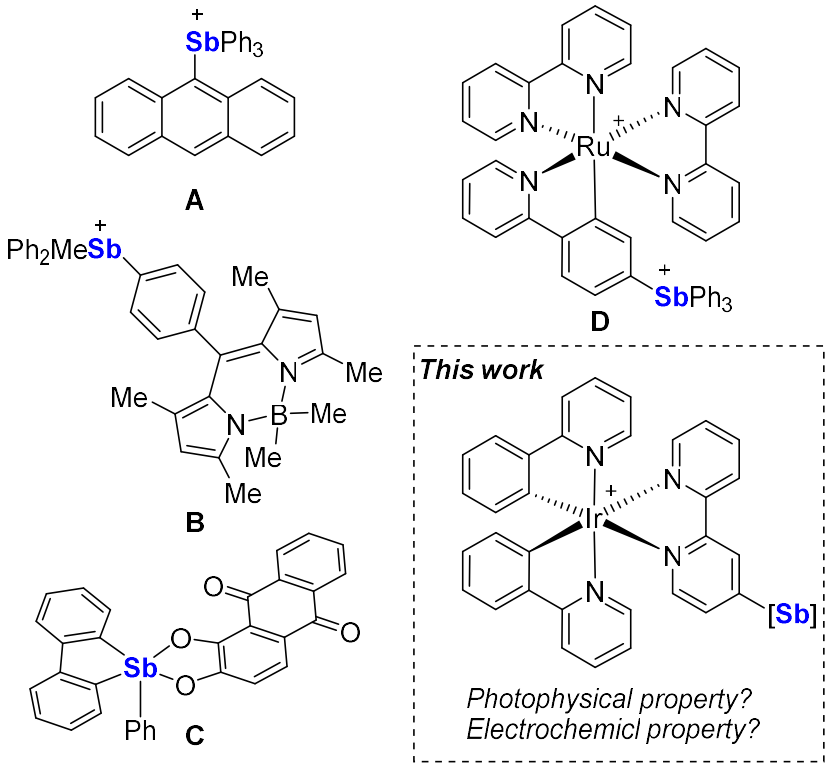

Figure 96. Structure of relevant antimony(V) Lewis acids and general structure targeted in this study.

Iridium (III) cyclometalated complexes constitute an important class of materials that have found applications in sensing, photocatalysis, and light emitting or harvesting materials.[206-209] The most important property of these complexes is the metal-to-ligand

charge transfer (MLCT) nature of their excited state as it influences the emissive properties of these materials as well as their photoredox properties. Because of the attractive features displayed by iridium (III) cyclometalated complexes, we have now become interested in investigating the incorporation of Lewis acidic antimony moieties at their periphery. In this paper, we describe a series of results obtained while pursuing this objective.

4.2 Synthesis of Ir complexes with Sb-substituted bipyridine ligands

We have previously described 4-(diphenylstibino)-2,2'-bipyridine (**54**), a ligand that we successfully incorporated in platinum(II) complexes.[210] We found that this ligand reacted cleanly with $[(ppy)_2Ir(\mu\text{-}Cl)]_2$ (ppy = 2-phenylpyridine) in refluxing methanol and dichloromethane (1:1 v/v) to afford, after anion exchange with KPF_6, the antimony-substituted iridium complex [**64**][PF_6] as a yellow solid (Figure 97).[211] This complex was subsequently allowed to react with excess phenyl iodine dichloride ($PhICl_2$) in wet DMSO to afford complex **65**-Cl which also displays a yellow color characteristic of the iridium tris-chelate chromophore. Dissolution of $PhICl_2$ in DMSO is exothermic, suggesting oxidation of DMSO,[212] which in the presence of water would release HCl and the resulting sulfone. We propose that this side reaction is the source of the third chloride anion coordinated to the antimony atom.

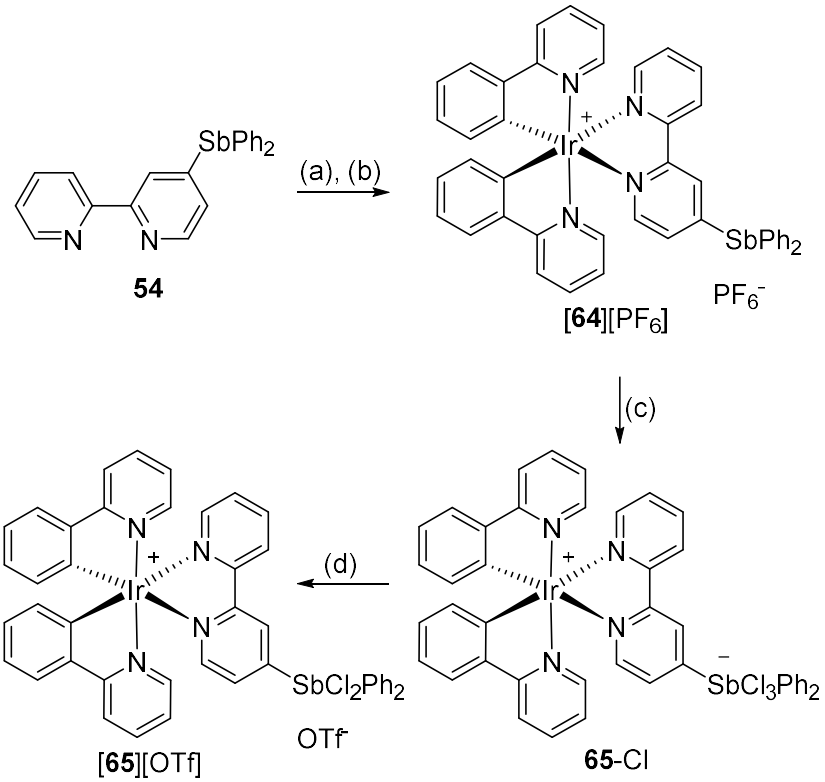

Figure 97. Synthesis of [**64**][PF_6], **65-**Cl, and [**65**][OTf].(a) 1 equiv. $[(ppy)_2Ir(\mu\text{-}Cl)]_2$, DCM/MeOH 1:1, reflux, 8 h. (b) KPF_6, MeOH (c) 4 equiv. $PhICl_2$, DMSO, 3 h. (d) 1 equiv. AgOTf, $CDCl_3$.

Both [**64**][PF_6] and **65**-Cl have been fully characterized by ^1H and ^{13}C NMR spectroscopy. The ^1H NMR spectra of [**64**][PF_6] and **65**-Cl display complicated spectra because the symmetry of the pseudo-octahedral iridium complex is broken by the coordination of the **54**, making each aromatic hydrogen magnetically non-equivalent. It is worth noting that the diagnostic peaks corresponding to the 3 position of the bipyridine ligand shifts from 8.63 ppm to 9.24 ppm upon oxidation. The resonances corresponding to the phenyl group bound to the antimony atom also display a significant shift from 7.35 ppm to 7.68 ppm, indicative of a more electrophilic environment as a

result of antimony oxidation (Figure 98). The ESI unit mass spectrum of **65**-Cl is dominated by a peak at m/z 1001 amu corresponding to [**65**]$^+$ (Figure 98) with an isotopic pattern consistent with the atomic make up of this cation. The detection of this complex suggest that **65**-Cl could release a chloride anion to afford the corresponding iridium-stiborane [**65**]$^+$. To test this possibility, **65**-Cl was suspended in $CDCl_3$, a solvent in which it is not soluble. Addition of AgOTf to this mixture resulted in dissolution of the complex and the appearance of ^{1}H NMR resonances assigned to the formation of [**65**][OTf] which could unfortunately not be isolated.

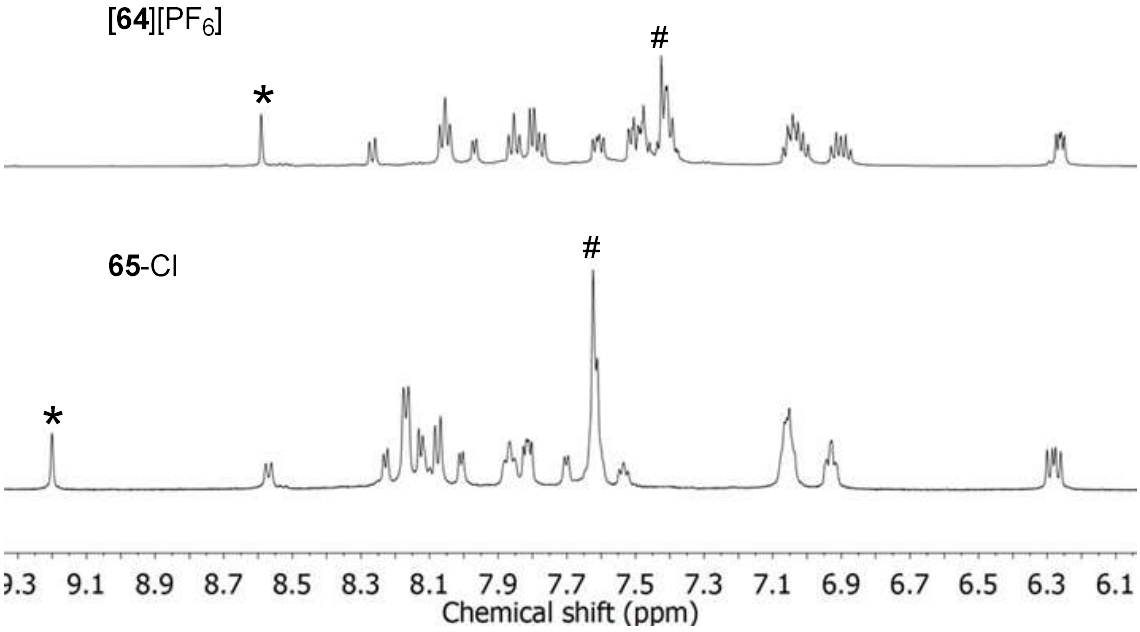

Figure 98. ^{1}H NMR spectra of complexes [**64**][PF_6] and **65**-Cl in CD_3CN. The proton corresponding to the 3 position of the bipyridine is indicated by an asterisk (*) for each spectrum. The protons corresponding to the phenyl group on the antimony are indicated by a pound sing (#).

The solid-state structure of complex **65**-Cl has been determined using single crystal X-ray diffraction analysis (Figure 99). The iridium (III) center adopts a distorted

octahedral geometry, with the N(1)–Ir(1)–N(2) bond angle compressed to 76.2(3)°, a feature consistent with literature precedents for these type of complexes.[85, 170, 213] A comparison of the structure of **65**-Cl with that of $[Ir(ppy)_2(bpy)]^+$ shows that the antimony moiety has negligible influence on the geometry of the iridium center.[87] The antimony center also displays a distorted octahedral geometry with the three chloride ligands in a *mer*-configuration. The longer Ir(1)–Cl(3) distance (2.547(2) Å), compared to Ir(1)–Cl(1) and Ir(1)–Cl(2) (2.370(5) Å and 2.472(3) Å) suggests that the pyridyl ring at the trans position exerts a greater trans influence than that of a chlorine ligand.

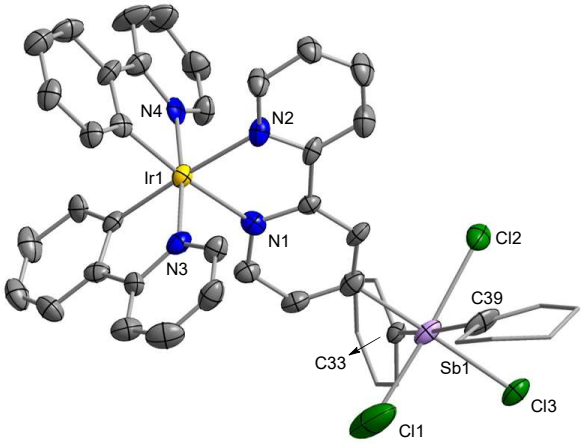

Figure 99. Solid-state structure of **65**-Cl. Thermal ellipsoids are drawn at the 50% probability level. The hydrogen atoms are omitted for clarity. Selected bond length (Å) and angles (deg): Sb1–Cl1 2.370(5), Sb–Cl2 2.472(3), 2.547(2), N1–Ir1–N2 76.2(3).

4.3 Photophysical and electrochemical properties of [64][PF_6] and 65-Cl

The photophysical properties of [**64**][PF_6] and **65**-Cl have been studied and compared with those of the parent complex [$(ppy)_2Ir(bpy)$][PF_6] for reference. The absorption spectrum of the two new iridium complexes and that of the reference are shown in Figure 100. The low energy absorption bands of all three complexes display a

similar profile. The absorption features at 350 nm – 450 nm are assigned to the ligand-to-ligand charge transfer (ppy to bpy, ^{1}LLCT) and metal-to-ligand charge transfer processes (iridium to ppy or bpy, ^{1}MLCT).[86] In addition, the very weak absorptions between 450 to 470 nm were assigned to ^{3}LLCT and ^{3}MLCT. The similarity of these three spectra indicates that the antimony moiety, oxidized or not, has negligible effects on the energy of these transitions. This may at first surprising, especially in the case of the oxidized complex **65**-Cl. We speculate that formation of the trichloroantimonate moiety somewhat counters the increased electron-withdrawing properties of the oxidized antimony center.

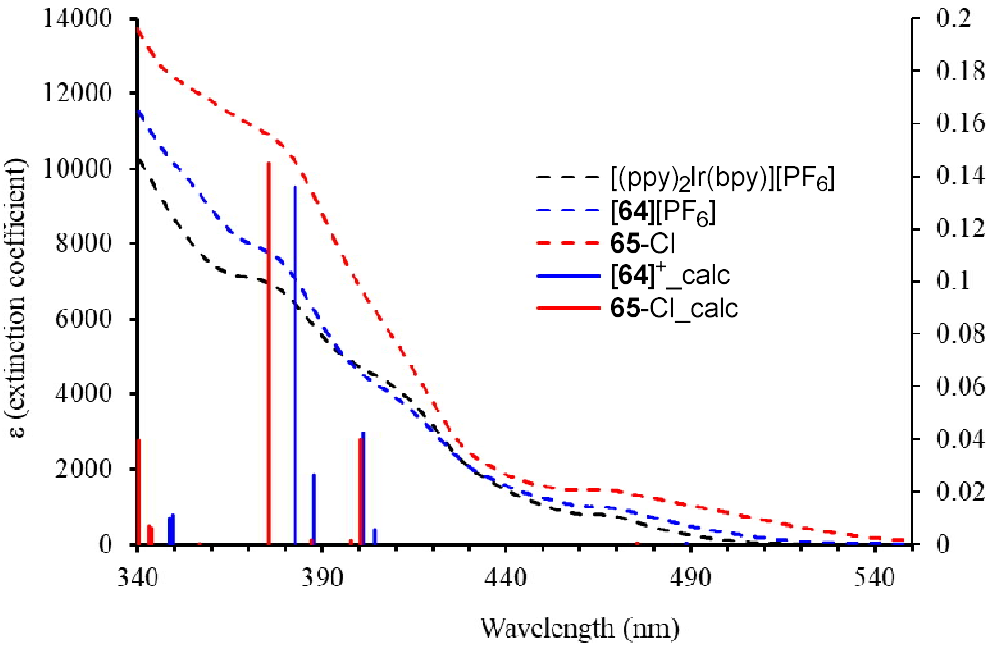

Figure 100. Experimental UV-vis spectrum and calculated vertical electronic transitions (represented by bars) for $[(ppy)_2Ir(bpy)][PF_6]$, [**64**][PF_6] and **65**-Cl in acetonitrile. The wavelengths of the calculated transitions are plotted against the oscillator strength.

We have also computed the electronic structure of [**64**]$^+$ and **65**-Cl using density functional theory (DFT). These calculations were carried out using the Gaussian program with B3LYP as a functional and a mixed basis set (Sb/Ir cc-pVTZ-PP; C/H/N/Cl 3/21G*).[88, 214] The optimized structures are in reasonable agreement with those measured using X-ray diffraction (see the Supporting Information). Figure 101 displays the contours and energies of the Kohn-Sham highest occupied molecular orbital (HOMO) and lowest occupied molecular orbital (LUMO). In both [**64**]$^+$ and **65**-Cl, the HOMO and LUMO are dominated by an iridium "t_{2g}" orbital and the bipyridine π*orbital, respectively. These frontier orbitals closely resemble those of $[(ppy)_2Ir(bpy)]^+$.[208] An interesting feature in the case of **65**-Cl is the contribution of a chloride p-orbital to the HOMO of the complex, consistent with the electron rich nature of the antimonate anion. There is a notable change in the HOMO-LUMO gap which increases from 2.8 ev in [**64**]$^+$ to 3.26 ev in **65**-Cl. This relatively large difference appears difficult to reconcilliate with the experimental spectroscopic results which show similar UV-vis absorption profiles for both [**64**]$^+$ and **65**-Cl. To shed light on this apparent discrepancy, we resorted to TD-DFT calculations using the solute electron density-based implicit solvation model (SMD) with acetonitrile as a solvent. The results of these calculations afford a series of intense vertical excitations, the energy of which nicely coincides with the main absorption features observed in the experimental spectra (Figure 100). There are also a series of weaker transitions, some of which appear in the lower energy range of the spectrum. To better understand the character of these vertical excitations, each of them were analyzed using the natural transition orbital (NTO)

method. The results of this analysis show that, for both complexes, the HOMO-LUMO transition has almost inexistent oscillator strength ($f = 0.001$). This simple computational indicates that the HOMO-LUMO transition does not contribute to the absorption spectrum of these derivatives which are, as a result, not affected by the respective energy of these two orbitals. The NTO analysis of the TD-DFT results shows that the first vertical excitation of respectable oscillator strength ($f > 0.04$) have HOMO to LUMO+1 character for [**64**]$^+$ and HOMO to LUMO+2 for **65**-Cl (Table 22). These excitations correspond to the third and second excited states in the case of [**64**]$^+$ and **65**-Cl, respectively. It is interesting to note the LUMO+1 for [**64**]$^+$ and LUMO+2 for **65**-Cl are π* orbitals delocalized on the phenylpyridine ligands rather than on the bipyridine ligand. Moreover, the energy of this transition (401.1 nm for [**64**]$^+$ with $f = 0.04$ and 400.4 nm for **65**-Cl with $f = 0.04$) is almost identical in both compounds, thereby providing a rationale for the similarity of the spectra of these two compounds. The next intense vertical excitation, which are calculated at 382.7 nm for [**64**]$^+$ (f = 0.14) and 375.5 nm for **65**-Cl (f = 0.15), correspond to the fifth singlet excited state for both complexes. The NTO analysis shows that this transition involves excitation from an orbital of HOMO-1/HOMO-2 character to the LUMO which as stated above has bipyridine π* character. Again, the similarity in the energy of these transitions in the two complexes explains why their UV-vis spectra are so alike.

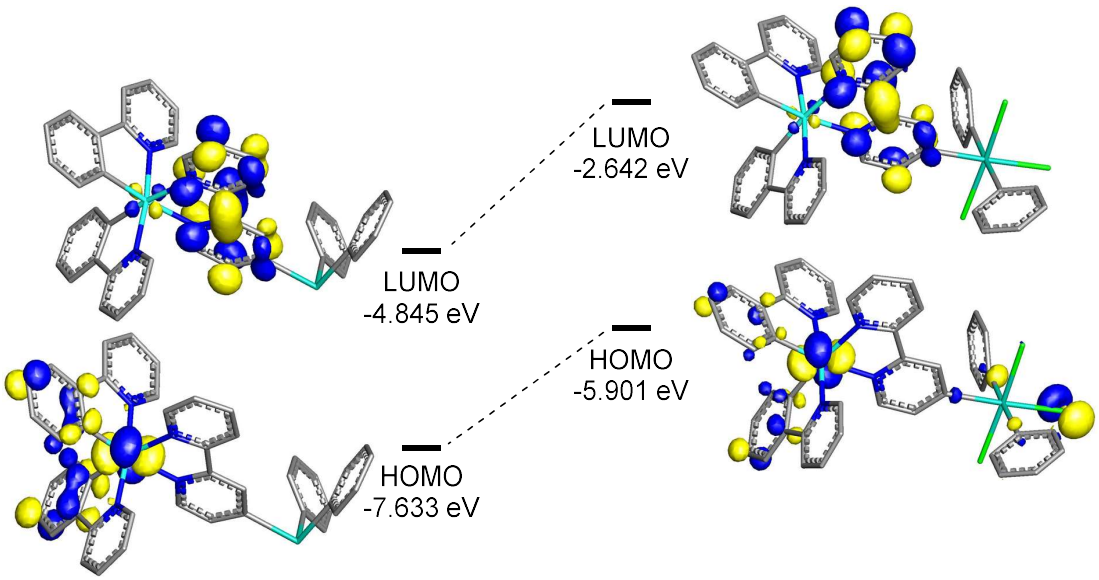

Figure 101. Frontier molecular orbitals (isovalue 0.05) and Energies (eV) of [**64**]$^+$ and **65**-Cl.

Table 22. Dominant NTOs, calculated wavelengths (λ), and oscillator strengths (f) for the excited singlet states of [**64**]$^+$ and **65**-Cl.

	[**64**]$^+$	**65**-Cl
Acceptor NTO	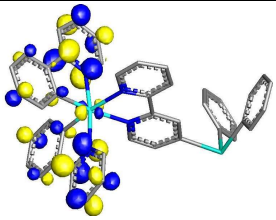	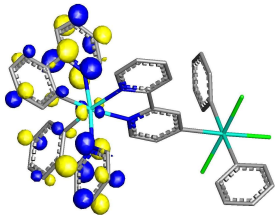
Donor NTO	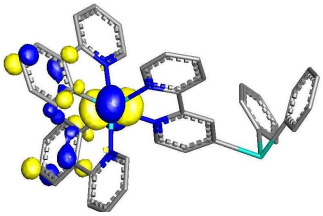	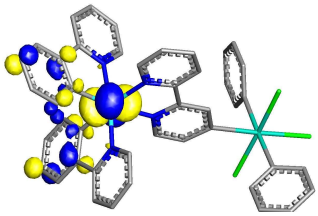
	λ = 401.1 nm, f = 0.043 3rd transition	λ = 400.4 nm, f = 0.040 2nd transition

Table 22 Continued

	[**64**]$^+$	**65**-Cl
Acceptor NTO	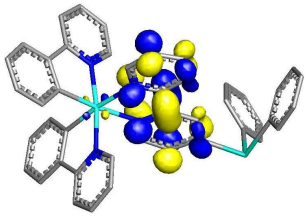	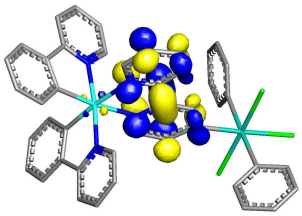
Donor NTO	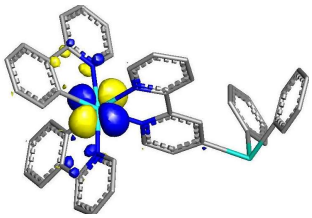	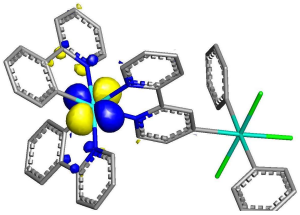
	λ = 382.7 nm, *f* = 0.136 5th transition	λ = 375.5 nm, *f* = 0.145 5th transition

The emission spectra of complex [(ppy)$_2$Ir(bpy)][PF$_6$], [**64**][PF$_6$] and **65**-Cl in acetonitrile are shown in Figure 102. Similar to the absorption spectrum, the emission maxima (λ_{em} = 595 nm) and quantum yield of [**64**][PF$_6$] (Φ = 9.3%) show almost no differences when compared to [(ppy)$_2$Ir(bpy)][PF$_6$] (λ_{em} = 592 nm, Φ = 9.3%).[214] This suggests that the diphenyl antimony substituent has no influence on the iridium-centered fluorophore. Interestingly, a noticeable red shift (25nm) is observed for the emission of **65**-Cl (λ_{em} = 617 nm) and the quantum yield drops to 2.2%. We propose that the lower quantum yield of **65**-Cl originates from a decrease in the transition dipole moment caused by the presence of the anitmonate moiety.[215]

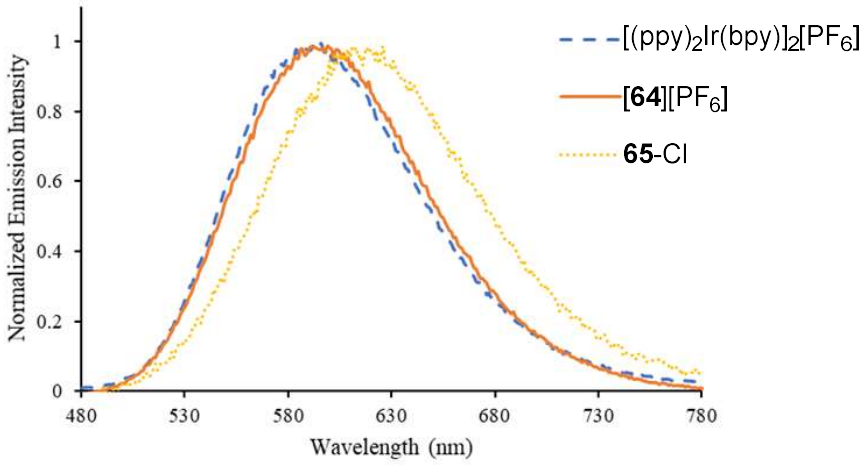

Figure 102. Luminescence spectra of $[(ppy)_2Ir(bpy)]^+$, $[\mathbf{64}]^+$ and **65**-Cl in CH_3CN solution at 298 k. λ_{ex} = 400 nm.

The cyclic voltammograms of [**64**][PF_6] and **65**-Cl were recorded and were also compared with that of [$(ppy)_2Ir(bpy)$][PF_6] (Figure 103). Both [**64**][PF_6] and **65**-Cl display a quasi-reversible reduction wave at $E_{1/2}$ = -1.78 V and -1.77 V, respectively, attributed to the reduction of the bipyridine ligand. This reduction is irreversible in the case of **65**-Cl, a feature that we correlate to the possible coupling of the electron transfer event to a reduction of the antimony (V) center, mediated by the bipyridine ligand. The voltammograms also display a quasi-reversible wave assigned to the Ir(III)/(IV) couple. This wave is observed 0.89 V for $[\mathbf{64}]^+$, which is also close to that of [$(ppy)_2Ir(bpy)$][PF_6] ($E_{1/2}$ = 0.88 V). The small difference in both redox potentials points to the innocence of the diphenylantimony moiety in $[\mathbf{64}]^+$. In the case of **65**-Cl, the Ir(III/IV) redox couple observed at 0.79 V is shifted cathodically by 80 mV. This shift indicates that iridium center in complex **65**-Cl is more electron-rich. This result is

consistent with the fact that this complex is neutral and thus more prone to oxidation than cationic [**64**]$^{+}$.

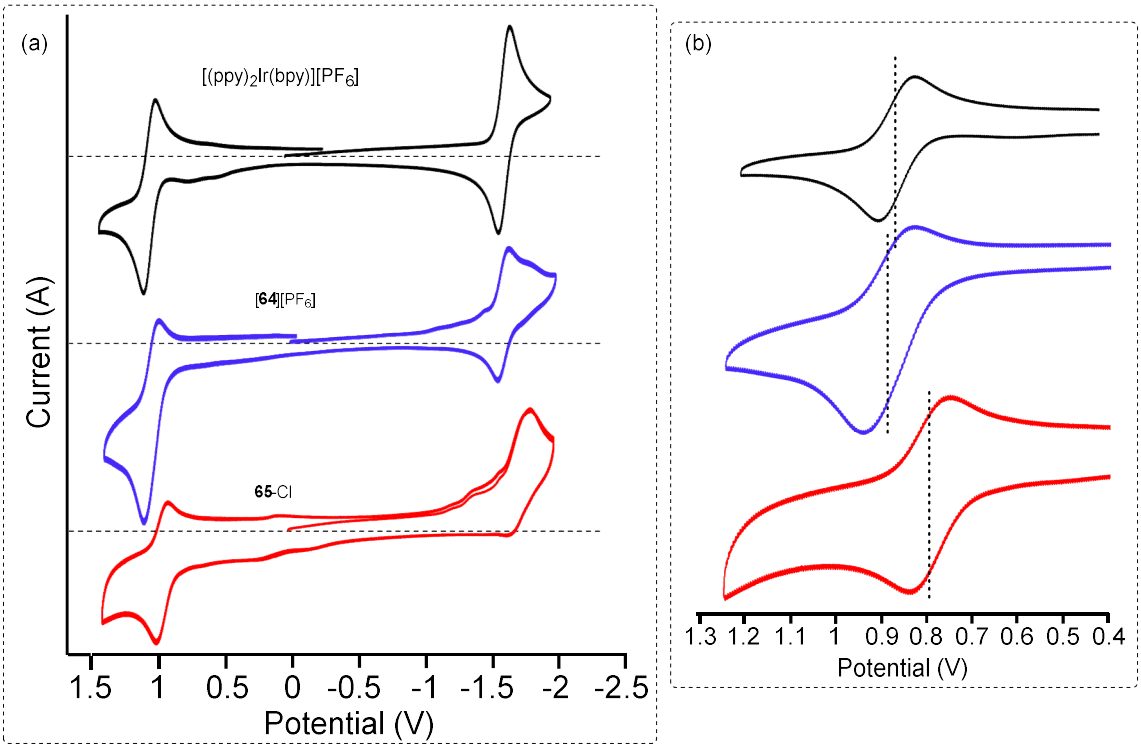

Figure 103. Cyclic voltammograms of [**64**][PF_6], **65**-Cl and [$(ppy)_2Ir(bpy)$][PF_6] in acetonitrile with 0.1 M [$^{n}Bu_4N$][PF_6] as electrolyte. The scan rate was 0.1 V/s, and potentials are referenced to Fc/Fc^{+} in the same solvent.

4.4 Synthesis of Ru complexes with the Sb-substituted bipyridine ligand

Ligand (**54**) ligand was treated with of *cis*-$Ru(bpy)_2Cl_2$ (phen = phenanthrene),[216] Subsequently anion exchange with KPF_6 afforded complex [**66**][PF_6]$_2$ as an orange air-stable solid (Figure 104). Complex [**66**][PF_6]$_2$ has been characterized by ^{1}H NMR and ESI unit mass spectrometry, which shows a major peak at m/z 1037 corresponding to [**66**][PF_6] with an isotopic pattern consistent with that calculated. The

structure of this complex was confirmed by single-crystal X-ray crystallography. (Figure 105).

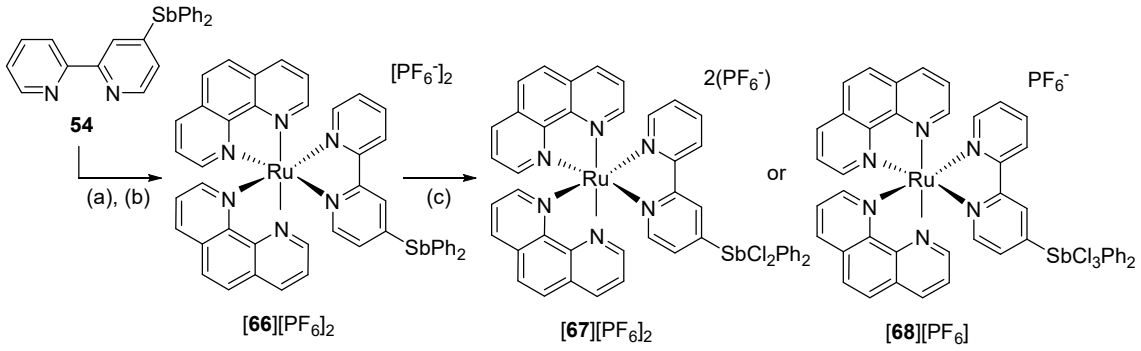

Figure 104. Synthesis of [**66**][PF_6]$_2$ and [**67**][PF_6]$_2$ or [**68**][PF_6]. (a) 1 equiv. (phen)$_2$$RuCl_2$, ethanol/$H_2O$ 1:1, reflux, 8 h. (b) KPF6, ethanol (c) 4 equiv. PhICl2, DMSO, 3 h.

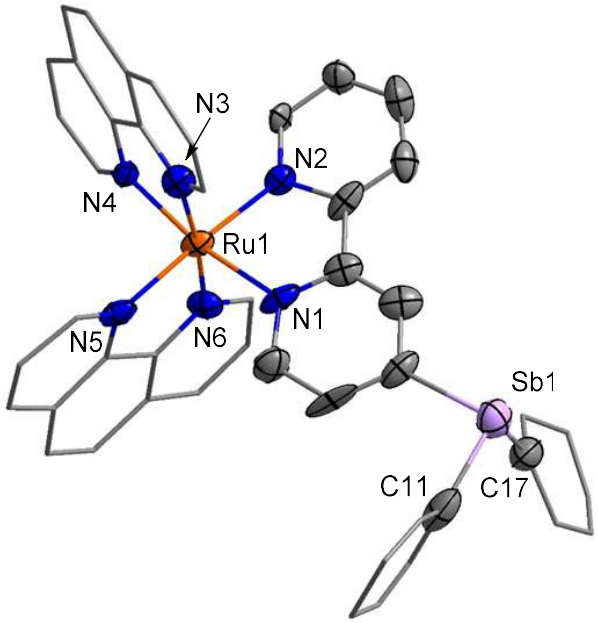

Figure 105. Solid-state structure of [**66**][PF_6]$_2$. Thermal ellipsoids are drawn at the 50% probability level. The hydrogen atoms are omitted for clarity.

Complex [**66**][PF_6]$_2$ reacts cleanly with $PhICl_2$ in DMSO and ^{1}H NMR spectroscopy shows the emergence of a new species, which we assign to the formation

of [**67**][PF_6]$_2$ or [**68**][PF_6]. The proton signals corresponding to the antimony-bound phenyl group and those at the 3-position proton of the pyridine ring of the bipyridine ligand show a significant downfielded shift, indicating the oxidation of the antimony center (Figure 106). ESI mass spectrum displays a peak at m/z 1105 amu corresponding to a formula of [**67**][PF_6]. However, the fragment can also be generated from [**68**][PF_6] by losing one antimony-bound chloride, a similar phenomenon observed at the iridium complex **65**-Cl.

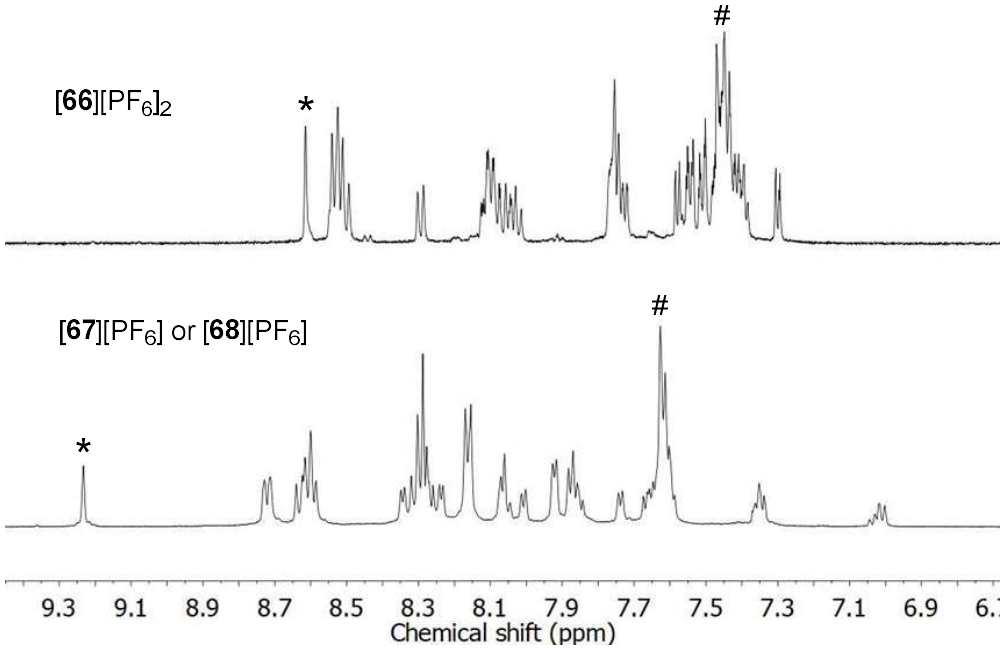

Figure 106. ^{1}H NMR spectra of complexes [**66**][PF_6]$_2$ and [**67**][PF_6]$_2$ or [**68**][PF_6] in CD_3CN. . The proton corresponding to the 3 position of the bipyridine is indicated by an asterisk (*) for each spectrum. The protons corresponding to the phenyl group on the antimony are indicated by a pound sing (#).

4.5 Conclusions

In summary, we have synthesized two cyclometalated iridium bipyridine complexes bearing a peripheral Sb(III) or Sb(V) substituent. The similar properties displayed by [**64**]$^+$ and the reference complex $[(ppy)_2Ir(bpy)]^+$ suggests that the diphenylantimony group does not interfere with the optoelectronic properties. Finally, we have also shown that the antimony moiety of [**64**]$^+$ can be oxidized into a stiborane unit which readily binds an extra chloride anion, leading to the formation of a trichloroantimonate moiety as in **65**-Cl. Formation of this anionic substituent renders the complex neutral and makes oxidation of the iridium center slightly more facile that in the cationic precursor. Finally, we note that **65**-Cl is also notably less emissive that its precursor [**64**]$^+$.

4.6 Experimental section

General Consideration. All preparations were carried out under an N_2 atmosphere using standard Schlenk techniques unless otherwise stated. 4-Bromobipyridine, Ph_2SbCl,[182] [183] $PhICl_2$,[184] were prepared according to previously reported procedures. Et_2O and THF were dried by refluxing under N_2 over Na/K. CH_3CN and $CHCl_3$ were dried over CaH_2. All other solvents were ACS reagent grade and used as received. All chemicals were purchased from Sigma-Aldrich, Merck, or Spectrochem and used as received. Thin-layer chromatography (TLC) was performed on a Merck 60 F254 silica gel plate (0.25 mm thickness). Column chromatography was performed on a Merck 60 silica gel (100−200 mesh). Ambient temperature NMR spectra were recorded on a Varian Unity Inova 500 FT NMR (499.42 MHz for ^{1}H, 125.58 MHz

for ^{13}C) spectrometer. Chemical shifts (δ) are given in ppm and are referenced against the solvent signals (^{1}H, ^{13}C). Elemental analyses were performed at Atlantic Microlab (Norcross, GA). Absorbance measurements were taken on a Shimadzu UV-2502PC UV-Vis spectrophotometer against a solvent reference.

Crystallography. All crystallographic measurements were performed at 110(2) K using a Bruker SMART APEX II diffractometer with a CCD area detector (graphite monochromated Mo Kα radiation, λ = 0.71073 Å, ω-scans with a 0.5° step in ω). In each case, a specimen of suitable size and quality was selected and mounted onto a nylon loop. The semiempirical method SADABS[148] was applied for absorption correction. The structures were solved by direct methods and refined by the full-matrix least-squares technique against F^2 with anisotropic temperature parameters for all non-hydrogen atoms. All H atoms were geometrically placed and refined using the riding model approximation. Data reduction and further calculations were performed using the Bruker Apex2 (2013) and SHELXTL[149] program packages. Structural refinements were performed using Olex2.[150]

Table 23. Crystallographic table for **65**-Cl.

Identification code	y_sq	
Empirical formula	C44 H33 Cl3 Ir N4 Sb	
Formula weight	1038.04	
Temperature	110 K	
Wavelength	0.71073 Å	
Crystal system	Monoclinic	
Space group	P 1 21/n 1	
Unit cell dimensions	a = 8.9221(19) Å	α= 90°.
	b = 20.377(4) Å	β= 93.589(2)°.
	c = 24.873(5) Å	γ = 90°.
Volume	4513.2(16) $Å^3$	
Z	4	
Density (calculated)	1.528 Mg/m^3	
Absorption coefficient	3.754 mm^{-1}	
F(000)	2016	
Crystal size	0.12 x 0.11 x 0.05 mm^3	
Theta range for data collection	1.921 to 27.685°.	
Index ranges	-11<=h<=11, -26<=k<=26, -32<=l<=32	
Reflections collected	97361	
Independent reflections	10499 [R(int) = 0.1488]	
Completeness to theta = 25.242°	100.0 %	
Absorption correction	Integration	
Max. and min. transmission	0.7456 and 0.5783	
Refinement method	Full-matrix least-squares on F^2	
Data / restraints / parameters	10499 / 108 / 521	
Goodness-of-fit on F^2	1.089	
Final R indices [I>2sigma(I)]	R1 = 0.0684, wR2 = 0.1381	
R indices (all data)	R1 = 0.1012, wR2 = 0.1500	
Extinction coefficient	n/a	
Largest diff. peak and hole	1.413 and -2.584 $e.Å^{-3}$	

Computational details. Density functional theory (DFT) structural optimizations were conducted using the Gaussian 09 program.[186] In all cases, the structures were optimized using the B3LYP[151-152] functional. In order to optimize the efficiency of our computations while still treating the heavy atoms at a sufficient level of theory, we used the following mixed basis set: Sb/Ir, cc-pVTZ-PP; C/H/N, 6-31g; Cl, 3-21g(d') with effective core potentials for the heavy elements.[154-155] Optimizations with the MPW1PW91 functional and the same basis sets were considered but abandoned because they afforded geometries exhibiting large deviations from the experimental ones. For all optimized structures, frequency calculations were carried out to confirm the absence of imaginary frequencies. TD-DFT calculations were carried out using the B3LYP functional and the SMD solvation model. The molecular orbitals were visualized and plotted using the Jimp2 program.[157-159]

Table 24. Selected X-ray and DFT (gas-phase) metrical parameters (distance in Å and angles in °) for **65**-Cl.

	DFT	X–ray
Sb1–Cl1	2.54846	2.547(2)
Sb1–Cl2	2.5025	2.472(3)
Sb1–Cl3	2.49423	2.370(5)
N1–Ir1	2.15205	2.123(7)
N2–Ir1	2.15861	2.124(7)
C32–Ir1	2.02826	2.001(9)
C21–Ir1	2.02982	2.006(9)
N1–Ir1–N2	76.61108	76.2(3)

Table 25. XYZ coordinates of the optimized geometry of [**64**]$^{+}$.

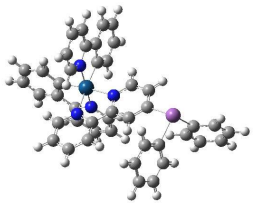

Ir	0.00000000	0.00000000	0.00000000	C	-2.38962231	0.11133898	-1.62011905
Sb	0.00000000	0.00000000	7.08746649	C	-3.76874813	0.03271857	-1.92358118
C	-1.55675345	0.55050923	-3.90965137	H	-4.07432913	0.19983918	-2.78388674
H	-2.41483985	0.58526868	-4.27148953	C	-4.63618903	-0.30335602	-0.93580719
C	3.26637091	2.75993382	6.80656763	H	-5.54283644	-0.34410643	-1.13923209
H	4.13437788	2.68705653	6.48403682	C	-4.23792312	-0.57885654	0.34467511
C	1.74866056	3.92403277	8.05912776	H	-4.84284565	-0.82562146	1.00255578
H	1.50394212	4.69666189	8.50606061	C	-2.89961820	-0.45944393	0.60614352
C	3.03372753	3.77190555	7.38535408	H	-2.60254782	-0.61366217	1.47442482
H	3.65935132	4.46202036	7.40787660	C	-1.03681945	4.23996409	0.17776100
C	2.42176460	1.64576566	6.52771719	H	-1.19794256	4.91524917	-0.43918471
H	2.63701580	0.96135964	5.93720569	C	-1.24803908	4.48078905	1.46106755
C	0.90458550	2.76756198	7.95865394	H	-1.58796989	5.29958730	1.74705543
H	0.08943445	2.75306634	8.40303989	C	-0.94088641	3.46915137	2.37443296
C	1.29306563	1.70235320	7.21889553	H	-1.00097089	3.63136903	3.28957113
C	-0.59214220	3.03447854	-0.26693993	C	-0.54681053	2.22735353	1.91217377
H	-0.44669035	2.90871205	-1.17624915	C	-0.26674282	1.08379777	2.79502804
N	-2.00789926	-0.14563444	-0.32663124	C	-0.29914375	1.10494515	4.17076502
N	-0.35938055	2.00865873	0.60169434	H	-0.48979343	1.90202279	4.60906272
N	-0.08338761	-0.08432599	2.12555133	C	-0.05866506	-0.01332479	4.90784486
C	2.66454638	-1.21689780	-0.07840615	C	0.15330847	-1.18863445	4.24829876
C	4.01392322	-1.32359808	-0.03748139	H	0.30478260	-1.96916000	4.72601491
H	4.42141518	-2.14059362	-0.23110720	C	0.14711280	-1.21377925	2.82483687
C	4.77698051	-0.23498624	0.29301849	H	0.30357770	-2.01380009	2.37767456
H	5.70449812	-0.30119619	0.30674985	C	-1.31190655	-1.65557320	7.33334696
C	4.15238225	0.99766287	0.60681433	C	-2.48122609	-1.71112667	6.61047056
H	4.63648193	1.74611649	0.86404105	H	-2.67512007	-1.03144213	6.00550188
C	2.75456874	0.99628046	0.51255954	C	-3.38643265	-2.76917502	6.76430927
H	2.31737224	1.79713645	0.70260952	H	-4.18655079	-2.79478003	6.28965587
C	1.71374648	-2.28599117	-0.41497565	C	-0.95975719	-2.69368183	8.19156080
C	2.10489719	-3.58368649	-0.67535478	H	-0.14789166	-2.66822400	8.64330987
H	3.00733842	-3.81071463	-0.64822099	C	-3.03378848	-3.78824840	7.66637712
C	1.18577051	-4.54628241	-0.96958811	H	-3.61940441	-4.49413843	7.79518712
H	1.45763545	-5.41938727	-1.12580625	C	-1.82226288	-3.75720735	8.36967753
C	-0.12975633	-4.22054492	-1.04320425	H	-1.60255194	-4.45281998	8.94938742
H	-0.74877222	-4.87363499	-1.27211120	C	0.33845483	-1.93525454	-0.44291546
C	-0.56773687	-2.91761541	-0.77748936	N	2.03505297	0.00000000	0.18420496
H	-1.47472615	-2.71962607	-0.82109189	C	0.84137549	0.60840067	-4.20694936
C	-1.33334163	0.35112945	-2.53808396	H	1.57606189	0.67317709	-4.77103264
C	-0.40621315	0.70582971	-4.71005162	C	1.03189645	0.40997727	-2.83063729
H	-0.51012347	0.87977924	-5.61573836	H	1.90368108	0.37351935	-2.50600781
C	0.01308736	0.27274616	-1.95734133				

Table 26. XYZ coordinates of the optimized geometry of **65**-Cl.

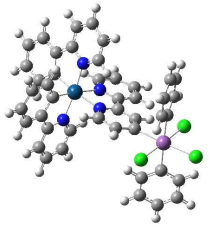

Ir	-2.737201	-0.103754	-0.040279	C	-4.178016	2.399672	-0.577737
N	-2.051849	-0.223925	-2.083674	C	-4.389170	3.774900	-0.746406
Cl	4.355127	0.493340	-2.371685	H	-5.382124	4.129644	-0.984766
C	-2.865302	-0.264783	-3.172638	C	-3.337388	4.671234	-0.602915
H	-3.926957	-0.266395	-2.967701	H	-3.505398	5.733448	-0.731016
Sb	4.504961	0.129115	0.146157	C	-2.061449	4.189091	-0.290282
N	-2.911201	1.941341	-0.271053	H	-1.218283	4.855305	-0.169109
Cl	6.978290	0.431379	0.087192	C	-2.466768	-3.091616	-0.606768
C	-0.973879	-0.278908	-4.649841	H	-2.250305	-2.737845	-1.603396
H	-0.550469	-0.298629	-5.646146	C	-2.461566	-4.442433	-0.299026
C	-0.691777	-0.205125	-2.253705	H	-2.238939	-5.168200	-1.069216
C	0.114333	-0.150303	-1.022658	C	-2.741129	-4.834919	1.015400
C	5.790976	-2.443112	-1.097541	H	-2.741080	-5.883499	1.286063
H	6.504059	-1.733469	-1.495848	C	-3.013656	-3.865901	1.971656
C	5.907205	-3.806638	-1.384718	H	-3.227572	-4.148895	2.992646
H	6.712882	-4.151813	-2.022904	C	-3.010915	-2.506466	1.627686
C	4.997122	-4.720810	-0.847064	C	-3.269768	-1.391740	2.531508
H	5.095441	-5.777960	-1.067633	C	-3.560351	-1.548225	3.897642
C	3.967900	-4.272584	-0.016642	H	-3.609123	-2.536106	4.342805
H	3.268145	-4.979747	0.415503	C	-3.785336	-0.430512	4.692685
C	3.842794	-2.909098	0.271799	H	-4.007409	-0.548171	5.746350
H	3.053948	-2.568405	0.931197	C	-3.722595	0.847981	4.123068
C	-2.359980	-0.295387	-4.465360	H	-3.900023	1.720076	4.743370
H	-3.038686	-0.327798	-5.307116	C	-3.436671	1.010613	2.766419
Cl	4.497674	-0.368891	2.598595	H	-3.401756	2.011495	2.352433
N	-0.593763	-0.106142	0.152334	C	-3.201444	-0.098921	1.934128
C	-0.137315	-0.232277	-3.539100	C	-1.884253	2.823434	-0.131990
H	0.936332	-0.212251	-3.662064	H	-0.920688	2.401621	0.110489
N	-2.735763	-2.137153	0.324863	C	4.300487	2.287863	0.524185
C	1.506678	-0.129688	-1.024321	C	3.870092	3.139661	-0.499250
H	2.055414	-0.135833	-1.956090	H	3.695268	2.745971	-1.491616
C	2.232488	-0.063791	0.174875	C	3.706626	4.505287	-0.242253
C	1.485268	-0.036332	1.365231	H	3.384228	5.164067	-1.041652
H	1.993817	-0.000121	2.320460	C	3.976148	5.020995	1.027003
C	0.093873	-0.059584	1.323105	H	3.857942	6.081467	1.220868
H	-0.506115	-0.039240	2.222840	C	4.753742	-2.000571	-0.273583
C	-4.722508	0.028111	-0.441957	C	4.575224	2.800397	1.796913
C	-5.662391	-1.015280	-0.534721	H	4.909745	2.141830	2.586991
H	-5.351871	-2.035296	-0.339367	C	4.412863	4.167681	2.042752
C	-6.996340	-0.761253	-0.859887	H	4.634630	4.561887	3.028376
H	-7.701595	-1.583493	-0.920499	C	-6.534239	1.601881	-1.015998
C	-7.435931	0.546676	-1.102669	H	-6.879637	2.613234	-1.202002
H	-8.472933	0.736475	-1.352175	C	-5.190344	1.352934	-0.690304

Electrochemistry. Electrochemical experiments were performed with an electrochemical analyzer from CH Instruments (model 610A) with a glassy-carbon working electrode and a platinum auxiliary electrode. The reference electrode was built from a silver wire inserted into a small glass tube fitted with a porous Vycor frit at the tip and filled with a THF solution containing tetrabutylammonium hexafluorophosphate ($TBAPF_6$, 0.1 M) and $AgNO_3$ (0.005 M). All three electrodes were immersed in a deoxygenated DMF solution (5 mL) containing $TBAPF_6$ (0.1 M) as a support electrolyte and platinum complexes ([**64**][PF_6], **65**-Cl and [$(ppy)_2Ir(bpy)$][PF_6] (0.001 M). Ferrocene was used as an internal standard, and all potentials are reported with respect to $E_{1/2}$ of the Fc / Fc^+ redox couple.

Determination of quantum yield.[199, 217] Quantum yields were determined relative to [$(ppy)_2Ir(bpy)$][PF_6] (λ_{ex} = 400 nm) in acetonitrile as a standard (Φ=9.3%).[214] Absorbance measurements were recorded on a Shimadzu UV-2502PC UV-Vis spectrophotometer. Phosphoresence measurements were recorded on samples in capped quartz cuvettes in solutions purged with N_2 using a PTI QuantaMaster spectrofluorometer with entrance and exit slit widths of 2 nm and an integration time of 1 s. Phosphorescence quantum yields were calculated based on the gradients of integrated emission (IE) versus absorbance at λ_{ex} (Abs) for a series of measurements on the sample or fluorescence standard, according to the following equation:

$$\Phi_{sample} = \Phi_{std} \times \frac{IE_{sample}}{IE_{std}} \times \frac{Abs_{std}}{Abs_{sample}} \times \left(\frac{\eta_{sample}}{\eta_{std}}\right)^2$$

$$= \Phi_{std} \times \frac{Grad_{sample}}{Grad_{std}} \times \left(\frac{\eta_{sample}}{\eta_{std}}\right)^2$$

where η was the same for $[(ppy)_2Ir(bpy)][PF_6]$, [**64**][PF_6] and **65**-Cl since all the measurements are in the same solvent (acetonitrile). The data obtained at different concentrations is plotted in Figure 107.

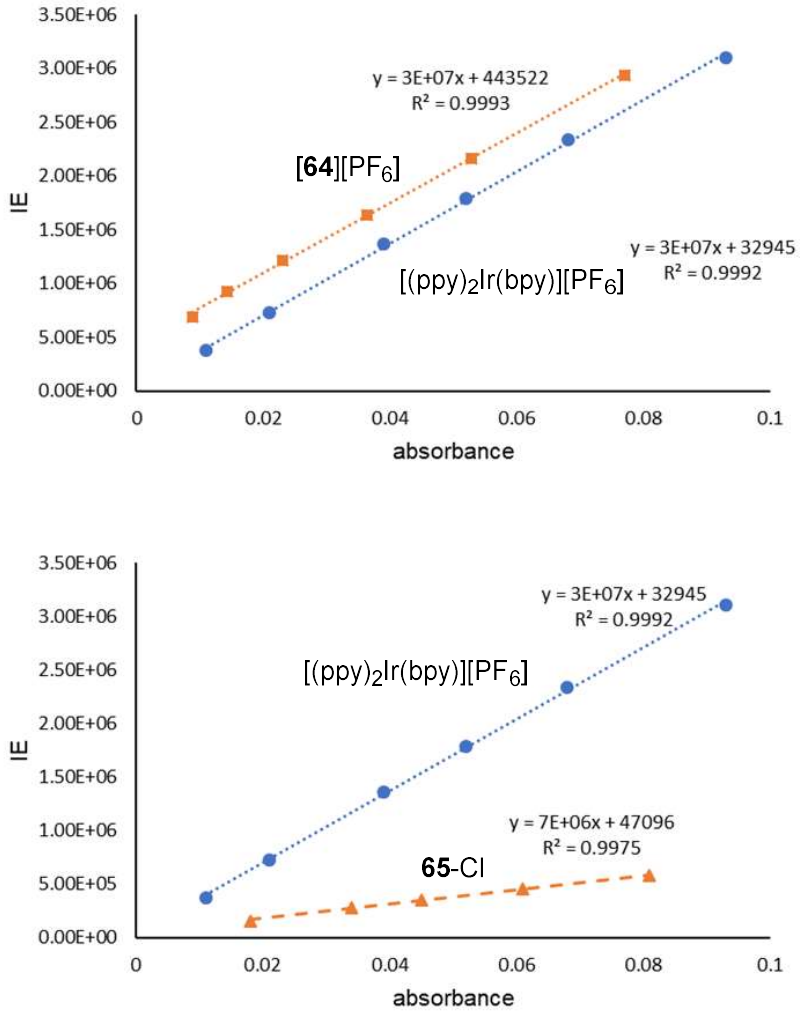

Figure 107. Plots of integrated emission (IE) vs. absorbance at λ_{ex} for [**64**][PF_6] (top), **65**-Cl (bottom) and $[(ppy)_2Ir(bpy)][PF_6]$.

Synthesis of [64][PF_6]. The ligand **54** (150 mg, 0.35 mmol) and $[(ppy)_2Ir(\mu\text{-}Cl)]_2$ (187 mg, 0.17 mmol) were combined in a methanol and dichloromethane mixture (1:1

v/v). The resulting suspension was stirred for 8 h under reflux. The solution was concentrated, and treated with KPF_6 (200 mg, 1.1 mmol). The precipitate was isolated by filtration and washed with water (3 × 5 mL), Et_2O (3 × 3 mL), and dried under vacuum to give a [**64**][PF_6] as a yellow solid. Yield: 309 mg (83%). ^{1}H NMR (499.42 MHz, (CD_3CN) δ 8.59 (s, 1H), 8.27 (d, *J* = 8.1 Hz, 1H), 8.08 – 8.03 (m, 4H), 7.97 (d, *J* = 5.5 Hz, 1H), 7.85 (t, *J* = 7.8 Hz, 2H), 7.82 – 7.76 (m, 3H), 7.61 (dd, *J* = 9.8, 5.8 Hz, 2H), 7.54 – 7.46 (m, 4H), 7.45 – 7.37 (m, 6H), 7.09 – 6.99 (m, 5H), 6.94 – 6.86 (m, 2H), 6.28 – 6.23 (m, 2H). ^{13}C NMR (125.58 MHz, CD_3CN) δ 168.32, 168.29, 156.66, 156.08, 155.41, 151.58, 151.45, 151.15, 150.16, 150.13, 150.04, 144.97, 144.94, 140.20, 139.47, 139.45, 138.15, 137.25, 137.19, 135.89, 132.43, 132.42, 131.30, 131.26, 130.41, 130.40, 130.31, 130.29, 129.24, 125.82, 125.77, 125.40, 124.44, 123.47, 123.44, 120.80. Elemental analysis (%) calculated for $C_{44}H_{33}F_6IrN_4PSb$: C, 49.08; H, 3.09. Found: C, 49.18; H, 3.17.

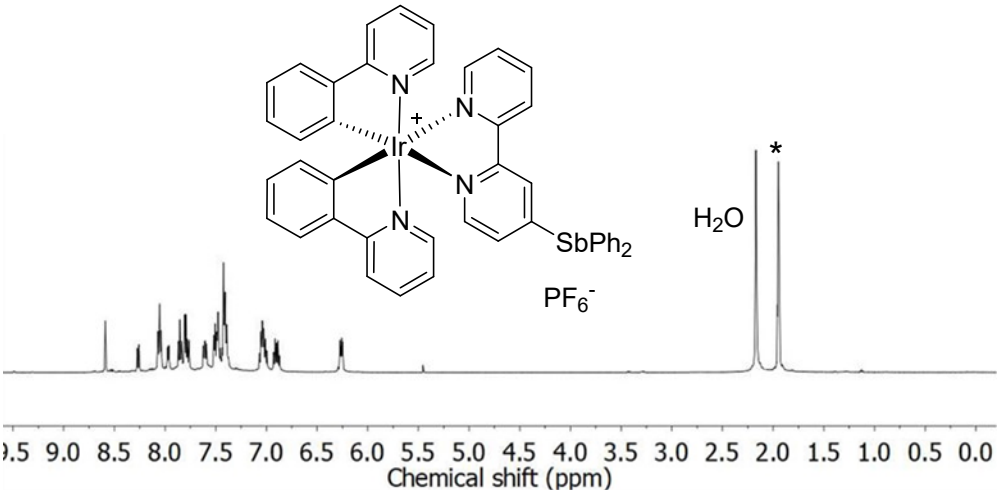

Figure 108. ^{1}H NMR spectrum of [**64**][PF_6] in CD_3CN. The CD_3CN solvent peak has been marked by an asterisk (*).

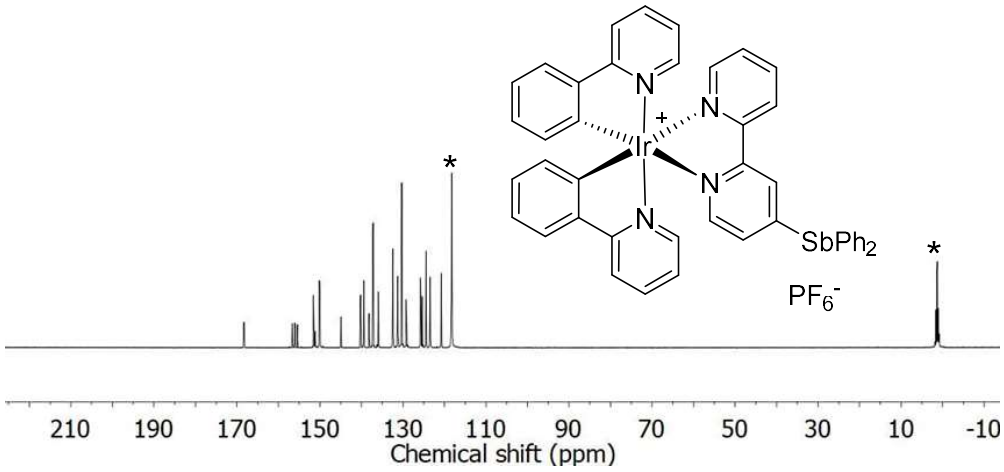

Figure 109. $^{13}C\{^{1}H\}$ NMR spectrum of [**64**][PF_6]in CD_3CN. The CD_3CN solvent peak has been marked by an asterisk (*).

Synthesis of 65-Cl. Complex [**64**][PF_6] (100 mg, 0.09 mmol) was dissolved in DMSO (5mL) and treated with $PhICl_2$ (99 mg, 0.36 mmol) in DMSO (1 mL). The resulting yellow solution was stirred for 3 hour. The solution was extracted with pentane (3× 3 mL) to remove PhI. Next the DMSO solution was treated with portions of diethyl ether (3 × 3 mL). After each addition of diethyl ether, the top layer was removed and discarded, leading to an effective concentration of the bottom DMSO layer. The resulting DMSO solution was treated with dichloromethane (1 mL) and diethyl ether (10 mL) leading to the formation of an orange solid precipitate identified as **65**-Cl. Yield: 69 mg (74%). Single crystals of **65**-Cl suitable for X-ray diffraction were obtained by diffusion of diethyl ether in to a solution of the compound in acetonitrile. ^{1}H NMR (499.42 MHz, CD_3CN) δ 9.20 (s, 1H), 8.60 (d, J = 8.2 Hz, 1H), 8.26 (d, J = 5.6 Hz, 1H), 8.20 (m, 4H), 8.14 (m,*2*H), 8.08 (d, J = 8.3 Hz, 2H), 8.02 (d, J = 5.4 Hz, 1H), 7.90 (m, 2H), 7.82 (d, J = 7.9 Hz, 2H), 7.70 (d, J = 5.7 Hz, 1H), 7.65 (m, 7H), 7.55 (dd, J = 7.5,

5.6 Hz, 1H), 7.06 (m, 4H), 6.93 (t, J = 7.4 Hz, 2H), 6.28 (dd, J = 12.3, 7.5 Hz, 2H).[13]C NMR (125.58 MHz, CD_3CN) δ 168.26, 168.18, 157.12, 156.06, 151.83, 151.60, 150.89, 150.71, 150.44, 150.41, 145.00, 144.90, 143.37, 140.45, 139.66, 139.60, 134.60, 133.88, 133.04, 132.46, 132.36, 131.82, 131.37, 131.35, 130.65, 130.03, 129.82, 128.34, 126.12, 125.86, 124.59, 124.51, 123.67, 123.63, 120.91, 120.88. Elemental analysis (%) calculated for $C_{44}H_{33}Cl_3IrN_4Sb$: C, 50.91; H, 3.20. Found: C, 50.66; H, 3.74.

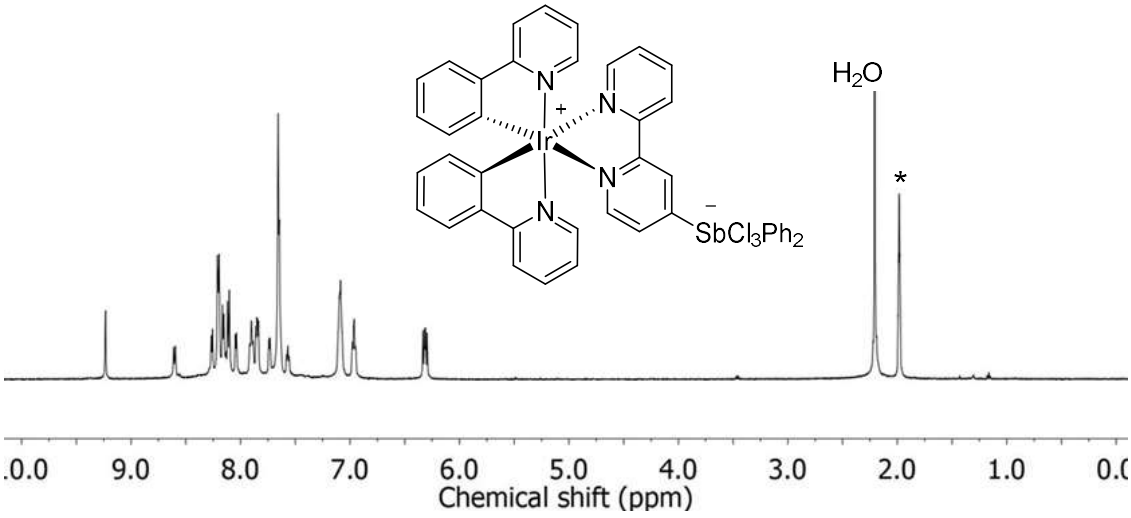

Figure 110. [1]H NMR spectrum of **65**-Cl in CD_3CN. The CD_3CN solvent peak has been marked by an asterisk (*).

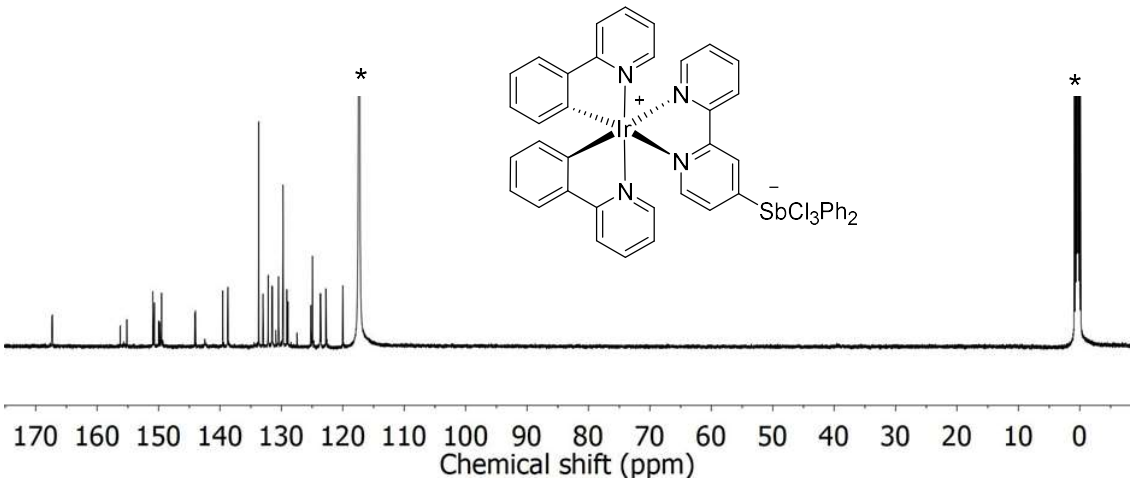

Figure 111. $^{13}C\{^{1}H\}$ NMR spectrum of **65**-Cl in CD_3CN. The CD_3CN solvent peak has been truncated and marked by an asterisk (*).

Generation of [65][OTf]. To a suspension of **65**-Cl (10 mg, 0.01 mmol) in $CDCl_3$ (0.5 mL) was added solid AgOTf (2.6 mg, 0.01 mmol). The yellow precipitate of **2**-Cl dissolved upon stirring while a AgCl precipitated as a white powder. The resulting yellow solution of [**65**][OTf] was analyzed by ^{1}H NMR spectroscopy. ^{1}H NMR (499.42 MHz, $CDCl_3$) δ 9.33 (s, 1H), 8.57 (d, J = 8.0 Hz, 1H), 8.28 (m, 3H), 8.14 (t, J = 7.9 Hz, 1H), 8.11 (d, J = 5.6 Hz, 1H), 7.97 (d, J = 5.3 Hz, 1H), 7.92 (d, J = 8.3 Hz, 2H), 7.78 (t, J = 7.8 Hz, 2H), 7.69 (t, J = 8.3 Hz, 2H), 7.61 (m, 10H), 7.45 (m, 1H), 7.07 (m, 4H), 6.93 (m, 2H), 6.29 (dd, J = 14.7, 7.6 Hz, 2H).

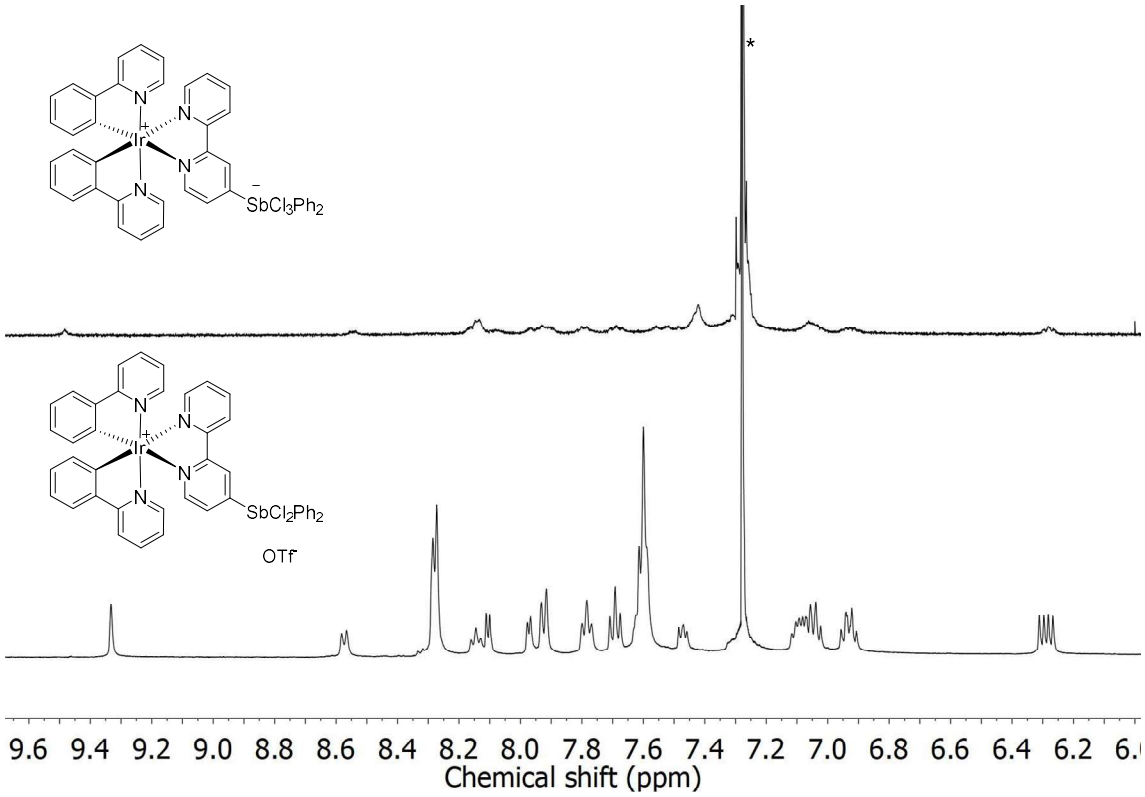

Figure 112. ^{1}H NMR spectrum of **65**-Cl and [**65**][OTf] in $CDCl_3$. The $CDCl_3$ solvent peak has been truncated and marked by an asterisk (*).

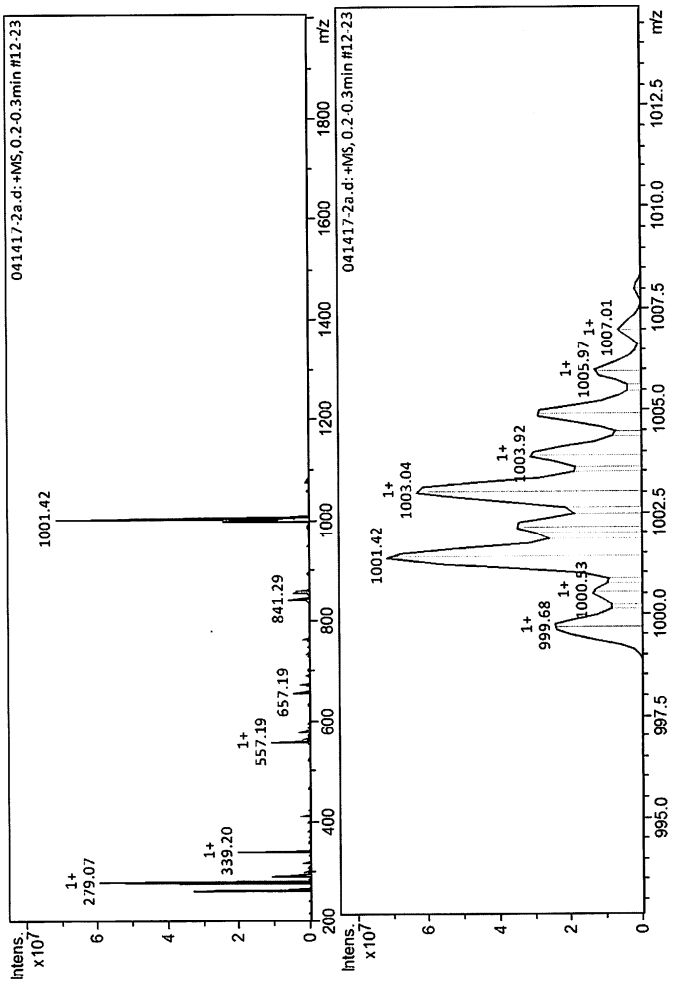

Figure 113. ESI unit mass spectrum of **65**-Cl.

Synthesis of [66][PF_6]$_2$. The ligand **54** (100 mg, 0.23 mmol) and $(phen)_2RuCl_2$ (122 mg, 0.23 mmol) were combined in an ethanol and water mixture (1:1 v/v). The resulting suspension was stirred for 8 h under reflux. The solution was concentrated, and treated with KPF_6 (200 mg, 1.1 mmol). The precipitate was isolated by filtration and washed with water (3 × 5 mL), Et_2O (3 × 3 mL), and dried under vacuum to give a [**66**][PF_6] as an orange solid. Yield: 182 mg (67%). ^{1}H NMR (499.42 MHz, CD_3CN) δ

8.61 (d, J = 1.1 Hz, 1H), 8.56 – 8.47 (m, 5H), 8.29 (d, J = 8.1 Hz, 1H), 8.15 – 7.98 (m, 6H), 7.78 – 7.70 (m, 5H), 7.61 – 7.37 (m, 15H), 7.30 (d, J = 5.6 Hz, 1H).

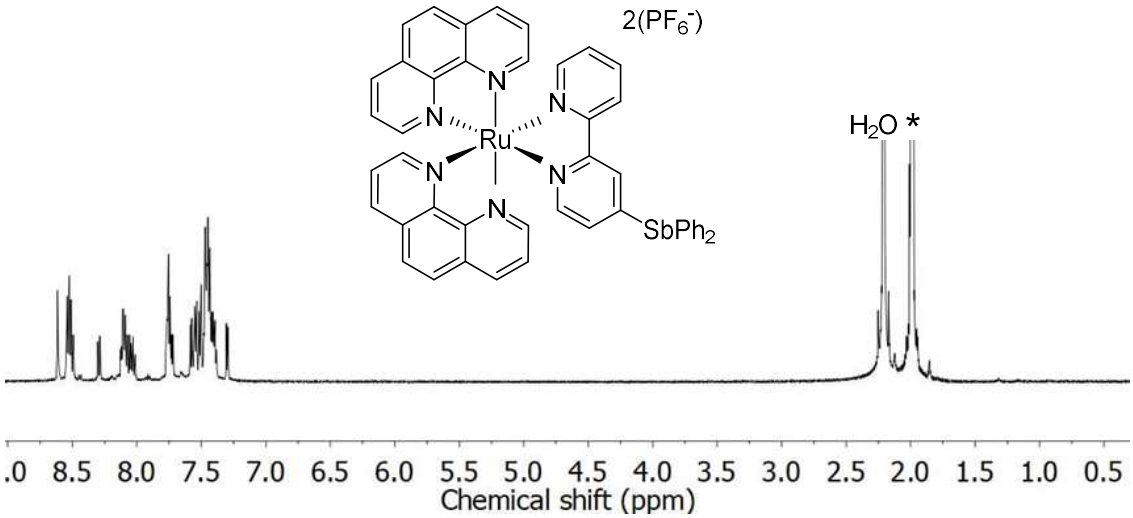

Figure 114. ^{1}H NMR spectrum of [**66**][PF_6]$_2$ in CD_3CN. The CD_3CN solvent peak has been truncated and marked by an asterisk (*).

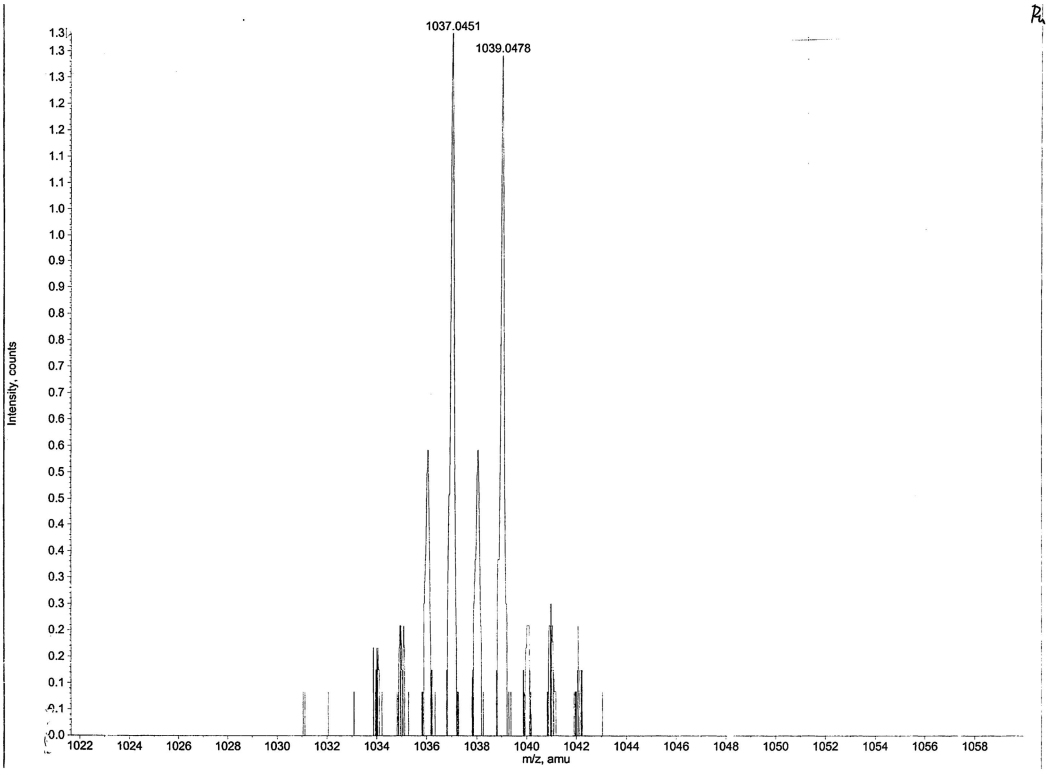

Figure 115. ESI unit mass spectrum of [**66**][PF_6]$_2$.

Synthesis of [67][PF_6]$_2$ or[68][PF_6]. Complex [**66**][PF_6]$_2$ (50 mg, 0.04 mmol) was dissolved in DMSO (3 mL) and treated with $PhICl_2$ (47 mg, 0.17 mmol) in DMSO (1 mL). The resulting yellow solution was stirred for 3 hour. The solution was extracted with pentane (3× 3 mL) to remove PhI. Next the DMSO solution was treated with portions of diethyl ether (3 × 3 mL). After each addition of diethyl ether, the top layer was removed and discarded, leading to an effective concentration of the bottom DMSO layer. The resulting DMSO solution was treated with dichloromethane (1 mL) and diethyl ether (10 mL) leading to the formation of an orange solid precipitate identified as [**67**][PF_6]$_2$ or [**68**][PF_6]. Yield: 20 mg (44% or 48%). ^{1}H NMR (499.42 MHz, CD_3CN) δ

9.23 (s, 1H), 8.72 (d, J = 8.0 Hz, 2H), 8.66 – 8.57 (m, 4H), 8.36 – 8.22 (m, 4H), 8.16 (d, J = 7.9 Hz, 4H), 8.10 – 8.04 (m, 2H), 8.01 (d, J = 5.9 Hz, 1H), 7.92 (d, J = 5.2 Hz, 2H), 7.86 (t, J = 8.0 Hz, 3H), 7.74 (d, J = 5.6 Hz, 1H), 7.63 - 7.53 (m, 6H), 7.35 (t, J = 6.9 Hz, 2H), 7.02 (dd, J = 7.7, 5.9 Hz, 1H). ^{13}C NMR (125.58 MHz, CD_3CN) δ 157.70, 156.80, 153.92, 153.05 (d, J = 8.3 Hz), 152.76, 152.61, 152.43, 152.24, 147.95, 147.78, 147.73, 147.51, 147.39, 137.93, 137.17, 137.08, 136.96, 136.78, 133.58, 131.96, 131.48, 131.12, 131.10, 131.05, 131.01, 130.92, 129.63, 129.56, 128.39, 128.12, 128.07, 127.82, 126.19, 126.10, 126.00 (d, J = 1.8 Hz), 125.90, 124.65, 121.46.

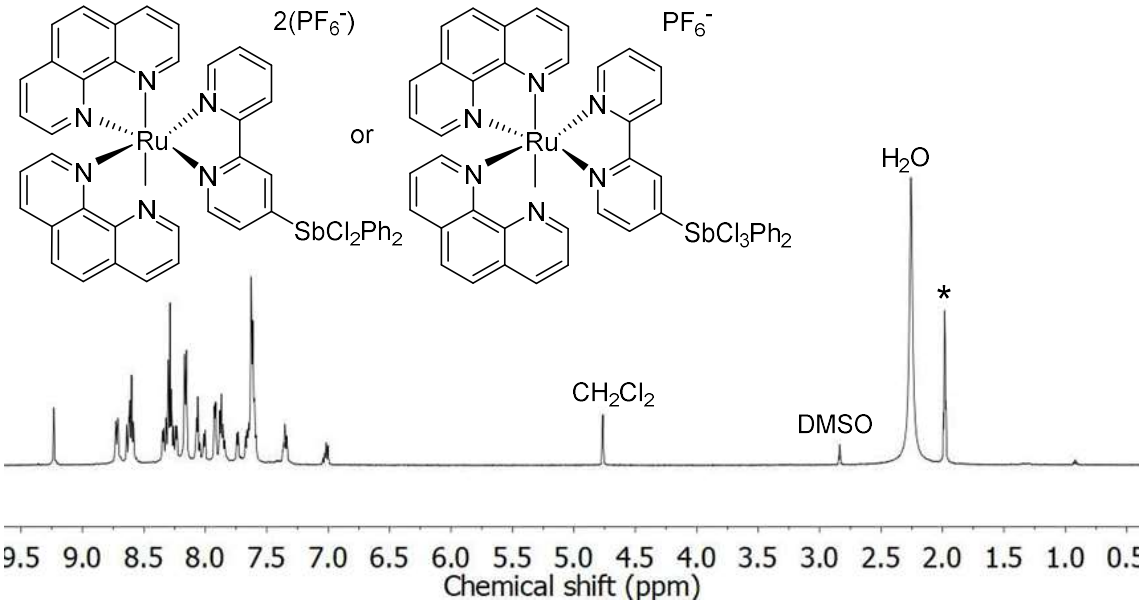

Figure 116. ^{1}H NMR spectrum of **[67]**$[PF_6]_2$ or [**68**]$[PF_6]$ in CD_3CN. The CD_3CN solvent peak has been truncated and marked by an asterisk (*).

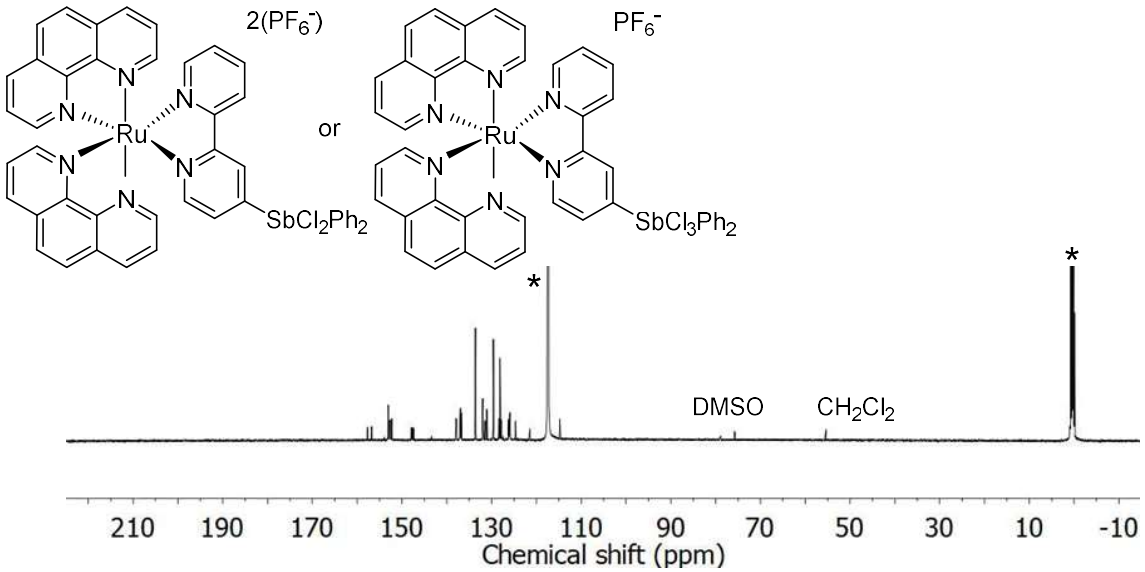

Figure 117. $^{13}C\{^{1}H\}$ NMR spectrum of [**67**][PF_6]$_2$ or [**68**][PF_6] in CD_3CN. The CD_3CN solvent peak has been truncated and marked by an asterisk (*).

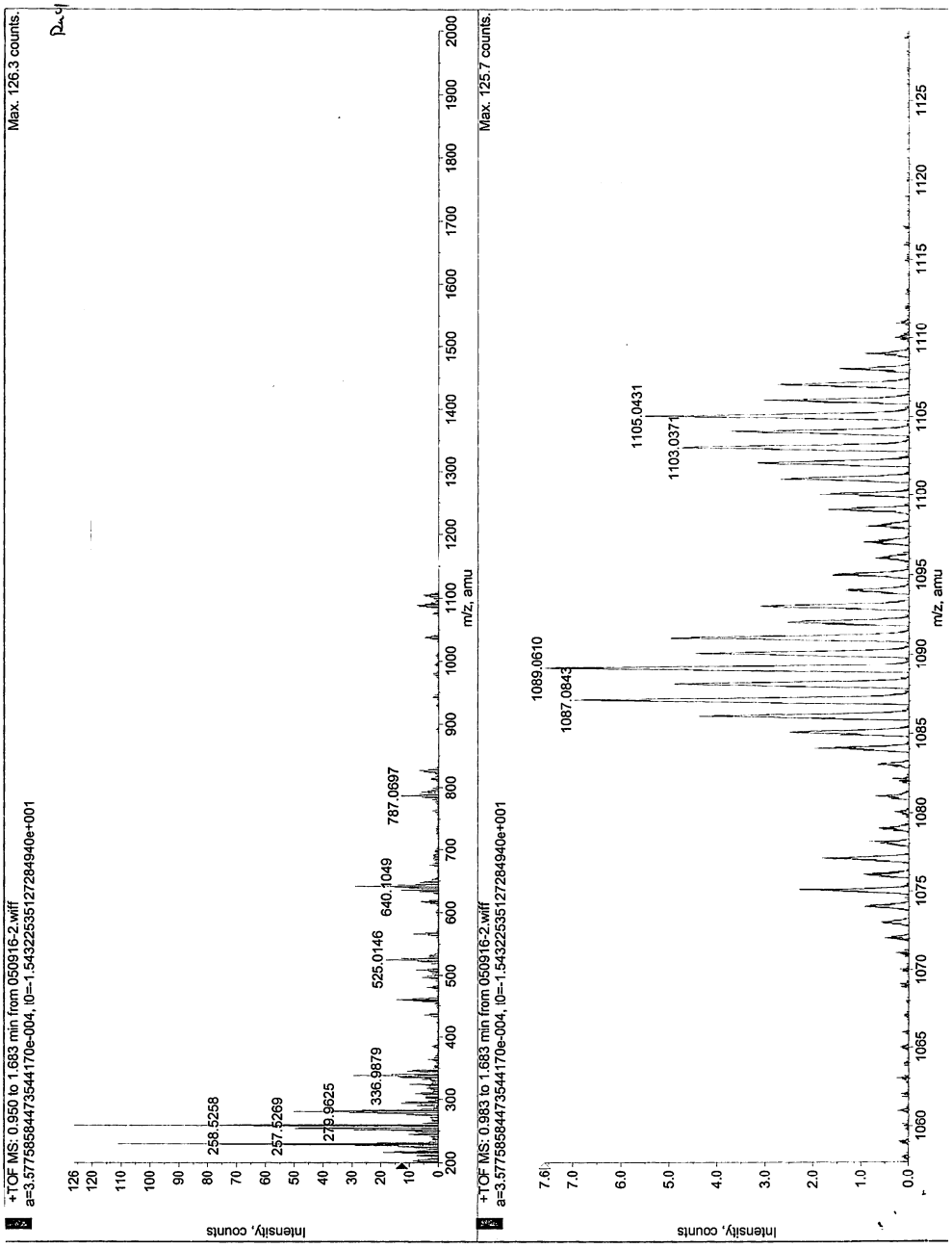

Figure 118. ESI unit mass spectrum of [**67**][PF_6] or [**68**][PF_6].

CHAPTER V

SUMMARY

This thesis has explored the synthesis and properties of antimony-based ligands with the view of exploiting the redox chemistry and variable coordination environment of antimony as a means to influence the properties of coordinated transition metals. Two main ligand architectures referred as **A** and **B** have been investigated (Figure 119). The first one features an antimony atom incorporated in a multidentate scaffold that contains ancillary phosphine arms. These phosphine arms are positioned to hold the coordinated transition metal atom in the immediate vicinity of the antimony atom. The second architecture investigated in this thesis is based on the popular 2,2'-bipyridine ligand with the antimony moiety installed on the outer rim of the chelating ligand.

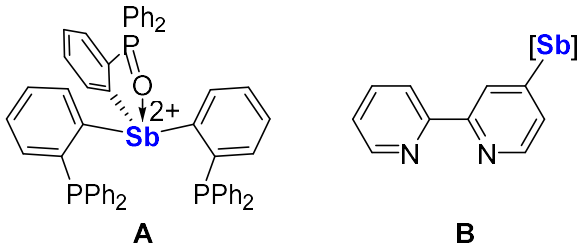

Figure 119. Two types of antimony-based ligands mentioned within.

The two ligand types described above have been successfully coordinated to late transition metals including gold in the case of ligands of type **A** and platinum and iridium in the case of ligands of type **B**. The resulting complexes have been thoroughly characterized and also evaluated as catalysts for reactions that necessitate the activation of an alkenyl or an alkynyl substrate.

The use of ligands of type **A** has enabled the synthesis of gold complexes featuring a gold(I) center directly connected to an antimony(V) dication (Figure 120). This antimony dication acts as a powerful Z-type ligand which drains electron density from the gold(I) center via a direct Au→Sb interaction. The gold center sees its electrophilicity notably increased, a feature that is reflected in the ability of the gold center to activate styrene in both polymerization and hydroamination reactions.

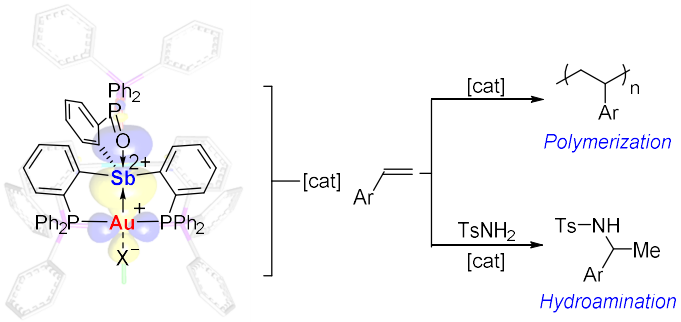

Figure 120. Influence of the ligand type **A** on the catalytic properties of gold complexes.

Ligands of type **B** has been used to synthesize bipyridine platinum complexes featuring a peripheral antimony moiety (Figure 121b). Upon oxidation from III to V, the antimony substituent becomes more electron withdrawing, leading to a more electrophilic complex, as supported by an observed red shift of the MLCT bands, and an anodic shift of the bipyridine reduction potential. These changes are concomitant with a higher catalytic activity of the platinum center in the hydroarylation of ethyl propiolate by mesitylene. The same ligand forms cyclometalated iridium(III) bipyridine complexes. Upon oxidation and chloride binding to the antimony center, an anionic antimonate

substituent is generated. Tha antimonate group increases electron density of the iridium complex and facilitates the oxidation of the iridium center

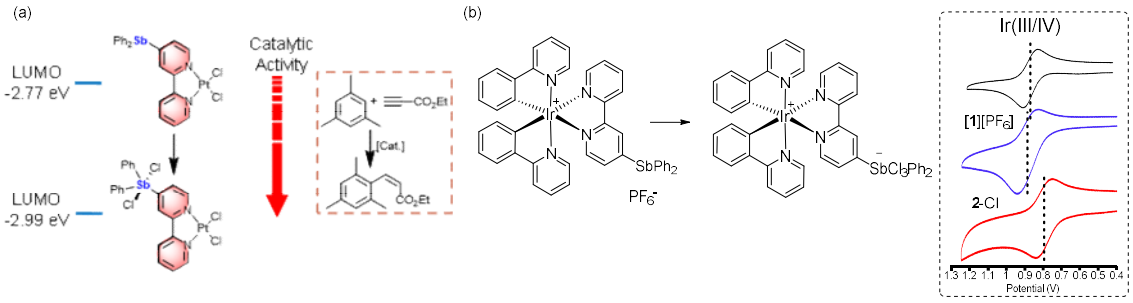

Figure 121. Influence of the ligand type **B** on the electronic and/or reactivity of platinum and iridium complexes.

We demonstrate that the antimony-based ligands can be used to coordinate to transition metal centers in two different architectures. Both of them are able to function as a handle to modulate the electronic property and reactivity of the coordinated transition metal by oxidizing the antimony center and by altering its coordination environment. The dicationic antimony Z-type ligand (type **A**) and antimony(V) substituted bipyridine ligand (type **B**) can effectively enhance the electrophilicity and hence the catalytic activity of the transition metal center in these complexes.

REFERENCES

1. Lewis, G. N., *Valence and the structure of atoms and molecules*. Dover Publications: New York, 1966.
2. Weicker, S. A.; Stephan, D. W., *Bull. Chem. Soc. Jpn.* **2015,** *88* (8), 1003-1016.
3. Ishihara, K. In *Chiral B(III) Lewis acids*, Wiley-VCH Verlag GmbH: 2000; pp 135-190.
4. Ishihara, K. In *Achiral B(III) Lewis acids*, Wiley-VCH Verlag GmbH: 2000; pp 89-133.
5. Ishihara, K.; Yamamoto, H., *Eur. J. Org. Chem.* **1999,** (3), 527-538.
6. Yao, M.-L.; Kabalka, G. W. In *Organic synthesis using boron and organoboron halides*, CRC Press: 2012; pp 579-621.
7. Chen, E. Y.-X.; Marks, T. J., *Chem. Rev.* **2000,** *100* (4), 1391-1434.
8. Erker, G., *Chem. Commun.* **2003,** (13), 1469-1476.
9. Simocko, C.; Wagener, K. B., *Organometallics* **2013,** *32* (9), 2513-2516.
10. Sivaev, I. B.; Bregadze, V. I., *Coord. Chem. Rev.* **2014,** *270–271*, 75-88.
11. Li, Y.-Q.; Wang, P.; Liu, H.; Lu, Y.; Zhao, X.-L.; Liu, Y., *Green Chemistry* **2016,** *18* (6), 1798-1806.
12. Córdoba, R.; Plumet, J., *Tetrahedron Lett.* **2003,** *44* (32), 6157-6159.
13. Gutmann, V.; Hubacek, H.; Steininger, A., *Monatsh. Chem.* **1964,** *95* (3), 678-86.
14. Krossing, I.; Raabe, I., *Chem. Eur. J.* **2004,** *10* (20), 5017-5030.
15. Piers, W. E.; Chivers, T., *Chem. Soc. Rev.* **1997,** *26* (5), 345-354.
16. Hirai, M.; Gabbaï, F. P., *Chemical Science* **2014,** *5* (5), 1886-1893.
17. Tofan, D.; Gabbaï, F. P., *Chemical Science* **2016,** *7*, 6768-6778.
18. Hirai, M.; Gabbaï, F. P., *Angew. Chem. Int. Ed.* **2015,** *54* (4), 1205-1209.
19. Hudnall, T. W.; Kim, Y.-M.; Bebbington, M. W. P.; Bourissou, D.; Gabbaï, F. P., *J. Am. Chem. Soc.* **2008,** *130* (33), 10890-10891.
20. Zhao, H. Y.; Gabbaï, F. P., *Nature Chem.* **2010,** *2* (11), 984-990.
21. Caputo, C. B.; Hounjet, L. J.; Dobrovetsky, R.; Stephan, D. W., *Science* **2013,** *341* (6152), 1374-7.
22. Yi, W.; Tan, N., *Acta Crystallogr., Sect. E* **2011,** *67* (7), m917.
23. Ohkata, K.; Takemoto, S.; Ohnishi, M.; Akiba, K.-Y., *Tetrahedron Lett.* **1989,** *30* (36), 4841-4844.
24. Althaus, H.; Breunig, H. J.; Lork, E., *Organometallics* **2001,** *20* (3), 586-589.
25. Copolovici, D.; Isaia, F.; Breunig, H. J.; Raţ, C. I.; Silvestru, C., *RSC Advances* **2014,** *4* (51), 26569-26576.
26. Bouhadir, G.; Bourissou, D., Coordination of Lewis acids to transition metals: Z-type ligands. In *Struct. Bond.*, 2017; Vol. 171, pp 141-201.
27. Kameo, H.; Nakazawa, H., *Chem. Rec.* **2017,** *17* (3), 268-286.
28. Amgoune, A.; Bourissou, D., *Chem. Commun.* **2011,** *47* (3), 859-871.
29. Green, M. L. H., *J. Organomet. Chem.* **1995,** *500* (1-2), 127-48.
30. Werner, H., *Angew. Chem. Int. Ed. Engl.* **1983,** *22* (12), 927-949.
31. Shriver, D. F., *J. Am. Chem. Soc.* **1963,** *85* (21), 3509-10.
32. Shriver, D. F., *Acc. Chem. Res.* **1970,** *3* (7), 231-8.

33. Shriver, D. F.; Sailor, M. J., *Acc. Chem. Res.* **1988,** *21* (10), 374-9.
34. Fischer, R. A.; Miehr, A.; Hoffmann, H.; Rogge, W.; Boehme, C.; Frenking, G.; Herdtweck, E., *Z. Anorg. Allg. Chem.* **1999,** *625* (9), 1466-1474.
35. Leiner, E.; Hampe, O.; Scheer, M., *Eur. J. Inorg. Chem.* **2002,** *2002* (3), 584-590.
36. Burlitch, J. M.; Leonowicz, M. E.; Petersen, R. B.; Hughes, R. E., *Inorg. Chem.* **1979,** *18* (4), 1097-1105.
37. Cokoja, M.; Gemel, C.; Steinke, T.; Schröder, F.; Fischer, R. A., *Dalton Transactions* **2005,** (1), 44-54.
38. Golden, J. T.; Peterson, T. H.; Holland, P. L.; Bergman, R. G.; Andersen, R. A., *J. Am. Chem. Soc.* **1998,** *120* (1), 223-224.
39. Steinke, T.; Gemel, C.; Cokoja, M.; Winter, M.; Fischer, R. A., *Dalton Transactions* **2005,** (1), 55-62.
40. Braunschweig, H.; Gruss, K.; Radacki, K., *Angew. Chem. Int. Ed.* **2007,** *46* (41), 7782-7784.
41. Braunschweig, H.; Gruss, K.; Radacki, K., *Inorg. Chem.* **2008,** *47* (19), 8595-8597.
42. Braunschweig, H.; Gruss, K.; Radacki, K., *Inorg. Chem.* **2008,** *47* (19), 8595-8597.
43. Hill, A. F.; Owen, G. R.; White, A. J. P.; Williams, D. J., *Angew. Chem. Int. Ed.* **1999,** *38* (18), 2759-2761.
44. Bontemps, S.; Bouhadir, G.; Miqueu, K.; Bourissou, D., *J. Am. Chem. Soc.* **2006,** *128* (37), 12056-12057.
45. Bontemps, S.; Gornitzka, H.; Bouhadir, G.; Miqueu, K.; Bourissou, D., *Angew. Chem. Int. Ed.* **2006,** *45* (10), 1611-1614.
46. Bontemps, S.; Bouhadir, G.; Dyer, P. W.; Miqueu, K.; Bourissou, D., *Inorg. Chem.* **2007,** *46* (13), 5149-5151.
47. Bontemps, S.; Sircoglou, M.; Bouhadir, G.; Puschmann, H.; Howard, J. A. K.; Dyer, P. W.; Miqueu, K.; Bourissou, D., *Chem. Eur. J.* **2008,** *14* (2), 731-740.
48. Sircoglou, M.; Bontemps, S.; Bouhadir, G.; Saffon, N.; Miqueu, K.; Gu, W.; Mercy, M.; Chen, C.-H.; Foxman, B. M.; Maron, L.; Ozerov, O. V.; Bourissou, D., *J. Am. Chem. Soc.* **2008,** *130* (49), 16729-16738.
49. Ke, I.-S.; Gabbaï, F. P., *Inorg. Chem.* **2013,** *52* (12), 7145-7151.
50. Wade, C. R.; Ke, I.-S.; Gabbaï, F. P., *Angew. Chem. Int. Ed.* **2012,** *51* (2), 478-481.
51. Ke, I.-S.; Jones, J. S.; Gabbaï, F. P., *Angew. Chem. Int. Ed.* **2014,** *53* (10), 2633-2637.
52. Jones, J. S.; Wade, C. R.; Gabbaï, F. P., *Angew. Chem. Int. Ed.* **2014,** *53* (34), 8876-8879.
53. Jones, J. S.; Gabbaï, F. P., *Chemistry – A European Journal* **2017,** *23* (5), 1136-1144.
54. Jones, J. S.; Wade, C. R.; Yang, M.; Gabbaï, F. P., *Dalton Transactions* **2017,** *46* (17), 5598-5604.

55. Benjamin, S. L.; Levason, W.; Reid, G.; Warr, R. P., *Organometallics* **2012,** *31* (3), 1025-1034.
56. Benjamin, S. L.; Levason, W.; Light, M. E.; Reid, G.; Rogers, S. M., *Organometallics* **2014,** *33* (11), 2693-2695.
57. Jones, J. S.; Wade, C. R.; Gabbaï, F. P., *Organometallics* **2015,** *34* (11), 2647-2654.
58. Jolleys, A.; Lake, B. R. M.; Krämer, T.; Benjamin, S. L., *Organometallics* **2018,** *37* (21), 3854-3862.
59. Plajer, A. J.; Colebatch, A. L.; Rizzuto, F. J.; Pröhm, P.; Bond, A. D.; García-Rodríguez, R.; Wright, D. S., *Angew. Chem. Int. Ed.* **2018,** *57* (22), 6648-6652.
60. Jones, J. S.; Gabbaï, F. P., *Acc. Chem. Res.* **2016,** *49* (5), 857-867.
61. Yang, H.; Gabbaï, F. P., *J. Am. Chem. Soc.* **2015,** *137* (41), 13425-13432.
62. You, D.; Yang, H.; Sen, S.; Gabbaï, F. P., *J. Am. Chem. Soc.* **2018,** *140* (30), 9644-9651.
63. Khusnutdinova, J. R.; Milstein, D., *Angew. Chem. Int. Ed.* **2015,** *54* (42), 12236-12273.
64. Grützmacher, H., *Angew. Chem. Int. Ed.* **2008,** *47* (10), 1814-1818.
65. Jones, J. S.; Gabbai, F. P., *Chem. Eur. J.* **2017,** *23* (5), 1136-1144.
66. You, D.; Gabbaï, F. P., *J. Am. Chem. Soc.* **2017,** *139* (20), 6843-6846.
67. Fox, B. J.; Millard, M. D.; DiPasquale, A. G.; Rheingold, A. L.; Figueroa, J. S., *Angew. Chem. Int. Ed.* **2009,** *48* (19), 3473-3477.
68. Barnett, B. R.; Figueroa, J. S., *Chem. Commun.* **2016,** *52* (96), 13829-13839.
69. Barnett, B. R.; Moore, C. E.; Chandrasekaran, P.; Sproules, S.; Rheingold, A. L.; DeBeer, S.; Figueroa, J. S., *Chemical Science* **2015,** *6* (12), 7169-7178.
70. Takaya, J.; Iwasawa, N., *J. Am. Chem. Soc.* **2017,** *139* (17), 6074-6077.
71. Steinhoff, P.; Steinbock, R.; Friedrich, A.; Schieweck, B. G.; Cremer, C.; Truong, K.-N.; Tauchert, M. E., *Dalton Transactions* **2018,** *47* (31), 10439-10442.
72. Fernández-Hernández, J. M.; Beltrán, J. I.; Lemaur, V.; Gálvez-López, M.-D.; Chien, C.-H.; Polo, F.; Orselli, E.; Fröhlich, R.; Cornil, J.; De Cola, L., *Inorg. Chem.* **2013,** *52* (4), 1812-1824.
73. Choy, W. C. H.; Chan, W. K.; Yuan, Y., *Adv. Mater.* **2014,** *26* (31), 5368-5399.
74. Rothe, C., Chiang, C. , Jankus, V. , Abdullah, K. , Zeng, X. , Jitchati, R. , Batsanov, A. S., Bryce, M. R. and Monkman, A. P., *Adv. Funct. Mater.* **2009,** *19* (13), 2038-2044.
75. Costa, R. D.; Ortí, E.; Bolink, H. J.; Graber, S.; Schaffner, S.; Neuburger, M.; Housecroft, C. E.; Constable, E. C., *Adv. Funct. Mater.* **2009,** *19* (21), 3456-3463.
76. Margapoti, E.; Shukla, V.; Valore, A.; Sharma, A.; Dragonetti, C.; Kitts, C. C.; Roberto, D.; Murgia, M.; Ugo, R.; Muccini, M., *J. Phys. Chem. C* **2009,** *113* (28), 12517-12522.
77. Fan, C.; Zhu, L.; Jiang, B.; Li, Y.; Zhao, F.; Ma, D.; Qin, J.; Yang, C., *J. Phys. Chem. C* **2013,** *117* (37), 19134-19141.
78. Kang, D. M.; Kang, J.-W.; Park, J. W.; Jung, S. O.; Lee, S.-H.; Park, H.-D.; Kim, Y.-H.; Shin, S. C.; Kim, J.-J.; Kwon, S.-K., *Adv. Mater.* **2008,** *20* (10), 2003-2007.

79. Rai, V. K.; Nishiura, M.; Takimoto, M.; Zhao, S.; Liu, Y.; Hou, Z., *Inorg. Chem.* **2012,** *51* (2), 822-835.
80. Kozhevnikov, V. N.; Zheng, Y.; Clough, M.; Al-Attar, H. A.; Griffiths, G. C.; Abdullah, K.; Raisys, S.; Jankus, V.; Bryce, M. R.; Monkman, A. P., *Chem. Mater.* **2013,** *25* (11), 2352-2358.
81. ten Brink, G.-J.; Arends, I. W. C. E.; Hoogenraad, M.; Verspui, G.; Sheldon, R. A., *Adv. Synth. Catal.* **2003,** *345* (4), 497-505.
82. Archer, S. A.; Keane, T.; Delor, M.; Bevon, E.; Auty, A. J.; Chekulaev, D.; Sazanovich, I. V.; Towrie, M.; Meijer, A. J. H. M.; Weinstein, J. A., *Chemistry – A European Journal* **2017,** *23* (72), 18239-18251.
83. Clauti, G.; Zassinovich, G.; Mestroni, G., *Inorg. Chim. Acta* **1986,** *112* (2), 103-106.
84. Reveco, P.; Cherry, W. R.; Medley, J.; Garber, A.; Gale, R. J.; Selbin, J., *Inorg. Chem.* **1986,** *25* (11), 1842-1845.
85. Skórka, Ł.; Filapek, M.; Zur, L.; Małecki, J. G.; Pisarski, W.; Olejnik, M.; Danikiewicz, W.; Krompiec, S., *J. Phys. Chem. C* **2016,** *120* (13), 7284-7294.
86. Wu, S.-H.; Ling, J.-W.; Lai, S.-H.; Huang, M.-J.; Cheng, C. H.; Chen, I. C., *The Journal of Physical Chemistry A* **2010,** *114* (38), 10339-10344.
87. Schwartz, K. R.; Chitta, R.; Bohnsack, J. N.; Ceckanowicz, D. J.; Miró, P.; Cramer, C. J.; Mann, K. R., *Inorg. Chem.* **2012,** *51* (9), 5082-5094.
88. Ladouceur, S.; Fortin, D.; Zysman-Colman, E., *Inorg. Chem.* **2011,** *50* (22), 11514-11526.
89. Chirdon, D. N.; McCusker, C. E.; Castellano, F. N.; Bernhard, S., *Inorg. Chem.* **2013,** *52* (15), 8795-8804.
90. Christianson, A. M.; Gabbaï, F. P., *J. Organomet. Chem.* **2017,** *847*, 154-161.
91. Wade, C. R.; Gabbaï, F. P., *Inorg. Chem.* **2010,** *49* (2), 714-720.
92. McKeown, B. A.; Gonzalez, H. E.; Friedfeld, M. R.; Brosnahan, A. M.; Gunnoe, T. B.; Cundari, T. R.; Sabat, M., *Organometallics* **2013,** *32* (9), 2857-2865.
93. Shriver, D. F., *Acc. Chem. Res.* **1970,** *3* (7), 231-238.
94. Parkin, G., *Organometallics* **2006,** *25* (20), 4744-4747.
95. Hill, A. F., *Organometallics* **2006,** *25* (20), 4741-4743.
96. Bouhadir, G.; Amgoune, A.; Bourissou, D., *Adv. Organomet. Chem.* **2010,** *58*, 1-107.
97. Amgoune, A.; Bourissou, D., *Chem. Commun.* **2011,** *47* (3), 859-871.
98. Braunschweig, H.; Dewhurst, R. D., *Dalton Trans.* **2011,** *40*, 549-558.
99. Owen, G. R., *Chem. Soc. Rev.* **2012,** *41* (9), 3535-3546.
100. Kameo, H.; Nakazawa, H., *Chemistry – An Asian Journal* **2013,** *8* (8), 1720-1734.
101. Jones, J. S.; Gabbaï, F. P., *Chem. Lett.* **2016,** *45* (4), 376-384.
102. Devillard, M.; Bouhadir, G.; Bourissou, D., *Angew. Chem. Int. Ed.* **2015,** *54* (3), 730-732.
103. Bouhadir, G.; Bourissou, D., *Chem. Soc. Rev.* **2016,** *45* (4), 1065-1079.
104. Bouhadir, G.; Bourissou, D., Coordination of Lewis Acids to Transition Metals: Z-Type Ligands. In *The Chemical Bond III*, Mingos, D. M. P., Ed. 2017; pp 141-201.

105. Harman, W. H.; Peters, J. C., *J. Am. Chem. Soc.* **2012,** *134* (11), 5080-5082.
106. Anderson, J. S.; Rittle, J.; Peters, J. C., *Nature* **2013,** *501* (7465), 84-87.
107. Inagaki, F.; Matsumoto, C.; Okada, Y.; Maruyama, N.; Mukai, C., *Angew. Chem. Int. Ed.* **2015,** *54* (3), 818-822.
108. Schindler, T.; Lux, M.; Peters, M.; Scharf, L. T.; Osseili, H.; Maron, L.; Tauchert, M. E., *Organometallics* **2015,** *34* (10), 1978-1984.
109. Inagaki, F.; Nakazawa, K.; Maeda, K.; Koseki, T.; Mukai, C., *Organometallics* **2017,** *36* (16), 3005-3008.
110. Steinhoff, P.; Paul, M.; Schroers, J. P.; Tauchert, M. E., *Dalton Transactions* **2019,** *48* (3), 1017-1022.
111. Cammarota, R. C.; Clouston, L. J.; Lu, C. C., *Coord. Chem. Rev.* **2017,** *334*, 100-111.
112. Ramirez, B. L.; Sharma, P.; Eisenhart, R. J.; Gagliardi, L.; Lu, C. C., *Chemical Science* **2019,** *10* (11), 3375-3384.
113. Cammarota, R. C.; Lu, C. C., *J. Am. Chem. Soc.* **2015,** *137* (39), 12486-12489.
114. Sen, S.; Ke, I.-S.; Gabbaï, F. P., *Organometallics* **2017,** *36* (21), 4224-4230.
115. Hudnall, T. W.; Chiu, C.-W.; Gabbaï, F. P., *Acc. Chem. Res.* **2009,** *42* (2), 388-397.
116. Bayne, J. M.; Stephan, D. W., *Chem. Soc. Rev.* **2016,** *45* (4), 765-774.
117. Chitnis, S. S.; Sparkes, H. A.; Annibale, V. T.; Pridmore, N. E.; Oliver, A. M.; Manners, I., *Angew. Chem. Int. Ed.* **2017,** *56* (32), 9536-9540.
118. Robertson, A. P. M.; Burford, N.; McDonald, R.; Ferguson, M. J., *Angew. Chem. Int. Ed.* **2014,** *53* (13), 3480-3483.
119. Robertson, A. P. M.; Chitnis, S. S.; Jenkins, H. A.; McDonald, R.; Ferguson, M. J.; Burford, N., *Chemistry – A European Journal* **2015,** *21* (21), 7902-7913.
120. Wade, C. R.; Gabbaï, F. P., *Angew. Chem. Int. Ed.* **2011,** *50*, 7369-7372.
121. CCDC 1905863 ([**2a**][Cl]) and 1905864 ([**3**][NTf_2]$_2$) contain the supplementary crystallographic data for this paper. These data can be obtained free of charge from The Cambridge Crystallographic Data Centre via www.ccdc.cam.ac.uk/data_request/cif.
122. Jia, M.; Bandini, M., *ACS Catalysis* **2015,** *5* (3), 1638-1652.
123. Mézailles, N.; Ricard, L.; Gagosz, F., *Org. Lett.* **2005,** *7* (19), 4133-4136.
124. Emre Hanhan, M., *Gold Bulletin* **2011,** *44* (1), 43-47.
125. Cinellu, M. A.; Maiore, L.; Minghetti, G.; Cocco, F.; Stoccoro, S.; Zucca, A.; Manassero, M.; Manassero, C., *Organometallics* **2009,** *28* (24), 7015-7024.
126. Hashmi, A. S. K.; Schäfer, S.; Göker, V.; Eisenbach, C. D.; Dirnberger, K.; Zhao-Karger, Z.; Crewdson, P., *Aust. J. Chem.* **2014,** *67* (3), 500-506.
127. Urbano, J.; Hormigo, A. J.; de Frémont, P.; Nolan, S. P.; Díaz-Requejo, M. M.; Pérez, P. J., *Chem. Commun.* **2008,** (6), 759-761.
128. Alcarazo, M., *Acc. Chem. Res.* **2016,** *49* (9), 1797-1805.
129. Dube, J. W.; Zheng, Y.; Thiel, W.; Alcarazo, M., *J. Am. Chem. Soc.* **2016,** *138* (21), 6869-6877.
130. Zhang, J.; Yang, C.-G.; He, C., *J. Am. Chem. Soc.* **2006,** *128* (6), 1798-1799.
131. Giner, X.; Nájera, C., *Org. Lett.* **2008,** *10* (14), 2919-2922.
132. Hammett, L. P., *J. Am. Chem. Soc.* **1937,** *59* (1), 96-103.

133. Hansch, C.; Leo, A.; Taft, R. W., *Chem. Rev.* **1991,** *91* (2), 165-195.
134. Wu, C.-Y.; Horibe, T.; Jacobsen, C. B.; Toste, F. D., *Nature* **2015,** *517* (7535), 449-454.
135. Reiner, B. R.; Bezpalko, M. W.; Foxman, B. M.; Wade, C. R., *Organometallics* **2016,** *35* (17), 2830-2835.
136. Homs, A.; Escofet, I.; Echavarren, A. M., *Org. Lett.* **2013,** *15* (22), 5782-5785.
137. Homs, A.; Obradors, C.; Lebœuf, D.; Echavarren, A. M., *Adv. Synth. Catal.* **2014,** *356* (1), 221-228.
138. Biasiolo, L.; Trinchillo, M.; Belanzoni, P.; Belpassi, L.; Busico, V.; Ciancaleoni, G.; D'Amora, A.; Macchioni, A.; Tarantelli, F.; Zuccaccia, D., *Chemistry – A European Journal* **2014,** *20* (45), 14594-14598.
139. Patil, R. D.; Joshi, G.; Adimurthy, S., *Monatshefte für Chemie - Chemical Monthly* **2010,** *141* (10), 1093-1099.
140. Haldar, S.; Koner, S., *The Journal of Organic Chemistry* **2010,** *75* (17), 6005-6008.
141. Yadav, J. S.; Reddy, B. V. S.; Sengupta, S.; Biswas, S. K., *Synthesis* **2009,** *2009* (08), 1301-1304.
142. Lin, L.; Zhang, G.; Kodama, K.; Yasutake, M.; Hirose, T., *J. Polym. Sci., Part A: Polym. Chem.* **2015,** *53* (17), 2050-2058.
143. Lin, L.; Zhang, G.; Kodama, K.; Shitara, H.; Hirose, T., *J. Polym. Sci., Part A: Polym. Chem.* **2016,** *54* (6), 861-870.
144. Pahadi, N. K.; Tunge, J. A., *Synlett* **2009,** *2009* (19), 3135-3138.
145. Couce-Rios, A.; Lledós, A.; Ujaque, G., *Chemistry – A European Journal* **2016,** *22* (27), 9311-9320.
146. Khusnutdinov, R. I.; Shchadneva, N. A.; Khisamova, L. F.; Dzhemilev, U. M., *Russ. J. Org. Chem.* **2011,** *47* (2), 155-160.
147. Hasegawa, K.-I.; Asami, R., *Journal of Polymer Science: Polymer Chemistry Edition* **1978,** *16* (6), 1449-1458.
148. Sheldrick, G. M. *SADABS, Version 2007/4*, Bruker Analytical X-ray Systems Inc.: Madison, Wisconsin, USA, 2007.
149. Sheldrick, G. M., SHELXTL-2008/4, *Structure Determination Software Suite*, Bruker AXS, Madison, Wisconsin, USA, 2008.
150. Dolomanov, O. V.; Bourhis, L. J.; Gildea, R. J.; Howard, J. A. K.; Puschmann, H., *J. Appl. Crystallogr.* **2009,** *42* (2), 339-341.
151. Becke, A. D., *The Journal of Chemical Physics* **1993,** *98* (7), 5648-5652.
152. Stephens, P. J.; Devlin, F. J.; Chabalowski, C. F.; Frisch, M. J., *The Journal of Physical Chemistry* **1994,** *98* (45), 11623-11627.
153. Peterson, K. A.; Figgen, D.; Goll, E.; Stoll, H.; Dolg, M., *The Journal of Chemical Physics* **2003,** *119* (21), 11113-11123.
154. Frisch, M. J.; Trucks, G. W.; Schlegel, H. B.; Scuseria, G. E.; Robb, M. A.; Cheeseman, J. R.; Scalmani, G.; Barone, V.; Mennucci, B.; Petersson, G. A.; Nakatsuji, H.; Caricato, M.; Li, X.; Hratchian, H. P.; Izmaylov, A. F.; Bloino, J.; Zheng, G.; Sonnenberg, J. L.; Hada, M.; Ehara, M.; Toyota, K.; Fukuda, R.; Hasegawa, J.; Ishida, M.; Nakajima, T.; Honda, Y.; Kitao, O.; Nakai, H.; Vreven, T.; Montgomery, J., J. A.; ;

Peralta, J. E.; Ogliaro, F.; Bearpark, M.; Heyd, J. J.; Brothers, E.; Kudin, K. N.; Staroverov, V. N.; Kobayashi, R.; Normand, J.; Raghavachari, K.; Rendell, A.; Burant, J. C.; Iyengar, S. S.; Tomasi, J.; Cossi, M.; Rega, N.; Millam, J. M.; Klene, M.; Knox, J. E.; Cross, J. B.; Bakken, V.; Adamo, C.; Jaramillo, J.; Gomperts, R.; Stratmann, R. E.; Yazyev, O.; Austin, A. J.; Cammi, R.; Pomelli, C.; Ochterski, J. W.; Martin, R. L.; Morokuma, K.; Zakrzewski, V. G.; Voth, G. A.; Salvador, P.; Dannenberg, J. J.; Dapprich, S.; Daniels, A. D.; Farkas, Ö.; Foresman, J. B.; Ortiz, J. V.; Cioslowski, J.; Fox, D. J., *Gaussian 09*, Revision D.01, Gaussian, Inc., Wallingford, CT: 2013.
155. Metz, B.; Stoll, H.; Dolg, M., *J. Chem. Phys.* **2000,** *113* (7), 2563-2569.
156. Glendening, E. D.; Landis, C. R.; Weinhold, F., *J. Comput. Chem.* **2013,** *34* (16), 1429-1437.
157. Manson, J.; Webster, C. E.; Pérez, L. M.; Hall, M. B., http://www.chem.tamu.edu/jimp2/index.html.
158. Hall, M. B.; Fenske, R. F., *Inorg. Chem.* **1972,** *11* (4), 768-775.
159. Bursten, B. E.; Jensen, J. R.; Fenske, R. F., *The Journal of Chemical Physics* **1978,** *68* (7), 3320-3321.
160. Baba, A.; Fujiwara, M.; Matsuda, H., *Tetrahedron Lett.* **1986,** *27* (1), 77-80.
161. Fujiwara, M.; Baba, A.; Matsuda, H., *J. Heterocycl. Chem.* **1988,** *25* (5), 1351-1357.
162. Burford, N.; Frazee, C.; McDonald, R.; Ferguson, M.; Patrick, B.; Decken, A., *Chem. Eur. J.* **2018,** *24* (16), 4011-4013.
163. Chitnis, S. S.; Robertson, A. P. M.; Burford, N.; Patrick, B. O.; McDonald, R.; Ferguson, M. J., *Chemical Science* **2015,** *6* (11), 6545-6555.
164. Li, N.; Qiu, R.; Zhang, X.; Chen, Y.; Yin, S.-F.; Xu, X., *Tetrahedron* **2015,** *71* (25), 4275-4281.
165. Hirai, M.; Cho, J.; Gabbaï, F. P., *Chemistry – A European Journal* **2016,** *22* (19), 6537-6541.
166. Arias Ugarte, R.; Devarajan, D.; Mushinski, R. M.; Hudnall, T. W., *Dalton Trans.* **2016,** *45* (27), 11150-11161.
167. Yang, M.; Gabbaï, F. P., *Inorg. Chem.* **2017,** *56* (15), 8644-8650.
168. Pan, B.; Gabbaï, F. P., *J. Am. Chem. Soc.* **2014,** *136* (27), 9564-9567.
169. Benjamin, S. L.; Levason, W.; Reid, G., *Chem. Soc. Rev.* **2013,** *42* (4), 1460-1499.
170. Mizuno, T.; Takeuchi, M.; Hamachi, I.; Nakashima, K.; Shinkai, S., *Journal of the Chemical Society, Perkin Transactions 2* **1998,** (10), 2281-2288.
171. Minghetti, G.; Stoccoro, S.; Cinellu, M. A.; Soro, B.; Zucca, A., *Organometallics* **2003,** *22* (23), 4770-4777.
172. Luzyanin, K. V.; Haukka, M.; Bokach, N. A.; Kuznetsov, M. L.; Kukushkin, V. Y.; Pombeiro, A. J. L., *J. Chem. Soc., Dalton Trans.* **2002,** (9), 1882-1887.
173. Canty, A. J.; Skelton, B. W.; Traill, P. R.; White, A. H., *Aust. J. Chem.* **1992,** *45* (2), 417-422.
174. Begley, M. J.; Sowerby, D. B., *Acta Crystallogr. Sect. C: Cryst. Struct. Commun.* **1993,** *49* (6), 1044-1046.

175. Chval, Z.; Sip, M.; Burda Jaroslav, V., *J. Comput. Chem.* **2008,** *29* (14), 2370-2381.
176. J. L. McInnes, E.; D. Farley, R.; C. Rowlands, C.; J. Welch, A.; Rovatti, L.; J. Yellowlees, L., *J. Chem. Soc., Dalton Trans.* **1999,** (23), 4203-4208.
177. Kelly, R. D.; Brent Young, G., *J. Organomet. Chem.* **1989,** *361* (1), 123-138.
178. Robinson, R.; Karikachery, A. R.; Sharp, P. R., *Dalton Transactions* **2012,** *41* (9), 2601-2611.
179. Oyamada, J.; Kitamura, T., *Tetrahedron Lett.* **2005,** *46* (22), 3823-3827.
180. Oyamada, J.; Kitamura, T., *Tetrahedron* **2007,** *63* (51), 12754-12762.
181. Jia, C.; Lu, W.; Oyamada, J.; Kitamura, T.; Matsuda, K.; Irie, M.; Fujiwara, Y., *J. Am. Chem. Soc.* **2000,** *122* (30), 7252-7263.
182. Chalmers, B. A.; Bühl, M.; Athukorala Arachchige, K. S.; Slawin, A. M. Z.; Kilian, P., *Chemistry – A European Journal* **2015,** *21* (20), 7520-7531.
183. Egbe, D. A. M.; Amer, A. M.; Klemm, E., *Designed Monomers and Polymers* **2001,** *4* (2), 169-175.
184. Zhao, X.-F.; Zhang, C., *Synthesis* **2007,** (4), 551-557.
185. Morgan, G. T.; Burstall, F. H., *J. Chem. Soc.* **1934**, 965-971.
186. Frisch, M. J.; Trucks, G. W.; Schlegel, H. B.; Scuseria, G. E.; Robb, M. A.; Cheeseman, J. R.; Scalmani, G.; Barone, V.; Mennucci, B.; Petersson, G. A.; Nakatsuji, H.; Caricato, M.; Li, X.; Hratchian, H. P.; Izmaylov, A. F.; Bloino, J.; Zheng, G.; Sonnenberg, J. L.; Hada, M.; Ehara, M.; Toyota, K.; Fukuda, R.; Hasegawa, J.; Ishida, M.; Nakajima, T.; Honda, Y.; Kitao, O.; Nakai, H.; Vreven, T.; Montgomery, J., J. A.; ; Peralta, J. E.; Ogliaro, F.; Bearpark, M.; Heyd, J. J.; Brothers, E.; Kudin, K. N.; Staroverov, V. N.; Kobayashi, R.; Normand, J.; Raghavachari, K.; Rendell, A.; Burant, J. C.; Iyengar, S. S.; Tomasi, J.; Cossi, M.; Rega, N.; Millam, J. M.; Klene, M.; Knox, J. E.; Cross, J. B.; Bakken, V.; Adamo, C.; Jaramillo, J.; Gomperts, R.; Stratmann, R. E.; Yazyev, O.; Austin, A. J.; Cammi, R.; Pomelli, C.; Ochterski, J. W.; Martin, R. L.; Morokuma, K.; Zakrzewski, V. G.; Voth, G. A.; Salvador, P.; Dannenberg, J. J.; Dapprich, S.; Daniels, A. D.; Farkas, Ö.; Foresman, J. B.; Ortiz, J. V.; Cioslowski, J.; Fox, D. J., *Gaussian 09*, Revision B.01, Gaussian, Inc.: Wallingford, CT: 2009.
187. Liu, R.; Zhou, D.; Azenkeng, A.; Li, Z.; Li, Y.; Glusac Ksenija, D.; Sun, W., *Chemistry – A European Journal* **2012,** *18* (36), 11440-11448.
188. Zhou, X.; Pan, Q.-J.; Xia, B.-H.; Li, M.-X.; Zhang, H.-X.; Tung, A.-C., *The Journal of Physical Chemistry A* **2007,** *111* (25), 5465-5472.
189. Benz, S.; Poblador-Bahamonde, A. I.; Low-Ders, N.; Matile, S., *Angew. Chem. Int. Ed.* **2018,** *57* (19), 5408-5412.
190. Yang, M.; Tofan, D.; Chen, C.-H.; Jack, K. M.; Gabbaï, F. P., *Angew. Chem. Int. Ed.* **2018,** *57* (42), 13868-13872.
191. Yang, M.; Pati, N.; Belanger-Chabot, G.; Hirai, M.; Gabbaï, F. P., *Dalton Transactions* **2018,** *47* (34), 11843-11850.
192. Arias-Ugarte, R.; Devarajan, D.; Mushinski, R. M.; Hudnall, T. W., *Dalton Transactions* **2016,** *45* (27), 11150-11161.
193. Arias-Ugarte, R.; Hudnall, T. W., *Green Chemistry* **2017,** *19* (8), 1990-1998.

194. Fukin, G. K.; Baranov, E. V.; Poddel'sky, A. I.; Cherkasov, V. K.; Abakumov, G. A., *ChemPhysChem* **2012,** *13* (17), 3773-3776.
195. Poddel'sky, A. I.; Kurskii, Y. A.; Piskunov, A. V.; Somov, N. V.; Cherkasov, V. K.; Abakumov, G. A., *Appl. Organomet. Chem.* **2011,** *25* (3), 180-189.
196. Cherkasov, V. K.; Abakumov, G. A.; Grunova, E. V.; Poddel'sky, A. I.; Fukin, G. K.; Baranov, E. V.; Kurskii, Y. V.; Abakumova, L. G., *Chem.--Eur. J.* **2006,** *12* (Copyright (C) 2012 American Chemical Society (ACS). All Rights Reserved.), 3916-3927.
197. Ke, I.-S.; Myahkostupov, M.; Castellano, F. N.; Gabbaï, F. P., *J. Am. Chem. Soc.* **2012,** *134* (37), 15309-15311.
198. Hirai, M.; Myahkostupov, M.; Castellano, F. N.; Gabbaï, F. P., *Organometallics* **2016,** *35* (11), 1854-1860.
199. Christianson, A. M.; Gabbaï, F. P., *Chem. Commun.* **2017,** *53* (16), 2471-2474.
200. Kumar, A.; Yang, M.; Kim, M.; Gabbaï, F. P.; Lee, M. H., *Organometallics* **2017,** *36* (24), 4901-4907.
201. Christianson, A. M.; Gabbaï, F. P., *Organometallics* **2017,** *36* (16), 3013-3015.
202. Christianson, A. M.; Rivard, E.; Gabbaï, F. P., *Organometallics* **2017,** *36* (14), 2670-2676.
203. Qiu, J.; Song, B.; Li, X.; Cozzolino, A. F., *PCCP* **2018,** *20* (1), 46-50.
204. Lee, L. M.; Tsemperouli, M.; Poblador-Bahamonde, A. I.; Benz, S.; Sakai, N.; Sugihara, K.; Matile, S., *J. Am. Chem. Soc.* **2019,** *141* (2), 810-814.
205. Park, G.; Brock, D. J.; Pellois, J.-P.; Gabbaï, F. P., *Chem* **2019**.
206. Twilton, J.; Le, C.; Zhang, P.; Shaw, M. H.; Evans, R. W.; MacMillan, D. W. C., *Nature Reviews Chemistry* **2017,** *1*, 0052.
207. Lo, K. K., *Acc. Chem. Res.* **2015,** *48* (12), 2985-2995.
208. Costa, R. D.; Ortí, E.; Bolink, H. J.; Monti, F.; Accorsi, G.; Armaroli, N., *Angew. Chem. Int. Ed.* **2012,** *51* (33), 8178-8211.
209. Dixon, I. M.; Collin, J.-P.; Sauvage, J.-P.; Flamigni, L.; Encinas, S.; Barigelletti, F., *Chem. Soc. Rev.* **2000,** *29* (6), 385-391.
210. Lo, Y.-H.; Gabbaï, F. P., *Organometallics* **2018,** *37* (15), 2500-2506.
211. Sauvageot, E.; Lafite, P.; Duverger, E.; Marion, R.; Hamel, M.; Gaillard, S.; Renaud, J.-L.; Daniellou, R., *J. Organomet. Chem.* **2016,** *808*, 122-127.
212. Barbieri, G.; Cinquini, M.; Colonna, S.; Montanari, F., *Journal of the Chemical Society C: Organic* **1968,** (0), 659-663.
213. Zhou, G.; Ho, C.-L.; Wong, W.-Y.; Wang, Q.; Ma, D.; Wang, L.; Lin, Z.; Marder, T. B.; Beeby, A., *Adv. Funct. Mater.* **2008,** *18* (3), 499-511.
214. Ladouceur, S.; Fortin, D.; Zysman-Colman, E., *Inorg. Chem.* **2010,** *49* (12), 5625-5641.
215. Dragonetti, C.; Falciola, L.; Mussini, P.; Righetto, S.; Roberto, D.; Ugo, R.; Valore, A.; De Angelis, F.; Fantacci, S.; Sgamellotti, A.; Ramon, M.; Muccini, M., *Inorg. Chem.* **2007,** *46* (21), 8533-8547.
216. Abrahamsson, M.; Becker, H.-C.; Hammarström, L.; Bonnefous, C.; Chamchoumis, C.; Thummel, R. P., *Inorg. Chem.* **2007,** *46* (24), 10354-10364.
217. Chen, C.-H.; Gabbaï, F. P., *Chemical Science* **2018,** *9* (29), 6210-6218.

APPENDIX

CHAPTER II SUPPLEMENT

A.1 Synthesis and characterization of cationic gold-germanium complex

To further understand the Z-type ligand effect by germanium center, we decided to work with Complex [**69**][Cl], which has been synthesized by Dr. Elham Tabei, presents some interesting opportunities for catalysis. To have a general picture about the catalytic activity of this complex, we chose the propargylic amide cyclization as our benchmark reaction catalyzed by 2 mol % [**69**][Cl] / 4 mol% $AgSbF_6$ in dichloromethane. A quantitative yield of cyclized product was observed after 8 hours (Figure 122).

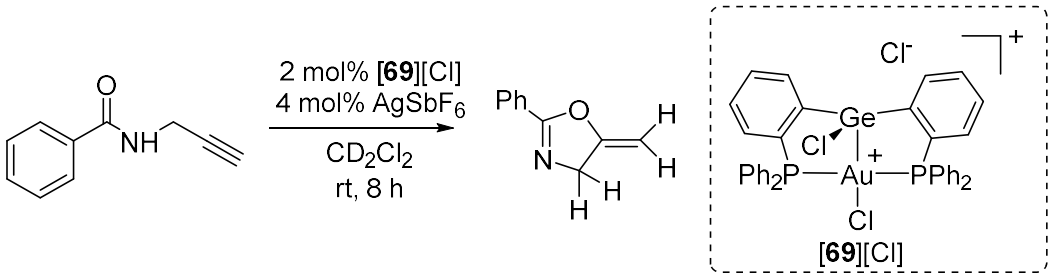

Figure 122. Propargylic amide cyclization catalyzed by [**69**][Cl]/$AgSbF_6$.

Although complex [**69**][Cl] displayed catalytic activity in this reaction, the slow reaction rate spurred us to question whether the substitution of chloride by fluoride would make the complex more acidic and more catalytic active. The study of complex [**20**]$^+$ has shown higher Lewis acidity after fluoride-chloride exchange at the antimony center.[61] With a similar transformation in mind, we treated [**69**][Cl] with 2 equivalents of AgF in dichloromethane for 16 hours (Figure 123a). ^{31}P NMR spectroscopy showed the

appearance of one new signal at 55.02 ppm. Single crystals were obtained by diffusion of diethyl ether into a solution of **70** in dichloromethane (Figure 123b). The asymmetric unit of the complex contains two independent molecules which display very similar geometries. The germanium center adopts a distorted trigonal bipyramidal geometry, in which the gold and one fluoride ligand are at the axial positions. The average of distances for the Au–Ge and Ge–F separations are of 2.878(2) Å and 1.80(1) Å, respectively. Another indicator of the geometry is the sum of C–Ge–C and F2–Ge–C angles, which is 358.9(6) °, close to ideal value of 360°. The bond distance between the germanium and the fluoride at the equatorial is 1.754(9)Å in average, which is shorter than Ge–F1, likely due to Au→Ge donation. The P–Au–P angle is 161.8(1) °, showing that the gold adopts a distorted square planar with a chloride attached to the gold center trans to the germanium center. The square planar geometry suggests strong donation from the d orbital of the gold center to the germanium atom, resulting in an electronic configuration close to a classical d^8 metal center.

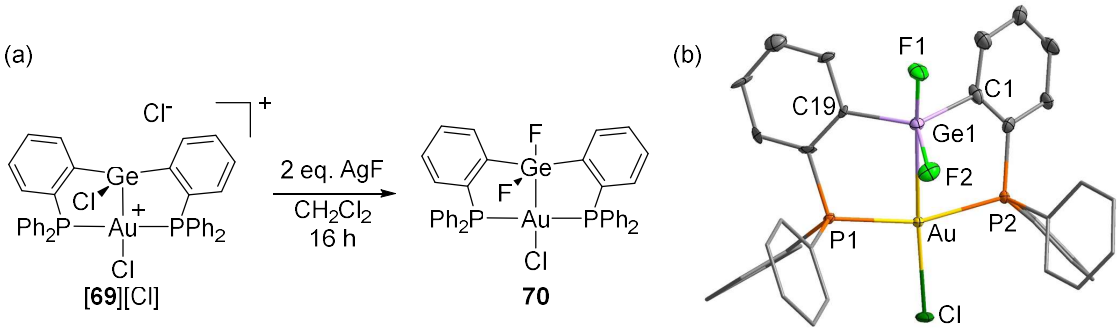

Figure 123. (a) Synthesis of complex **70**. (b) Solid-state structure of **70**. Thermal ellipsoids are drawn at the 50% probability level. The phenyl groups are drawn in wireframe, the hydrogen atoms, interstitial solvent molecules and counteranions are omitted for clarity.

With the aim of isolating the active gold complex, we treated complex **70** with $AgSbF_6$ in dichloromethane for chloride abstraction, which lead to the clean formation of the corresponding cationic complex $[\mathbf{71}]^+$ with a hexafluoroantimonate as an anion. (Figure 124). The ^{31}P NMR spectrum of [**71**][SbF_6] shows a signal at 48.38 ppm. The ^{19}F NMR spectrum displays two broad signals at -118.6 and -132.6 ppm and we assign the former one corresponding to germanium-bound fluoride ligands, and the latter one corresponding to the SbF_6^- anion.

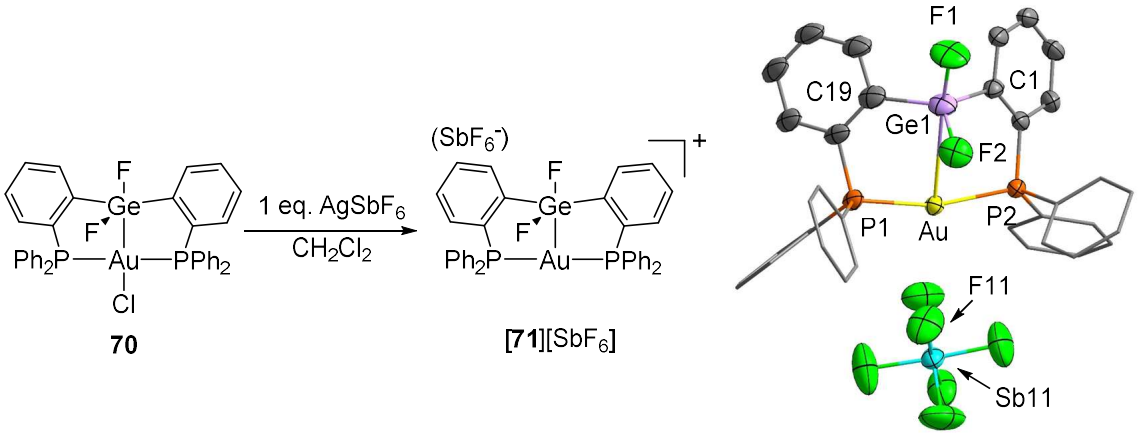

Figure 124. (a) Synthesis of complex [**71**][SbF_6]. (b) Solid-state structure of [**71**][SbF_6]. Thermal ellipsoids are drawn at the 50% probability level. The phenyl groups are drawn in wireframe, and the hydrogen atoms are omitted for clarity.

A crystal of [**71**][SbF_6] suitable for X-ray diffraction was obtained by diffusion of diethyl ether into a solution of [**71**][SbF_6] in dichloromethane. The germanium center adopts a distorted trigonal bipyramidal geometry, indicated by the fact that sum of C–Ge–C and F2–Ge–C angles is equal to 352.5(2) °. The Ge–Au bond distance is 3.0617(7)Å, which is longer than that in complex **70**. A similar phenomenon was observed upon the formation of complex $[\mathbf{20}]^+$ via chloride abstraction. It is suggested

that the removal of the chloride from the gold center reduce the metallobasicity, causing a weaker Au→Ge donation. The weaker donation from gold to germanium also affect the length of Ge–F bond lengths, which both become shorter in complex [**71**]$^+$ (Ge–F1 = 1.739(4); Ge–F2 = 1.727(4)Å) than those in complex **70**. Long interaction between complex [**71**]$^+$ and the SbF_6^- anion was observed. The bond distance between Au and F11 is 3.030(5)Å, which suggest the strong Lewis acidity of the gold center.

We also make an interesting observation when [**69**][Cl] was treated with $AgSbF_6$ (Figure 125). The first and second equivalents of $AgSbF_6$ both lead to the clean formation of a new species, whose ^{31}P resonances are at 68.65 ppm and 69.16 ppm, respectively. The third equivalent of $AgSbF_6$ lead to a new signal emerging at 48.38 ppm and 7 equivalents of $AgSbF_6$ is necessary to complete the transformation. The resulting complex was crystalized by the diffusion of diethyl ether into a solution of dichloromethane. Surprisingly, the structure of the resulting complex was that of [**71**][SbF_6], indicating halide exchange between the germanium center and the SbF_6^- anion.

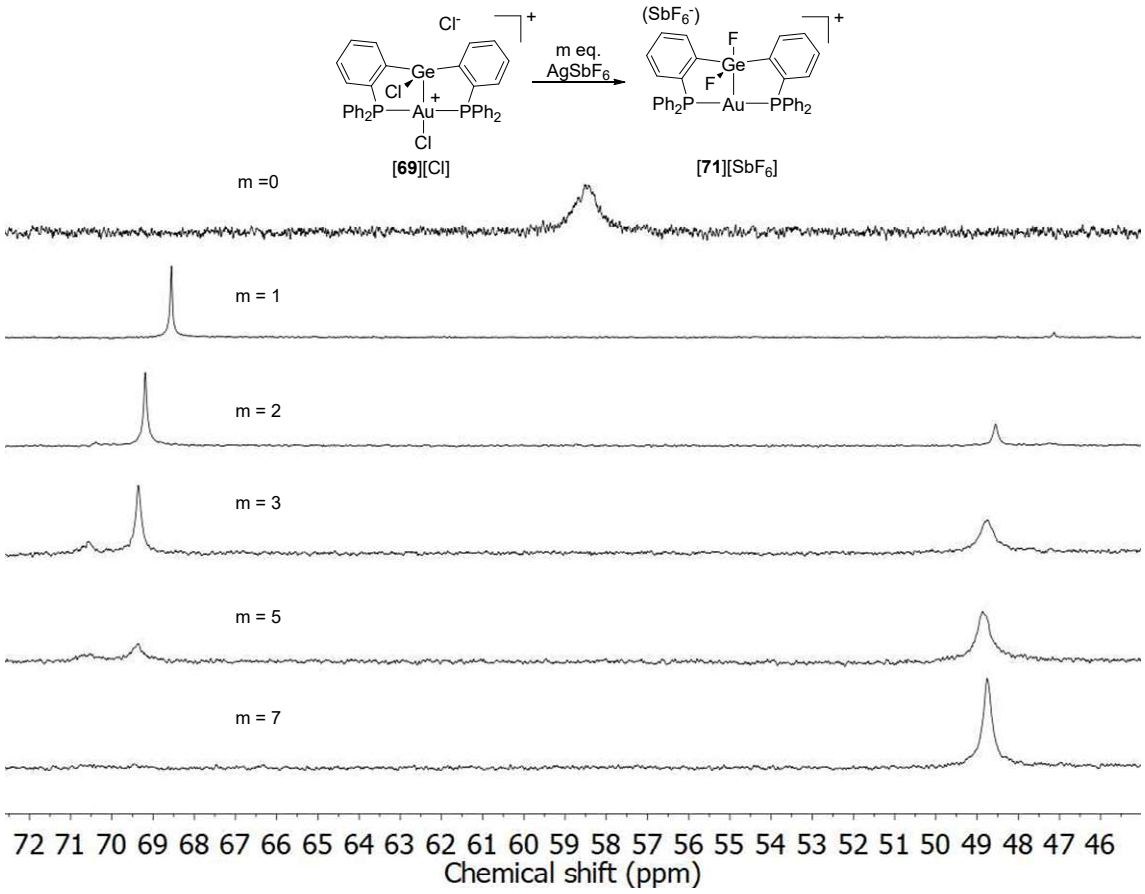

Figure 125. Synthesis of [**71**][SbF_6] from [**69**][Cl].

A.2 Experimental Section

Synthesis of 70 To a stirred solution of [**69**][Cl] (50 mg, 0.056 mmol) in CH_2Cl_2 (5 mL) was added solid AgF (15 mg, 0.12 mmol). After the resulting mixture was stirred for 12 h, the solution was filtered and the solvent was evaporated under vacuum. Recrystallization of the residue from CH_2Cl_2/diethyl ether yielded a colorless solid of **70** (30 mg, 62%). Single crystals of **70** suitable for X-ray diffraction were obtained by diethyl ether slowly diffusion into a CH_2Cl_2 solution at room temperature. $^{31}P\{^1H\}$ NMR (202.16 MHz; CD_2Cl_2): δ 55.02.

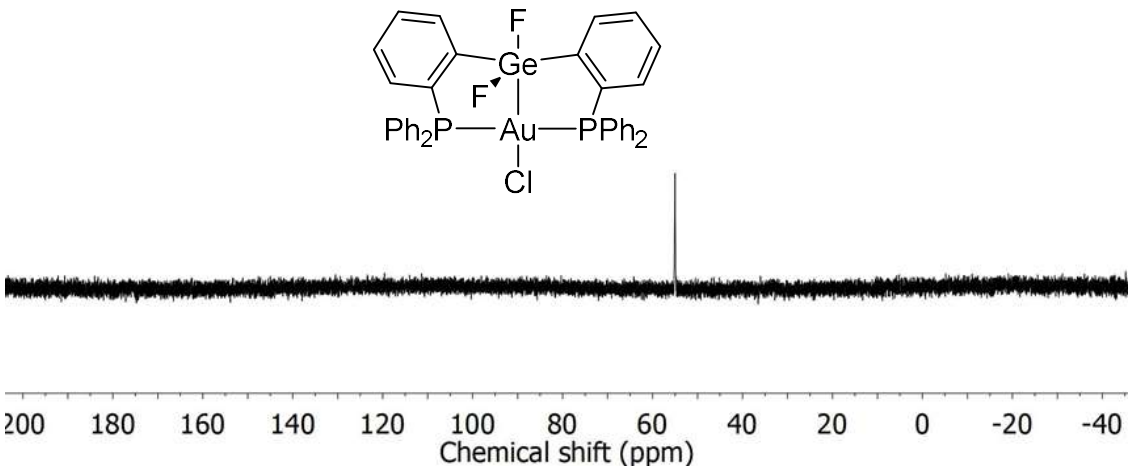

Figure 126. $^{31}P\{^{1}H\}$ NMR spectrum of **70** in CD_2Cl_2.

Synthesis of [71][SbF$_6$] Method a: To a stirred solution of **70** (30 mg, 0.035 mmol) in CH_2Cl_2 (5 mL) was added solid $AgSbF_6$ (12 mg, 0.035 mmol). After the resulting mixture was stirred for 10 minutes, the solution was filtered and the solvent was evaporated under vacuum. Recrystallization of the residue from CH_2Cl_2/diethyl ether yielded a colorless solid of [**71**][SbF_6] (28 mg, 75%). Method b: To a stirred solution of [**69**][Cl] (50 mg, 0.056 mmol) in CH_2Cl_2 (5 mL) was added solid $AgSbF_6$ (135 mg, 0.40 mmol). After the resulting mixture was stirred for 1 h, the solution was filtered and the solvent was evaporated under vacuum. Recrystallization of the residue from CH_2Cl_2/diethyl ether yielded a colorless solid of [**71**][SbF_6]. (41 mg, 68%). Single crystals of [**71**][SbF_6] suitable for X-ray diffraction were obtained by slow diffusion of diethyl ether into a CH_2Cl_2 solution at room temperature. $^{31}P\{^{1}H\}$ NMR (202.16 MHz; CD_2Cl_2): δ 48.38. $^{19}F\{^{1}H\}$ NMR (469.89 MHz; CD_2Cl_2): δ -118.6 (br), -132.6 (br).

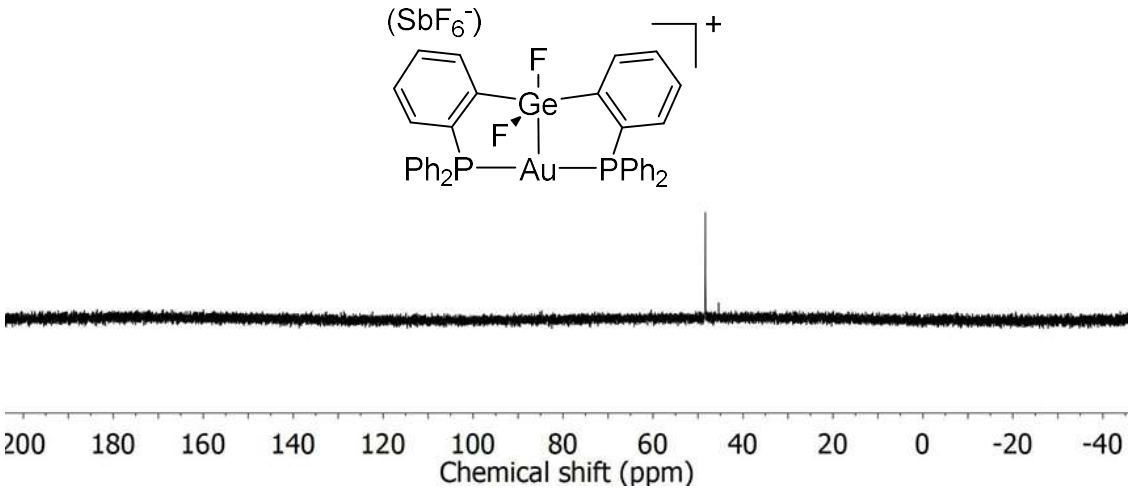

Figure 127. $^{31}P\{^{1}H\}$ NMR spectrum of [**71**][SbF_6] in CD_2Cl_2.

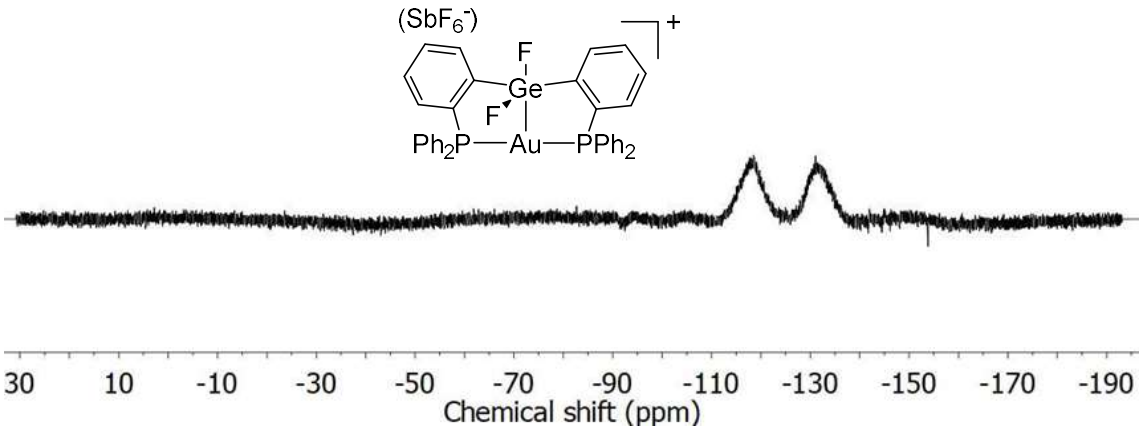

Figure 128. $^{19}F\{^{1}H\}$ NMR spectrum of [**71**][SbF_6] in CD_2Cl_2.

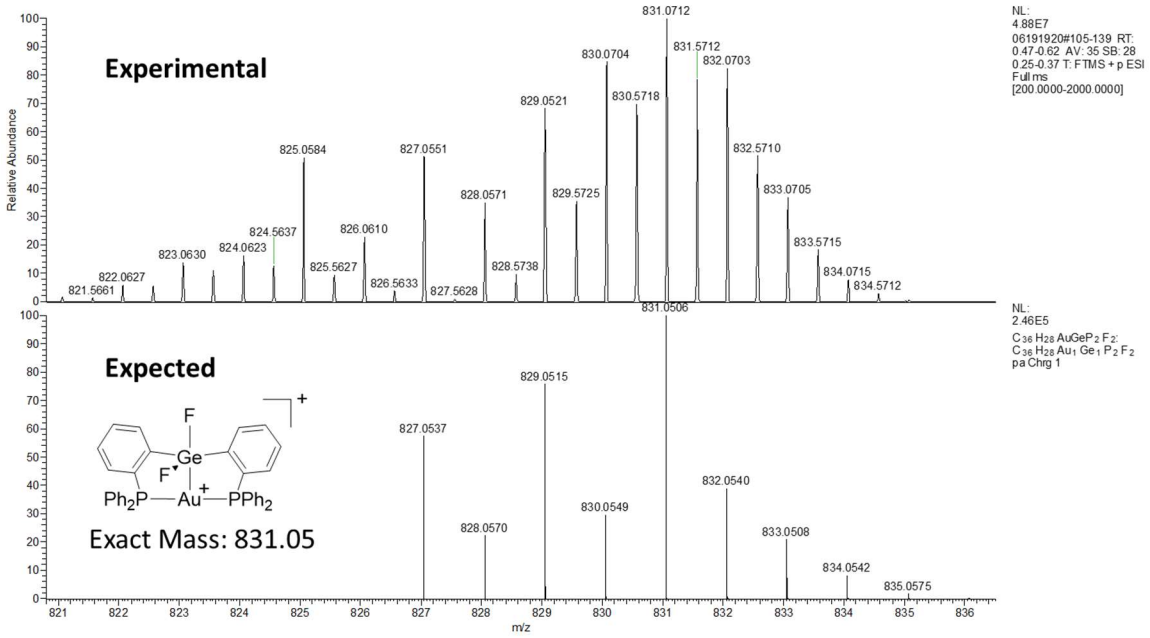

Figure 129. ESI unit mass spectrum of [**71**][SbF_6].